

AN EXPERIMENTAL INVESTIGATION OF SMOOTH-BODY FLOW  
SEPARATION

A Dissertation

Submitted to the Graduate School  
of the University of Notre Dame  
in Partial Fulfillment of the Requirements  
for the Degree of  
Doctor of Philosophy

by  
Daniel J. Simmons

---

Flint O. Thomas, Director

Graduate Program in Aerospace and Mechanical Engineering

Notre Dame, Indiana

July 2020

© Copyright 2020

Daniel J. Simmons

All Rights Reserved

# AN EXPERIMENTAL INVESTIGATION OF SMOOTH-BODY FLOW SEPARATION

Abstract

by

Daniel J. Simmons

The accurate and reliable simulation of smooth-body turbulent flow separation represents a considerable challenge for current CFD turbulence models. Consequently, there has been a recent push for high quality, experimental, benchmark flow separation studies to be conducted for the purpose of CFD validation. This dissertation documents a series of benchmark experimental studies on smooth-body flow separation. Three flow experiments are investigated over a single two-dimensional ramp geometry—two undergoing flow separation (one larger-scale and one smaller-scale) and one attached flow—all of which result from a user-imposed adverse pressure gradient (APG) applied to a turbulent boundary layer. These data sets and associated documentation are now available on the NASA Langley Research Center Turbulence Modeling Resource website [1].

Although the geometry and incoming flow in these experiments are spanwise two-dimensional in the mean, oil-film surface flow visualization shows that in each case separation is three-dimensional in character while reattachment is two-dimensional.

Utilizing multiple flow visualization images, both surface and off-surface topology maps of separation were created. These maps indicate that the central flow separation is characterized by the owl-face pattern of the fourth kind. It is found that this pattern is an ubiquitous feature of flow separation. Additional investigation revealed that this owl-face pattern is part of a generic and simple structure consisting of a repeating pattern of saddle points and foci for separation and nodes and saddle points for reattachment. The pattern results when the streamwise surface curvature induces a small secondary flow, which interacts with the wind tunnel sidewalls. Furthermore, passive flow control studies reveal that, while the centerline flow separation extent is highly influenced by the sidewall separation, its characteristic separation structure is independent of the sidewall separation.

Extensive off-surface flow measurements, conducted via two-component LDV, were used to characterize the streamwise and spanwise flow development. Despite its three-dimensionality, the streamwise mean flow develops in a typical fashion—becoming inflectional due to the imposed streamwise APG—resulting in the formation of an embedded shear layer. Attempts to scale the flow using embedded shear layer scaling highlight that, while the mean profiles exhibit excellent collapse, the scaled turbulent stress profiles do not exhibit collapse due to streamwise surface curvature effects. Furthermore, experimental evidence is provided indicating that the Reynolds stresses are effectively “frozen”, with streamwise changes resulting from a rotating local wall-normal coordinate. A coordinate system fixed at the no-curvature transition from convex to concave ramp curvature yields turbulent shear stress magnitudes that are constant with streamwise development.

This dissertation is dedicated to my wife, Lauren, for her love, support, and encouragement.

## CONTENTS

Figures.....	vii
Tables .....	xx
Acknowledgments.....	xxi
Chapter 1: Introduction .....	1
1.1 Motivation.....	1
1.2 Background and Literature Review .....	4
1.3 Objectives and Organization.....	14
Chapter 2: Experimental Facility, Setup, and Introduction .....	18
2.1 White Field Mach 0.6 Wind Tunnel Facility .....	18
2.2 Model Geometry and Wind Tunnel Installation .....	19
2.3 Coordinate Systems .....	23
2.4 Diagnostic Techniques.....	26
2.4.1 Surface Pressure Instrumentation .....	26
2.4.2 Pitot-Tube Instrumentation .....	28
2.4.3 Hot-Wire Anemometry Instrumentation.....	31
2.4.4 Oil-Film Interferometry Instrumentation .....	37
2.4.5 Laser Doppler Velocimetry Instrumentation .....	42
2.4.6 Surface Flow Visualization Technique .....	49
Chapter 3: Boundary Conditions .....	52
3.1 Operating Conditions .....	52
3.2 Ceiling Configuration of Separation Cases A, B, and C .....	55
3.3 Surface Pressure Measurements .....	56
3.4 Surface Skin Friction Measurements .....	58
3.5 Incoming Boundary Layer Profiles.....	60
3.5.1 Development Plate .....	60
3.5.2 Sidewalls .....	68
Chapter 4: Surface Flow Characteristics.....	74
4.1 Surface Flow Topography.....	75
4.1.1 Case A – Larger-Scale Separation .....	76
4.1.2 Case B – Smaller-Scale Separation.....	85
4.1.3 Case C – Attached Flow .....	88
4.2 Commonality of the Surface Flow Patterns .....	89

4.3 Aspect Ratio Effects on Smooth-Body Flow Separation.....	95
 Chapter 5: Flow Topology .....	102
5.1 Overview of Separation Topology .....	102
5.2 Flow Topology .....	107
5.2.1 Surface Flow Topology.....	107
5.2.2 Off-Surface Flow Topology.....	108
5.3 The Owl-Face Patterns.....	116
5.3.1 The Four Types of Owl-Face Patterns .....	116
5.3.2 Simplified Surface Flow Topology.....	120
5.3.3 Surface Flow Topology Comparison .....	124
5.4 Generalized Separation Structure .....	125
5.5 Realized Separation Structures .....	129
 Chapter 6: Streamwise Surface Curvature and Sidewall Effects.....	133
6.1 Surface Curvature and Sidewall Effects .....	134
6.2 Passive Flow Control Experiments.....	146
6.2.1 Ramp Application .....	147
6.2.2 Sidewall Application.....	154
6.2.3 Summary .....	163
6.3 Preliminary CFD Comparison .....	164
 Chapter 7: Flow Field Development.....	167
7.1 Overview of Flow Field Measurements.....	167
7.2 Mean Flow Development.....	170
7.2.1 Case A – Larger-Scale Separation .....	170
7.2.2 Case B – Smaller-Scale Separation.....	176
7.2.3 Case C – Attached Flow .....	179
7.3 Turbulent Stress Development.....	182
7.3.1 Case A – Larger-Scale Separation .....	182
7.3.2 Case B – Smaller-Scale Separation.....	186
7.3.3 Case C – Attached Flow .....	189
7.4 Separation Extent .....	192
 Chapter 8: Scaling the Flow Development .....	200
8.1 Review of Scaling APG Flows .....	201
8.2 Shear Layer Growth Rate and Scaling Applicability.....	204
8.3 Outer Variable Scaling.....	211
8.4 Embedded Shear Layer Scaling .....	213
8.5 Accounting for the Wall-Normal Variation in Stress Peak .....	215
8.6 Modified Embedded Shear Layer Scaling .....	219
8.7 Streamwise Surface Curvature Effects .....	222
8.8 Coordinate Rotation for Reynolds Shear Stress.....	229
 Chapter 9: Conclusions and Recommendations for Future Work .....	239
9.1 Conclusions.....	239
9.2 Future Work .....	246

9.3 Practical Considerations for Future Validation Experiments .....	249
Appendix A: Experimental Geometry .....	252
A.1 Additional Experimental Geometry Images .....	252
A.2 Ramp Model Geometry.....	253
A.3 Internal Inlet Contour.....	254
A.4 Turbulent Boundary Layer (TBL) Development Plate .....	255
A.5 Flexible Top Wall Insert / Turnbuckle Assembly.....	256
A.6 Diffuser Transition.....	264
A.7 Adjustable Wind Tunnel Sidewall .....	266
Appendix B: Diagnostic Techniques .....	268
B.1 Surface Pressure Tap Locations .....	268
B.2 Oil-Film Interferometry Silicone Oil .....	271
B.3 Laser Doppler Velocimetry Particle Seeding.....	272
Appendix C: Operating Test Conditions.....	275
C.1 Temperature .....	275
C.2 Pressure .....	278
C.3 Relative Humidity .....	278
C.4 Density .....	280
C.5 Viscosity.....	281
C.6 Freestream Velocity .....	281
C.7 Reynolds Number.....	284
Appendix D: Uncertainty Analysis .....	285
D.1 Surface Pressure Uncertainty Analysis .....	285
D.2 Pitot-Tube Measurement Uncertainty Analysis .....	289
D.3 Hot-Wire Anemometry Uncertainty Analysis .....	293
D.4 Oil-Film Interferometry Uncertainty Analysis .....	303
D.5 Laser Doppler Velocimetry Uncertainty Analysis.....	305
D.5.1 Processing of Data: .....	306
D.5.2 Uncertainty Analysis:.....	310
D.5.2.1 Uncertainty Analysis – Local Values.....	311
D.5.2.1.1 Random Uncertainty .....	311
D.5.2.1.2 Filtering Uncertainty .....	311
D.5.2.1.3 Temperature Variation Uncertainty .....	313
D.5.2.1.4 Calibration Uncertainty .....	314
D.5.2.1.5 Instrument Uncertainty .....	315
D.5.2.1.6 Velocity Bias Uncertainty .....	315
D.5.2.1.7 Validation Bias Uncertainty .....	316
D.5.2.1.8 Systematic Standard Uncertainty .....	316
D.5.2.1.9 Combined and Expanded Uncertainties .....	317
D.5.2.2 Uncertainty Analysis – Global Values:.....	319
D.5.2.2.1 Combined and Expanded Uncertainties .....	321
Appendix E: Flow Separation Characteristics .....	322

E.1 Surface Flow Visualization of Downward Angled VGs Installed on the Sidewalls .....	322
Appendix F: Flow Characteristics and Analysis.....	325
F.1 Ratio of Vorticity Thickness to Boundary Layer Thickness .....	325
F.2 Embedded Shear Layer Scaling of the Mean Flow .....	326
F.3 Time Scales of the Flow .....	326
Bibliography .....	328

## FIGURES

Figure 1.1 Classification of typical flow problems. I: separation fixed by the geometry, II: separation induced by a pressure gradient on a curved surface, III: separation strongly influenced by the dynamics of the incoming boundary layer (Figure and caption modified from Deck [16]) .....	7
Figure 2.1 Schematic of the White Field Mach 0.6 wind tunnel facility.....	19
Figure 2.2 Drawing of the model geometry installed in the Notre Dame Mach 0.6 wind tunnel test section viewed from the outer wind tunnel loop side.....	20
Figure 2.3 Labeled schematic drawing of the test section and model geometry viewed from the inner wind tunnel loop side .....	21
Figure 2.4 Photograph of the test section model with the sidewall door removed viewed from the outer wind tunnel loop. Note that the sidewall door absent in this photograph is the adjustable one.....	23
Figure 2.5 Side view schematic of the global (X, Y, Z) and local (x, y, z) coordinate systems with respect to the ramp geometry .....	25
Figure 2.6 Schematic showing both the streamwise and multiple spanwise static pressure taps on the convex ramp surface and the global (X, Y, Z) and local (x, y, z) coordinate systems .....	25
Figure 2.7 Sample calibration curve for the Scanivalve SSS-48C pneumatic scanner using an NI USB-6343 DAQ.....	28
Figure 2.8 Wall-normal sidewall boundary layer profiles for inside loop (a) and outside loop (b) for Case A. The uncertainty intervals are on the order of the symbol size. Note that the profile location is not the same on both sides, see Table 2.1.....	31
Figure 2.9 Photograph of custom camera alignment device used to determine and align the hot-wire's position above the surface .....	32
Figure 2.10 Typical hot-wire calibration curve with voltage (a) and temperature (b) as functions of velocity. Note that confidence intervals are included in the voltage plot and are due to the calibration uncertainty.....	35

Figure 2.11 Typical mean velocity (a) and turbulent normal stress (b) profiles plotted with confidence intervals. These profiles are for Case B with the origin of the profile located at (X, Y, Z) = (-0.678, 0.600, 0.457). ....	37
Figure 2.12 Photograph (a) and illustration (b) of test fixture, shown in place at the X = -0.678 m location, developed to illuminate and photograph the interferogram images .....	39
Figure 2.13 Example interferogram for Case B taken at X = 0.007 m and yielding a fringe spacing of $\Delta x = 3.55$ mm and skin friction coefficient of $C_f = 0.00272$ .....	40
Figure 2.14 Example histogram (a) and Fourier series fit (b) for the 7 <sup>th</sup> and 2 <sup>nd</sup> order Fourier series corresponding to the interrogation region for Case B, X = 0.007 m .....	41
Figure 2.15 Example kinematic viscosity (a) and dynamic pressure and temperature (b) curves as functions of time for Case B, X = 0.007 m, with a 30 minutes tunnel run time .....	42
Figure 2.16 Photograph of the LDV system, utilizing the 400 mm lens, in operation, taking a profile at the start of the ramp, X = 0 m.....	43
Figure 2.17 Schematic of LDV probe alignment relative to test section. Note, the image is oriented looking downstream.....	45
Figure 2.18 Example wall-normal mean (a) and turbulent stress (b) profiles plotted with 95% confidence intervals for Case B, located at X = 0.75 m and Z = 0 m .....	48
Figure 2.19 Typically convergence plots of the turbulent shear stress for a profile point with a low magnitude (a) and high magnitude (b), showing a running average of the turbulent shear stress versus the number of samples with red lines representing the final value $\pm 5\%$ .....	49
Figure 2.20 Photographs of the diffuser mounted video camera (a) and the UV light fixture installed and illuminating the surface flow (b).....	51
Figure 3.1 Illustration of ceiling configurations of separation cases A and B, and of attached flow case C .....	56
Figure 3.2 Centerline static pressure coefficient distributions for Cases A, B, and C. Note that closed symbols represent the pressure coefficient distribution and open symbols represent the pressure coefficient gradient distribution.....	57
Figure 3.3 Spanwise pressure coefficient distributions for Cases A, B, and C. Note that the uncertainty in the measurements is on the order of the symbol size.....	58

Figure 3.4 Boundary layer profiles acquired on the development plate at $X = -0.678$ m and scaled using outer variables for Cases A, B and C compared to both preliminary hot-wire data acquired at $X = -0.56$ m and data from Klebanoff [65]	61
Figure 3.5 Centerline hot-wire (HW) boundary layer profiles, plotted in inner variables, for Case A, $X = -0.678$ m, compared to both preliminary hot-wire, and LDV profiles acquired at $X = -0.56$ m .....	64
Figure 3.6 Turbulence intensity profiles acquired via hot-wire anemometry on the development plate at $X = -0.678$ m with comparisons to the LDV data, $X = -0.56$ m, and Klebanoff [65].....	65
Figure 3.7 Turbulence intensity profiles plotted in inner variables, for Case A with comparisons of: hot-wire (HW) located at $X = -0.678$ m, LDV located at $X = -0.56$ m, Klebanoff [65], and the predicted turbulence peak magnitude calculated via Eqn. (3.14) from Hutchins et al. [67] .....	66
Figure 3.8 Test section cross-sectional view, oriented looking upstream, highlighting the starting locations of the development plate and sidewall boundary layer profiles acquired using hot-wire anemometry. All profiles shown here are located at $X = -0.678$ m with the coordinate [Y, Z] pair denoting each profile location. ....	69
Figure 3.9 Sidewall boundary layer profiles, scaled using outer variables, for all three test cases using both hot-wire anemometry (HW) and pitot-tube (PT) measurements. Note that the legend provides the surface starting point for each profile given in [X,Y,Z] coordinates, with circle and diamond symbols representing the wind tunnel outer and inner loops respectively. ....	71
Figure 3.10 Sidewall turbulence intensity profiles, scaled using outer variables, for all three test cases using hot-wire anemometry (HW). Note that the legend provides the surface starting point for each profile given in [X,Y,Z] coordinates, with circle and diamond symbols representing the wind tunnel outer and inner loops respectively. ....	73
Figure 4.1 Global surface flow visualization for Case A, with four interrogations regions highlighted. Incoming flow is from right to left. ....	77
Figure 4.2 View 1, from Figure 4.1, with the yellow dashed line indicating separation and the orange dashed line showing how the near sidewall flow is topologically isolated from the central flow separation. Incoming flow is from top to bottom. .	78
Figure 4.3 View 2, Figure 4.1, with the yellow dashed line indicating separation and the orange dashed line showing how the near sidewall flow is topologically isolated from the central flow separation. Incoming flow is from top to bottom.....	80
Figure 4.4 Close up views of the reattachment in the central ramp region (View 4) and near the wind tunnel outer loop sidewall (View 3). Incoming flow in both images is from right to left. ....	81

Figure 4.5 (a) Surface flow visualization on the ramp surface and wind tunnel outer loop sidewall, (b) with close up views highlighting the sidewall juncture flow separation and (c) sidewall reattachment. Incoming flow is from left to right in all images.....	82
Figure 4.6 Two-dimensionality of the reattachment region, captured using two different UV illuminating surface flow solutions. Note that incoming flow is from left to right in both images.....	84
Figure 4.7 Global surface flow visualization for the small-scale separation, Case B, highlighting two viewing regions to be analyzed in greater detail. The incoming flow is from right to left.....	86
Figure 4.8 View 1, from Figure 4.7, highlighting the topological features on the far side (wind tunnel inner loop) with yellow dashed lines indicating separation, orange dashed lines showing the isolation of the near sidewall flow from the central flow separation, and red dashed lines indicating reattachment. The incoming flow is from right to left.....	87
Figure 4.9 View 2, from Figure 4.7, highlighting the topological features on the near side (wind tunnel outer loop) with yellow dashed lines indicating separation, orange dashed lines showing how the near sidewall flow is topologically isolated from the central flow separation, and magenta dashed lines indicating reattachment. The incoming flow is from right to left.....	88
Figure 4.10 Global surface flow visualization for the attached flow, Case C, highlighting the symmetric pockets of sidewall separation that remain. The incoming flow is from top to bottom.....	89
Figure 4.11 Comparison of the baseline surface flow visualization of Jenkins et al. [48] (c), and Koklu and Owens [52] (b), utilizing the same Stratford ramp geometry, (a), in both studies.....	93
Figure 4.12 Comparison of the Notre Dame (ND) ramp profile to that of similar studied ramp geometries. All geometries were scaled to match the height of the ND ramp, with their respective aspect ratios maintained. Note that symbols are used when the geometry was not adequately defined and had to be digitized from images. ..	97
Figure 4.13 Effect of aspect ratio, L/W/H, on the spanwise extent of secondary flow structures. The simulation was conducted at the University of Notre Dame by Wang and Zhou [80] and utilized 3D-RANS simulations with the SA-RC turbulence model.....	100
Figure 5.1 Singular point classifications based off of their mathematical description stemming from the negative trace and determinant of the Jacobian formed from the wall shear stress vector. ....	104

Figure 5.2 Topological map (phase portrait) sketch of the flow for the large-scale separation case, Case A, roughly drawn to scale with the flow field topography presented in the previous chapter.....	108
Figure 5.3 Streamwise slice of the centerline flow topology for Cases A, B, and C, highlighting the process leading to the inverse saddle node bifurcation that yields attached flow for Case C.....	110
Figure 5.4 Illustration of the off-surface separating flow for Case A as it advects downstream with blue lines representing the surface flow, red lines representing the dividing line of separation as it departs from the surface, and purple lines representing the central separation region .....	113
Figure 5.5 Sketch of the expected topology of the flow taken at reattachment (a), and mean velocity acquired via LDV at $X = 0.9$ m highlighting crossflow (b). Note that in the given velocity data only the $V$ -component was available at $z = 0$ , with a symmetry assumption yielding $W = 0$ .....	114
Figure 5.6 Mean flow profiles of the streamwise, $U$ , wall-normal, $V$ , and spanwise, $W$ , components of velocity acquired at $X = 0.9$ m and $Z = -0.26$ m. Note that the wall-normal coordinate, $y$ , is in local coordinates while the profile location is defined in global coordinates. ....	116
Figure 5.7 Topological structures of owl face patterns of the first (a), second (b), third (c), and fourth (d) kinds as defined by Perry and Hornung [91] .....	117
Figure 5.8 Synthesized version (c) of the topography (a) and topology (b) of the surface flow over Fairlie's [75] prolate spheroid at $5^\circ$ angle of incidence .....	119
Figure 5.9 Synthesized version (c) of the topography (a) and topology (b) of the surface flow over the leeward side of Wickens' [95] slender rectangular wing at $20^\circ$ angle of attack, with the topology interpretation of (b) taken from Tobak and Peake [96] .....	120
Figure 5.10 An equivalent redrawing of the topological map in Figure 5.2 highlighting the separation and reattachment regions which together form (what we label) a "generalized owl face pattern".....	122
Figure 5.11 The topological map for Case B drawn in generic form highlighting the generalized owl face pattern. Note that the only differences between Case B and Case A are found on the reattachment line. ....	123
Figure 5.12 The topological map for Case C drawn in generic form highlighting the generalized owl face pattern, now broken to yield two distinct owl-face patterns of the first kind, see Figure 5.7. ....	123

Figure 5.13 The surface topology map of Case A, Figure 5.10, highlighting the common topology of Fairlie's [75] spheroid, Figure 5.8, and the attached flow case, Case C, Figure 5.12 .....	125
Figure 5.14 Illustration of generic separation and reattachment structures as repeating patterns of either saddle/node or saddle/foci pairs.....	127
Figure 5.15 Example of a non-homogeneous flow for both the two-dimensional separation structure (a) and the three-dimensional separation structure (b) .....	128
Figure 5.16 Examples of two possible separation patterns that agree well with what was shown about sidewall separation and contain the generalized owl-face patterns. Note, the sidewalls are shown laid flat as if bent from 90° to 180°.....	130
Figure 5.17 Example flow topologies with reattachment included for the separation patterns shown in Figure 5.16; Option 1 contains the OFP of the 4 <sup>th</sup> kind and Option 2 the OFP of the 2 <sup>nd</sup> kind .....	131
Figure 6.1 Illustration of secondary flow (a) generated in an s-duct (b) due to streamwise surface curvature and the resulting three-dimensional surface flow pattern in the form of the OFP of the first kind (c) .....	135
Figure 6.2 Illustration of expected secondary flow (a) generated over the ND Ramp (b) due to streamwise surface curvature and the resulting central three-dimensional surface flow pattern in the form of the OFP of the fourth kind (c).....	136
Figure 6.3 Radius of streamwise surface curvature comparison between the ND Ramp and three s-duct studies [101–103] with positive and negative values representing convex and concave curvature, respectively .....	137
Figure 6.4 Qualitative analysis of the $u_x(\theta)$ and $u_\theta(x)$ mean velocity profiles in an s-duct of circular cross-section and the resulting wall-normal vorticity, $\omega_r$ , that leads to the formation of the foci of separation. Here the flow in (a) is representative of the start of the duct, $x = 0$ , and the flow in (b) is representative of a location further downstream but prior to separation.....	139
Figure 6.5 Qualitative analysis of the $U(z)$ and $W(x)$ mean velocity profiles over the ND Ramp at two different streamwise locations (a) and (b), and the wall-normal vorticity, $\omega_y$ , causing the formation of the central foci when separation occurs .	140
Figure 6.6 Qualitative analysis of the $U(z)$ and $W(x)$ mean velocity profiles over the ND Ramp (b) with the presence of sidewall separation (a) leading to the generation of wall-normal vorticity, $\omega_y$ , and the likely formation of foci of separation in the central region .....	142
Figure 6.7 Centrifugal force per unit mass induced by streamwise surface curvature along the centerline of the ND Ramp over the convex (a) and concave (b) regions .....	144

Figure 6.8 Cross-section view of the expected secondary flow generated due to the centrifugal force over the convex surface of the ramp imposed on the off-surface flow topology (a) and a top view of the expected near surface secondary flow generated due to centrifugal forces over the convex and concave regions of the ramp surface (b) .....	145
Figure 6.9 Tab-style vortex generators (VGs) used on the ramp surface, highlighting the Large, Medium, and Small VGs that were tested as well as the adhesive strip (a), the Large VG installed on the ramp (b), and a schematic of the VG placement with respect to the sidewall and ramp leading edge (c) .....	149
Figure 6.10 Surface flow visualization showing the ability to manipulate the flow structures using the large single tab-style vortex generators (b) compared to the baseline flow (a).....	151
Figure 6.11 Boundary layer profile (a) and turbulent shear stress (b) comparison of large tab-style VGs to the baseline flow for a wall-normal profile located at $X = 0.5$ m and $Z = -0.1$ m.....	152
Figure 6.12 Surface flow visualization comparison for the baseline (a) medium (b), small (c), and adhesive strip (d) tab-style VGs placed near the sidewall/ramp juncture on each side of the ramp with the centerline separation and reattachment locations noted in red circles and baseline separation and reattachment locations noted in black squares .....	153
Figure 6.13 Sidewall flow control devices including: co-rotating VGs angled down (a), co-rotating VGs angled up (b), counter-rotating delta VGs (c), and v-shaped boundary layer trip (d), all applied upstream of the ramp leading edge .....	155
Figure 6.14 Illustration of the vortex path induced by the vortex image for co-rotating vortex generators angled up (a), and angled down (b) with both views oriented looking downstream.....	156
Figure 6.15 Surface flow pattern for sidewall flow VGs angled down, including overview (a) close up views highlighting the singular points on the inner loop (b) and outer loop (c) sides. Note the extra pair of singular points, S6 and F7, present on the outer loop side (c), but not on the inner loop side (b).....	157
Figure 6.16 Surface flow pattern for sidewall flow VGs angled up including overview (a) and close up views highlighting the singular points on the inner loop (b) and outer loop (c) sides. Note the extra pair of singular points, F5 and S6, present on the outer loop side (c) but not on the inner loop side (b).....	159
Figure 6.17 Images of the surface flow pattern using the multiple dye method with upward angled VGs installed on the sidewalls, highlighting that while there is increased uniformity of the flow in the separation region, two new separation structures are beginning to form .....	160

Figure 6.18 Sketches of the surface flow topology resulting from the sidewall application of downward (a) and upward (b) facing VGs and of the baseline flow (c) .....	161
Figure 6.19 Surface flow visualization for the application of counter-rotating delta VGs (a) and v-shaped boundary layer trip (b) highlighting the extreme difference in centerline separation extent.....	162
Figure 6.20 Preliminary CFD conducted in FUN3D with the SA-RC-QRC model for a baseline flat ceiling configuration (a) and for this formation with an inviscid condition upstream and viscous condition starting at the ramp leading edge (b). Figures courtesy of Chris Rumsey.....	165
Figure 7.1 Sketch providing the local coordinate system and three spanwise locations of the LDV measurements overlaid on the surface flow visualization of Case A ...	168
Figure 7.2 Spanwise average boundary layer growth and separation regions for all three test cases highlighting the 19 streamwise locations of the wall-normal LDV profiles, the local coordinates, the ramp geometry, and the global coordinates..	170
Figure 7.3 Evolution of wall-normal profiles for Case A showing spanwise variation in streamwise mean velocity, $U$ , for flow starting on the boundary layer development plate, $X = -0.56$ m, and continuing along the ramp through separation, reattachment, and recovery, $X = 0.95$ m .....	172
Figure 7.4 Evolution of wall-normal profiles for Case A showing: spanwise variation of wall-normal mean velocity, $V$ , for flow starting on the boundary layer development plate, $X = -0.56$ m, and continuing along the ramp through separation, reattachment, and recovery, $X = 0.95$ m .....	175
Figure 7.5 Evolution of wall-normal profiles for Case B showing spanwise variation of streamwise mean velocity, $U$ , for flow starting on the boundary layer development plate, $X = -0.56$ m, and continuing along the ramp through separation, reattachment, and recovery, $X = 0.95$ m .....	177
Figure 7.6 Evolution of wall-normal profiles for Case B showing spanwise variation of wall-normal mean velocity, $V$ , for flow starting on the boundary layer development plate, $X = -0.56$ m, and continuing along the ramp through separation, reattachment, and recovery, $X = 0.95$ m .....	178
Figure 7.7 Evolution of wall-normal profiles for Case C showing spanwise variation of streamwise mean velocity, $U$ , for flow starting on the boundary layer development plate, $X = -0.56$ m, and continuing along the ramp through separation, reattachment, and recovery, $X = 0.95$ m .....	180
Figure 7.8 Evolution of wall-normal profiles for Case C showing spanwise variation of wall-normal mean velocity, $V$ , for flow starting on the boundary layer development plate, $X = -0.56$ m, and continuing along the ramp through separation, reattachment, and recovery, $X = 0.95$ m .....	181

Figure 7.9 Streamwise development of the turbulent normal stresses for Case A with solid symbols corresponding to the streamwise component, $u'u'$ , and open symbols corresponding to the wall-normal component, $v'v'$ .....	184
Figure 7.10 Streamwise development of the turbulent shear stresses for Case A at multiple spanwise locations .....	185
Figure 7.11 Streamwise development of the turbulent normal stresses for Case B with solid symbols corresponding to the streamwise component, $u'u'$ , and open symbols corresponding to the wall-normal component, $v'v'$ .....	187
Figure 7.12 Streamwise development of the turbulent shear stresses for Case B at multiple spanwise locations .....	188
Figure 7.13 Streamwise development of the turbulent normal stresses for Case C with solid symbols corresponding to the streamwise component, $u'u'$ , and open symbols corresponding to the wall-normal component, $v'v'$ .....	190
Figure 7.14 Streamwise development of the turbulent shear stresses for Case C at multiple spanwise locations .....	191
Figure 7.15 Fraction of downstream flow, $\gamma_p$ , just above the surface for Case A, B, and C, with red dashed lines highlighting incipient detachment (ID), $\gamma_p = 0.99$ , intermittent transitory detachment (ITD), $\gamma_p = 0.8$ , and transitory detachment (TD), $\gamma_p = 0.5$ .....	196
Figure 7.16 Streamwise pressure (a) and pressure gradient (b) and (c) distributions for Cases A, B, and C. Detachment and reattachment locations, corresponding to $\gamma_p = 0.5$ , are highlighted by vertical dashed lines for (a1)-(c1) while incipient detachment and full reattachment locations corresponding to $\gamma_p = 0.99$ and $\gamma_p = 1$ are highlighted by vertical dashed lines for (a2)-(c2), respectively. Note the ramp height, $H$ , is used to non-dimensionalize the pressure gradient distributions.....	198
Figure 8.1 Illustration of embedded shear layer scaling parameters for an inflectional mean velocity profile .....	206
Figure 8.2 Vorticity thickness growth rates for Cases A, B, and C highlighting an initial uniform growth rate for Cases B and C and higher growth rate for Case A. Note that the solid lines are spanwise-averaged linear curve fits.....	207
Figure 8.3 Modified vorticity thickness growth rate for Cases A, B, and C with the solid lines giving the spanwise averaged linear curve fits.....	209
Figure 8.4 Generalized momentum thickness growth rates for Cases A, B and C, with the solid lines giving the spanwise averaged linear curve fits .....	210
Figure 8.5 Conventional outer variable scaling of the mean flow of the centerline data for Case B (a) and Case C (b).....	212

Figure 8.6 Conventional outer variable scaling of the turbulent normal, (a) and (b) and shear, (c) and (d), stresses of the centerline data for Case B, (a) and (c), and Case C, (b) and (d).....	212
Figure 8.7 Embedded shear layer scaling of the inflectional mean velocity profiles of the centerline data for Case B (a) and Case C (b).....	214
Figure 8.8 Embedded shear layer scaling of the turbulent normal, (a) and (b), and shear, (c) and (d), stresses of the centerline data for Case B, (a) and (c), and Case C, (b) and (d). Note the black dashed lines show the deviation of the peak turbulent stresses from $\eta = 0$ .....	215
Figure 8.9 Wall-normal growth of the location of the peak turbulent normal stress and upper mean profile inflection point for the centerline data for Case B (a) and Case C (b) .....	216
Figure 8.10 Plots showing the centerline peak turbulent normal stress location as it falls below the mean profile inflection point location and stabilizes around 0.82 (a), and the centerline peak turbulent normal stress location versus the mean profile inflection point location showing constant proportional growth for both cases (b) .....	218
Figure 8.11 Illustration of the modified embedded shear layer scaling parameters for an inflectional mean velocity profile .....	220
Figure 8.12 Modified embedded shear layer scaling of the inflectional mean velocity profiles for Case B (a) and Case C (b) for all spanwise locations .....	221
Figure 8.13 Modified embedded shear layer scaling of the turbulent normal, (a) and (b), and shear, (c) and (d), stresses of the centerline data for Case B, (a) and (c), and Case C, (b) and (d) .....	222
Figure 8.14 The significance of surface curvature along the ramp plotted as the ratio of local boundary layer thickness to local radius of curvature with convex curvature being positive and concave curvature negative .....	223
Figure 8.15 Streamwise growth of the peak turbulent normal and shear stresses scaled using both original (a) and modified (b) embedded shear layer scaling with linear fit(s) applied to each data set .....	226
Figure 8.16 Modified embedded shear layer scaling and peak stress normalization of the turbulent normal, (a) and (b), and shear, (c) and (d), stresses of the centerline data for Case B, (a) and (c), and Case C, (b) and (d) .....	229
Figure 8.17 Illustration of the rotated turbulent shear stress correlation for a single point (a) and for an entire profile (b). Part (b) shows the original turbulent shear stress at $X = 0.6$ m and $X = 0.45$ m and the turbulent shear stress at $X = 0.6$ m rotated so that its coordinate system matches that of $X = 0.45$ m .....	231

Figure 8.18 Comparison of unscaled turbulent shear stresses, (a) and (b), and unscaled turbulent shear stresses now rotated to wall-normal reference frame at $X = 0.45$ m, (c) and (d).....	233
Figure 8.19 Turbulent shear stress profiles rotated to the $X = 0.45$ m wall-normal reference frame and scaled using the modified embedded shear layer scaling for Case B (a) and Case C (b).....	234
Figure 8.20 Comparison of peak turbulent normal and shear stresses with that of those rotated to the $X = 0.45$ m wall-normal reference frame and scaled using both original (a) and modified (b) embedded shear layer scaling with linear fits applied to each data set .....	235
Figure 8.21 Streamwise development of TKE production for Case B (a) and Case C (b) showing that once the shear layer develops, the outer production peak does not change significantly .....	236
Figure 8.22 Peak TKE production appears to be roughly constant from $0.45 \text{ m} < X < 0.8 \text{ m}$ .....	237
Figure 8.23 Growth of the scaled difference in peak normal stresses for the wall-normal coordinate system (a) and rotated coordinate system (b).....	238
Figure A.1 Schematic drawing of the test section and model geometry including dimensions in inches .....	252
Figure A.2 Photographs of the top (a) and bottom (b) assembled ramp model just after polishing showing the three separate sections bolted together .....	253
Figure A.3 Underside view of the central section of the ramp model showing pressure tubulations and tubing.....	254
Figure A.4 Supporting structure for ramp model that provides the necessary 0.152 m (6 in) of vertical offset required for optical access to the recovery region .....	254
Figure A.5 Internal inlet contour sections outside (a) and installed in the wind tunnel contraction (b).....	255
Figure A.6 Views of the boundary layer development plate during the installation process highlighting the aluminum plate (c), the steel support legs (b), and the tripping roughness element (a) and (d).....	256
Figure A.7 Model of the flexible top wall insert and turnbuckle assembly viewed from the wind tunnel inner loop side.....	258
Figure A.8 Schematic top view of test section ceiling showing locations for measuring the position of the flexible ceiling contour. Note sections 1, 2, and 3 are shown from left to right.....	258

Figure A.9 Photograph (a) and schematic (b) of the diffuser hinged assembly transition piece .....	264
Figure A.10 Schematic top view of the piano hinge transition piece showing the diffuser cruciform (a), and photograph of the hexagonal grids installed in the diffuser (b) .....	265
Figure A.11 Comparison of original test section sidewall (a) and new adjustable sidewall (b). Note that the new adjustable sidewall is positioned 51 mm lower and allows the central supports to be repositioned, as necessary.....	267
Figure B.1 Viscosity temperature dependence for Clearco pure silicone fluids.....	271
Figure B.2 Internal inlet contour modified with a particle seeding manifold to allow localized seeding of the upstream boundary layer highlighting the top view (a) internal view (b) and top view of additional modification for y-connectors (c)..	273
Figure B.3 Comparison of incoming mean flow (a) and turbulent stress (b) boundary layers both with and without the modified seeding tubes installed showing negligible difference in flow condition. Note that the profiles were taken using hot-wire anemometry for the C.....	274
Figure C.1 A typical temperature variation for Case C showing both the tunnel temperature (a) and lab temperature (b). Each test is plotted over its duration which goes from start (0) to finish (1) with each data point being taken approximately 15 minutes apart.....	276
Figure C.2 A typical temperature variation for Case B showing both the tunnel temperature (a) and lab temperature (b). Each test is plotted over its duration which goes from start (0) to finish (1) with each data point being taken approximately 15 minutes apart.....	277
Figure C.3 A typical temperature variation for Case A showing both the tunnel temperature (a) and lab temperature (b). Each test is plotted over its duration which goes from start (0) to finish (1) with each data point being taken approximately 15 minutes apart.....	278
Figure C.4 A typical relative humidity variation for Case C showing both the tunnel humidity (a) and lab humidity (b). Each test is plotted over its duration which goes from start (0) to finish (1) with each data point being taken approximately 15 minutes apart.....	279
Figure C.5 A typical relative humidity variation for Case B showing both the tunnel humidity (a) and lab humidity (b). Each test is plotted over its duration which goes from start (0) to finish (1) with each data point being taken approximately 15 minutes apart.....	279

Figure C.6 A typical relative humidity variation for Case A showing both the tunnel humidity (a) and lab humidity (b). Each test is plotted over its duration which goes from start (0) to finish (1) with each data point being taken approximately 15 minutes apart.....	280
Figure D.1 Plot of drift voltage (a) and drift velocity (b) as functions of wall-normal height for a test with no air flow, i.e. $M = 0$ . Note that near the surface the voltage (a) drifts causing an “artificial” velocity (b) to appear. ....	299
Figure D.2 Plot of the relative uncertainty due to each of the sources discussed as a function of the boundary layer height. Here the uncertainty of each source is written as a percentage of the total uncertainty at each point. Note that the profile point starts just off the surface, Profile Point 1, and continues into the freestream, Profile Point 48. ....	302
Figure D.3 Local and reference coordinate system relations.....	308
Figure E.1 Surface flow visualization with green dye placed upstream near the ramp leading edge and blue dye placed downstream in the separation and reattachment regions.....	322
Figure E.2 Surface flow visualization with green dye placed near the sidewall/ramp juncture flow separation and blue dye placed in the central region of the flow ..	323
Figure E.3 Surface flow visualization with green dye placed near the sidewall/ramp juncture flow separation and blue dye placed in the central region of the flow ..	323
Figure E.4 Surface flow visualization with green dye placed near the sidewall/ramp juncture flow separation and blue dye placed in the central region of the flow ..	324
Figure F.1 Ratio of vorticity thickness to local boundary layer thickness for Cases A, B, and C all showing a roughly constant ratio of 0.3 .....	325
Figure F.2 Embedded shear layer scaling of all the inflectional mean flow profiles for all three spanwise locations for (a) Case B and (b) Case C .....	326
Figure F.3 Ratio of Turbulent to Mean Flow Time Scales for (a) Case B and (b) Case C .....	327

## TABLES

Table 2.1 Sidewall boundary layer profile locations .....	29
Table 3.1 Skin friction coefficient measurements .....	60
Table 3.2 Development plate boundary layer parameters .....	62
Table 3.3 Boundary layer parameters .....	72
Table 4.1 Aspect ratio comparison .....	98
Table 6.1 Tab-style vortex generator parameters .....	149
Table 6.2 Sidewall flow control device parameters.....	154
Table 6.3 Centerline separation extent.....	164
Table 7.1 Mean flow detachment and reattachment .....	195
Table A.1 Flexible ceiling position for Case A .....	261
Table A.2 Flexible ceiling position for Case B.....	262
Table A.3 Flexible ceiling position for Case C.....	263
Table B.1 Surface pressure tap locations .....	269
Table C.1 Uncertainty estimates for Cases A, B and C .....	283
Table D.1 Systematic uncertainty sources .....	301
Table D.2 Uncertainty sources and estimate values .....	305

## ACKNOWLEDGMENTS

My graduate school experience at Notre Dame has been filled with many great opportunities and memories. With deepest gratitude, I must recognize the people in my life who made this process a pleasant one and who made this dissertation possible.

First and foremost, I would like to express my deepest appreciation to my advisor, Dr. Flint Thomas. Without his persuasion, unwavering support, and deep confidence in me, I would not have made it this far. I am deeply indebted to my wife, Lauren Simmons, for her encouragement and patience with me throughout graduate school and for the long hours she spent proof reading and editing this document. I would also like to extend my sincere thanks to my committee members, Dr. Thomas Corke, Dr. Stanislav Gordeyev, and Dr. Hirotaka Sakaue. Each of these men gave me unique opportunities to learn throughout my time in graduate school. I would also like to thank Dr. Chris Rumsey of NASA Langley Research Center for his suggestions, feedback, and insight. His profound knowledge of CFD was very greatly appreciated. I would also like to acknowledge NASA for their financial support through award NNX15AU26A.

The practical aspects of this work would not have been possible without the staff at White Field and the Hessert machine shop. Rob Chlebek, Jim Marnocha, Paul McGinty, Gene Heyse, Terry Jacobsen, Mike Sanders, and Rod McClain were all instrumental in the fabrication, assembly, and testing of this set of experiments. Rob Chelbek was always there when I needed to come up with a quick fix. His ingenuity and humor were good companions. Jim Marnocha spent countless months with me setting up equipment, running

tests, and tearing down and cleaning out the facility. Without his help and camaraderie, the process would have been far more demanding. I could not have asked for better support.

In addition to those who contributed directly to this research effort, there are many others who also deserve recognition for their love, encouragement, and support throughout this time. I would like to extend my deepest gratitude to my family and to my parents, Randy and Sally Simmons. They were my first teachers and role models and raised me with engineering curiosity. Without their love and support, I would never have made it this far. I am also very grateful to my in-laws, David and Ellie Lee, who have been a wonderful blessing. Finally, I would like to thank the congregation of Michiana Covenant Presbyterian Church for being such a great influence during the last five years. I could not have asked for a better church family.

## CHAPTER 1:

### INTRODUCTION

#### 1.1 Motivation

The use of computational fluid dynamics (CFD) in aerodynamic design and analysis has slowly been taking over the role long held by experimentalists conducting wind tunnel tests. Just over a decade ago, a NASA review study compiled by Malik and Bushnell [2] stated that “CFD will continue to encroach upon the need for physical testing requirements and eventually will replace the wind tunnel.” This shift from experiment to simulation is not due to any inherent fault with testing facilities or techniques, but rather to the rapid growth and availability of computational processing power, the ingenuity of fluid physicists creating better simulation models and algorithms, and the relatively low cost to conduct CFD simulations.

As useful as CFD is now, and with a presumably bright future, there is still a long road ahead before it is reliable enough to be considered the sole design, analysis, and testing tool for fluid dynamics problems in the aerospace industry. While CFD is prevalent in non-aerospace industries that possess their own challenging applications in these fields, the level of uncertainty is often not as strictly monitored because adverse consequences of a miscalculation are much lower [2]. One area in which CFD cannot produce accurate simulations with low uncertainty levels is in the simulation of complex fluid phenomenon

often occurring in off-design flight conditions. For example, a key finding of the CFD Vision 2030 study [3], published in 2014, states that “the use of CFD in the aerospace design process is severely limited by the inability to accurately and reliably predict turbulent flows with significant regions of separation.” The inaccurate prediction of turbulent boundary layer (TBL) separation is a very well-known [2–4] deficiency of many CFD methods, but it is not the sole problem. Other problematic areas for CFD include: modeling embedded instabilities in turbulent flows [2,5], shock capturing and shock dynamics [2], high lift prediction [2,6,7], flow control [2,8] and other off-design conditions [2,6]. Even more problematic, the applications that CFD simulations fail to adequately solve represent a large portion of the flight envelope. Because of these limitations, CFD is often only fully trusted for use near design cruise conditions [6].

What must improve for CFD simulations to give acceptable predictions in these areas of challenging physics? The CFD Vision 2030 study [3] identified five areas that need substantial research and development to overcome the technological gaps above. Nonetheless, the “pacing item” was “the ability to adequately predict viscous turbulent flows with possible boundary layer transition and flow separation present.” Technological improvements in computing will increase the range of accessible problems and likely allow numerical error to be reduced. Additional development of adaptive and robust meshing schemes will improve the user experience and reduce model development time and cost. However, the greatest challenge is to overcome the inherently poor turbulence models that produce physical error; thus, the potential improvement benefit is significant.

Ideally, direct numerical simulation (DNS) of the Navier-Stokes (N-S) equations would be employed as the CFD method of choice, as the N-S equations themselves

represent the most accurate governing form of fluid motion. Currently, however, DNS simulations are only feasible at low Reynolds numbers, and relevant high Reynolds number aerospace applications are not expected to be widely available in the foreseeable future. Thus turbulence modeling, which consists of creating approximate, reduced complexity, closed form, solutions of the N-S equations, remains a permanent fixture. Other than DNS, the two main approaches to CFD are Reynolds-Averaged Navier-Stokes (RANS) and Large eddy simulations (LES) methods, both of which rely on turbulence modeling. While 2<sup>nd</sup> order accurate finite volume RANS solvers have become ubiquitous due to their low computational cost and ease of use, they are the most unreliable when solving complex separated, unsteady, and vortex dominated flows [4]. LES codes show the most potential for use and are likely the method of the future; however, full wall-resolved LES (WRLES) simulations are still too computationally expensive to be used outside of a research environment. As a result, a host of wall-modeled LES (WMLES) and hybrid RANS-LES schemes, with great potential, have been investigated [3,4,9,10]. Fundamentally, all of these methods must address the problem of near wall turbulence, which, though unavoidable, is the Achilles heel of turbulence modeling [5].

While the road to turbulence model improvement is likely an arduous one, there are several steps that can be taken to enhance both the timeline and the outcome. First, there is a deep need to better understand the physics of adverse pressure gradient (APG) TBL flows and the separation process that often ensues. This can be explored via the analysis of experimental wind tunnel studies as well as high resolution DNS and LES simulations. Second, in developing new models and evaluating existing ones, high quality benchmark experimental data sets are needed to provide additional validation capabilities. The

problem is that many currently available “traditional” experimental studies have either incomplete data sets and documentation, quality control issues or both [3,11,12]. Moreover, the geometries are often ill-suited for CFD as grid generation issues or discretization errors arise [2,3]. Finally, CFD workshops are needed that bring the broader technical community together to compare and analyze new turbulence models and build data bases for future model assessment. This has already begun through programs such as the Drag Prediction Workshop initiated in 2001 [13], the High-Lift Prediction Workshop Series [7], and the NASA Turbulence Modeling Resource website [14].

As outlined above, the process of improving turbulence models will still require significant effort in the area of wind tunnel testing. Experimental fluid dynamicists are better equipped to accurately and reliably measure turbulent separating flows than CFD practitioners, thus, the elimination of wind tunnel testing will not occur any time soon. Instead, there is a growing need for additional experimental studies that can be used as a tool both to validate CFD codes, and to analyze the corresponding flow physics. This is the primary motivation for this work, wherein a series of archival, benchmark, smooth-body, APG TBL flow separation studies are examined. Ironically, in this endeavor the experimentalist is supporting the eventual demise of experimental fluid dynamics with the hope that our efforts provide an understanding of the field that will allow CFD to one day take the place of experimental studies.

## 1.2 Background and Literature Review

Fundamentally, the goal of a model validation experiment differs from that of a traditional experiment. Most traditional experiments aim to discover or provide an improved understanding of physical phenomena, measure empirical constants to calibrate

models, or to improve a products safety and reliability. Oberkampf and Smith [11] explain that the model validation experiment is a new type of experiment “designed, executed, and analyzed for the goal of quantitatively determining the ability of the mathematical model (and its embodiment in a computer code) to predict the physical processes occurring in the model validation experiment.” With this new type of experiment comes a plethora of requirements (mainly in the form of additional measurements, documentation, and uncertainty quantification) not fulfilled in traditional experiments.

Oberkampf and Smith [11] go on to provide extensive guidelines for model validation experiment completeness (MVEC) that include 6 attributes with 4 possible levels of completeness which must be analyzed and confirmed solely via the experimental documentation. While many of these attributes are addressed in a typical experiment, the level of characterization and documentation in these typical experiments is far below that suggested for validation quality experiments. Oberkampf and Smith [11] recognize that these requirements have been thought of as “unreasonably demanding on experimentalists” and that “no present experiment would score at the top levels”; therefore, they should be used as a comparative standard for existing experiments and as idealized guidelines for the design of new experiments. These guidelines highlight that (1) currently, there are no ideal CFD validation experimental data sets available and (2) a new wave of validation experiments is starting to be conducted in an attempt to meet these guidelines.

While the guidelines of Oberkampf and Smith [11] are quite generic and principally consider the thoroughness of the experiments and documentation, they (and others [2,3]) also point to the need for flow physicists, CFD practitioners and experimentalist to work together to design validation experiments. For example, many quality flow-physics

experiments have been conducted that are not suitable for CFD simulation. While perfectly fine for experimentation, geometries that are either too complex or not defined analytically are not suitable for CFD because grid generation and discretization issues introduce uncertainty and numerical rounding errors [2,3]. Inflow and boundary conditions also often lack sufficient measurement and documentation [12]. Notably, Disotell and Rumsey [15] point out that a reproducible set of boundary values is the “most basic” requirement for a validation experiment. While the complete geometry and inflow conditions provide the necessary “input” for CFD simulation, validation itself cannot occur without *both* extensive documentation and adequate *uncertainty quantification* of the mean and turbulent flow field variables and any other necessary quantities of interest.

The qualities of a validation experiment are very important, but, arguably, the physical aspects to be studied, and hopefully validated, in the computational simulations are of more importance. We must ask: are we investigating the appropriate problems? As mentioned above, separating and reattaching turbulent boundary layer flows are one of the problems of key importance, yet they are more often, and appropriately, treated as a classification of problems. The differences in Reynolds number, surface curvature, pressure gradient, compressibility, and three-dimensionality are just some of the features that cause these flows to differ in form and ultimately negate the usefulness of the experiments. One important driving factor for the manifestation of these features is the nature of the model geometry. For example, Deck [16] presents three categories of flow problems shown in Figure 1.1. Here he defines category I as flows where separation is fixed by the geometry, category II as flows where separation occurs over a smooth surface and is dictated by the pressure gradient, and category III as flows where the boundary layer

dynamics, along with the pressure gradient, strongly influence separation. He goes on to classify category I and II as massively separated flows where developing instabilities overwhelm the incoming flow turbulence. Additionally, categories II and III are known as *smooth-body* flows, and they will receive special attention throughout this work.

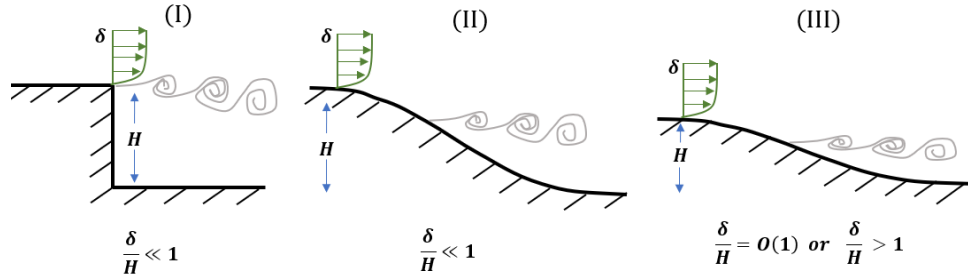


Figure 1.1 Classification of typical flow problems. I: separation fixed by the geometry, II: separation induced by a pressure gradient on a curved surface, III: separation strongly influenced by the dynamics of the incoming boundary layer (Figure and caption modified from Deck [16])

The prime example of a category I flow is that of the backward facing step. It is one of the most widely studied, and often considered ideal [17], flow separation geometries. Of the many studies of this geometry [18–23], the work of Driver and Seegmiller [24] stands out, as it represents a set of experiments employed to evaluate turbulence models. The simplistic geometry and two-dimensionality of the separation make this geometry relatively easy to study; however, the efforts of these studies are necessarily focused on downstream reattachment instead of separation. The sharp corner of the step fixes the separation location, allowing the remaining flow parameters (i.e. step height and width, incoming boundary layer thickness and turbulence level, Reynolds number etc.) to dictate the reattachment process and location.

While studying the shear layer dynamics and the reattachment process is important, Williams et al. [25] notably point out that “new validation tests must challenge CFD capabilities to predict not only the turbulent separated region and reattachment but also the separation point.” This is well recognized by the CFD community as the CFD Vision 2030 Study [3] emphasized that “while all turbulent separated flows are difficult to predict, smooth-body separation stands out as the most challenging.” Furthermore, the study goes on to state that “in general, two critical components of flow physics need to be modeled accurately: the exact location of separation as controlled by the boundary-layer physics and the feedback from the separated region to the boundary layer.” Thus there is a clear need to develop new, improved validation studies on the smooth-body geometries of categories II and III as defined in Figure 1.1. Here we will present a brief overview of some of the TBL flow separation studies already conducted for the purpose of CFD validation.

Two decades ago, researchers began modifying the traditional backward facing step by replacing the step edge with a large arc in an effort to allow the pressure gradient, instead of the geometry, to dictate the separation location. Several, excellent experimental studies, utilizing rounded backward facing steps (ramps), have been conducted by groups at Stanford. Song et al. [26] investigated the separation, reattachment, and recovery process of a turbulent boundary layer developing over a rounded backward facing step. Later, Song and Eaton conducted follow-up work investigating the flow structures [27] and Reynolds number effects [28]. Since the boundary layer thickness to ramp height ratio at the start of the ramp ( $\delta/H$ ) was 1.2 in these studies, they would be considered a category III flow as defined by Deck [16]. Their experimental results [28] show that for  $Re_\theta$  above 3,400 “the

mean separation and reattachment points are at most a very weak function of Reynolds number.”

Following this experimental work, LES and RANS simulations were conducted by Wasistho and Squires [29] on this same geometry but with a much lower  $\delta/H$  (thus a category II flow) yielding significant differences in the flow field properties, such that their results are not comparable to Song and Eaton [28]. Shortly thereafter, Radhakrishnan et al. [30] conducted multiple RANS and WMLES simulations at  $Re_\theta = 13,200$ . All the RANS and WMLES simulations were able to predict the separation location within 12%; however, reattachment prediction was far worse, with up to 37% and 14% differences for the RANS and WMLES simulations, respectively. Additionally, RANS and WMLES produced opposite error, early reattachment for RANS and late reattachment for WMLES. Even the more recent LES simulations of El-Askary [31] conducted at  $Re_\theta = 1,100$ , which showed good overall agreement with the experiment and were able to predict separation, poorly predicted reattachment.

While Song et al. [26] saw the need to study a flow wherein naturally occurring interactions between the separation and reattachment process were not artificially impeded, one could argue that the sharp discontinuity in surface curvature in the middle of the separation region limited the extent of feedback from the reattachment region to the separation region. Additionally, while the separation location was dictated by the pressure gradient, the flow was bound to separate due to the sharp discontinuity—attached flow would be unachievable on this geometry. A geometry that avoids this issue is the wall-mounted hump model representing the suction surface of a modified Glauert-Glas II airfoil, first investigated by Seifert and Pack [32]. This well documented, canonical geometry has

been used for TBL separation studies, validation campaigns, and flow control experiments and is the focus of many experimental [12,32–34] and computational [8,9,35] studies.

Like the rounded, backward facing step, the separation process over the hump model is a smooth-body flow separation; however, the surface curvature is continuous throughout the separation region, which likely improves the feedback from reattachment to separation. Still, the location of separation is virtually insensitive to Reynolds number and incoming boundary layer thickness [12,32,33], which may be why DNS [35], LES [9], and RANS [8] simulations have been able to match the experimentally determined separation location fairly accurately. However, the inaccuracies in the reattachment locations from the simulations are all over the board, occurring both early and late, with RANS models performing noticeably worse than DNS and LES. Rumsey et al. [8] pointed out that this may be because the Reynolds stresses are seriously underpredicted by the RANS models in the separated region. As for discrepancies in the LES predictions, Uzun and Malik [9] recently found that the span of the computational domain highly influenced the separation-bubble length. For this reason, they cautioned users attempting to employ spanwise-periodic domains that omit the effects present at the end plates used in the experiments.

In order to avoid sidewall interference, or “3-D contamination” [15], issues associated with finite span models, axisymmetric geometries have also been employed as a test bed for two-dimensional TBL separation studies. The transonic flow of Bachalo and Johnson [36] is a classic example of a shock-boundary-layer interaction leading to smooth-body flow separation and reattachment. The geometry consists of an annular, circular-arc bump mounted to a streamwise aligned cylinder. Over 30 years later, turbulence modelers

are still struggling to accurately simulate this case. The frequently observed problem with RANS simulations—the inability to predict separation and reattachment—is apparent [37]. Furthermore, recent DNS and WMLES have noticeable disagreements with the experimental Reynolds shear stress measurements [38]. Moreover, the WMLES has additional issues capturing the mean flow, for which Spalart et al. [38] called the lack of agreement “disappointing” and the role of wall curvature “poorly understood”.

Recently, Disotell and Rumsey [15] began design efforts toward another axisymmetric flow separation experiment, consisting of a series of interchangeable boattail geometries, aimed at CFD validation. The interchangeable geometries allow multiple flow separation configurations, resulting in different separation extents, as well as an attached flow case to be studied on the same test bed. Here the Mach number is about 0.1, which is much lower than that of Bachalo and Johnson [36] ( $M = 0.875$ ), so no shocks are present, while it remains sufficiently high to avoid CFD preconditioners. Early experimental risk reduction efforts and accompanying RANS simulations were recently reported by Gildersleeve and Rumsey [39] and show, yet again, that while RANS can predict the separation location reasonably well, reattachment location is mispredicted. This promising study, currently under investigation, is the analogous, axisymmetric version of the work conducted in this dissertation, employing an interchangeable geometry of very similar form to the ramp geometry discussed in chapter 2.

The studies reviewed thus far all focus on examining two-dimensional separation regions as it is a more tractable problem. However, real engineering flows are very rarely truly two-dimensional, and even the flows that have uniform spanwise flow properties may suffer from sidewall interference issues. While axisymmetric geometries do not suffer in

the same way as conventional finite span models, they too are not immune to 3-D contamination. If high spatial resolution is desired, the increased blockage associated with larger models may result in slightly non-uniform pressure distributions when a circular cross-sectional geometry is placed in a wind tunnel with a rectangular cross-section. These types of issues have led to a recent push to examine three-dimensional separated flows as a means of CFD validation, even though the efforts are more laborious for both the experimentalist and CFD modelers. The experimental geometries often take the form of three-dimensional wall-mounted bumps or hills. A few notable three-dimensional flow separation studies are the FAITH “Hill” model [40], the NASA juncture flow experiment [41,42], the Virginia Tech wall-bounded bump [43], and the Boeing “speed bump” [25], the last three of which have attempted or are attempting new levels of validation under Oberkampf and Smith’s [11] guidelines, and the last two of which, at the time of this writing, are currently undergoing experimental testing.

Flow separation and reattachment prediction is not the only area where current CFD simulations are frequently inaccurate. Attached flows developing in APG environments often result in non-equilibrium boundary layers that can also be challenging to accurately predict, especially at the more-applicable, higher Reynolds numbers [44]. The changing inflectional mean velocity profiles and associated growth in the Reynolds stress outer peak challenge even the most advanced turbulence modeling techniques [45]. This type of flow development is a sort of middle ground between well-behaved equilibrium boundary layers and fully separated flows and has many of the features of the latter. A common geometry employed to study APG flows is the two-dimensional, downward angled ramp, which has

been utilized in a number of high-quality, experimental [5,44] and computational [45] CFD validation studies.

Since turbulence models need improvement for both smooth-body TBL separated flows and attached flows on the verge of separation, it would be ideal for a series of experiments to be conducted on the same geometry that can achieve both of these cases. This would not only ease CFD implementation but would also provide a more direct comparison of attached and separated flows without the influence of geometric differences. While the downward angled ramp geometry could be, and has been [46,47], used to study separated flows in addition to attached flows, the prominent transition from the flat plate to the angled ramp becomes significant and would ultimately initiate the separation process, therefore this is not truly a smooth-body separation. Debien et al. [46] showed that a prominent edge can produce a turbulent separation region about twice that of a rounded edge for the same ramp geometry. Additionally, the influence of model curvature, not present on a downward angled ramp, is difficult for turbulence models to capture and is therefore desirable in a validation study.

In an attempt to contribute to this need for experimental validation studies, the work presented in this dissertation consists of a series of flow experiments conducted on a single two-dimensional, smooth-body, backward facing ramp geometry (ND ramp) featuring continuous curvature. While similar geometries have been studied experimentally [48–53] and computationally [54,55], most of the focus has been on the efficacy of various passive and active flow control methods. None of these studies have the extensive characterization and documentation necessary for CFD validation, so they will not be discussed here;

however, most of them will be reviewed in chapter 4 to contrast their surface flow features to those of the ND ramp flows.

### 1.3 Objectives and Organization

The primary objective of this dissertation is *to produce a series of benchmark data sets on smooth-body flow separation for CFD validation and turbulence model development*. The geometry examined is a low aspect ratio, continuously smooth, backward-facing ramp that exhibits quasi two-dimensional flow separation and reattachment imparted by a streamwise adverse pressure gradient. This experiment is unique in that (1) it includes larger-scale separation, smaller-scale separation, and attached flow development, occurring on a single, analytically defined geometry with the separation extent dictated by an adjustable ceiling contour, (2) it occurs at a practical Reynolds number (per meter of length) of  $\text{Re} \approx 10^6$  ( $\text{Re}_0 \approx 10^4$ ), low enough to be accessible to various CFD methods yet high enough that Reynolds number independence can be expected, (3) it includes extensive, detailed measurements of the flow field, such as first and second order turbulence quantities at 19 different streamwise and 3 different spanwise locations, surface pressure, skin friction, inflow conditions on both the flat plate and sidewall boundary layers, and, to the author's knowledge, the most complete surface flow visualization analysis conducted on this type of geometry, and; (4) it exhibits a series of three-dimensional surface flow separation patterns that, while not usually sought after, are in fact commonly observed in many practical aerodynamic flows and hence presents a challenging, yet tractable, problem for CFD simulations.

Throughout the design and characterization of this series of benchmark experiments, it became apparent just how little documentation exists on three-dimensional

flow separation occurring on two-dimensional ramp geometries. Many different preliminary RANS simulations showed much larger sidewall/ramp juncture separation structures than either our CFD turbulence modeling colleagues or we, the experimentalist, expected. This prompted us, at the recommendation of our CFD turbulence modeling colleagues, to conduct extensive surface flow visualization on the ramp surface and sidewalls. It also led to the second emphasis of this dissertation, *to characterize the smooth-body flow separation and reattachment surface topography and topology and both its generic character and the influence of the sidewall/ramp juncture flow separation.*

Attempts to scale APG flow development have been made by many researchers. Similarity scalings not only provide trends based on the scaling parameters that can be used for engineering design, but also provide physical insights by indicating which aspects of the flow dictate its development. The recent work of Schatzman and Thomas [56] emphasized how the inflectional nature of APG boundary layers and the rapid growth and departure from the wall of the Reynolds stress outer peak mimic shear layers and can be scaled in a similar way using free shear layer parameters. The remarkable collapse of their non-equilibrium mean velocity and turbulence profiles prompted the investigation of whether this scaling was applicable to APG TBLs developing over curved geometries as well as in separated flows. This led to the third emphasis of this dissertation, *scaling the mean and Reynolds stress profiles to account for wall curvature and coordinate system reference frame effects.*

Documentation of the experimental facility, model geometry and instrumentation, and diagnostic techniques are provided in chapter 2. The installation of the model geometry is quite involved and extends into the wind tunnel inlet contraction and diffuser, so an

overview approach will be taken with much of the detailed supporting documentation provided in Appendix A. Details of the local and global coordinate systems used will be presented with the bulk of the chapter providing extensive descriptions of the instrumentation employed and any required calibrations. Chapter 3 provides the boundary conditions. This includes the adjustable ceiling configurations that dictate APG for the three benchmark test cases, the resulting surface pressure and skin friction measurements, and the inflow mean and turbulent boundary layer profiles on both the flat plate and wind tunnel sidewalls.

In chapter 4, the surface flow characteristics are discussed. This primarily takes the form of analyzing oil-film surface flow visualization images and identifying flow features that visually illustrate the three-dimensionality of the flow. The chapter concludes with a review of similar smooth-body flow separation experiments and demonstrates that the surface flow patterns observed, while not commonly examined in depth, are in fact typical. In chapter 5, the surface flow patterns are analyzed in more detail and surface flow topology maps are presented. Using what is known of the surface flow and select off-surface flow information, the flow topology maps are extended off the surface to illustrate how the separation structures may advect downstream and form the central separation region. These topology maps are then shown to contain the so-called owl-face patterns which represent the simplest form of three-dimensional flow separation and are in fact common in flow separation studies. The chapter concludes with the extension of the surface topology maps to a more generalized form.

Chapter 6 discusses the role of the ramp surface curvature on the mean flow and compares it, and the resulting separation structure, to that of a typical s-duct to examine

the role of the wind tunnel sidewalls. A series of passive flow control experiments seeking to control the sidewall and sidewall/ramp juncture flow are then presented. The results indicate that the extent of the sidewall/ramp juncture flow separation is inversely related to the extent of the centerline separation.

The off-surface flow field development is presented in chapter 7 and provides both measured mean and turbulence stress quantities. The mean and unsteady separation and reattachment locations are then discussed in detail with correlations to the pressure and pressure gradient distributions also analyzed. Chapter 8 discusses scaling the mean and turbulence quantities using embedded shear layer parameters and examines the importance of coordinate system orientation. Finally, conclusions and recommended future work are presented in chapter 9, and supplemental experimental documentation, details of the data uncertainty analysis, and additional analysis is presented in the appendices.

## CHAPTER 2: EXPERIMENTAL FACILITY, SETUP, AND INTRODUCTION

This chapter describes the experimental facility in which this work was conducted, the dedicated test section and installation of the model geometry, and the flow diagnostic techniques and instrumentation utilized to characterize the flow and acquire the data presented in the database accompanying this experiment.

### 2.1 White Field Mach 0.6 Wind Tunnel Facility

All experiments were performed in the Notre Dame Mach 0.6 closed-circuit wind tunnel facility at White Field. This is a large-scale, variable-speed, low-turbulence wind tunnel designed for fundamental aerodynamic research. A schematic of the wind tunnel is given in Figure 2.1. Some key features of this facility are its low freestream turbulence level,  $\sqrt{\bar{u}^2}/U_\infty \leq 0.5\%$ , its large test section size, 0.91 m x 0.91 m (3 ft x 3 ft) cross-section by 2.74 m (9 ft) length, its high powered, 1750 horsepower, variable r.p.m. AC motor, and its chilled-water temperature-controlled environment. The model for this experiment was installed in its own dedicated removable test section, which facilitated the ease of repeated experimental entries.

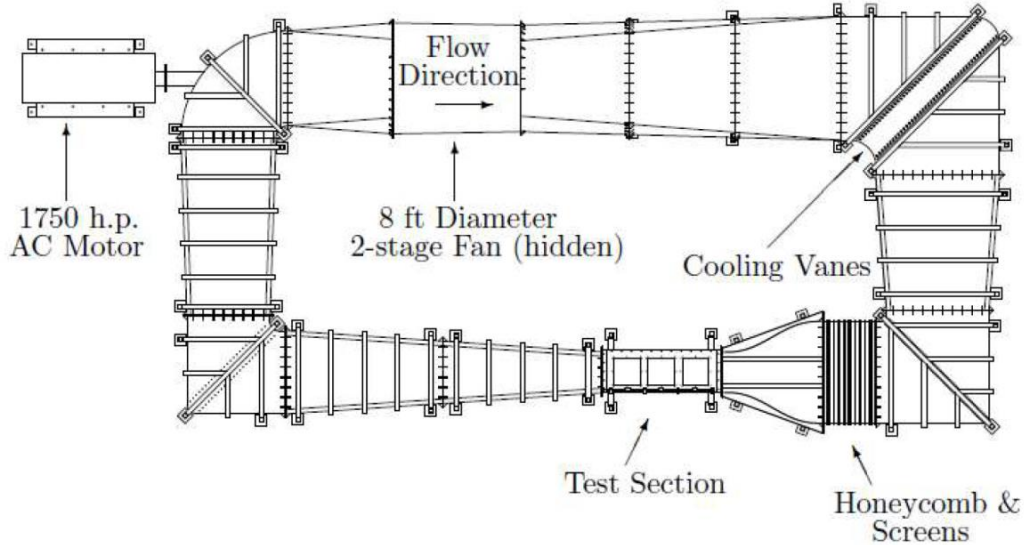


Figure 2.1 Schematic of the White Field Mach 0.6 wind tunnel facility

## 2.2 Model Geometry and Wind Tunnel Installation

The experimental geometry was designed to provide initial turbulent boundary layer (TBL) growth under nominally zero pressure gradient (ZPG) conditions subsequently imposed upon by an adverse pressure gradient (APG) that is fully adjustable over a smooth, backward facing ramp geometry. In this manner, the streamwise extent of the flow separation could be controlled with a fixed ramp geometry. Initially, this experiment sought to produce a turbulent flow whose statistical results were homogeneous in the spanwise direction. This turned out to only be realizable upstream of flow separation, as the separation process itself introduced inherent three-dimensionality. Hence, the focus of this work changed to accept the naturally occurring three-dimensionality and instead provide extensive characterization and documentation throughout this dissertation. The experimental geometry designed to achieve these objectives is shown in Figure 2.2, which presents a CAD model of the test section installed in the wind tunnel.

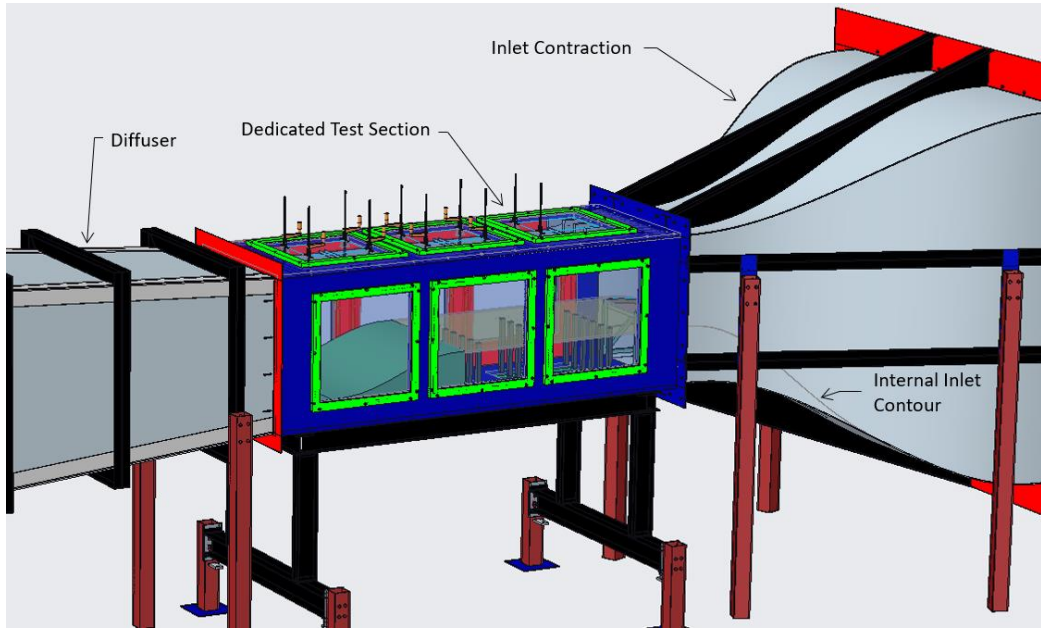


Figure 2.2 Drawing of the model geometry installed in the Notre Dame Mach 0.6 wind tunnel test section viewed from the outer wind tunnel loop side

Important features of the experiment are highlighted in Figure 2.3 and will be briefly discussed here, with more details available in Appendix A. On the lower half of the wind tunnel contraction, an internal inlet contour is installed, see Appendix A.3. The contour brings the flow smoothly from the wind tunnel inlet contraction up to a flat boundary layer development plate where the incoming flow is tripped with a 101.6 mm (4 in) wide strip of distributed sand grain roughness with an average roughness element size of 46  $\mu\text{m}$ , mounted 1.2 m (47.2 in) upstream of the ramp leading edge. The boundary layer development plate, see Appendix A.4, spans the full 0.914 m (3 ft) width of the test section and is 1.462 m (57.57 in) in streamwise length. Its top surface is raised 0.352 m (13.88 in) off of the test section floor. It allows a uniform turbulent boundary layer to grow before reaching the ramp leading edge.

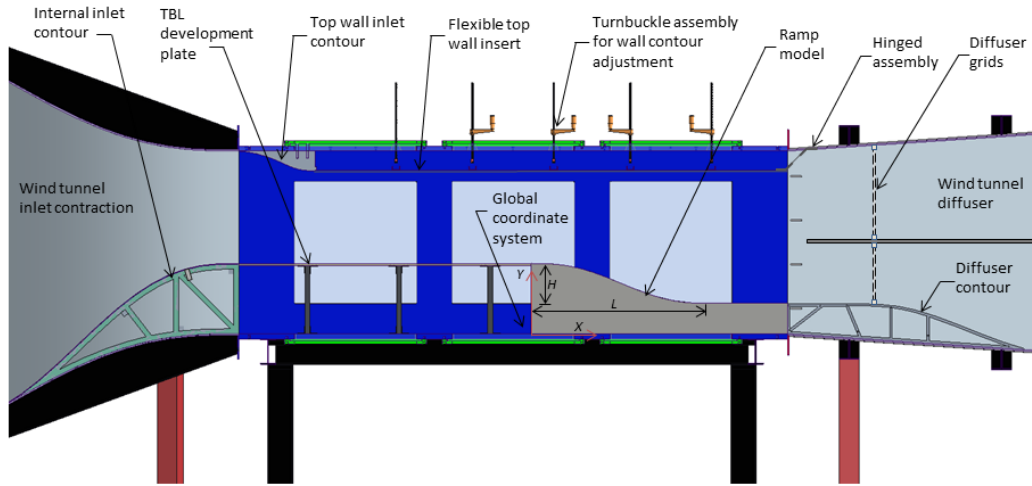


Figure 2.3 Labeled schematic drawing of the test section and model geometry viewed from the inner wind tunnel loop side

At the termination of the boundary layer development plate is the ramp model geometry, the primary focus of this experiment. It was designed in partnership with the CFD group at NASA Langley Research Center and consists of a fifth-order polynomial contour with zero first and second derivative end conditions at both upstream and downstream ends of the geometry. The geometry of the ramp, which extends the entire width of the test section, is given by the following parametric form,

$$Y(X) = a_1 + a_2 X^3 + a_3 X^4 + a_4 X^5 \quad (2.1)$$

where the  $X$  denotes the streamwise distance from the end of the boundary layer development plate and  $Y(X)$  is the height of the ramp, both in the global coordinate system (see Figure 2.3 & Figure 2.5). The constants are given in terms of the ramp length,  $L = 0.9$  m, the ramp height,  $H = 0.2$  m, and the vertical offset,  $H_{off} = 0.152$  m (6 in), as follows:

$$a_1 = (H + H_{off}), \quad a_2 = -10H/L^3, \quad a_3 = 15H/L^4, \quad a_4 = -6H/L^5 \quad (2.2)$$

The ramp is made from machined aluminum that was polished and toleranced to within 0.025 mm (0.001 in). Additional details are available in Appendix A.2. Downstream of the ramp the flow smoothly transitions into the diffuser via removable contours installed on the diffuser floor, see Appendix A.6.

On the upper half of the test section, a top wall inlet contour smoothly transitions the flow from the inlet onto a flexible-top wall insert (see Figure 2.3 and Figure 2.4). Like the ramp geometry, this contour is machined aluminum in the form of a fifth-order polynomial with zero first and second derivative end conditions. It is described by the following parametric form,

$$Y(X) = b_1 + b_2 X^3 + b_3 X^4 + b_4 X^5 \quad \text{for } [-1.4623 < X < -1.0813] \quad (2.3)$$

where  $X$  and  $Y$  are both in the global coordinate system. The constants are given in terms of the ramp length,  $L_2 = 0.3810$  m, the ramp height,  $H_2 = 0.0986$  m, and the vertical offset,  $H_{off2} = 0.8158$  m, as follows:

$$b_1 = (H + H_{off2}), \quad b_2 = -10H_2/L_2^3, \quad b_3 = 15H_2/L_2^4, \quad b_4 = -6H_2/L_2^5 \quad (2.4)$$

The flexible-top wall insert (adjustable ceiling contour), manufactured from 10-gauge aluminum sheet metal, covers the entire test section and acts as a false ceiling. As shown in Figure 2.4, it features two rows of turnbuckles that allow a continuous modification of the streamwise pressure gradient. At the end of this flexible insert, which approximately corresponds to the end of the test section, is a hinge assembly that transitions the flexible

ceiling into the diffuser, see Appendix A.6. Figure 2.4 is a photograph of the test section which highlights both the size of the ramp model geometry and the flexible insert and provides a reference for the coordinate systems that are used in this work. Note that in Figure 2.4 the test section sidewall is removed for improved visibility of key components. This sidewall, located on the wind tunnel outer loop (-Z axis), is not the same as the one on the inner loop side. Instead, it features adjustable window positioning and was fabricated to allow complete sidewall optical access at any streamwise location. See Appendix A.7 for further details.

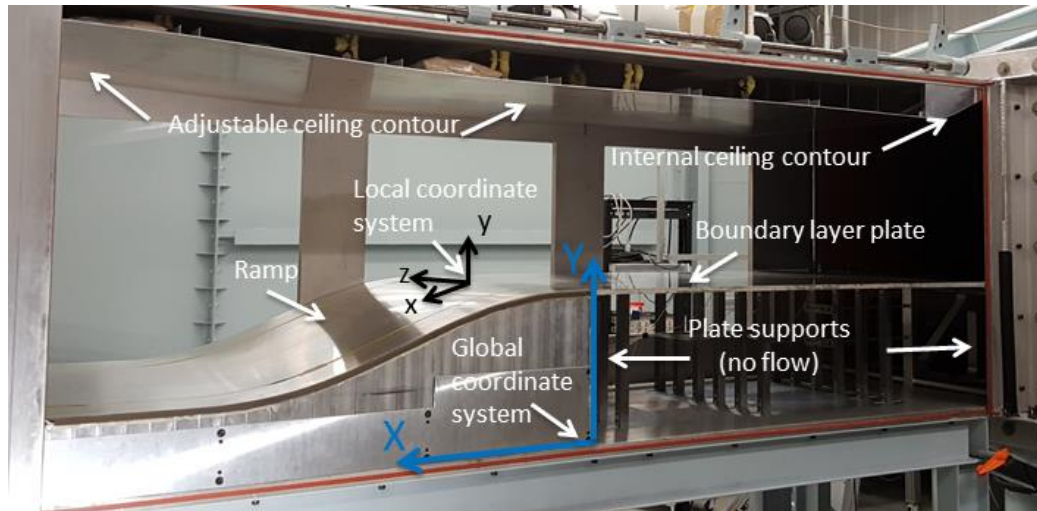


Figure 2.4 Photograph of the test section model with the sidewall door removed viewed from the outer wind tunnel loop. Note that the sidewall door absent in this photograph is the adjustable one.

### 2.3 Coordinate Systems

There are two primary right-hand, Cartesian coordinate systems used in the data collection and data presentation of this experiment: the global and the local coordinate systems, both shown schematically in Figure 2.5 and Figure 2.6. The global coordinate system ( $X, Y, Z$ ) has its origin at the start of the ramp and bottom mid-span of the test

section. The global coordinate system is used to represent the physical geometry and the start of each LDV profile. The local coordinate system ( $x$ ,  $y$ ,  $z$ ) is different for each ramp location and has the same spanwise,  $z$ , coordinate as the global coordinate system; however, its other two axes are locally wall-normal,  $y$ , and wall-tangent,  $x$ , oriented. The origin of the local coordinate system is on the surface of the ramp geometry and is defined by a single value of the streamwise global variable,  $X$ , or the surface streamwise coordinate,  $x_s$ . The angle  $\theta$  as given for each local coordinate system is defined as the wall-parallel direction,  $x$ , rotated counter-clockwise into the tunnel streamwise direction,  $X$ . It is primarily used to convert the local flow values from their native, locally collected coordinate system to the global coordinate system. The details of the coordinate system rotation applied to the LDV data are provided in Appendix D.5.

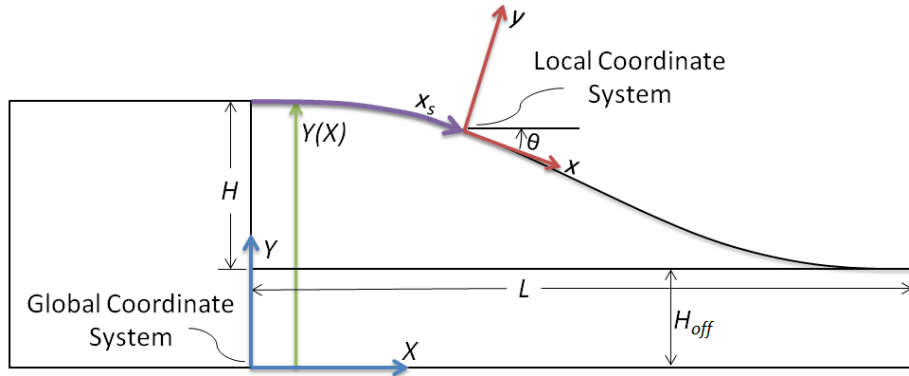


Figure 2.5 Side view schematic of the global ( $X$ ,  $Y$ ,  $Z$ ) and local ( $x$ ,  $y$ ,  $z$ ) coordinate systems with respect to the ramp geometry

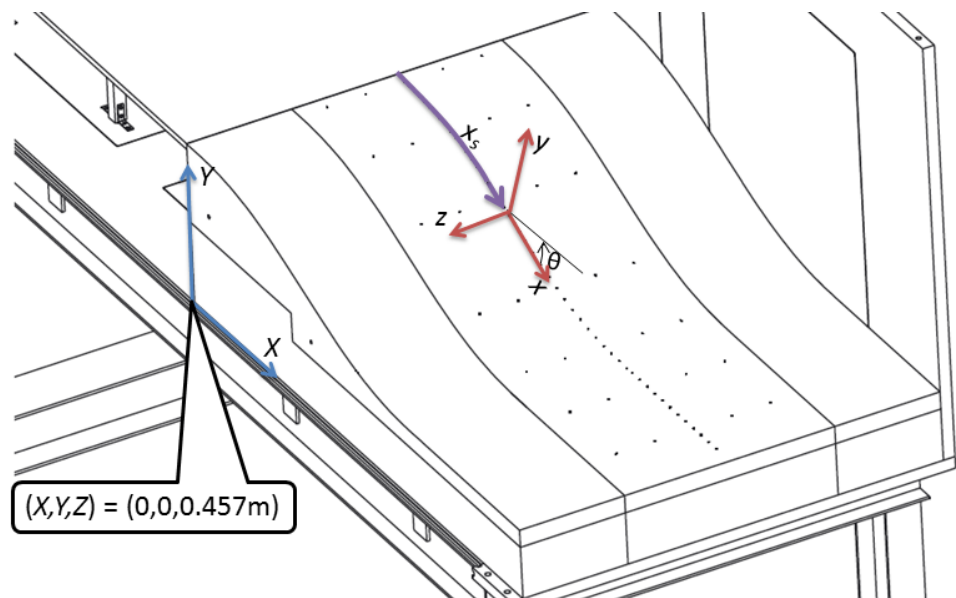


Figure 2.6 Schematic showing both the streamwise and multiple spanwise static pressure taps on the convex ramp surface and the global ( $X$ ,  $Y$ ,  $Z$ ) and local ( $x$ ,  $y$ ,  $z$ ) coordinate systems

## 2.4 Diagnostic Techniques

### 2.4.1 Surface Pressure Instrumentation

The boundary layer development plate and ramp, taken together, contain a total of 89 surface pressure taps: 61 in the streamwise direction along the central axis,  $Z = 0$ , and the remainder in 7 different spanwise arrays along the ramp, as shown in Figure 2.6. See Appendix B.1 for tabular data providing each pressure tap location. All pressure taps are confined to central section of the ramp geometry and were drilled wall-normal using a 5-axis CNC milling machine. Scanivalve 063 stainless steel tubulations, each 25.4 mm (1 in) in length with an internal diameter of 1.1 mm (0.0425 in), were superglued flush with the ramp surface in the holes. The tubulations were then connected to the pressure transducer via 063 urethane tubing and three separate 31-port circular connectors, both from Scanivalve.

Pressure data were acquired via the Scanivalve SSS-48C9 pneumatic scanner which houses a PDCR23D pressure transducer and a SCSG2 signal conditioner. This system has 48 pressure ports that can be measured sequentially using the internal pressure transducer, which has a differential range of 10 in of  $H_2O$  with an accuracy of 0.30% of full scale. Due to the large number of pressure taps, pressure measurements were taken in three sequential groups using the Scanivalve's 31-port circular quick connectors. Each channel was sampled sequentially at 1 or 2 kHz for 15 seconds, which was sufficient to provide converged mean values. The reference pressure for each measurement was the freestream static pressure collected via a pitot tube located at  $X = -0.97$  m,  $Y = 0.58$  m, and  $Z = 0.19$  m.

The Scanivalve device was calibrated in the wind tunnel against the Setra pressure transducers, which were used to set the wind tunnel freestream speed. A sample calibration curve for this device is given in Figure 2.7 below. The Mach 0.6 wind tunnel uses two Setra Model 270 absolute pressure transducers to measure pitot static and total pressures, respectively, with a range of 600-1100 HPa and an accuracy of 0.05% of full scale. The Scanivalve sensor was calibrated by connecting the Scanivalve and each of the Setra's pressure lines to the freestream pitot tube. The freestream Mach number was then varied between 0 - 0.217 using the Setra's output, and the Scanivalve voltage was recorded. The difference in the Setra outputs, the pitot dynamic pressure, was used as the known pressure to calibrate the Scanivalve.

The individual data files for each group were loaded into and processed in MATLAB. Pressure data are reported in terms of a pressure coefficient defined as follows:

$$C_p \equiv \frac{(P_i - P_\infty)}{(P_T - P_\infty)} = \frac{\Delta P_i}{q} \quad (2.5)$$

where  $P_i$  is the local static pressure,  $P_\infty$  is the freestream static pressure,  $P_T$  is the freestream total pressure and  $q$  is the freestream dynamic pressure. For the reported surface pressure measurements, the 95% uncertainty in  $C_p$  is on the order of 0.007. The full uncertainty analysis provided in Appendix D.1.

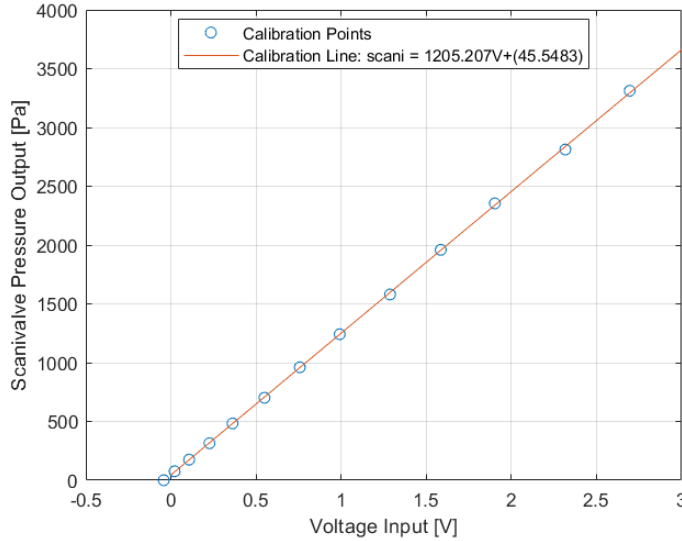


Figure 2.7 Sample calibration curve for the Scanivalve SSS-48C pneumatic scanner using an NI USB-6343 DAQ

#### 2.4.2 Pitot-Tube Instrumentation

Sidewall boundary layer profiles of mean velocity were taken using a United Sensor type BA-020-12-C-650 total pressure probe. The probe is made of a 5.1 mm (0.020 in) nominal diameter steel tube that is flattened on the tip to an opening of 2.8 mm (0.011 in). The measured total pressure was referenced to a wall-normal static pressure line located nominally at the boundary layer profile location. The profile was traversed using a hand operated traverse with 1 mm gradations. Each profile began with the probe contacting the wall and ended with the probe in the freestream. All measurements were conducted using the Scanivalve SSS-48C pneumatic scanner, which houses, a PDCR23D differential pressure transducer and a SCSG2 signal conditioner. This Scanivalve device is the same one used for the surface pressure measurements. The data were sampled digitally via an NI USB 6343 DAQ and samples were taken at 100 Hz for 30 seconds per point. The lab

atmospheric conditions were recorded at the start of each run and the wind tunnel temperature was recorded at both the start and end of each run.

The starting location of each profile within the wind tunnel is listed in Table 2.1. Notice that the height off the boundary layer development plate, or  $Y$  coordinate, is not the same on each side. This occurs because the same removable window mounted traverse was used for all the pitot-tube profiles and the window openings of the test section sidewall on the outer loop side are lower than the inner loop side, i.e. the window positions are not symmetric about the tunnel centerline. For additional clarity, see Appendix A.8.

TABLE 2.1  
SIDEWALL BOUNDARY LAYER PROFILE LOCATIONS

	<b>X [m]</b>	<b>Y [m]</b>	<b>Z [m]</b>
Inside Loop	-0.090	0.457	0.457
Outside Loop	-0.090	0.406	-0.457

The individual data file for each location was imported into and processed in MATLAB. Streamwise velocity was calculated from pressure using Bernoulli's equation as follows:

$$U = \sqrt{\frac{2\Delta P}{\rho}} \quad (2.6)$$

where  $\Delta P$  is the local dynamic pressure, measured as the difference between the pitot pressure and the wall static pressure. The density,  $\rho$  [ $kg/m^3$ ], was calculated as a function of pressure, temperature and relative humidity using Jones's formula [57],

$$\rho = \frac{0.0034848}{T + 273.15} (P_a - 0.0037960 * RH * P_{sat}) \quad (2.7)$$

where  $P_a$  is the atmospheric pressure [Pa],  $T$  is the temperature [C],  $RH$  is the relative humidity [%], and  $P_{sat}$  is the saturated water vapor pressure. Teten's formula was used to calculate the saturated water vapor pressure as follows:

$$P_s = 611 \times 10^{7.5T/(T+237.3)} \quad (2.8)$$

Information regarding the uncertainty analysis of the pitot-tube measurements is provided in Appendix D.2. Sample plots of the sidewall boundary layers, including 95% confidence intervals, for Case A are shown in Figure 2.8. Note that the uncertainty is on the order of the symbol size.

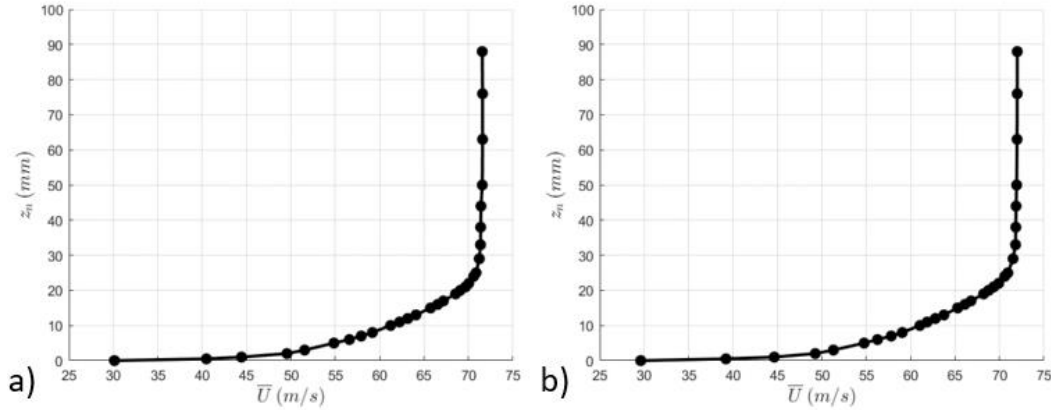


Figure 2.8 Wall-normal sidewall boundary layer profiles for inside loop (a) and outside loop (b) for Case A. The uncertainty intervals are on the order of the symbol size. Note that the profile location is not the same on both sides, see Table 2.1.

#### 2.4.3 Hot-Wire Anemometry Instrumentation

Boundary layer mean velocity and turbulent stress profiles were taken on the boundary layer development plate and sidewalls using hot-wire anemometry. An A.A. Lab Systems AN-1003 anemometer and a conventional straight sensor probe (Auspex type AHWU-100) were used for the boundary layer surveys. The probe wire was made of  $5 \mu\text{m}$  diameter tungsten with a length of 1.78 mm (0.07 in). The data were acquired at 10 kHz for 20 seconds per point with a 10 kHz low pass filter used before the signal was digitized with a NI USB 6343 DAQ. The viscous scaled wire length,  $l^+$ , discussed in section 3.5, was 146. An overheat ratio,  $a_r$ , of 2.0 was used with a signal gain of 4.0. Traversing of each profile was achieved using a DC stepper motor with a step size of 0.0127 mm (0.0005 in) per step. Each profile consisted of 48 points with step increments as small as 0.0254 mm (0.001 in). In order to reduce heat transfer from the wire to the plate when the wire was close to the wall, 0.05 mm (0.002 in) Kapton tape was placed on the surface where each profile was taken.

Alignment of the hot-wire probe with the surface was done using a custom camera-based alignment device shown in Figure 2.9. The device consisted of a horizontally mounted camera pointed at the upper edge of a machined aluminum block of known height placed on the ramp surface. To align the hot-wire, the probe was first traversed upward, and the camera device positioned underneath the wire. Then both the traverse and camera could be remotely controlled from the computer to precisely lower the hot-wire just over the edge of the block. Once satisfactorily aligned, the camera device could be removed and the probe finally lowered to its starting location just above the surface. This was done by subtracting the aluminum block offset height ( $3.345 \text{ in} \pm 0.001 \text{ in}$ ) and adding in the Kapton thickness (0.004 in with adhesive) and the desired starting height off the surface (typically 0.002 - 0.010 in).

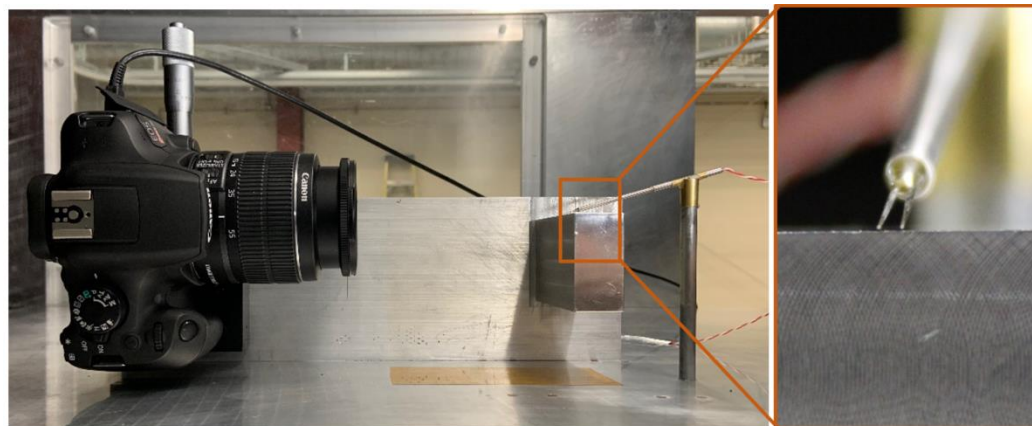


Figure 2.9 Photograph of custom camera alignment device used to determine and align the hot-wire's position above the surface

Calibration of the hot-wire was completed in situ in the wind tunnel freestream using installed pitot tube and Setra pressure transducers that were used to set the wind tunnel freestream speed. The Mach 0.6 wind tunnel uses two Setra Model 270 absolute pressure transducers to measure local static and total pressures, respectively, each with a range of 600-1100 HPa and an accuracy of 0.05% of full scale. Calibrations were done each day of testing and for each separation case. A series of 13 or 14 Mach numbers,  $M_i$ , ranging from 0 to 0.217 or 0.233 were run and the anemometer output voltages,  $E_i$ , were recorded along with the ambient fluid temperatures,  $T_i$ . Here the subscript ‘ $i$ ’ is used to denote the calibration points. The calibration points were then converted from Mach number to velocity as follows:

$$U_i = M_i \sqrt{\gamma R T_i} \quad (2.9)$$

where  $U_i$  is the calibration velocity,  $\gamma$  is the specific heat ratio (taken as 1.4 for air), and  $R$  is the gas constant for air (taken as 287.05 J/(kg·K)). The acquired voltages,  $E_i$ , were corrected for temperature variation to a reference temperature,  $T_r$ , as follows:

$$E_{i,r} = E_i \left[ \frac{T_{wc} - T_r}{T_{wc} - T_i} \right]^{\frac{1}{2}} \quad (2.10)$$

where  $E_{i,r}$  is the corrected calibration wire voltage at the reference condition,  $T_r$  is the ambient fluid temperature at the reference condition (taken as room temperature 23 °C), and  $T_{wc}$  is the wire temperature.  $T_{wc}$  is defined as follows:

$$T_{wc} = T_i + \frac{a_r - 1}{\alpha_{20}} \quad (2.11)$$

where  $a_r$  is the overheat ratio,  $a_r = R_w/R_a$ , and  $\alpha_{20}$  is the thermal coefficient of resistivity measured at 20 °C (for Tungsten wire  $\alpha_{20} = 0.0036 \text{ } ^\circ\text{C}^{-1}$ ). These corrected voltage,  $E_{i,r}$ , and velocity,  $U_i$ , data were then used to generate a calibration plot and the data were fit to a 7th order polynomial, yielding voltage as a function of velocity, defined as:

$$E(U) = p_1 U^7 + p_2 U^6 + p_3 U^5 + p_4 U^4 + p_5 U^3 + p_6 U^2 + p_7 U + p_8 \quad (2.12)$$

where  $E = f(U)$  (given by eqn. (2.12)) and the inverse of this equation is referred to as  $U = g(E)$ . A typical calibration curve is shown in Figure 2.10, below, along with the temperature variation. Note that while the temperature drops for the low velocity calibration points, this part of the calibration region is not used because the measured velocity of the boundary layer profiles does not fall below 20 m/s.

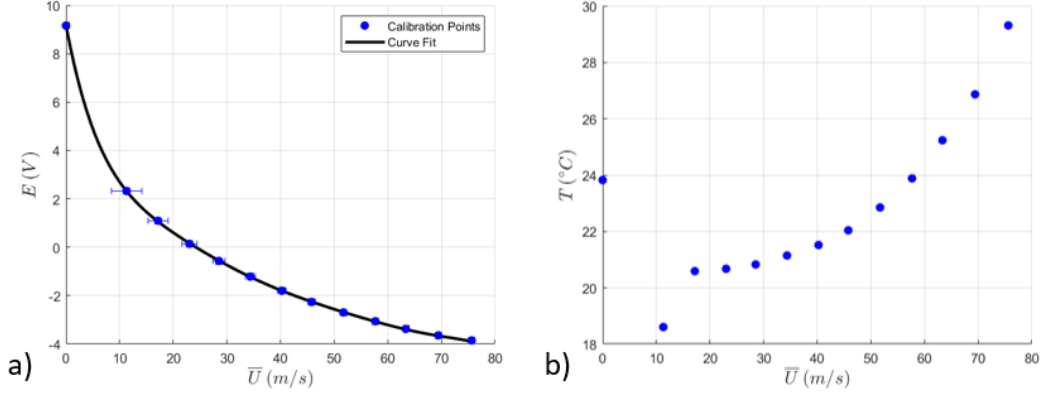


Figure 2.10 Typical hot-wire calibration curve with voltage (a) and temperature (b) as functions of velocity. Note that confidence intervals are included in the voltage plot and are due to the calibration uncertainty.

Each profile measurement began with the probe just off the surface (estimated at 0.05 - 0.254 mm) and traversing wall-normally into the freestream. For separation Case A there was very little temperature variation during each run, typically 1-2 °C, however for Cases B and C the temperature variation became more significant, with the variation approaching 10 °C. To correct for temperature effects, the temperature,  $T_a$ , was recorded for each profile. Temperature was recorded via digital data acquisition for Case B; however, for Cases A and C, temperature was only recorded manually. The hot-wire voltage was corrected to the reference temperature condition using equation (2.10) applied as:

$$E_{w,r} = E_w \left[ \frac{T_w - T_r}{T_w - T_a} \right]^{\frac{1}{2}} \quad (2.13)$$

where  $E_w$  is the recorded probe voltage,  $E_{w,r}$  is the wire voltage corrected to the reference condition, and  $T_w$  is the wire temperature, defined as follows:

$$T_w = T_a + \frac{a_0 - 1}{a_{20}} \quad (2.14)$$

The corrected voltage for each data point,  $E_{w,r}{}_j$ , was then inserted into equation (2.12) and the equation was solved implicitly for velocity,  $u_j$ , via a bisection method. This process was repeated for each data point at each location in the profile. Using the velocity time series, the mean velocity for each location was calculated as follows:

$$\bar{U} = \frac{\sum_{j=1}^N u_j}{N} \quad (2.15)$$

where  $u_j$  is the instantaneous velocity measurement and  $N$  is the number of samples. For most of the measurements  $N = 200,000$  with preliminary tests indicating that this was more than sufficient for the data to converge. The variance was calculated as follows:

$$\overline{u'^2} = \frac{\sum_{j=1}^N |u_j - \bar{U}|^2}{N - 1} \quad (2.16)$$

Sample plots of the mean and variance profiles, including 95% confidence intervals, are given in Figure 2.11. The details of the uncertainty analysis for the hot-wire measurements can be found in Appendix D.3.

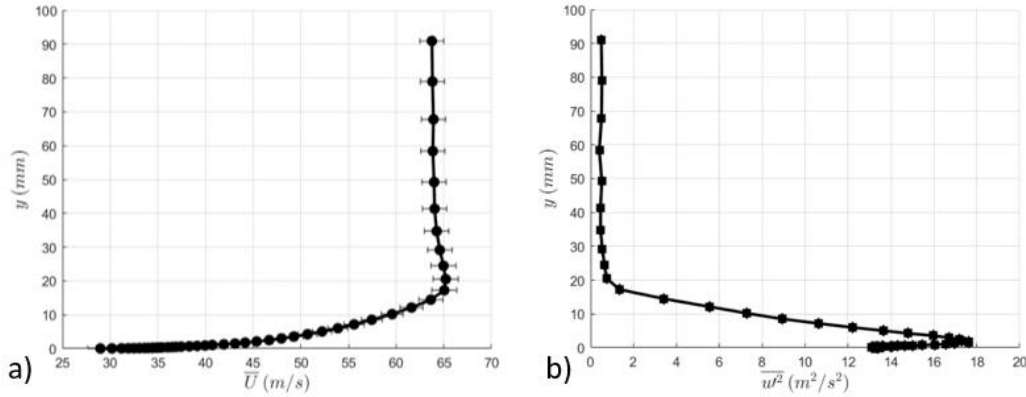


Figure 2.11 Typical mean velocity (a) and turbulent normal stress (b) profiles plotted with confidence intervals. These profiles are for Case B with the origin of the profile located at  $(X, Y, Z) = (-0.678, 0.600, 0.457)$ .

#### 2.4.4 Oil-Film Interferometry Instrumentation

Skin friction measurements on both the boundary layer development plate and upstream and downstream ends of the ramp were acquired using the oil-film interferometry (OFI) technique. This technique relates the skin friction to the thickness of a sheared oil film which, in turn, is related to the distance between optical interference fringes produced by monochromatic light that reflects from both the bottom and top of the film. Clearco silicon oils with nominal viscosities of 1,000 and 200 cSt were used as the shearing fluids. Their corresponding specific gravities were 0.974 and 0.969 with refractive indices of 1.4031 and 1.4026, respectively, for the 1,000 and 200 cSt oils. Since the aluminum surface of the ramp produces inherently poor fringe patterns, the oil was applied to a layer of 5 mil Kapton, placed over the polished aluminum surface. This method was found to produce adequate optical fringe patterns. Adjacent to the Kapton film, a small, thin stainless-steel ruler was secured to the surface to serve as a fiduciary marker for the measurement of the fringe spacing. The ruler was located along the tunnel centerline and the Kapton to either side of it. This ensured that all measurements were collected in the uniform flow region.

For the skin friction measurements, the wind tunnel was run for 20, 30, 40, or 50 minutes, and the freestream temperature and dynamic pressure were recorded at 10 Hz over the entire length of the run, including startup and shut down. The temperature was recorded using a K-type thermocouple protruding through the -Z wall and located at  $X = -0.91$  m and  $Y = 0.42$  m. The dynamic pressure was recorded using a pitot-static tube located at  $X = -0.87$  m,  $Y = 0.52$  m, and  $Z = -0.19$  m and connected to the Scanivalve SSS-48C pneumatic scanner discussed previously.

To acquire the interferogram images, a test fixture, shown in Figure 2.12, was constructed that allowed the camera and monochromatic light source to be fixed with respect to one another and to be quickly positioned in the wind tunnel after the test. A sodium lamp with wavelength of 589 nm was used as the monochromatic light source and images were acquired using a Canon Rebel t6 camera featuring a resolution of 5184 x 3456 pixels. The camera was focused and triggered remotely via a computer desktop application. Multiple images were acquired during each run and multiple runs, with differing run times, were conducted for each location of interest.

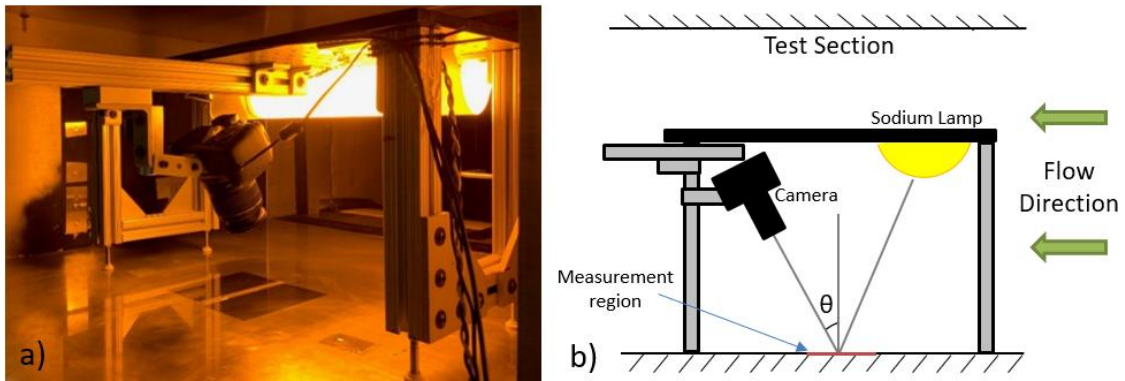


Figure 2.12 Photograph (a) and illustration (b) of test fixture, shown in place at the X = -0.678 m location, developed to illuminate and photograph the interferogram images

The resulting interferogram images were analyzed in MATLAB to determine the fringe spacing, which was defined as the distance between successive minima or maxima in light intensity. To summarize, first, the images were loaded into MATLAB and two points on the ruler were selected in terms of their pixel locations. This pixel distance was then converted to physical distance using an L2-norm and the known distance on the ruler. Next, a subregion of the image was selected as the interrogation region to determine the fringe spacing. This region was divided into pixel-wide streamwise slices over which each region was fit with two Fourier series of different orders, ranging from 2<sup>nd</sup> order to 8<sup>th</sup> order (2<sup>nd</sup> order and 7<sup>th</sup> order series were used in the example below). The mean of the fit was removed and the distance between each minimum value was calculated and converted to physical distance. These distances were then filtered to remove outliers and partial fringes, and the mean of the remaining values was taken. This process was repeated over the entire span of the interrogation region, and the distances were averaged for both order Fourier series. If the difference in the final mean fringe spacing between the two different fits was substantial, the filtering criteria was adjusted or the interrogation region was modified until a satisfactory agreement was reached. The fringe spacing value used for each run was the

average of the fit of each of the Fourier series. Figure 2.13 provides an example interferogram image highlighting the ruler and interrogation regions. The flow is from top to bottom with the start of the ramp,  $X = 0$  m, occurring at the 2 in mark on the ruler; this location is designated as  $X = 0.007$  m. Once processed, the fringe spacing was calculated to be  $\Delta x = 3.542$  mm and  $\Delta x = 3.560$  mm for 7<sup>th</sup> and 2<sup>nd</sup> order Fourier series, respectively. Figure 2.14 shows the histograms and sample Fourier series fits for this interrogation region.

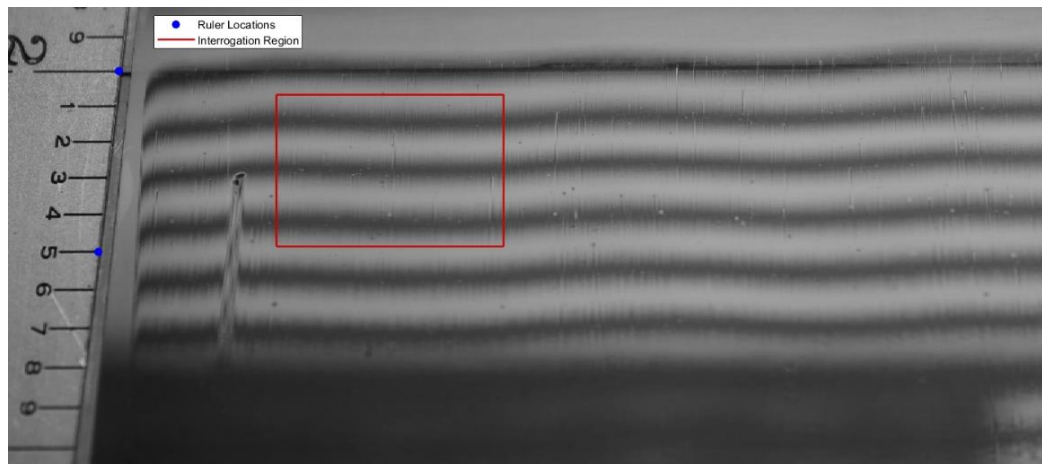


Figure 2.13 Example interferogram for Case B taken at  $X = 0.007$  m and yielding a fringe spacing of  $\Delta x = 3.55$  mm and skin friction coefficient of  $C_f = 0.00272$

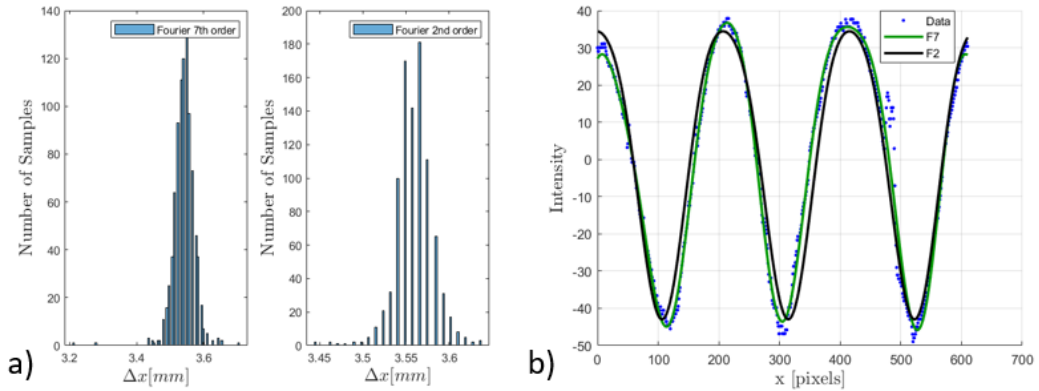


Figure 2.14 Example histogram (a) and Fourier series fit (b) for the 7<sup>th</sup> and 2<sup>nd</sup> order Fourier series corresponding to the interrogation region for Case B, X = 0.007 m

The fringe spacing was used to calculate to the skin friction via equation (2.17):

$$C_f = \frac{2n\cos(\theta)\Delta x}{\lambda \int_0^{t_{run}} \frac{q_\infty(t)}{\mu(t)} dt} \quad (2.17)$$

where  $n$  is the index of refraction of the silicon oil,  $\theta$  is the incident angle of the reflected light (in other words, the angle of the camera with respect to the local wall-normal),  $\Delta x$  is the measured fringe spacing,  $\lambda$  is the wavelength of the light source used,  $q_\infty(t)$  is the freestream dynamic pressure as a function of time,  $\mu(t)$  is the dynamic viscosity of the silicone oil as a function of time, and  $t_{run}$  is the total run time of the wind tunnel. Since accurate knowledge of the viscosity of the oil is critical, the viscosity of the oil was determined as a function of temperature utilizing the curve fit provided by Clearco (See Appendix B.2), rewritten below in a modified form.

$$\mu(T, v_0) = \rho 10^{\left(-6 + \left(\frac{763.1}{273+T} - 2.559 + \log(v_0)\right)\right)} \quad (2.18)$$

Here  $\mu$  is the dynamic viscosity (Pa·s),  $\rho$  is the density ( $\frac{kg}{m^3}$ ),  $T$  is the temperature (°C), and

$v_0$  is the kinematic viscosity (cSt) at 25 °C, all of which are properties of the silicone oil.

Figure 2.15 shows the variation of kinematic viscosity, dynamic pressure, and temperature as functions of time for the wind tunnel run in the example above.

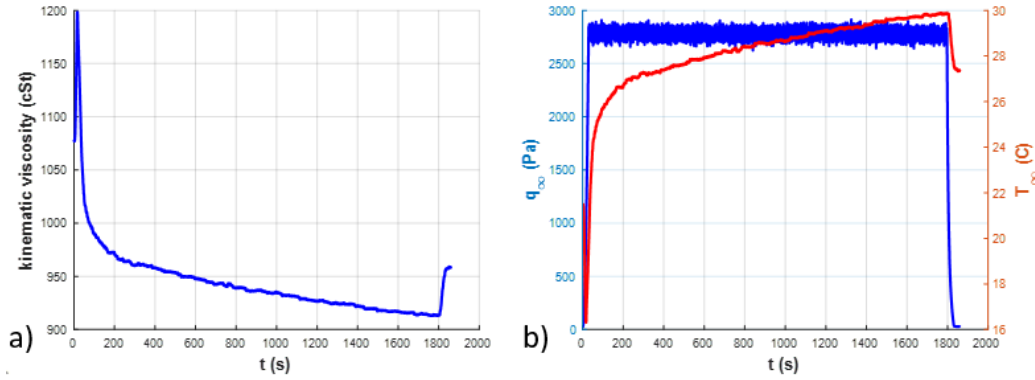


Figure 2.15 Example kinematic viscosity (a) and dynamic pressure and temperature (b) curves as functions of time for Case B,  $X = 0.007$  m, with a 30 minutes tunnel run time

#### 2.4.5 Laser Doppler Velocimetry Instrumentation

Off-surface flow field measurements were acquired using laser Doppler velocimetry (LDV), which is a non-intrusive flow field diagnostic technique. The laser used in this system is a Spectra Physics Stabilite 2017 Argon Ion Laser. It is used in conjunction with a two-component Dantec Dynamics Fiber Flow laser Doppler velocimetry system. The Doppler bursts were measured using a BSA F60 Flow processor and BSA Flow Software Version 4.10 initially, and later Version 6.5. The processor was

operated in coincidence mode so that all samples collected could be used to determine the Reynolds shear stress correlations. The Fiber Flow system splits the laser beam into two different wavelengths, a blue beam with a wavelength of 532 nm and a green beam with a wavelength of 488 nm. After the beams are split, one beam is shifted by a constant 40 MHz via a Bragg cell to unambiguously detect flow direction. The fiber optic LDV system was operated in 180-degree backscatter mode. Two lenses of different focal lengths were used on the 2D 60 mm fiber optic probe head. A 600 mm focal length lens was employed for all profiles taken on the center-span location. For many of the off-span profiles, a 400 mm focal length lens was utilized for its ability to yield higher data rates, thereby accelerating the data collection process. A photograph of the LDV system in operation is given in Figure 2.16 below.

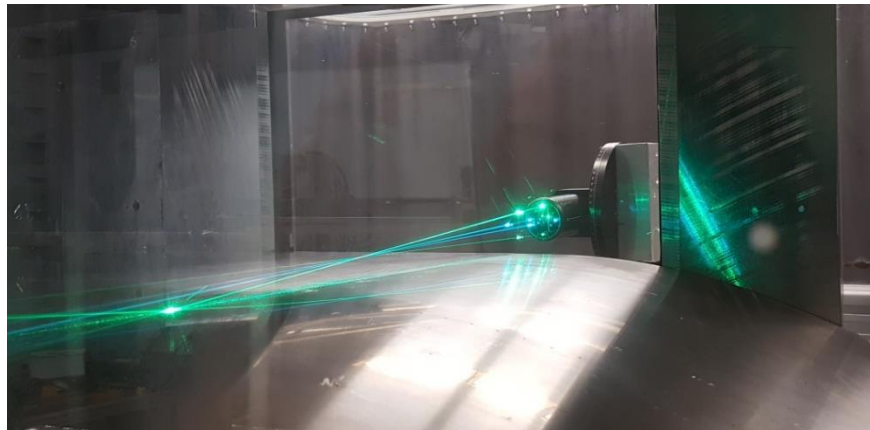


Figure 2.16 Photograph of the LDV system, utilizing the 400 mm lens, in operation, taking a profile at the start of the ramp, X = 0 m

In order to obtain near wall measurements, the LDV probe head was tilted by a small angle (angle,  $\varphi$ , in Figure 2.17) to align the bottom beam to be nearly parallel to the ramp surface. This corresponds to the alignment of the wall-normal component of velocity that is tilted approximately  $3^\circ$ - $7^\circ$  in the normal direction, which was deemed negligible. The probe measurement volume has a wall-normal dimension of approximately 0.35 mm and 0.78 mm for the 400 mm and 600 mm focal length lenses, respectively. This sets the effective wall-normal spatial resolution of the mean and turbulent stress measurements. The utilized offset height of each first point should be approximately half of the probe wall-normal dimension (i.e.  $0.35/2 = 0.18$  mm and  $0.78/2 = 0.39$  mm), however, the data sets were calculated using a prior value of  $0.38/2 = 0.19$  mm. The user may easily compensate for this difference by shifting the data, although this difference is likely within the uncertainty of the starting position, which is estimated as  $dy = \pm 0.25$  mm (the step value used in the alignment process).

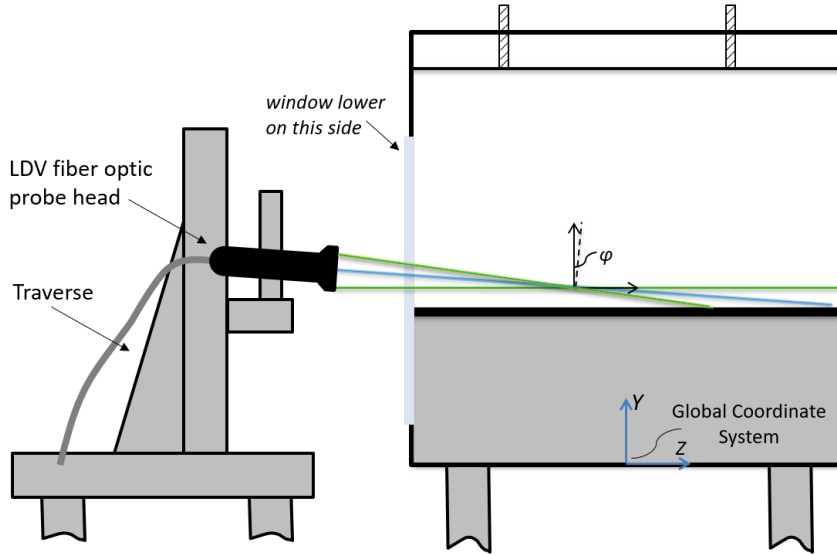


Figure 2.17 Schematic of LDV probe alignment relative to test section. Note, the image is oriented looking downstream.

To acquire the wall-normal profiles, a three-axis Aerotech traverse system was utilized in conjunction with a Unidex 11S controller. The controller uses the DM6006 Stepping Drive Module with 300SM / ES12271 stepper motors and a Parker Positioning Systems linear sled. The system has a minimum of 200 steps/rev with 1 rev = 5 mm. This yields a resolution of 0.025 mm per step. Because the controller had one inoperable axis, only two axes were able to be utilized at a time. Thus, for each wall-normal profile the z-axis of the traverse was positioned manually before the start of the run. The uncertainty for manual alignment is estimated to be  $dz = \pm 2$  mm, however, since the flow is quasi two-dimensional, its sensitivity in this spanwise direction is very small. The traverse was positioned on the lab floor with casters and then lifted using solid, threaded feet such that its position was stationary during the entire measurement process. Due to vibration of the test section, the actual location of the LDV probe volume varied relative to the model

geometry, thus the uncertainty in the measurement location is larger than the traverse resolution.

The wind tunnel was seeded with Di-Ethyl-Hexyl-Sebacot (DEHS) particles of nominally 1-micron diameter using a TSI Six-Jet Atomizer 9306 high volume liquid droplet seeding generator. Typically, only three or four jets, of the six, were used at a time. Seeding particles were introduced locally wall-normal in the upstream internal inlet contraction. For details on how the seeding particles were introduced into the flow, see Appendix B.3.

For each test, the tunnel was warmed-up and allowed to reach steady state before any LDV measurements were acquired. For each profile, the probe locations were preset in the BSA flow software and the data collection process was semi-automated. A typical profile took anywhere from 30 minutes to 3 hours to collect sufficient statistically-converged data. The number of samples collected per probe location varied significantly due to the high variation in the data rate throughout the flow measurement region. In many cases, multiple runs were acquired for a particular profile and the results were then ensemble-averaged. The data output for each probe location consisted of a separate text file containing the row number, arrival time [ms], transit time [ms], and the instantaneous streamwise,  $u$  [m/s], and wall-normal,  $v$  [m/s], velocity components for each sample. The individual text files for each probe location were imported into and processed in MATLAB. The streamwise,  $U$ , and wall-normal,  $V$ , mean velocities are defined as

$$U = \frac{1}{N} \sum_{j=1}^N u_j \quad (2.19)$$

$$V = \frac{1}{N} \sum_{j=1}^N v_j \quad (2.20)$$

Where both  $u_j$  and  $v_j$  are the instantaneous velocity measurements of the data set and  $N$  is the number of samples. Here the mean velocities ( $U$ ,  $V$ ,  $W$ ) are defined in the local coordinate system (x, y, z), whose origin is the surface location of each profile. The variances, or turbulent normal stresses, are calculated as

$$\overline{u'^2} = \frac{1}{N-1} \sum_{j=1}^N |u_j - U|^2 \quad (2.21)$$

$$\overline{v'^2} = \frac{1}{N-1} \sum_{j=1}^N |v_j - V|^2 \quad (2.22)$$

and the covariance, or turbulent shear stresses, as

$$\overline{u'v'} = \frac{1}{N-1} \sum_{j=1}^N (u_j - U)(v_j - V) \quad (2.23)$$

Sample wall-normal mean and turbulence stress profiles, including 95% confidence intervals, are plotted in Figure 2.18. This example is for Case B data taken at  $X = 0.75$  m and  $Z = 0$  m. For the mean profiles, the uncertainty is on the order of the symbol size. The details of the uncertainty analysis are provided in Appendix D.5.

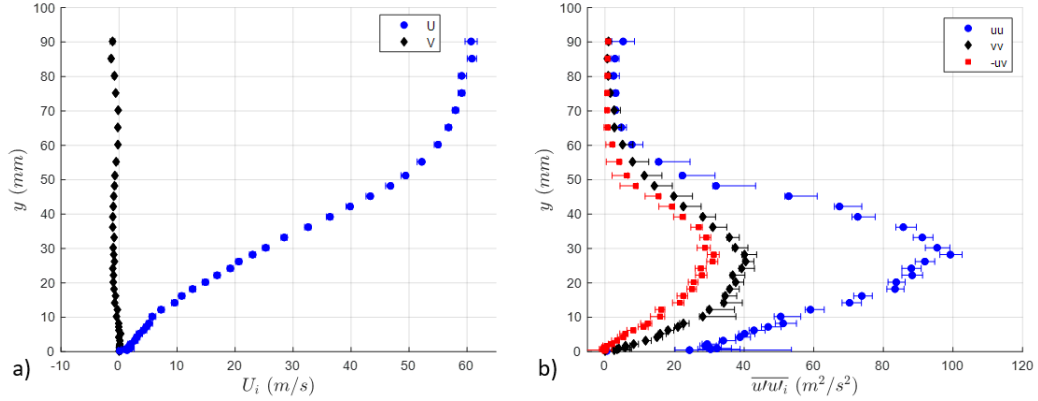


Figure 2.18 Example wall-normal mean (a) and turbulent stress (b) profiles plotted with 95% confidence intervals for Case B, located at  $X = 0.75$  m and  $Z = 0$  m

The number of samples required to achieve converged statistics varied significantly throughout both the wall-normal extent and streamwise development. Example convergence plots of the turbulent shear stress, which takes the longest to converge, are shown in Figure 2.19. The figure gives a running average of the turbulent shear stress for each additional sample with horizontal red lines representing  $\pm 5\%$  of the final value. While the figure below indicates that a few thousand samples are required for converged statistics, this is not always the case. Many of the profiles near the freestream, where the turbulent shear stress is very low, converge in fewer than 100 samples. Thus, many of the profile points in these regions still converge even though few samples were acquired. The data set accompanying this dissertation provides the number of samples acquired for each profile point.

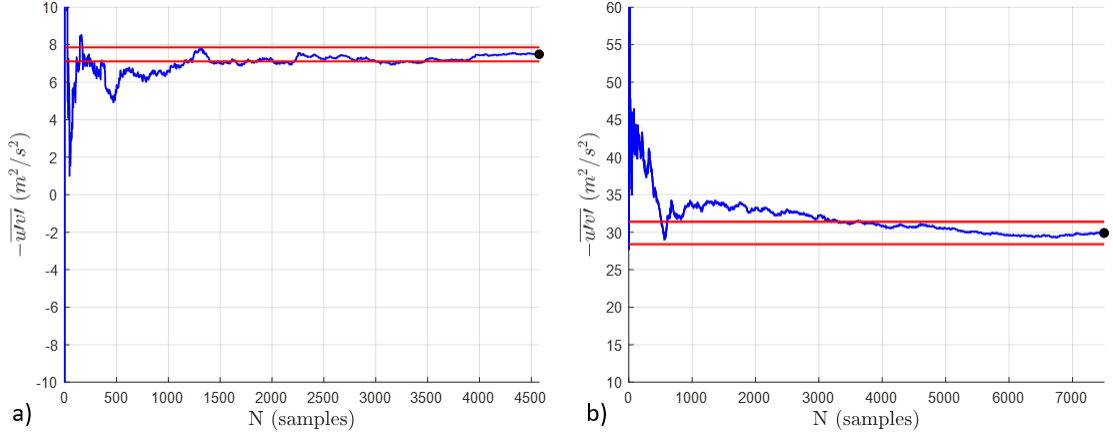


Figure 2.19 Typically convergence plots of the turbulent shear stress for a profile point with a low magnitude (a) and high magnitude (b), showing a running average of the turbulent shear stress versus the number of samples with red lines representing the final value  $\pm 5\%$

#### 2.4.6 Surface Flow Visualization Technique

There is a plethora of approaches to surface flow visualization. One of the most classic, tried-and-true methods is oil-film flow visualization. While really an assortment of methods, as most reported studies have their own experimental recipes [58], the object is always the same—visualize the skin-friction lines on the surface. Lu [59] comments on the variation among studies by noting that it is difficult to suggest a single approach as facilities and applications vary and that experimental trial-and-error appears to be the best approach. Thus, there are numerous sources for experiments both utilizing this method and discussing its theory and application [58,60–62]

Many variations of oil-film surface flow visualization were tried in this study, the most useful being a combination of two approaches: the kerosene and titanium dioxide approach combined with the aviation oil and kerosene approach. This was inspired by a recently-developed method from NASA Langley [52] where they used aviation oil, kerosene, and nanosized fumed silica particles. The final recipe used here consists of:

(67%) kerosene, (20%) w100 aviation oil, (12%) titanium dioxide and (1%) oleic acid, all combined by weight and applied to the surface by lightly brushing. Aviation oil fluoresces under ultraviolet (UV) light, leaving luminous flow patterns on the surface. It was found that the titanium dioxide, with the addition of oleic acid to prevent clumping, aids the aviation oil by enhancing the surface skin friction lines.

The basic theory is that when a light coating of the mixture is applied to the surface and a shear is applied by running the wind tunnel, the kerosene acts as a carrier agent and allows the aviation oil and titanium dioxide to flow along the surface. The air flow accelerates the evaporation of kerosene, which ultimately leaves behind the titanium dioxide powder and aviation oil. Since the layer of oil on the surface is thin, it retains the surface flow pattern with plenty of time to stop the tunnel, apply a UV light, and photograph the final steady-state results.

The procedure used in the oil-film surface flow visualization studies was as follows. First, the ramp surface was cleaned to remove any residue. Next, a flexible, adhesive-backed measuring tape was placed over the centerline pressure ports. This serves as a fiducial marker and prevents the oil mixture from clogging the ports. The oil mixture was then thoroughly mixed to keep the titanium dioxide particles from sinking to the bottom. A thin coat of this mixture was brushed on surface. After this, the removable window was bolted in place and wind tunnel was quickly turned on to the desired speed of Mach 0.2. In most cases, the test duration was approximately 30-60 minutes, which allowed most of the kerosene to evaporate. After stopping, the window was removed and a custom UV light booth, shown in Figure 2.20-b, was placed above the ramp. Finally, multiple photographs were acquired using a Canon Rebel t6 camera featuring a resolution of 5184 x 3456 pixels.

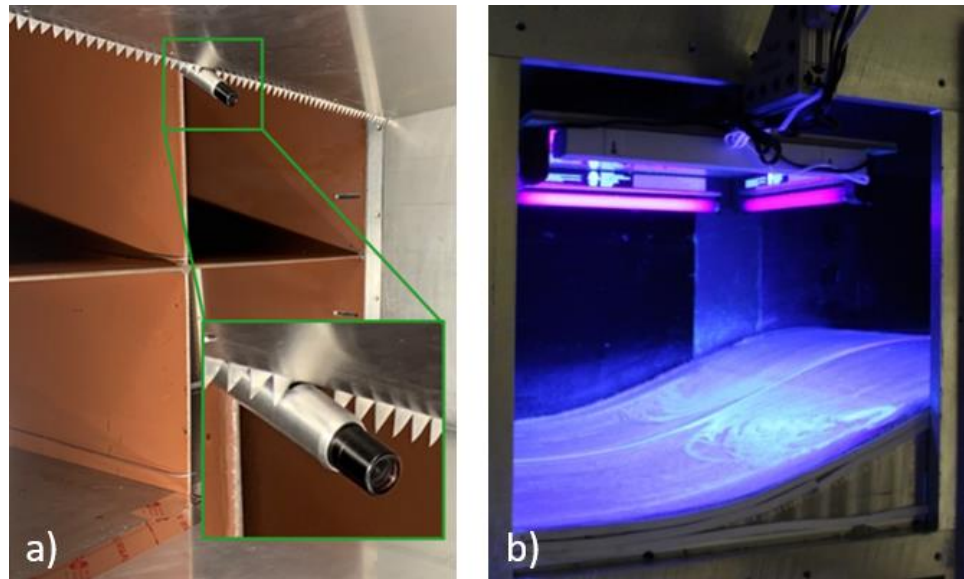


Figure 2.20 Photographs of the diffuser mounted video camera (a) and the UV light fixture installed and illuminating the surface flow (b)

In some of the surface flow visualization studies, a video camera was placed in the test section to record the development of the surface flow patterns. This camera was a 5-megapixel, HD lipstick camera provided by CCTV Camera Pros and featured a CMOS image sensor and a 3.6 mm wide angle lens. The camera was mounted to the central section of the diffuser cruciform, as shown in Figure 2.20.a.

## CHAPTER 3: BOUNDARY CONDITIONS

The adequate documentation of boundary conditions is one of the important factors that governs the usability of an experimental data set for comparison with CFD. This chapter aims to provide complete documentation of flow conditions that encompass this set of experiments. First, the basic test conditions are given. The geometry that defines each flow separation case is then introduced. Next, the mean surface pressure measurements are presented, both in their streamwise and spanwise spatial coordinates. After this, surface skin friction measurements, acquired at select streamwise locations, are presented. The incoming boundary layer and turbulence profiles are then presented and compared to a classical data set. Finally, the sidewall boundary layer and turbulence intensity profiles are shown and used to examine the uniformity of the incoming flow. What can be considered an additional boundary condition, the surface flow visualization, will receive special consideration and thus is presented in the next chapter.

### 3.1 Operating Conditions

The laboratory test conditions were recorded for each test at least once per day; these included ambient temperature, pressure, and relative humidity. All the experiments described in this work were conducted at Mach 0.2, corresponding to a freestream speed of approximately 70 m/s, unless otherwise specified. This speed was chosen so that

compressible flow solvers could be used to simulate the flow field without the need for low-speed preconditioning. While the Mach number was fixed at 0.2, there was some minor variation in the freestream velocity due to increasing tunnel temperatures. This is easily seen in the definition of the Mach number as

$$M_\infty = \frac{U_\infty}{\sqrt{\gamma RT}} \quad (3.1)$$

where  $\gamma$  is the specific heat ratio and  $R$  is the gas constant, both for air, and taken as 1.4 and 287.05 [J/(kg\*K)] respectively. With the typical variations in tunnel temperature,  $T$ , the freestream velocity,  $U_\infty$ , varied up to 0.5 – 1 m/s depending on the test configuration and run time. The details of the temperature variation and its impact on the freestream velocity are given in Appendix C. The Reynolds number was based off the ramp height,  $H$  = 0.2 [m], and is given as

$$Re_H = \frac{U_\infty H}{\nu} \approx 8.4 \times 10^5 \quad (3.2)$$

where  $U_\infty$  is the freestream velocity recorded with the pitot tube and  $\nu$  is kinematic viscosity of air. The density,  $\rho$  [kg/m<sup>3</sup>], was calculated as a function of pressure temperature and relative humidity using Jones's formula [57]

$$\rho = \frac{0.0034848}{T+273.15} (P - 0.0037960 * RH * P_s) \quad (3.3)$$

where  $P$  is the atmospheric pressure [Pa],  $T$  is the temperature [C],  $RH$  is the relative humidity [%], and  $P_s$  is the saturated water vapor pressure. Teten's formula was used to calculate the saturated water vapor pressure as

$$P_s = 611 \times 10^{\left(\frac{7.5T}{T+237.3}\right)} \quad (3.4)$$

The dynamic viscosity was calculated using Sutherland's law [63] with three coefficients which has the form

$$\mu = \mu_0 \left(\frac{T}{T_0}\right)^{\frac{3}{2}} \left(\frac{T_0+S}{T+S}\right) \quad (3.5)$$

where  $T$  is the temperature [K],  $\mu_0 = 1.7894 \times 10^{-5}$  [kg/(m\*s)] is a reference viscosity,  $T_0 = 273.11$  [K] is a reference temperature, and the Sutherland constant  $S = 110.56$  [K] is the effective temperature. The kinematic viscosity is related to the dynamic viscosity and density as

$$\nu = \frac{\mu}{\rho} \quad (3.6)$$

and has units of [m<sup>2</sup>/s].

### 3.2 Ceiling Configuration of Separation Cases A, B, and C

One of the primary goals of this work is to produce a set of three smooth-body flow, benchmark validation experiments, where the important flow features develop over the same geometric boundary. These cases include a larger-scale separation case, a smaller-scale separation case, and an attached flow case, where the scale of the separation refers to the streamwise extent of the mean separation region in relation to the length of the ramp geometry. In Chapter 7, the mean separation extents will be shown to be approximately 39%, 24%, and 0% of the ramp length for the three cases listed, respectively. Additionally, Deck [16] would classify these separation cases as belonging to the family of massively separated flows since the initial boundary layer thickness to ramp height ratio,  $\frac{\delta_{99}}{H}$ , is on the order 0.1.

The geometry, (described in Chapter 2) consisting of the boundary layer development plate and the smooth-body ramp, remained identical for all experiments. The desired variation in the three data sets was achieved by varying the streamwise adverse pressure gradient (APG), which in turn was imposed by differing the position of the flexible ceiling. A wide range of ceiling positions were examined and their respective streamwise pressure distributions recorded. These results, in conjunction with preliminary surface flow visualization and LDV measurements, were used to select three different ceiling positions, which were, in turn, chosen to best produce the desired large- and small-scale separation cases and a fully attached flow case (designated as Cases A, B, and C, respectively). The larger-scale separation case, Case A, represents the largest streamwise separation extent that can be achieved with reattachment still occurring within the optical access window. For all these cases, a semi-linear variation in ceiling position was maintained over the ramp

region, with an approximate downward ceiling tilt angle,  $\alpha$ , of  $3.2^\circ$ ,  $5.6^\circ$ , and  $7.7^\circ$  for Cases A, B, and C, respectively. The ceiling configurations corresponding to these three test cases are shown in Figure 3.1, with the detailed position data provided in Appendix A.5. Upstream from the ramp, the ceiling geometry is approximately identical for the three separation cases, with the variation beginning at the start of the ramp,  $X = 0$ .

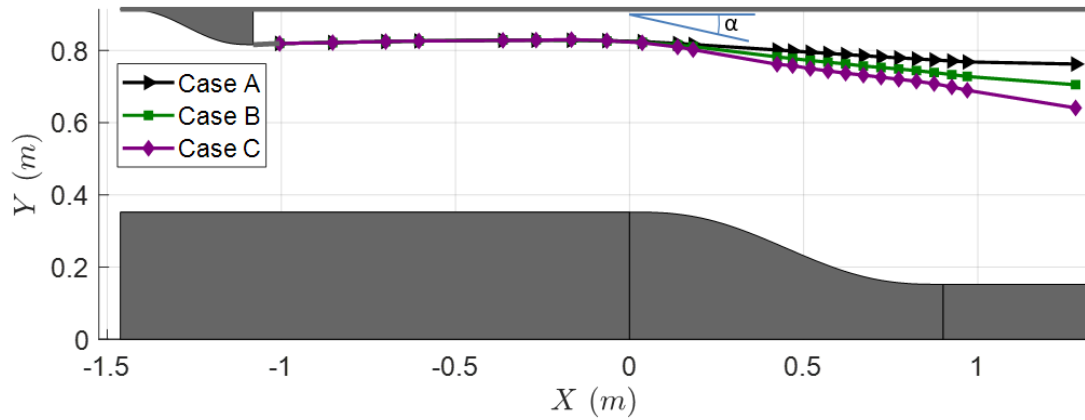


Figure 3.1 Illustration of ceiling configurations of separation cases A and B, and of attached flow case C

### 3.3 Surface Pressure Measurements

The streamwise pressure coefficient and pressure coefficient gradient distributions along the centerline are shown in Figure 3.2. Due to the upper ceiling contour at the inlet, there is a favorable pressure gradient over the first part of the boundary layer development plate followed by a nominally zero pressure gradient region, common to all cases. The location  $X = -0.56$  m was originally selected to define the inflow conditions and is the location where the LDV profiles for this experiment begin; however, due to geometric constraints on obtaining hot-wire measurements, the location  $X = -0.678$  m was subsequently selected as the initial condition and is where the recorded inflow boundary

layers and skin friction measurements begin. In all cases there is a favorable pressure gradient near the ramp's leading edge which is followed by a strong adverse pressure gradient commencing near  $X = 0.2$  m. Around  $X = 0.5$  m the pressure gradient flattens, roughly corresponding to separation, and then remains mildly adverse over the rest of the ramp and test section.

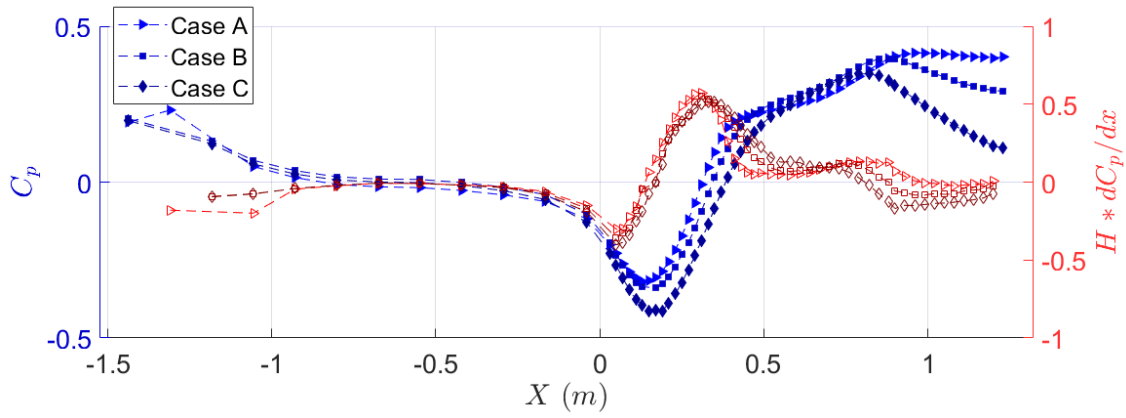


Figure 3.2 Centerline static pressure coefficient distributions for Cases A, B, and C. Note that closed symbols represent the pressure coefficient distribution and open symbols represent the pressure coefficient gradient distribution.

Spanwise pressure measurements were made at seven streamwise locations on and just downstream of the ramp geometry. At each of these locations, five pressure taps, covering approximately the central third of the span, were used to record and analyze the uniformity of the flow. If any significant variation in spanwise pressure was observed, the side-to-side ceiling positioning was reexamined and adjusted to eliminate this behavior. Figure 3.3 shows the spanwise pressure distributions for Cases A, B, and C. All appear to be quite flat without a significant spanwise pressure gradient. However, it is noted by Jenkins et al. [48] that without further flow visualization, a spanwise pressure distribution similar to the distribution measured here could easily be interpreted to represent uniform,

two-dimensional flow. When, in fact, it will be shown in Chapter 4 that this is not the case. Additionally, the small spanwise pressure gradient and pressure minima and maxima will be shown to correspond well with the observed surface flow features.

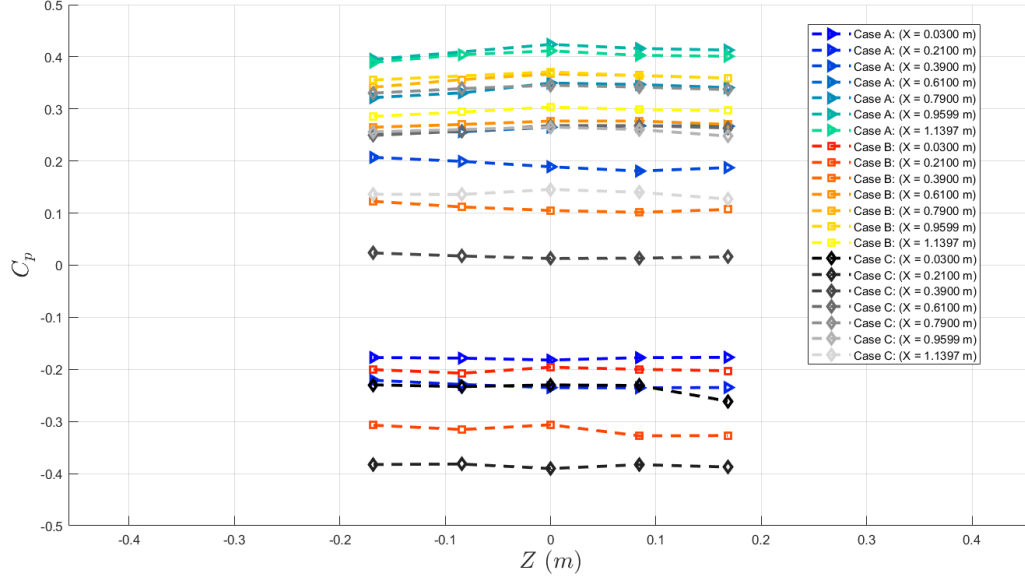


Figure 3.3 Spanwise pressure coefficient distributions for Cases A, B, and C. Note that the uncertainty in the measurements is on the order of the symbol size.

### 3.4 Surface Skin Friction Measurements

Skin friction measurements make up one of the important data components necessary for the validation of off-design RANS simulations [64]. Furthermore, in the initial presentation of this work, many researchers voiced their desire for the inclusion of such skin friction measurements. While much of the surface flow over the ramp is three-dimensional, and hence it would be very difficult to accurately measure skin friction, where possible, measurements were acquired via the oil-film interferometry (OFI) method. These measurement regions include three streamwise locations,  $X = -0.678$  m,  $X = 0.007$  m, and  $X = 0.907$  m, and were chosen because they exhibit no surface curvature and experience

relatively spanwise uniform flow. They include the turbulent boundary layer initial condition, the condition at the start of the ramp, and condition at the end of the ramp, respectively. All reported measurements were made within  $Z = \pm 0.05$  m of the tunnel centerline and are reported in the form of the skin friction coefficient defined as

$$C_f = \frac{\tau_w}{\frac{1}{2}\rho U_\infty^2} \quad (3.7)$$

The results, including 95% confidence intervals, are reported in Table 3.1 below.

From the initial condition to the start of the ramp, all three cases have approximately the same skin friction coefficients, considering the given uncertainty. At the end of the ramp,  $X = 0.907$  m, the skin friction coefficient increases monotonically from Cases A to C. As will be shown in the following chapters, this agrees well with the surface flow patterns and the LDV flow field measurements. This location represents the beginning of the recovery region for Case A, so the skin friction has just started to increase from its prior negative and zero values, whereas for Case C, the flow is attached, indicating that the skin friction never quite dropped to zero.

TABLE 3.1  
SKIN FRICTION COEFFICIENT MEASUREMENTS

	<b>X = -0.678 [m]</b>	<b>X = 0.007 [m]</b>	<b>X = 0.907 [m]</b>
Case A	0.00235 ± 0.00016	0.00268 ± 0.00019	0.00019 ± 0.00002
Case B	0.00229 ± 0.00017	0.00272 ± 0.00020	0.00055 ± 0.00005
Case C	0.00241 ± 0.00020	0.00241 ± 0.00020	0.00084 ± 0.00007

### 3.5 Incoming Boundary Layer Profiles

#### 3.5.1 Development Plate

The incoming boundary layers for all test cases were measured using hot-wire anemometry. The profiles were acquired along the boundary layer development plate at a streamwise position of  $X = -0.678$  m and along the tunnel centerline,  $Z = 0$  m. Figure 3.4 shows these mean velocity profiles plotted using outer variable scaling. Since the pressure and pressure gradient distribution(s) are almost identical along the development plate leading up to the location where the boundary layer profiles are taken, the profiles would be expected to follow the same trend. Upon comparison, the mean profiles show excellent agreement between cases, as well as with the canonical ZPG boundary layer data of Klebanoff [65], taken at  $Re_\theta \approx 7,000$ . Also included in Figure 3.4 is a preliminary mean velocity profile acquired along the tunnel centerline,  $Z = 0$  m, at  $X = -0.56$  m using hot-wire anemometry. This profile, acquired during the initial risk reduction testing phase, confirms that there is no noticeable change in the outer variable scaled mean velocity

profile between the original initial condition,  $X = -0.56$  m, and the new initial condition located roughly 12 cm upstream at  $X = -0.678$  m.

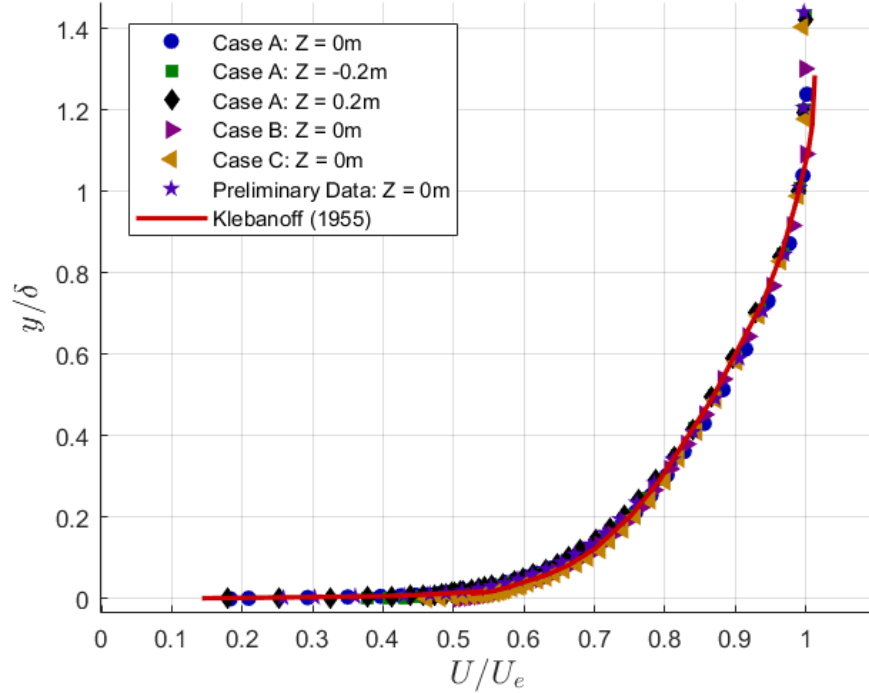


Figure 3.4 Boundary layer profiles acquired on the development plate at  $X = -0.678$  m and scaled using outer variables for Cases A, B and C compared to both preliminary hot-wire data acquired at  $X = -0.56$ m and data from Klebanoff [65]

In the near-wall region there is a slight variation between the cases, with Case C exhibiting a fuller profile than Case B and Case B exhibiting a fuller profile than Case A. This is demonstrated by the decrease in the shape factor from 1.30 to 1.17 for Cases A to C, respectively, Table 3.2. Regardless, the shape factors exhibited here are in the range expected of a near ZPG turbulent boundary layer,  $H = 1.3 – 1.4$ , with the lower values occurring because the boundary layer is subjected to a slight FPG just upstream from the hot-wire profile location. In addition, the spanwise uniformity of the flow was documented

via two off-center profiles taken at  $Z = \pm 0.2$  m. This was only done for Case A, as the results, shown in Figure 3.4, exhibit excellent spanwise agreement.

TABLE 3.2  
DEVELOPMENT PLATE BOUNDARY LAYER PARAMETERS

<b>Case</b>	<b>X [m]</b>	<b>Y [m]</b>	<b>Z [m]</b>	<b><math>U_e</math> [m/s]</b>	<b><math>\delta_{99}</math> [mm]</b>	<b><math>\theta</math> [mm]</b>	<b><math>\delta^*</math> [mm]</b>	<b>H</b>
A	-0.678	0.352	0.000	69.22	16.59	2.20	2.87	1.30
A	-0.678	0.352	-0.200	69.22	17.09	2.31	2.98	1.29
A	-0.678	0.352	0.200	70.68	17.20	2.36	3.09	1.31
B	-0.678	0.352	0.000	68.61	15.85	2.82	3.43	1.21
C	-0.678	0.352	0.000	66.36	14.88	3.72	4.34	1.17
PD <sup>1</sup>	-0.560	0.352	0.000	70.24	16.83	2.30	2.99	1.30

The centerline mean profile,  $Z = 0$  m, for Case A was also plotted in inner variable scaling, Figure 3.5. The inner variables are defined as

$$u^+ = \frac{\bar{U}}{U_\tau} \quad (3.8)$$

and

$$y^+ = \frac{yU_\tau}{\nu} \quad (3.9)$$

where the friction velocity,  $U_\tau$ , is

---

<sup>1</sup> Here PD stands for preliminary data, acquired during the initial risk reduction phase using the same ceiling configuration over the development plate and a slightly different one downstream over the ramp.

$$U_\tau = \sqrt{\frac{\tau_w}{\rho}} = U_\infty \sqrt{\frac{C_f}{2}} \quad (3.10)$$

Figure 3.5 also includes the log-law defined as

$$u^+ = \frac{1}{\kappa} \ln(y^+) + B \quad (3.11)$$

where  $\kappa$  is the von Karman constant, taken as 0.384, and  $B$  is an additive constant taken as 4.17, the values suggested by Nagib and Chauhan [66] for ZPG TBLs. The skin friction coefficient used in calculating the friction velocity was determined via the Clauser method and found to be  $C_f = 0.00255$ . Initially the OFI measurement,  $C_f = 0.00235$ , was used; however, a slight bias was observed in the log region that upon further investigation was determined to be caused by a low skin friction coefficient. While the OFI skin friction coefficient measurement is low, it is only 8.5% below the Clauser determined measurement and only marginally, 1.6%, below the 95% confidence interval. The mean profile at  $X = -0.678$  m displays good log-law behavior and excellent agreement with both the preliminary hot-wire, and LDV mean velocity profiles, taken roughly 12 cm downstream at  $X = -0.56$  m.

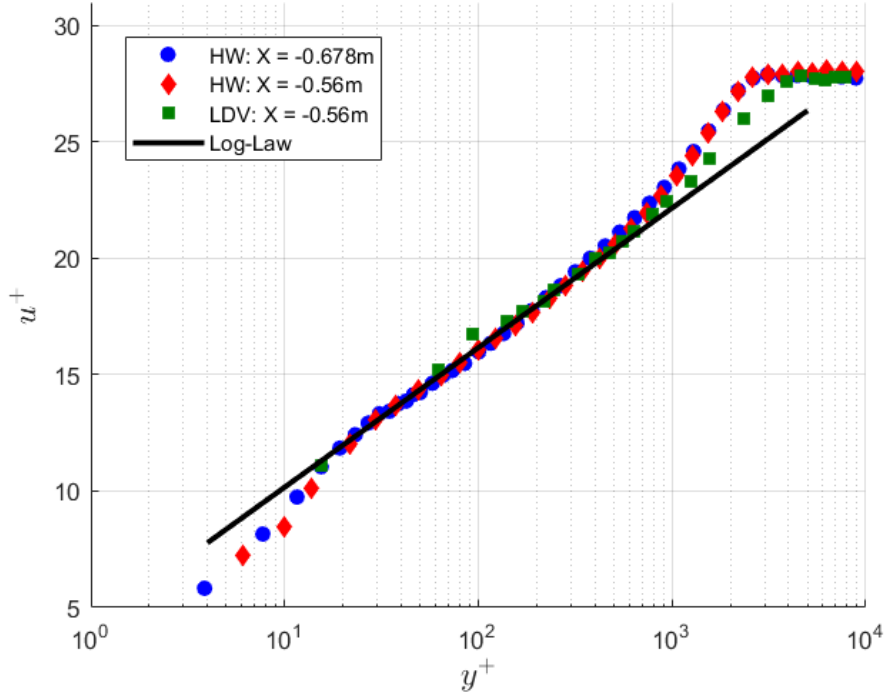


Figure 3.5 Centerline hot-wire (HW) boundary layer profiles, plotted in inner variables, for Case A,  $X = -0.678$  m, compared to both preliminary hot-wire, and LDV profiles acquired at  $X = -0.56$  m

While the mean hot-wire profiles agree well with the classical data of Klebanoff [65] and exhibit good log-law behavior, the turbulence intensity profiles only show partial agreement. Figure 3.6 shows the turbulence intensity profiles corresponding to the same data sets as the mean profiles shown in Figure 3.4. Over the central third of the boundary layer the agreement between the hot-wire data and the results of Klebanoff [65] is quite good; however, the near-wall peak is not observed and the freestream turbulence intensity is quite large, approaching 0.01. Nevertheless, the spanwise uniformity of the turbulence intensity is quite good and there is very little variation observed between flow cases.

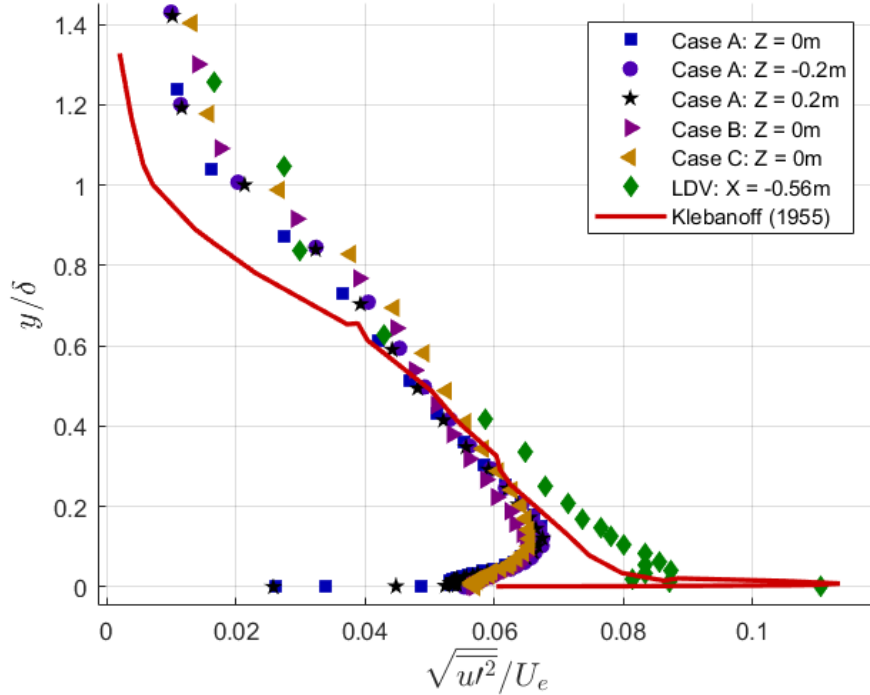


Figure 3.6 Turbulence intensity profiles acquired via hot-wire anemometry on the development plate at  $X = -0.678$  m with comparisons to the LDV data,  $X = -0.56$  m, and Klebanoff [65]

The high turbulence levels in the freestream could likely be associated with a number of factors including: the dramatic alteration of the test section due to a blockage of approximately 49%, imposition of the roughness strip only 0.52 m upstream of the profiles, and electrical signal noise in the hot-wire data acquisition. The low turbulence levels in the near wall region are more clearly shown when plotted using inner variable scaled turbulence intensity, as done in Figure 3.7. The figure shows that the inner peak of the hot-wire data is dramatically attenuated while the outer peak is pronounced as compared to the typical ZPG turbulent boundary layer such as Klebanoff [65].

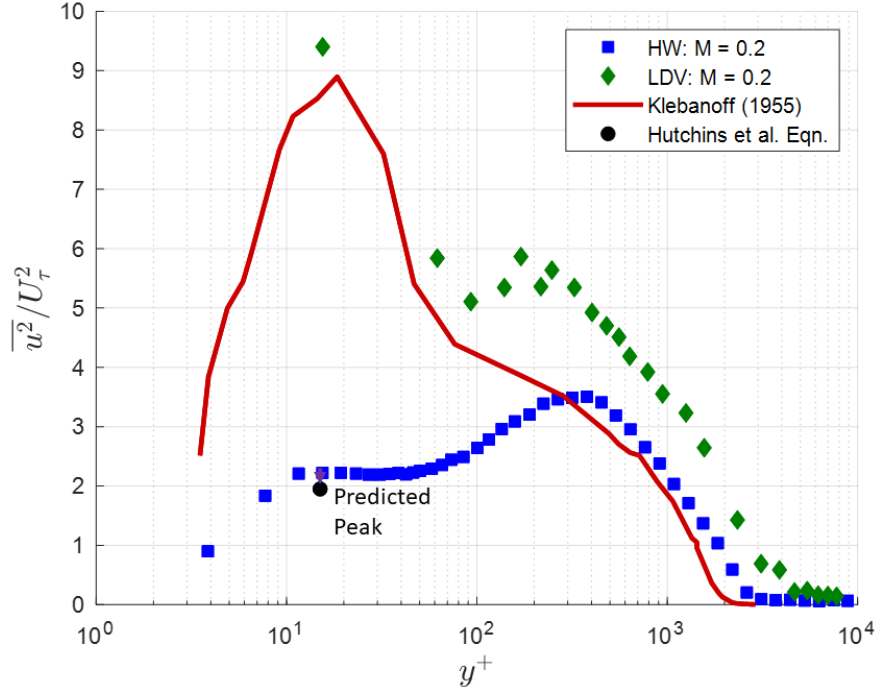


Figure 3.7 Turbulence intensity profiles plotted in inner variables, for Case A with comparisons of: hot-wire (HW) located at  $X = -0.678$  m, LDV located at  $X = -0.56$  m, Klebanoff [65], and the predicted turbulence peak magnitude calculated via Eqn. (3.14) from Hutchins et al. [67]

To accurately classify this phenomenon we must examine the hot-wire parameters, including the viscous scaled wire length,  $l^+$ , defined as:

$$l^+ = \frac{lU_\tau}{\nu} \quad (3.12)$$

and the length to diameter ratio,  $\frac{l}{d}$ , of the wire sensing element. Ligrani & Bradshaw [68]

recommend that  $l^+ < 20$  and  $\frac{l}{d} > 200$  for accurate hot-wire measurements in turbulent

boundary layers. The wire used in this study has an  $\frac{l}{d} \approx 200$ , so the slender rod

approximation is good and not expected to adversely affect the measurement; however,  $l^+$

$\approx 146$  which is significantly higher than the recommended value. The effects of this large  $l^+$  likely manifest themselves in the form of spatial averaging over the span of the hot-wire sensor length, which in turn influences the shape and magnitude of the turbulence profiles.

Hutchins et al. [67] provide a likely explanation for this phenomenon—suggesting that the attenuation of small scales due to a large viscous scaled wire length is responsible. Mathis et al. [69] explore this phenomenon further by decomposing the viscous scaled turbulence intensity into large-scale and small-scale components. The small-scale component is approximately independent of Reynolds numbers and contains the near-wall inner peak while the large-scale component increases in magnitude with increasing Reynolds number and contains the outer peak. Note that the Reynolds number referred to is the skin friction Reynolds number,

$$Re_\tau = \frac{\delta U_\tau}{\nu} \quad (3.13)$$

where  $Re_\tau \approx 2,400$  for the tests, conducted at Mach 0.2, which is just below the range examined by Mathis et al. [69]. Due to the large  $l^+$ , the data shown here are expected to contain primarily the large-scale filtered component of the turbulence intensity. Comparing Figure 3.7 with the filtered data from Mathis et al. [69], the substantial agreement indicates that sensor filtering is likely the culprit.

Additionally, Hutchins et al. [67] also provided a way to quantitatively compare the effects that  $l^+$  and  $Re_\tau$  have on the inner variable scaled turbulence peak by examining numerous studies and developing a nonlinear least squares regression fit to the available experimental data, which takes on the form

$$\left. \frac{\overline{u^2}}{U_\tau^2} \right|_m = A \log_{10}(Re_\tau) - Bl^+ - C \left( \frac{l^+}{Re_\tau} \right) + D \quad (3.14)$$

where  $A = 1.0747$ ,  $B = 0.0352$ ,  $C = 23.0833$ ,  $D = 4.8371$ , and the subscript  $m$  stands for the peak value. Our experimental data is just within the range of this function,  $3 < l^+ < 153$  and  $316 < Re_\tau < 25,000$ , which predicts the inner variable scaled turbulence peak to be 2.0. This predicted value compares well to the observed inner peak value of 2.2 in Figure 3.7. Considering the experimental basis of this prediction equation (3.14), the substantial agreement provides additional evidence that sensor spatial filtering is the cause of the reported low near-wall turbulence values.

While this demonstrates that the hot-wire data is attenuated due to the sensor size, the LDV measurements do not suffer in the same way. The turbulence intensity measurements acquired via LDV, shown in Figure 3.6 and Figure 3.7, agree with Klebanoff [65] and the outer unaffected region of the hot-wire measurements. Although they are not without their own problems, as they suffer from poor near-wall resolution, low sample size approaching the freestream, and enhanced freestream turbulence levels, they do manage to capture more of the near-wall turbulence peak. Again, this provides supporting evidence that the incoming boundary layer features all the aspects typical of a near ZPG TBL.

### 3.5.2 Sidewalls

Documentation of the sidewall boundary layer profiles is important for accurately modeling the flow using CFD. Nonetheless, this is one of the features that is often overlooked in most experimental studies which prompted the acquisition of multiple sidewall boundary layer profiles in this study to best characterize the flow and highlight

the symmetry. Sidewall boundary layer profiles were acquired using hot-wire anemometry at the same streamwise location,  $X = -0.678$  m, that was used on the development plate for all three test cases. Figure 3.8 presents a schematic highlighting the location of each profile, designated by the nearest surface starting point given in the form of the coordinate triple [X, Y, Z].

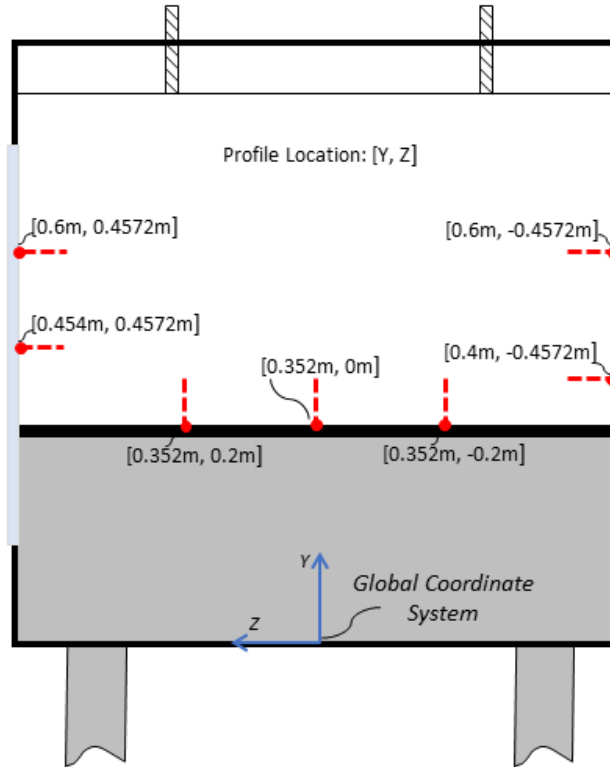


Figure 3.8 Test section cross-sectional view, oriented looking upstream, highlighting the starting locations of the development plate and sidewall boundary layer profiles acquired using hot-wire anemometry. All profiles shown here are located at  $X = -0.678$  m with the coordinate [Y, Z] pair denoting each profile location.

Figure 3.9 presents the boundary layer profiles for the sidewall locations given in Figure 3.8. For all cases, profiles located 24.8 cm above the development plate,  $Y = 0.600$  m, are included on both inner and outer loop sidewalls, with Case A including an additional profile closer to the development plate on each sidewall. In general, there is agreement among the profiles taken at  $Y = 0.600$  m with excellent side-to-side symmetry. Similar to the development plate profiles, the one noticeable variation among the profiles is the slight loss in momentum transitioning from Cases A to C. This is evident because the momentum thickness increases more than the displacement thickness, equating to a slight drop in the shape factor from  $H = 1.27$  to  $H = 1.17$  from Cases A to C. This is more apparent in Table 3.3, which includes all the relevant boundary layer parameters for the profiles presented in Figure 3.9.

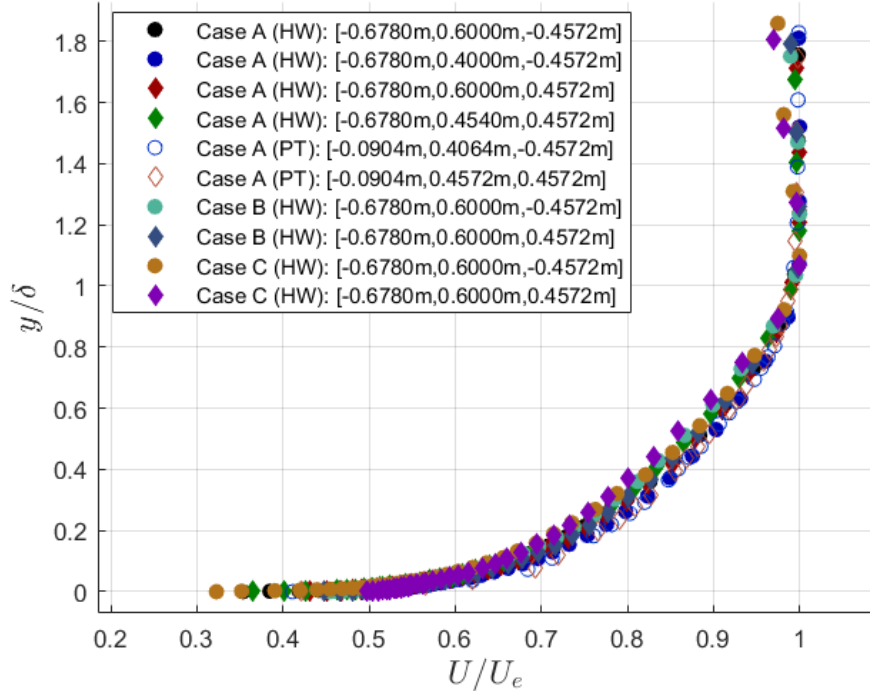


Figure 3.9 Sidewall boundary layer profiles, scaled using outer variables, for all three test cases using both hot-wire anemometry (HW) and pitot-tube (PT) measurements. Note that the legend provides the surface starting point for each profile given in [X,Y,Z] coordinates, with circle and diamond symbols representing the wind tunnel outer and inner loops respectively.

For Case A, additional sidewall boundary layer profiles were acquired downstream from the initial condition location to check the symmetry as the boundary layer developed. These profiles, shown in Figure 3.9, were located at  $X = -0.0904$  m, approximately 9 cm before the start of the ramp, and acquired using a small boundary layer probe. The figure shows that the flow is still developing symmetrically here, with the profiles agreeing well with one another, and depicts little change in profile shape compared to the upstream boundary layers. Over this 59 cm stretch, the sidewall boundary layers grow approximately 50% in thickness, increasing from about 17 cm to 26 cm as shown in Table 3.3.

TABLE 3.3  
BOUNDARY LAYER PARAMETERS

<b>Case</b>	<b>X [m]</b>	<b>Y [m]</b>	<b>Z [m]</b>	<b>U<sub>e</sub> [m/s]</b>	<b>δ<sub>99</sub> [mm]</b>	<b>θ [mm]</b>	<b>δ* [mm]</b>	<b>H</b>
A	-0.678	0.400	-0.457	69.20	19.26	2.20	2.84	1.29
A	-0.678	0.600	-0.457	67.83	16.61	2.48	3.14	1.27
A	-0.678	0.600	0.457	67.93	17.03	2.35	3.01	1.28
A	-0.678	0.454	0.457	68.58	17.26	3.03	3.76	1.24
A	-0.090	0.457	0.457	71.59	24.78	2.67	3.48	1.30
A	-0.090	0.406	-0.457	71.99	26.90	2.85	3.72	1.30
B	-0.678	0.600	-0.457	71.34	16.58	3.72	4.47	1.20
B	-0.678	0.600	0.457	65.19	16.19	3.09	3.73	1.21
C	-0.678	0.600	-0.457	70.65	15.67	5.71	6.70	1.17
C	-0.678	0.600	0.457	71.70	16.06	4.82	5.65	1.17

The turbulence intensity profiles, corresponding to the mean profiles presented in Figure 3.9, are given in Figure 3.10. The near-wall turbulence peak shows excellent symmetry and overlap among cases and aligns well with development plate profiles, although it suffers from the same hot-wire sensor spanwise filtering effect described for the development plate profiles; i.e. the peak levels near the wall are underrepresented. The outer region shows good side-to-side symmetry as well, with sequentially increasing turbulence levels from Cases A to C.

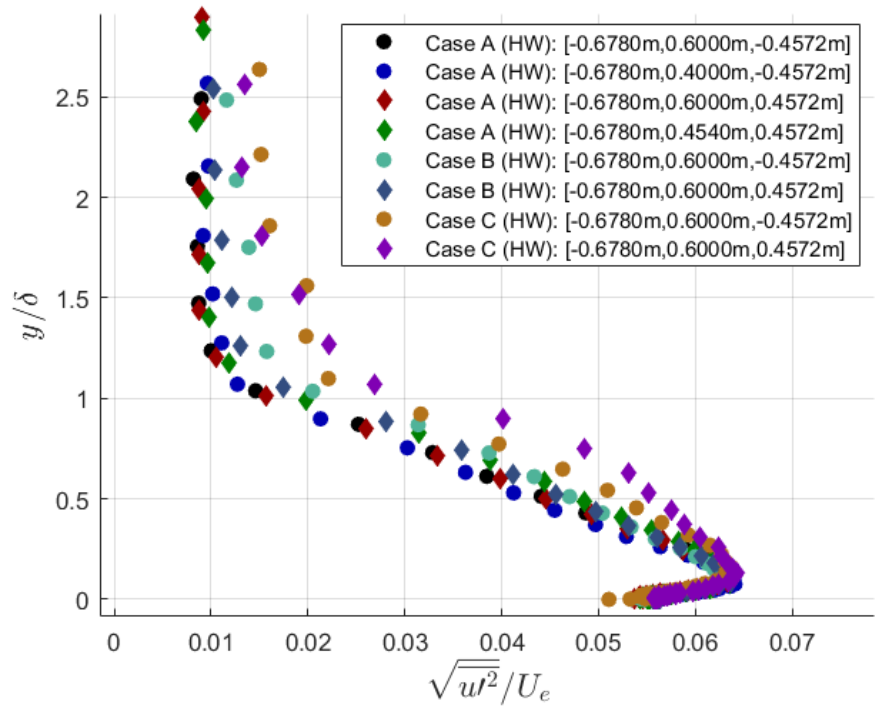


Figure 3.10 Sidewall turbulence intensity profiles, scaled using outer variables, for all three test cases using hot-wire anemometry (HW). Note that the legend provides the surface starting point for each profile given in [X,Y,Z] coordinates, with circle and diamond symbols representing the wind tunnel outer and inner loops respectively.

## CHAPTER 4: SURFACE FLOW CHARACTERISTICS

Some of the earliest studies of turbulent flow date back to the time of Leonardo da Vinci. These studies came in the form of the careful observation of flows in nature and were recorded using detailed sketches that highlight the nature and scale of the observable flow structures. Remarkably, over 500 years later, a variation of this form of study is still useful to understand fluid motion and give the researcher a global view. It is the modern equivalent of this form of observation that will be utilized and discussed here. The primary goal of this chapter is to give a visual depiction of the time mean surface flow on the ramp that will enhance understanding of measurements presented throughout the rest of this work.

Oil-film flow visualization was used to provide an initial assessment of the surface flow pattern including qualitative information regarding separation, reattachment and overall spanwise flow uniformity. The surface flow topography is presented for all three separation cases, using images acquired via oil-film flow visualization. Topological flow features in the form of singular points are identified throughout these images as they will be used in the following chapter to construct surface flow topological maps of the separation and reattachment regions. Due to the nature of the three-dimensional separation patterns, a lengthy review is presented on their apparent ubiquity in cases involving

smooth-body flow separation. Finally, the chapter concludes with a discussion of the ramp aspect ratio and how that contributes to the three-dimensionality of the separation structure.

#### 4.1 Surface Flow Topography

It is useful to distinguish between topography and topology, as these terms will be frequently used throughout this chapter and the next. The surface flow topography is the surface flow pattern observed over the ramp via the application of oil-film flow visualization. It presents the relationship between surface flow features, including their respective sizes and positions. Topology, which will be discussed in detail in Chapter 5, primarily differs from topography in that while the topography is concerned with the flow features, including size, strength and their respective locations to one another, topology is only concerned with the connections between features. Topology is a subset of mathematics concerned with spatial properties that are preserved under continuous deformations of objects. Hence a topographical map/pattern could be thought of as what is physically observed in an experiment, whereas a topological map is a mathematical description of that topographical map (and likely many others) that need not be drawn to scale.

Throughout this chapter, the topographical flow features/structures will frequently be identified using terms such as *vortical structure*. Since the goal of the following chapter is to present and discuss the flow topology, the equivalent topological terminology used to describe these features will be given. Here a *vortical structure* would equate to a topological singular/critical point of a *focus* (an inward or outward spiraling node). In surface topology there are saddle points (the flow entering on one axis and departing on another) and nodes (the flow entering or departing from both axes). A focus is a type of

node. In the terminology used here, “S” will stand for a saddle point, “F” for a focus, and “N” for a node, with the number following identifying which particular feature is being discussed, e.g. S1 stands for saddle point 1.

#### 4.1.1 Case A – Larger-Scale Separation

Here we will describe in detail the topography of the surface flow pattern for the large-scale separation case, Case A. The global surface flow visualization, consisting of the pattern of skin-friction lines, is presented in Figure 4.1. The surface flow pattern is clearly dominated by the presence of two large, symmetric, counter-rotating vortical structures in the central region of the ramp and a spanwise uniform reattachment location farther downstream; together they extend over approximately 50% of the ramp surface. The surface flow pattern over the majority of the ramp is inherently three-dimensional. The flow approaching the ramp from the boundary layer development plate is two-dimensional in nature, except very near the sidewalls where the presence of the boundary layer retards the flow. Once the flow starts to pass over the ramp, the presence of the adverse pressure gradient and/or wall curvature begins to morph the flow into a seemingly complex three-dimensional structure that exhibits a considerable degree of side-to-side symmetry with respect to the spanwise center plane.

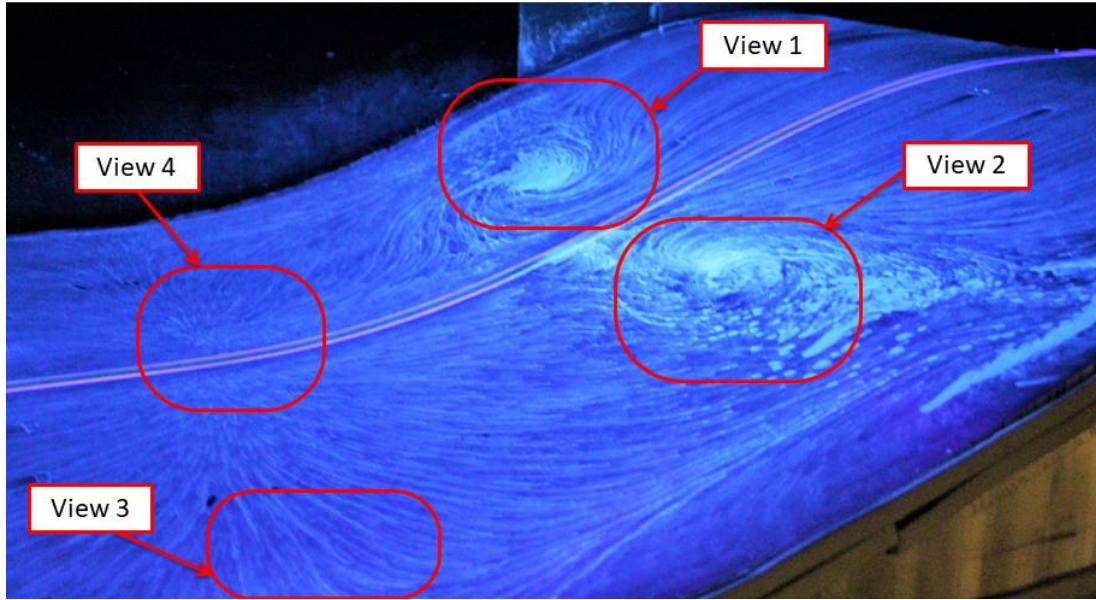


Figure 4.1 Global surface flow visualization for Case A, with four interrogations regions highlighted. Incoming flow is from right to left.

Due to the large spatial extent of the ramp geometry and the detailed surface flow features, four interrogation regions will be presented in more detail and described separately before a global analysis of the entire ramp surface will be presented. View 1 of Figure 4.1 is highlighted in Figure 4.2. This figure presents the surface detail of the separation structure and surrounding smaller-scale flow topography on the far side (inner loop side) of the wind tunnel. Note that there are two prominent saddle points. Along the centerline, the flow is drawn toward saddle point 1 (S1), whereas the flow nearer the sidewall is drawn toward saddle point 3 (S3). Both saddle points then divert the flow into the central focus 2 (F2), where the flow must lift off of the surface due to the Helmholtz vorticity theorem (i.e. a vortex tube cannot end within a fluid). The line dividing the upstream region from the downstream region, shown as the yellow dashed line, is known as the global line of separation. The line of separation forms the base of the stream surface,

which is called a dividing surface [70], where the flow detaches from the ramp. This dividing surface extends into the flow and advects downstream.

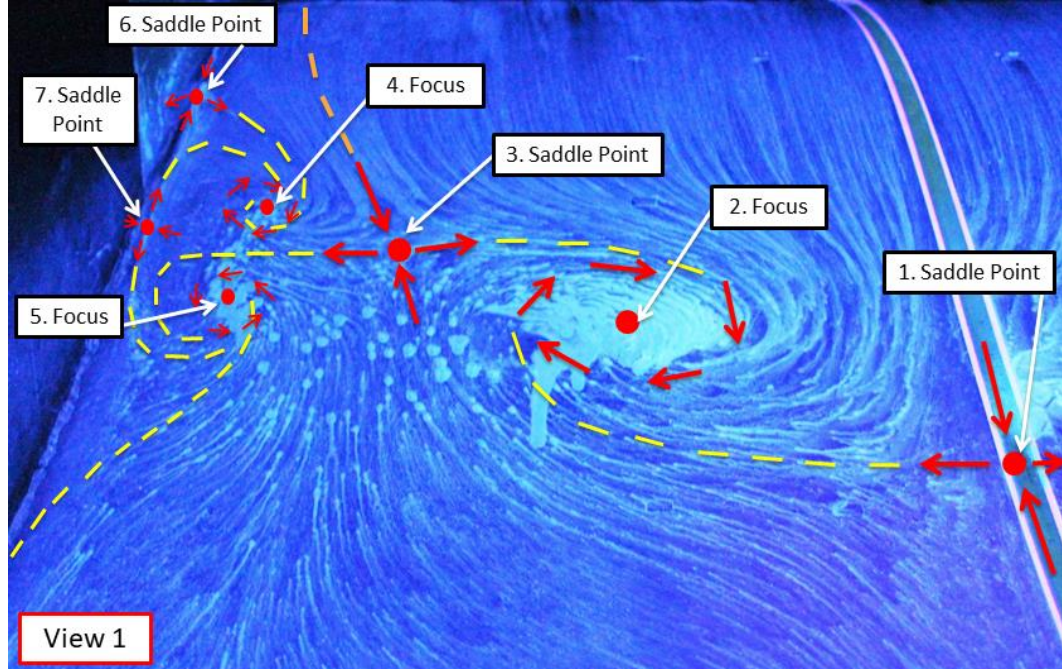


Figure 4.2 View 1, from Figure 4.1, with the yellow dashed line indicating separation and the orange dashed line showing how the near sidewall flow is topologically isolated from the central flow separation. Incoming flow is from top to bottom.

Nearer the tunnel sidewall, there are a number of smaller scale structures (also connected to the dividing surface just mentioned); two appear to be the counter-rotating foci, F4 and F5, which are bounded by two saddle points, S6 and S7, which are very near the sidewall. The farthest upstream saddle point, S6, appears to be the source of the sidewall separation. Its extent is limited by S3 as the skin-friction lines that were moving away from the sidewall are diverted back and around F4.

As was the case in View 1, shown in Figure 4.2, View 2, shown in Figure 4.3, presents the separation topography occurring on the near side (wind tunnel outer loop).

Despite some small near-wall differences, globally, the centerline symmetry is very good. What is apparent from images taken on both sides of the tunnel centerline is that the sidewall separation, emanating from S6 and S16, is topologically isolated from F2 and F12 by S3 and S13; hence, *from a skin-friction line point of view, the sidewall flow does not directly influence the central separation structures.* This indicates that sidewall separation is *not* the main cause of the formation of vortical structures on the ramp. Instead, any direct influence the sidewall boundary layers have on the central vortical structures is limited to the area farther upstream, prior to the location where boundary layer separation occurs. While sidewall separation does not directly cause the central vortical structures, it does indirectly affect them. This modulating effect of the sidewall flow on the central flow will be discussed in Chapter 6.

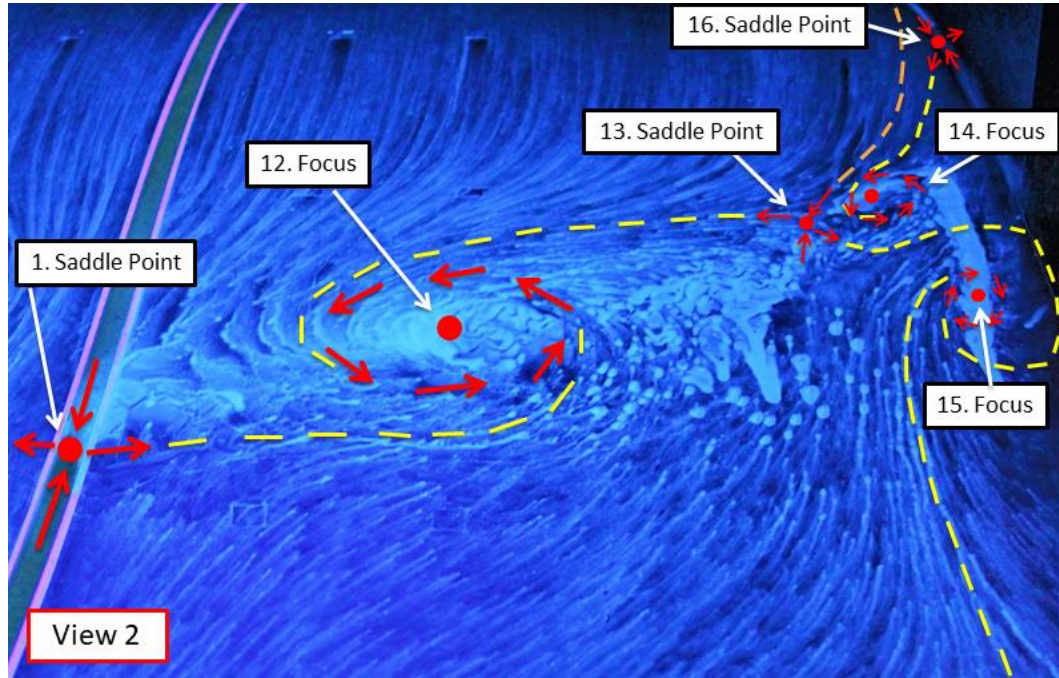


Figure 4.3 View 2, Figure 4.1, with the yellow dashed line indicating separation and the orange dashed line showing how the near sidewall flow is topologically isolated from the central flow separation. Incoming flow is from top to bottom.

The reattachment region, which is highlighted in Views 3 and 4, is shown in Figure 4.4. While the separation region is three-dimensional, the reattachment is, in contrast, quite two-dimensional. This is highlighted by the red dashed line. Central reattachment initiates at node N22, which acts as a source, feeding in all directions with an almost pure crossflow component along the reattachment line. Just up or downstream of this line there is still a major crossflow component that appears to vary slightly with spanwise location, indicating some limited degree of three-dimensionality. As the flow approaches the near wall, it is redirected by saddle point S21, after which point the crossflow component changes direction. Another near-sidewall nodal source, N20, feeds into S21 as well as into the upstream focus F15. Note that due to the nearly perfect symmetry, the far wall topography is not presented here.

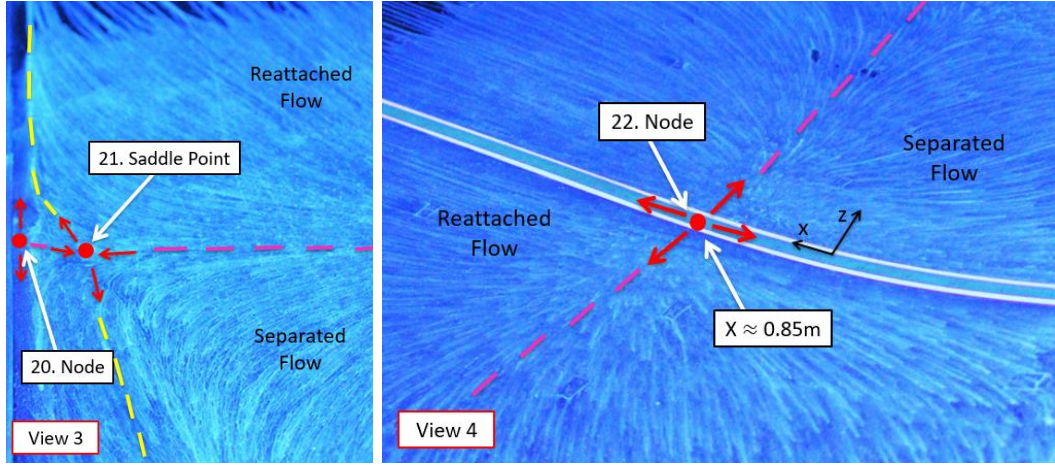


Figure 4.4 Close up views of the reattachment in the central ramp region (View 4) and near the wind tunnel outer loop sidewall (View 3). Incoming flow in both images is from right to left.

All the surface flow images shown in Figure 4.1, Views 1-4, were taken as part of a single wind tunnel run. Later, flow visualization was conducted on each sidewall to individually capture the associated topological features there. Close-up photographs were taken in-situ, as well as with the window insert removed. Figure 4.5 shows the surface flow visualization on the wind tunnel outer loop sidewall and highlights both the sidewall juncture flow separation and sidewall reattachment. Figure 4.5.b, shows the initiation of separation from both the ramp surface and sidewall juncture. Both lines of separation initiate from saddle point S16 (see Figure 4.3) and terminate into foci F14 and F18. It is likely that in the flow above the surface, F14 and F18 are connected by the same stream surface spiraling into their cores. In essence, one vortex curves and impinges on the surface leaving “footprints”, F14 and F18, on the ramp and sidewall. Saddle point S17, which was not visible in Figure 4.3, is located on the sidewall. It is connected to F14, which was determined in additional flow visualization experiments that are not shown here.

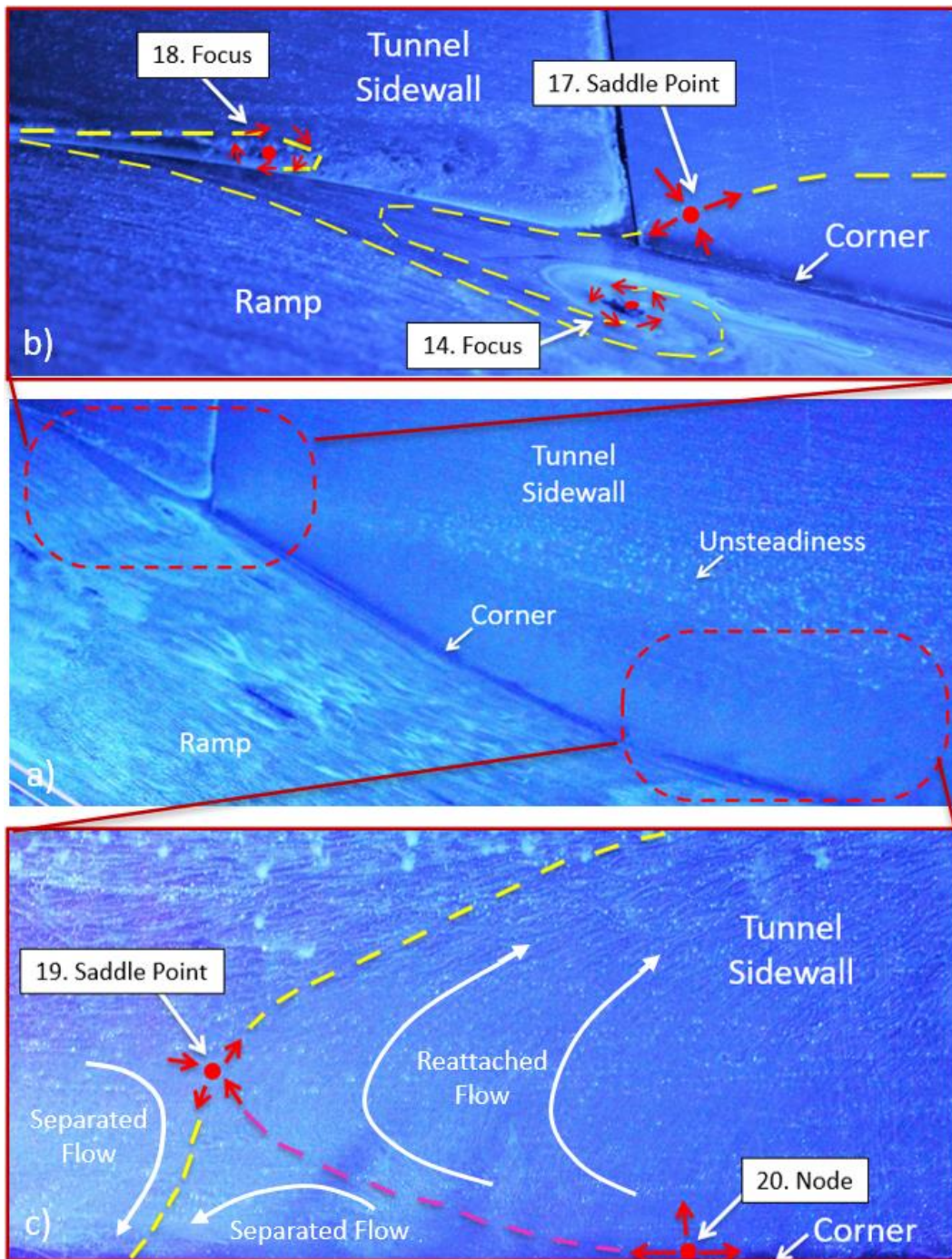


Figure 4.5 (a) Surface flow visualization on the ramp surface and wind tunnel outer loop sidewall, (b) with close up views highlighting the sidewall juncture flow separation and (c) sidewall reattachment. Incoming flow is from left to right in all images.

Figure 4.5.c highlights the reattachment region. The reattachment line on the surface of the ramp passes through N20, as also seen in Figure 4.4, and then leads up the sidewall surface into saddle point S19. Looking closely, one can see many reattached source lines leaving node N20 and heading upstream before being diverted back downstream by saddle point S19. This saddle point is the last singular point in the reattachment line and divides the separated flow, which heads upstream into F15 (see Figure 4.3) from the reattached flow, which heads downstream.

For this experiment to be well-suited for a benchmark CFD validation study, the repeatability of the previously described surface flow is a primary concern. To ensure a high degree of repeatability, numerous individual flow visualization runs were conducted each time the experimental setup was reinstalled or altered. Furthermore, many flow visualization techniques were implemented, utilizing varied solution fluid viscosities. This was done to minimize the effect of pressure/gravitational forces and to capture the best representation of the actual surface flow pattern which is important for revealing the underlying topological features of the surface flow.

One such variation in method was to use two solutions that would illuminate in different colors under UV lighting. The base solution, which illuminated light in a blue color, was the same aviation oil solution described in Chapter 2, while a different solution consisting of kerosene, silicone oil and UV leak detection dye, illuminated light in a bright green color. The primary advantage of using two different colored solutions was that the distinction of the various flow regions could be emphasized in more detail. For example, the reattachment of the flow is highly two-dimensional and repeatable. To highlight this, Figure 4.6 shows a test run where the blue solution was placed in the separated flow region

and the green solution was placed just downstream from the reattachment region. After approximately an hour of run time, the wind tunnel was stopped and the results were photographed. Remarkably, there is almost no mixing of the two solutions, thereby indicating the temporal stability of the flow reattachment pattern. Where the blue dye is placed, almost all the flow is reversed, characteristic of the separation region. In contrast, where the green dye is placed, all the flow is directed downstream, characteristic of attached flow. The only region where mixing occurs is on the far side where the reattachment line is biased slightly upstream from where the blue dye was placed and hence the flow diverted by S21 can be clearly seen heading downstream.

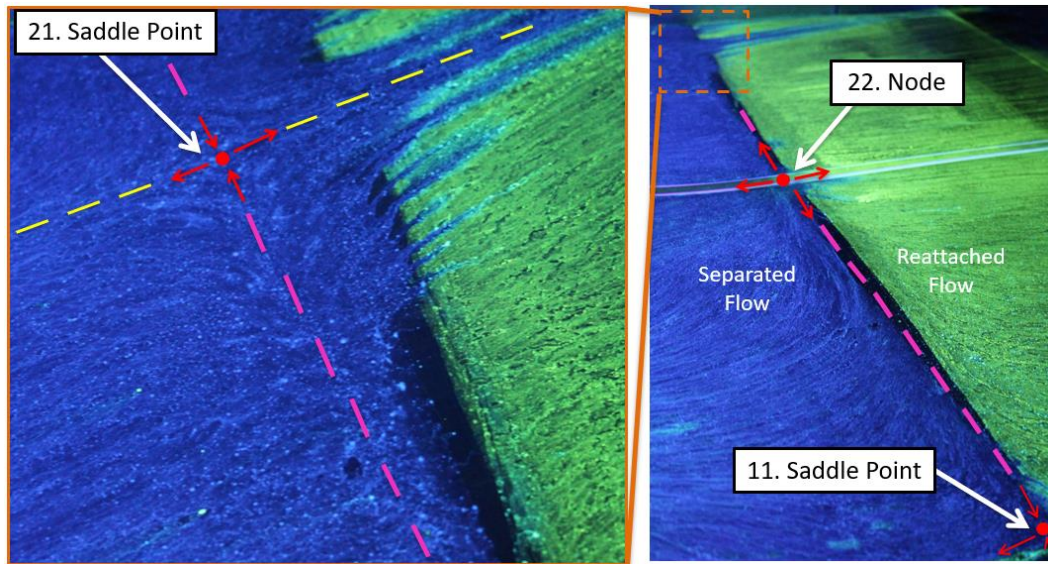


Figure 4.6 Two-dimensionality of the reattachment region, captured using two different UV illuminating surface flow solutions. Note that incoming flow is from left to right in both images.

The oil-film flow visualization is a very sensitive diagnostic tool. The dramatic mixing of the blue dye near S21 shows just how much surface movement in the fluid occurs. Furthermore, this mixing is only apparent since the blue dye was initially applied just over the reattachment line, highlighting just how remarkably spanwise uniform the reattached flow is. One possible physical explanation for this strong two-dimensionality is that the embedded free shear layer (discussed in detail in Chapter 8) exhibits such rapid spatial growth that any effect of spanwise variation in upstream separation location becomes largely irrelevant by the reattachment location.

The previously described surface flow separation pattern was very repeatable run-to-run. However, unlike reattachment, the separation process seems to be quite sensitive to upstream flow conditions. Due to this sensitivity, great care was necessary in the test section installation process to ensure that the flow conditions did not change. Additional work discussing the sensitivity of the surface flow patterns will be presented in the following chapter.

#### 4.1.2 Case B – Smaller-Scale Separation

The global surface flow visualization for the small-scale separation case is shown in Figure 4.7. This image also includes flow visualization of the far sidewall. Many of the topological features of this case are quite similar to those occurring in the large-scale separation case and therefore will not be discussed in detail. Instead, the focus of this section will highlight the important similarities and differences between these two cases. The primary vortical flow patterns in the central region are still prominent, remain spanwise symmetric, and exhibit a significant degree of three-dimensionality.

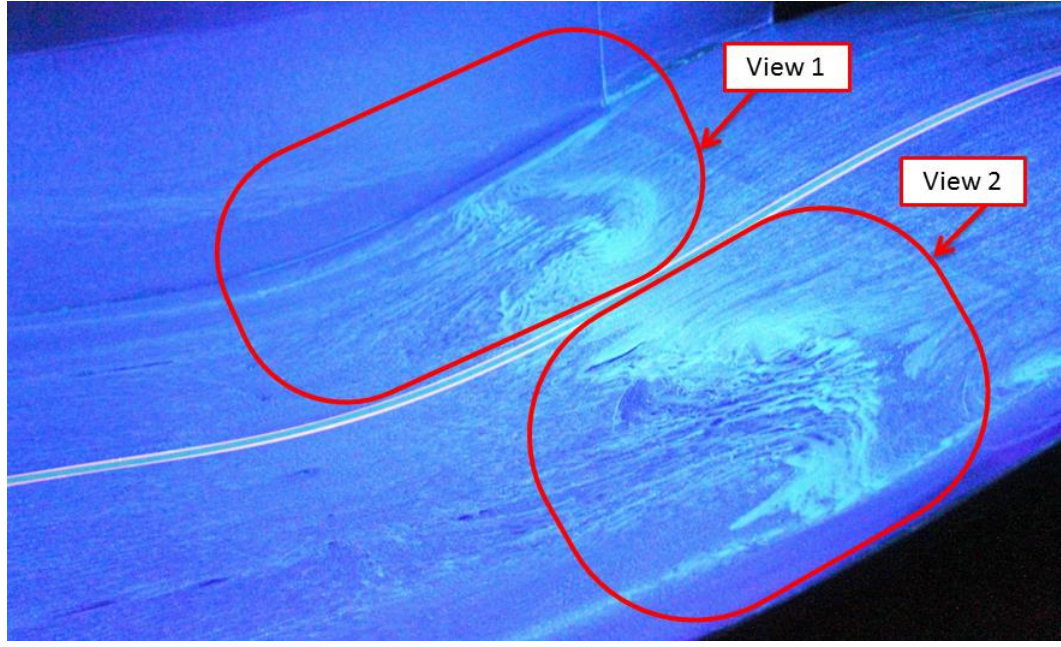


Figure 4.7 Global surface flow visualization for the small-scale separation, Case B, highlighting two viewing regions to be analyzed in greater detail. The incoming flow is from right to left.

Figure 4.8 shows a detailed view of the topological features within View 1 of Figure 4.7. The topography and topology of the global line of separation are approximately the same here as they were in Case A. The most notable difference is in the topology of the reattachment line where an extra pair of singular points, saddle point S23 and node N24, are present. Both of these features terminate in focus F5 and do not appear to affect the two-dimensionality of the reattachment line. Centerline symmetry is also maintained with the addition of an extra pair of singular points, saddle point S25 and node N26, on the near side reattachment line, as shown in Figure 4.9, View 2. This near side view also highlights the improved centerline symmetry in the global line of separation, as compared to Case A. Here saddle point S13 is located farther from the sidewall, balancing the centerline symmetry with saddle point S3 (Figure 4.8). In light of this, Views 1 and 2 show the distinct central flow leading into saddle points S3 and S13 (the orange dashed lines) demonstrating

that the central three-dimensional flow separation pattern is isolated from the sidewall separation.

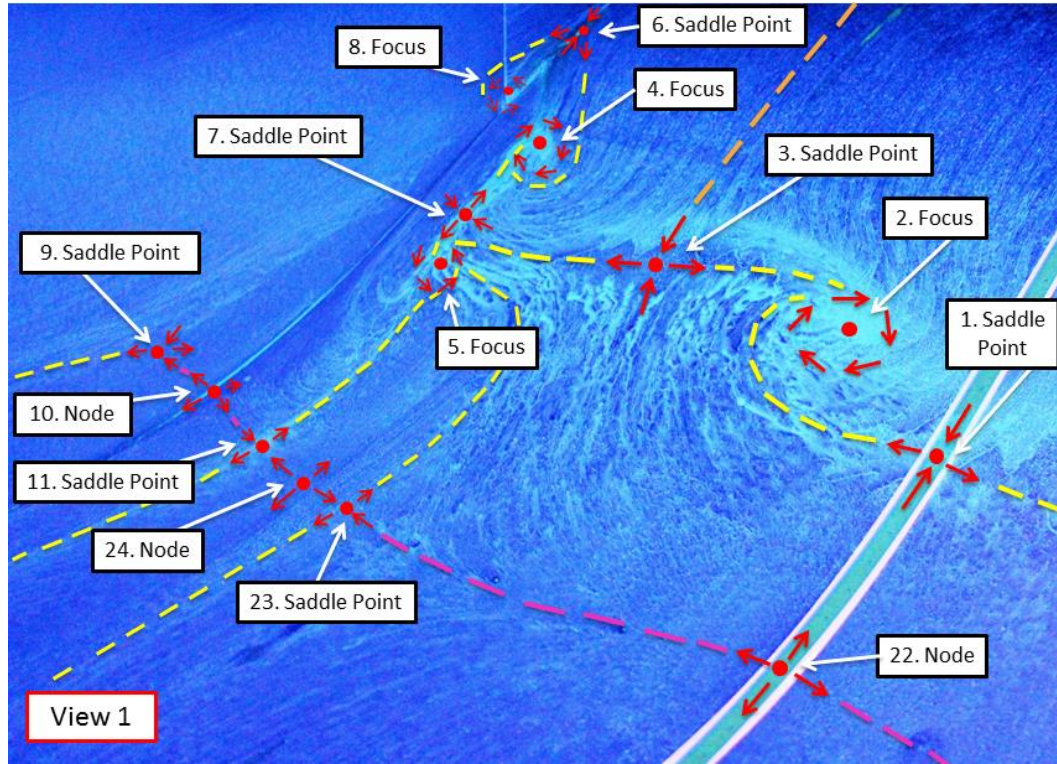


Figure 4.8 View 1, from Figure 4.7, highlighting the topological features on the far side (wind tunnel inner loop) with yellow dashed lines indicating separation, orange dashed lines showing the isolation of the near sidewall flow from the central flow separation, and red dashed lines indicating reattachment. The incoming flow is from right to left.

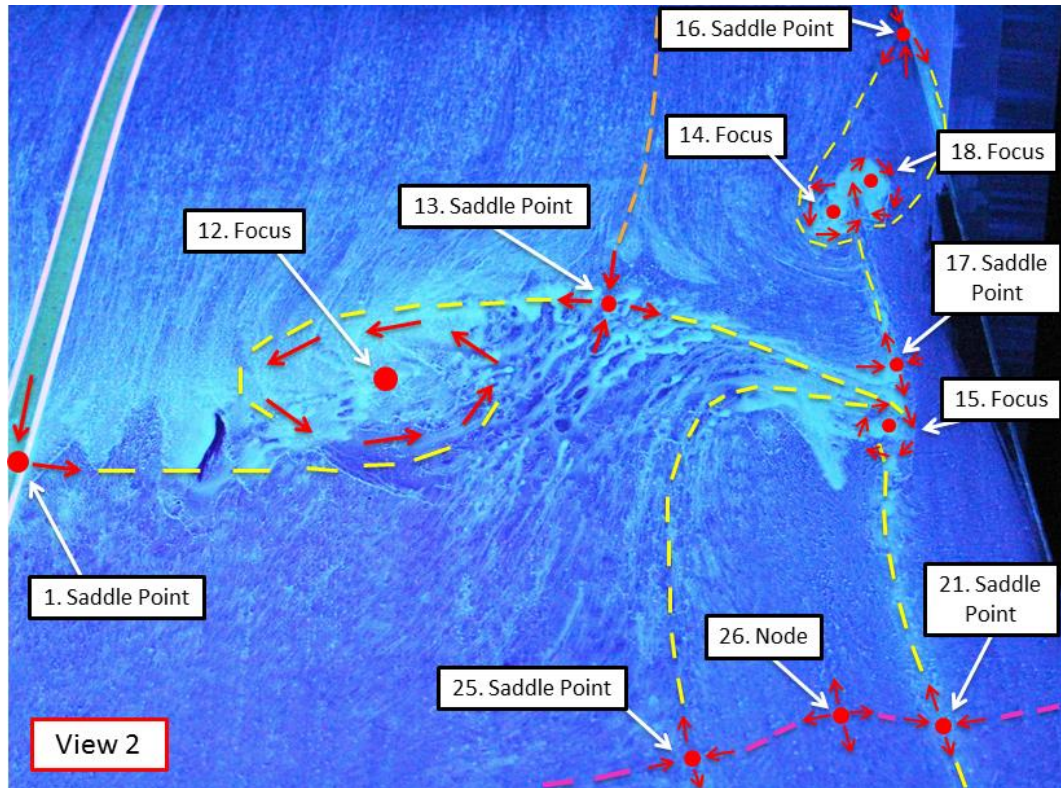


Figure 4.9 View 2, from Figure 4.7, highlighting the topological features on the near side (wind tunnel outer loop) with yellow dashed lines indicating separation, orange dashed lines showing how the near sidewall flow is topologically isolated from the central flow separation, and magenta dashed lines indicating reattachment. The incoming flow is from right to left.

#### 4.1.3 Case C – Attached Flow

The global surface flow pattern for the attached flow case, Case C, is shown in Figure 4.10. This is the simplest of the three cases because the only surface flow features remaining are due to the sidewall flow separation. In the central region of the ramp, the flow remains attached, in the mean sense, with a strong degree of side-to-side symmetry present. However, while the flow remains attached here, there is still evidence of a component of crossflow, directed from the central region of the ramp surface toward the tunnel sidewalls. Near both sidewalls, pockets of separation appear in the form of two saddle-foci pairs, one on each side.

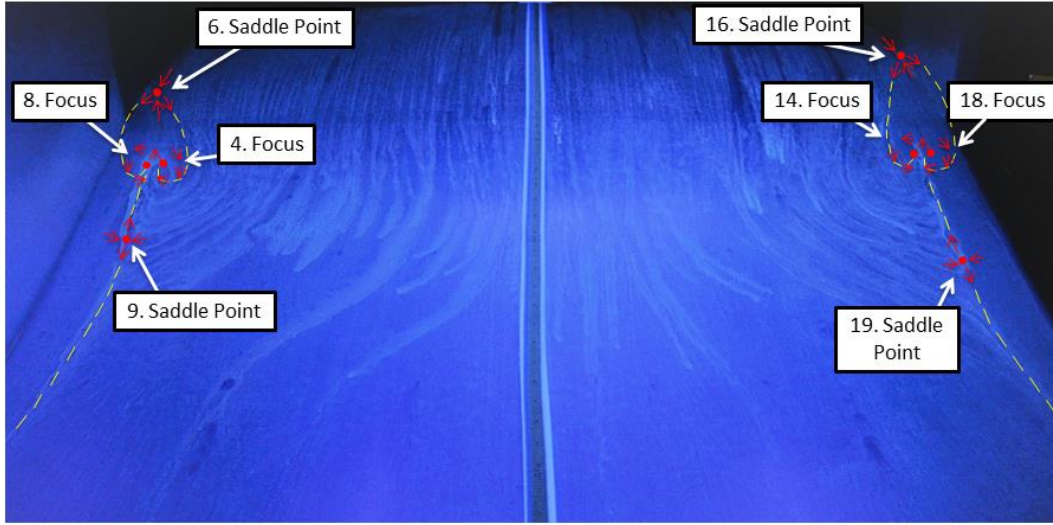


Figure 4.10 Global surface flow visualization for the attached flow, Case C, highlighting the symmetric pockets of sidewall separation that remain. The incoming flow is from top to bottom.

#### 4.2 Commonality of the Surface Flow Patterns

Through the presentation of the surface flow topography above, it is readily apparent that while reattachment is two-dimensional, the flow does not undergo a two-dimensional separation process. Instead, separation occurs via a symmetric pair of three-dimensional vortical structures. It would be easy to suspect that the three-dimensional surface flow observed in this study was just the result of an abnormality in the experimental testing conditions; however, this is unlikely. We must ask: *how common is this type of three-dimensional flow separation?* Furthermore, if this flow pattern is a common occurrence, *is there a way to make it more two-dimensional?* The remainder of the chapter will address these questions.

Many studies utilizing flow over smooth-body backward facing ramp geometries have reported some form of three-dimensional flow phenomena. One of the most widespread smooth-body backward facing ramp geometries is the Stratford ramp.

Originally proposed by Stratford in a series of papers [49,71] in the 1950s, the Stratford ramp is a geometry intended to produce incipient separation along its entire length, thereby yielding zero skin friction, while achieving a given pressure rise in the shortest distance possible. Given these potential benefits, much interest has been devoted to its study. At the time of Stratford's initial experiments, secondary flow effects were a concern. While no surface flow visualization results were reported in the experiments, numerous modifications to the incoming boundary layer and sidewall conditions were made, though final accepted conditions still only provided an estimated spanwise uniformity of 40% of the central region.

As a point of clarification, there are two uses of the term “Stratford ramp” widely adopted in literature. The first use of the term is: a classification of geometry that yields a particular result, i.e. the geometry a flexible floor or ceiling exhibits when the flow is held at the verge of separation along its entire length. In this case, the ramp geometry is dependent on the flow and therefore a byproduct of it.<sup>2</sup> The second use of the term is: a geometry that is similar in form to the one used in Stratford’s original experiment. Due to differing wind tunnel geometries and experimental conditions, in this instance, the flow is not necessarily on the verge of separation but may undergo a separated region. In the second definition, the ramp geometry is set, and the flow is a byproduct of it. In either case, most Stratford ramps take on very similar forms that fall under the classification of smooth-body backward facing ramp, although some have attached flows and some have separated flows.

---

<sup>2</sup> The Stratford ramp concept extends the experimental geometry to that of a flat plate, with an opposing wall employed to create the necessary pressure gradient. This will not be addressed, as its geometry is not a smooth backward facing ramp and therefore does not possess surface curvature.

Starting in the late 1990s two groups from the University of Arizona conducted experimental [50] and computational [54,55] studies using Stratford ramp geometries on the verge of separation, which the authors claim as the first comprehensive studies of their kind. In their experimental work, Elsberry et al. [50] indicate the problem of sidewall interference prematurely separating the boundary layer. While not shown with surface flow visualization, a satisfactory two-dimensional flow was only achieved with the application of the sidewall suction devices, installed at the start of each side of ramp to remove the boundary layer. Following these experiments, direct numerical simulations (DNS), conducted by Zhang and Fasel [54], made “a first ever attempt to numerically capture the physics of the Stratford ramp flow”. Instantaneous contours, show that spanwise vortical structures (“rollers”) are formed which advect and grow downstream, corresponding to the emergence of a shear layer. More importantly, by analyzing the spanwise cross-sectional time-averaged contours of spanwise vorticity and velocity on the concave portion of the ramp they noted the existence of a pair of streamwise counter-rotating (longitudinal) vortices whose strength and size grows in the downstream direction which they likened to Görtler vortices. While there was some experimental evidence of these structures based upon spanwise correlations, they remark that no flow visualization was conducted in cross-sectional planes, making a direct comparison not possible.

Shortly thereafter, in 2001, Fasel et al. [55] conducted additional studies, consisting of DNS, LES, and two-and-three-dimensional RANS codes, that were deemed necessary, as all of the prior studies had “unexplained differences” between the simulations and experiments, leaving the authors to conclude that the simulations were missing an additional piece of physics, present in the experiments. For example, using the same ramp

geometry and APG as that of the experiments [50], led to massive flow separation in the simulations. This required the researchers to alter the ramp profile in the simulations in order to maintain attached flow. The authors also postulated that longitudinal vortices may have been present in the experiments and functioned to keep the flow attached. While the work was not finished at the time of their report, the published results that were shown “provide strong evidence that dominant coherent structures, both two-dimensional and three-dimensional, are present [on] a Stratford ramp flow” [55].

Not long after these studies were conducted at the University of Arizona, Stratford ramp geometries were utilized (without attribution) by Jenkins et al. [48], Kumar [51,72], and Kumar and Alvi [73,74] for experiments utilizing flow control to reduce the extent of the separation region and examine control authority. In all of these cases, their work differed slightly from that of Stratford and the Arizona Groups in that they did not regulate the pressure gradient over the ramp to ensure incipient separation, but instead used the ramp’s shape to produce a separating and reattaching flow—the second use of the term Stratford ramp—similar to the work conducted here.

When conducting their baseline flow visualization, Jenkins et al. [48] observed the formation of two large vortical structures that they attribute to the interaction of the sidewall boundary layer with the adverse pressure gradient, see Figure 4.11.c. They state that:

The vortical structures are similar to what might be expected from secondary flow and vortex liftoff in a duct, so no attempt was made to control the vortices for this investigation. Rather, it was thought that the challenges of the strong vortical flow field would provide a better indication of how the flow control devices would work in a realistic inlet configuration. It should be noted that the vortices are highly unsteady and appear to have a trajectory that departs from the surface of the ramp and extends downstream in the tunnel. [48]

Additionally, they point out that the spanwise pressure distribution along the central region of the ramp is quite uniform and that by solely examining this piece of information one could easily misinterpret the flow to be two-dimensional.

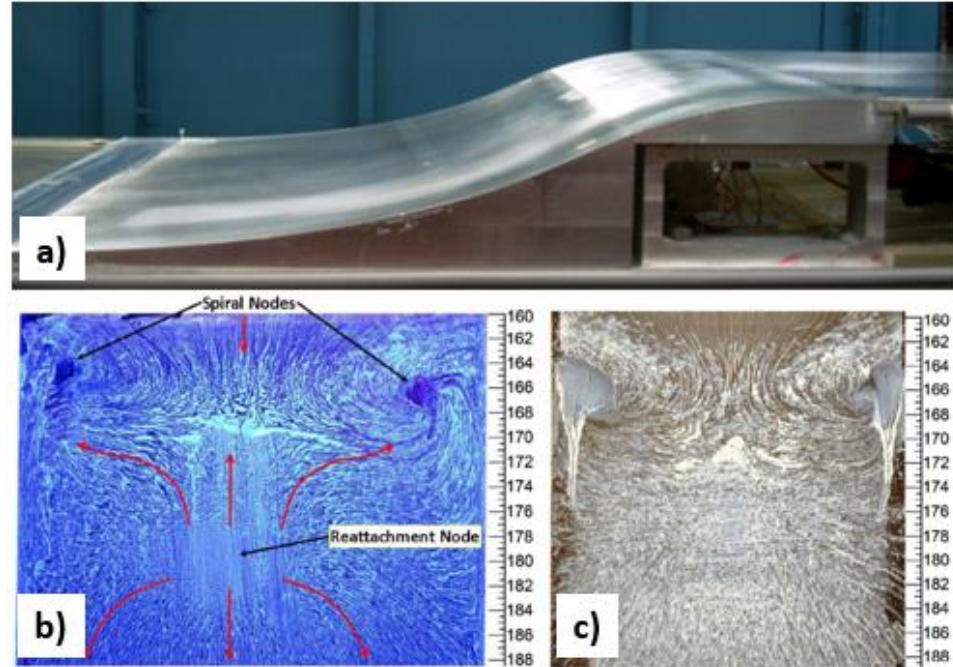


Figure 4.11 Comparison of the baseline surface flow visualization of Jenkins et al. [48] (c), and Koklu and Owens [52] (b), utilizing the same Stratford ramp geometry, (a), in both studies

Kumar's work [51,72], which focused on controlling separation using microjets, examined flow over a ceiling mounted Stratford ramp. The initial work was conducted on a ramp without sidewalls [72,73]. Water based paints were used to visualize the surface flow both with and without flow control. Kumar states that the flow pattern is similar to that of the *owl face of the first kind*<sup>3</sup> and “shows a trapped separation bubble, generated due

---

<sup>3</sup> The name *owl structure* was coined by Fairlie [75] and later became owl face.

to the ramp surface curvature” [73]. Secondary flow is also observed near the edge of the ramp, but its effect on the flow and its nature is still unknown, and Kumar states that the lack of sidewalls may be responsible. He also cites Jenkins et al. [48] as observing a similar flow pattern with bounded sidewalls. The observed three-dimensionality also extended into the flow, as planar PIV taken at 0.1 span off-center showed a larger bubble size compared to PIV taken on the centerline. Further studies [51,74] were conducted with the addition of sidewalls, to simulate the flow in inlet ducts, and with an adjustable pivot angle of the ramp, effectively changing the streamwise APG. Kumar’s illustrations and description of the surface flow visualization indicate that there was very little change in the flow pattern from these adjustments.

More recently, Koklu [33,76] and Koklu and Owens [52] continued the work of Jenkins et al. [48] at NASA Langley. Using a newly improved surface oil flow visualization technique that was developed during that project, they also observe the formation of what they call two large corner vortices—the same ones observed by Jenkins and labelled as spiral nodes in Figure 4.11.b—and cite their occurrences in similar problems such as juncture and endwall flows. Furthermore, they considered the separation of the “corner vortices” as unrelated to the main flow and made no attempt to control them, fearing that they might hinder the actuator performance. They summarize by saying that “[a]lthough the control of the corner vortex was also important and attracted much interest due to its potential to improve the performance of a system, the control of these corner vortices was deemed beyond the scope of this study” [52].

The type of three-dimensional flow separation observed in this study on the ND ramp is not limited only to Stratford ramp geometries. Other non-Stratford ramp geometries

feature similar separation characteristics. These include the smooth backward facing ramp geometry studied by Gardarin et al. [53], a two-dimensional bump with leeward separation studied by IMP Gdansk, as described in Délery [77], and serpentine inlet ducts, or S-ducts, studied by Anderson et al. [78].

All the work discussed thus far indicates that the three-dimensional flow separation observed on the ND ramp is not unique to the experiment or test conditions. Rather, it is a commonly observed result, likely due to the geometry and flow conditions. It is also important to note that not all studies conducted on two-dimensional geometries of this type have reported three-dimensional flow effects. Debien et al. [46] conducted experiments on a set of two slightly different ramp geometries: one with a sharp leading edge and one with a rounded leading edge. In both configurations, no three-dimensional flow effects were mentioned, and the flow was reported using two-dimensional terminology. Other similar studies include that of Schatzman and Thomas [56] who investigated unsteady separation on a rounded backward facing ramp, and Lin [79] who conducted extensive passive and active flow control experiments on a rounded backward facing step. These studies also reported no three-dimensional flow effects. As will be discussed in the next section, in the cases of both Debien et al. [46] and Lin [79], the aspect ratios are likely a significant factor in the flows being reported as two-dimensional.

#### 4.3 Aspect Ratio Effects on Smooth-Body Flow Separation

It is common to try to produce a two-dimensional flow separation for experimental study because it dramatically simplifies the fluid flow problem. It was initially sought after in this study and will likely be the intended focus of many future studies; however, for smooth-body backward facing ramp geometries this “two-dimensionality” is, as

demonstrated above, the exception and not the rule. To examine this further, the aspect ratio of the studies presented in the last section, as well as preliminary CFD simulations of the ND ramp, will be compared to see how the flow features scale with the geometry.

Many of the geometries discussed in the last section are very similar to one another. In order to gauge just how similar these geometries are, they are scaled and plotted in Figure 4.12. Here symbols are used to indicate that the geometry was not explicitly given, via either analytical or tabular means, and had to be digitized from images at discrete points. The coordinates are scaled, with their aspect ratio maintained, to match the leading edge and height of the ramp geometry studied here, referred to as the ND Ramp. The figure shows that most of the geometries are remarkably similar in profile. All, except that of Lin, possess a convex region upstream and a concave region downstream.

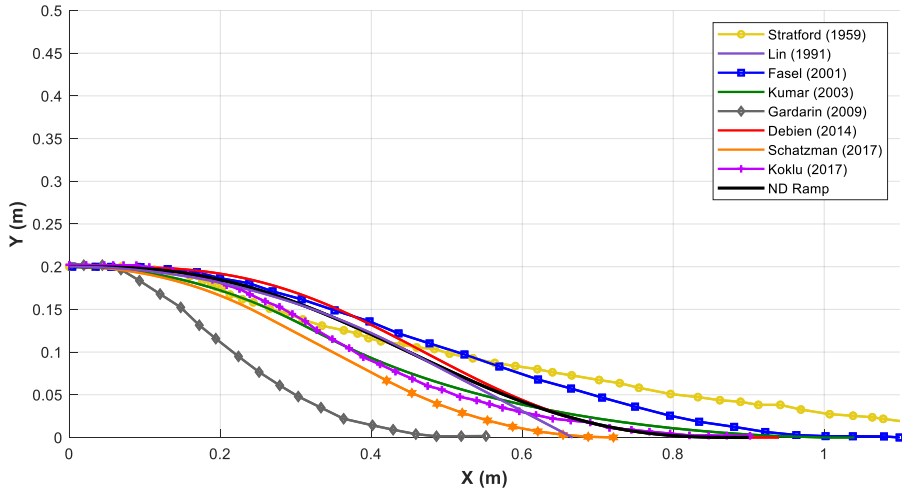


Figure 4.12 Comparison of the Notre Dame (ND) ramp profile to that of similar studied ramp geometries. All geometries were scaled to match the height of the ND ramp, with their respective aspect ratios maintained. Note that symbols are used when the geometry was not adequately defined and had to be digitized from images.

Other than the common two-dimensional profile of the geometries, the main defining physical feature exhibited by the studies examined here is the aspect ratio, or the ratio of the length-to-width-to-height (L/W/H). The approximate ramp aspect ratios of these studies are shown in Table 4.1 Most of the geometries in question have similar aspect ratios of,  $L/H \sim 3 - 5$ . The ratio of length-to-height (L/H) has significant impact on the streamwise pressure gradient, influencing the occurrence and extent of separation.

TABLE 4.1  
ASPECT RATIO COMPARISON

Ramp Geometry	Aspect Ratio: L/W/H	Notes
ND Ramp	4.5 / 4.6 / 1	Actual
Koklu [76]	5.3 / 5.0 / 1	Actual
Kumar [72]	4.8 / 4.3 / 1	Actual
Elsberry [50]	2.7 / 2.0 / 1	Estimated
Schatzman [56]	3.0 / 3.6 / 1	Estimated
Gardarin [53]	2.6 / 1.4 / 1	Estimated
Stratford [49]	6.4 / 1.3 / 1	Estimated
Lin [79]	3.3 / 18.7 / 1	Actual
Debien [46]	4.7 / 20.0 / 1	Actual

The ratio of length-to-width ( $L/W$ ) is believed to affect the spanwise uniformity of the flow. If  $L/W \ll 1$ , the flow is expected to be uniform, with the secondary flow effects limited to the sidewall regions. However, when  $L/W \sim 1$  it is uncertain whether the flow will exhibit a significant region of spanwise uniformity or strong three-dimensional flow. Of the geometries examined, most fall in the range of  $L/W \sim 1$ . The studies that differ, on opposite accounts, are (1) that of Stratford [49], who willfully admits the high aspect ratio as an “embarrassing feature of the design”, and (2) that of Debien et al. [46] and Lin [79], whose low aspect ratios are due to a uniquely wide, 2 m, test section and a small ramp length, respectively. Since the ND ramp shares a common aspect ratio with these experiments as well as similar flow separation patterns, this begs the question—*Do these flow separation patterns scale with the ramp aspect ratio?*

To examine this question further, 3D-RANS simulations were conducted at the University of Notre Dame [80]. The simulations utilized the SA-RC turbulence model and were conducted on three different scaled versions of the ND ramp, all having the same adverse pressure gradient. The scaling was such that the  $L/H$  ratio was fixed at 4.5 and

three ramps of different heights,  $H$ ,  $H/2$ , and  $H/4$ , were simulated. In effect, this increases the spanwise width of the ramp. The simulation results, shown in Figure 4.13, should only be interpreted qualitatively. The main vortical structures seen here in the full-scale simulation are similar to those observed in the ND experiments, so changes in the general surface flow pattern simulated should be indicative of the experiment. The results demonstrate that the secondary flow structures scale with the height or, equivalently, the length, of the ramp. This provides supporting evidence that to achieve a spanwise uniform flow, the width of the ramp must be significantly longer than its length,  $L/W \ll 1$ , with increased spanwise uniformity resulting as  $L/W$  decreases.

For practical reasons, it is difficult to have an aspect ratio of  $L/W \ll 1$  while maintaining a sufficiently large ramp length so as to provide sufficient spatial resolution. Since the width of a wind tunnel is fixed, only the length of the ramp can vary, and most wind tunnels don't have the width necessary to accommodate sufficiently large ramp lengths. While the length of the ramp could be reduced, this would severely limit the spatial resolution of any data taken, hence the commonality of high aspect ratios in these experiments. Additionally, reducing the ramp length in order to increase the width has the effect of reducing the ramp height, since  $L/H$  should be constant. The ratio of the ramp height,  $H$ , to local boundary layer thickness,  $\delta$ , defines the category of flow separation [16], so simply reducing  $H$  would change the significance of the boundary layer in the separation process.

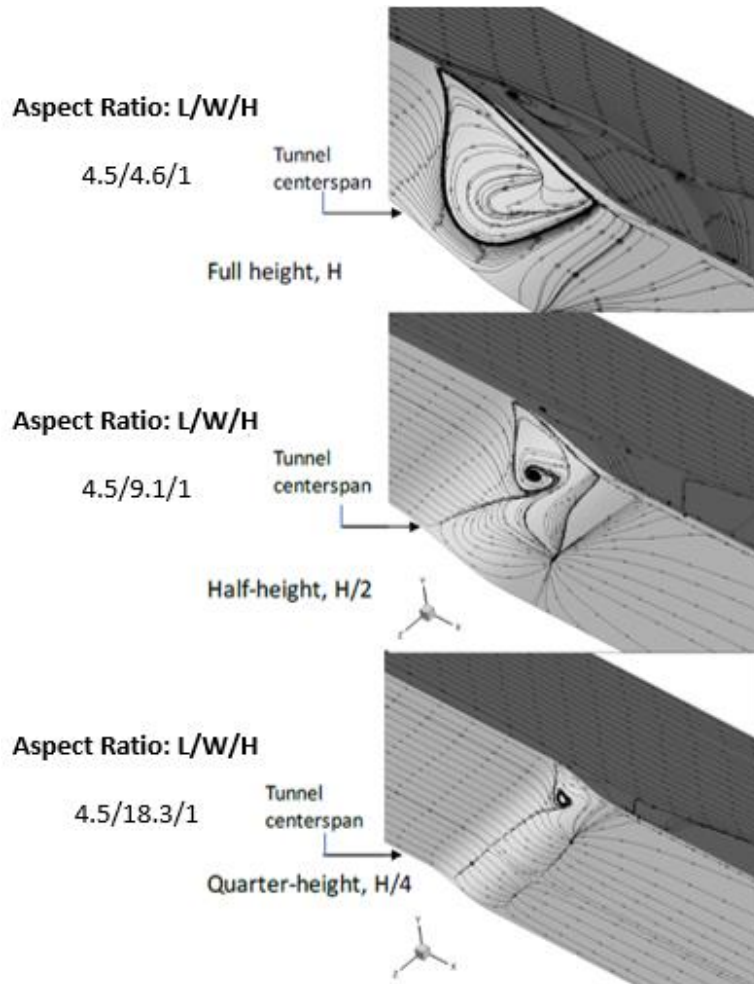


Figure 4.13 Effect of aspect ratio, L/W/H, on the spanwise extent of secondary flow structures. The simulation was conducted at the University of Notre Dame by Wang and Zhou [80] and utilized 3D-RANS simulations with the SA-RC turbulence model.

The evidence presented indicates that the uniformity of the flow scales with the aspect ratio of the geometry; however, *it does not suggest that the flow becomes two-dimensional*. In fact, it appears that *the primary separation structure does not depend on the ramp aspect ratio*, but instead remains unchanged. While future studies could adjust the ramp aspect ratio to produce more uniform flow, unless an axisymmetric geometry is used under careful application of a uniform flow with low blockage ratio, true two-

dimensional separation is unlikely to occur. Despite the three-dimensional separation, the current geometry (with the given aspect ratio) is still a very useful one to study as a benchmark CFD experiment. It is not only common to both wind tunnel tests and practical applications, but also likely captures physics ignored by only examining the central, uniform region of a lower aspect ratio,  $L/W$ , flow. Furthermore, the aforementioned studies highlight that our understanding of the vortical separation structures is limited. Therefore, the following chapter will examine the ND ramp flow separation via topological analysis to both provide a better understanding of the flow field and characterize the structure of the separation patterns.

## CHAPTER 5: FLOW TOPOLOGY

Having documented the surface flow topography, attention can now be given to the corresponding flow topology—the underlying structure of the flow separation. First, the topological flow features, in the form of singular points, that were identified in the flow visualization images in the last chapter are used herein to construct surface flow topological maps of the entire separation and reattachment region. Attention is then given to the larger-scale separation case, Case A, to construct a mathematically plausible off-surface flow field, which is fully consistent with the available flow field data. The central features of the separation topology are shown to contain so-called owl-face surface flow patterns which are ubiquitous in fluid dynamics. Furthermore, it is proposed that the owl-face patterns are frequently part of larger topological structures, which are dubbed the “generalized owl-face patterns”. Finally, the chapter concludes with a discussion of this generalized three-dimensional separation topology and its comparison to two-dimensional flows.

### 5.1 Overview of Separation Topology

As briefly introduced in the last chapter, topology primarily differs from topography in that, while the topography is concerned with the flow features, including size, strength and location(s) respective to one another, topology is only concerned with

the connections between features. Topology follows a set of rules that constrain the reconstruction of the surface flow patterns and clarify the possible structures (connections of singular points) a flow can take. Once these structures are understood topologically, proper design may be used to enhance or attenuate select features, in the topographical sense, by knowing which features, if any, are sensitive to small geometric perturbations. Here we briefly lay the groundwork of the surface flow topology.

In three-dimensional flows, there are two vector components of local wall shear stress. They are only both uniquely zero at the singular points, not uniform spanwise lines on the surface as would be expected for two-dimensional flow. Three-dimensional, steady flow separation is usually viewed from the lens of dynamical systems theory. The basic framework is the analysis of the pattern of skin-friction lines, which is termed the phase portrait of the surface shear-stress vector by Tobak and Peak [70], who adopt the terminology from Andronov [81]. The surface skin-friction lines are the limit of the streamlines as the flow approaches the surface and, as such, they have the same characteristics, that the flow must be locally tangent to them. Each unique, regular point on the surface lies on one skin-friction line and follows one distinct path. This characteristic only breaks down at certain special points, called singular points<sup>4</sup>, where multiple input and output paths are possible, hence the interest in their identification.

There are two primary types of singular points, the node (N) and saddle point (S), with the node also taking the form of a focus (F) or center (C). Any of these singular points can take on an attachment or separation form. For example, a node of separation or

---

<sup>4</sup> Singular points, also frequently called critical points, are locations on the surface where the magnitude of the local skin friction vector vanishes, and its direction is undefined. The terminology singular point will be used here.

attachment would behave as a sink or source respectively. An illustration of these singular points is shown in Figure 5.1. The singular points stem from an eigenvalue problem formed from the local wall shear stress vector [70,77,81,82] and are instrumental in understanding the phase portrait or surface skin-friction lines. The unique connection between singular points is called the topological structure and can be used to map out the surface flow field and distinguish one flow pattern from another.

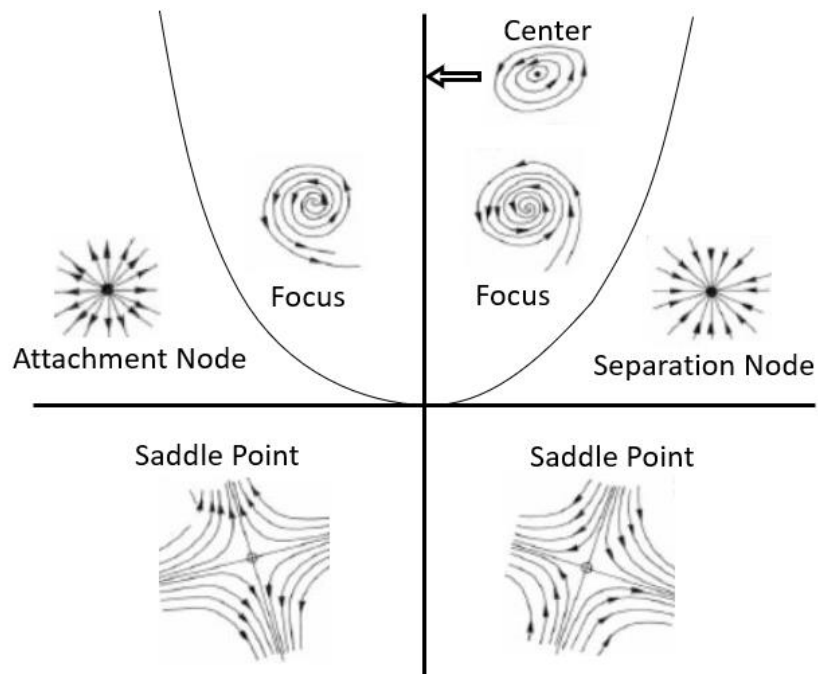


Figure 5.1 Singular point classifications based off of their mathematical description stemming from the negative trace and determinant of the Jacobian formed from the wall shear stress vector.

Using the information gleaned from the topographical images presented in the last chapter, a sketch of the global flow topology can be created. It is well known that this is a difficult task [83] and one quite prone to error. However, every effort was made to accurately capture all the flow features and their singular points. As Hunt et al. [84] puts it, “one of the main reasons for classifying the zero-shear-stress or singular points in topological terms as nodes and saddle points is because there is a relation between the number of nodes and the number [of] saddles.” This relation, which comes from the Poincaré-Bendixson theorem [70,84], takes many forms with the most common being

$$\sum_N - \sum_S = 2 \quad (5.1)$$

where N is a node (including foci) and S is a saddle point. It is colloquially known simply as *the summation rule* and states that there must be two more nodes than saddle points. A more useful form of the summation rule is derived when Equation (5.1) is modified for a three-dimensional body (B) and plane surface (P) in a wind tunnel. This occurs by treating the upstream flow as emanating from a source and the downstream flow terminating in a sink. When this source and sink are accounted for the following form is reached:

$$(\sum_N - \sum_S)_{P+B} = 0 \quad (5.2)$$

Here the body (B) represent the given geometry, which is connected to the wind tunnel interior walls, the plane surface (P), without any gaps. This is the form commonly used in

wind tunnel surface flows and states that the number of saddle points must equal the number of nodes.

While equations (5.1-5.2) are only valid along surface skin-friction lines, Hunt et al. [84] develop(s) a form of the summation rule that can be applied to streamlines via planar slices of the flow. For a two-dimensional streamwise or cross-sectional slice, singly connected, Equation (5.2) takes the form

$$\left( \sum_N + \frac{1}{2} \sum_{N'} \right) - \left( \sum_S + \frac{1}{2} \sum_{S'} \right) = 0 \quad (5.3)$$

where N is a node (including foci), S is a saddle point, and primes indicate half-nodes or saddle points bound with a surface. An example of half-saddle points bound with the surface are S1 and N22, as shown in the following section in Figure 5.3.

When using these equations to validate a possible flow field, care must be taken. Because complete isolation of the body is rare, wind tunnel experiments must account for the model, support, test section walls, etc. [77]. While this is not practically feasible, if it is assumed that all singular points occur on the ramp surface and adjacent wind tunnel sidewalls, and any other singular points occur in offsetting pairs (a reasonable assumption), equations (5.2-5.3) can be readily applied. If the appropriate equation is satisfied, the map is a possible solution to the flow field. If it does not hold, there is an error in either the identified singular points or their connectivity, or there is missing information. Keep in mind that satisfying equations (5.2-5.3) does not guarantee that the proposed map correctly portrays the flow, only that it is a mathematically viable solution. In other words, while

satisfying the summation rule does not confirm the flow pattern with certainty, it can very quickly rule out erroneous maps.

## 5.2 Flow Topology

### 5.2.1 Surface Flow Topology

To create a topological map for Case A, the entire surface flow field was carefully inspected, and the flow features and their singular points were identified. This was then checked against Equation (5.2) to ensure that a valid number of singular points were identified. Subsequently, a connection between singular points was proposed that agreed with the surface flow visualization and the general consistency of flow direction in the vicinity of singular points. Once a valid map was proposed, it was checked with additional surface flow visualization and close-up inspection of the singular points. This process was iterated until a satisfactory solution was reached. The final topological map for case A is shown in Figure 5.2. It contains 22 identifiable singular points on the ramp and sidewall surfaces—11 nodes and 11 saddle points.

The topological surface map's orientation is such that it starts at the leading edge of the ramp, spans partway up both wind tunnel sidewalls, and continues along the surface to the end of the ramp. For ease of comparison to the topographical images, the map is drawn roughly to the scale of the flow features. Note that while the topology is symmetric about the tunnel centerline, the topography of some of the flow features near the sidewalls varies slightly run-to-run; to represent this variation, some of the singular points at these locations were not drawn in a centerline symmetric fashion. The topological map shown in

Figure 5.2 provides a visual interpretation of the overall surface flow that previously was only available in fragmentary pieces in the surface flow visualization.

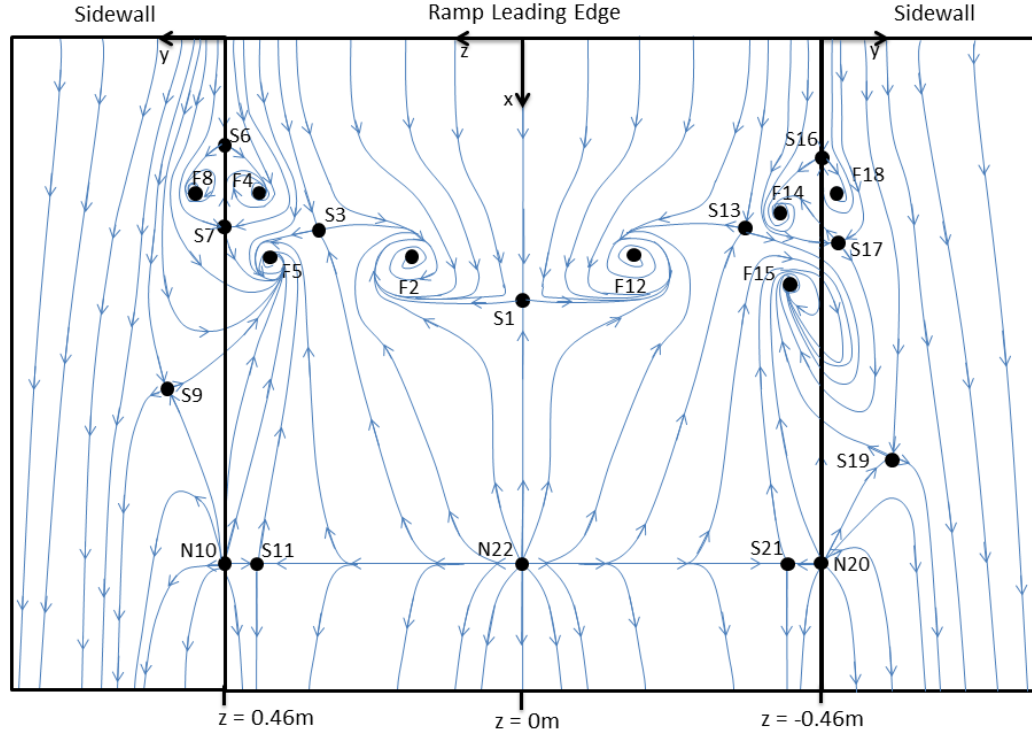


Figure 5.2 Topological map (phase portrait) sketch of the flow for the large-scale separation case, Case A, roughly drawn to scale with the flow field topography presented in the previous chapter

### 5.2.2 Off-Surface Flow Topology

Analyzing the skin-friction lines on the surface via oil film patterns does not fully characterize the separation topology—one must examine the off-surface flow to form a more complete picture. Topological analysis provides a broad understanding of the off-surface flow field. While there is no unique relationship between the surface flow pattern and the topology of the whole three-dimensional flow [85], some off-surface flow information can be inferred from the skin-friction patterns. One such example is the flow

along the tunnel centerline plane that includes separation, via saddle point S1, and reattachment, via node N22, both of which can be seen in Figure 5.2. Chapman and Yates [86] point out that whenever a saddle point and node of opposite type are formed from a bifurcation (as is the case here), an isolated singular point appears in the flow above the surface. This singular point is depicted as focus F27 in Figure 5.3, which shows streamlines taken in a wall-normal plane along the ramp centerline for Cases A, B and C. Here the flow separates from S1 and wraps its way around the newly discussed singular point, F27. Downstream from this point, the flow reattaches at N22.

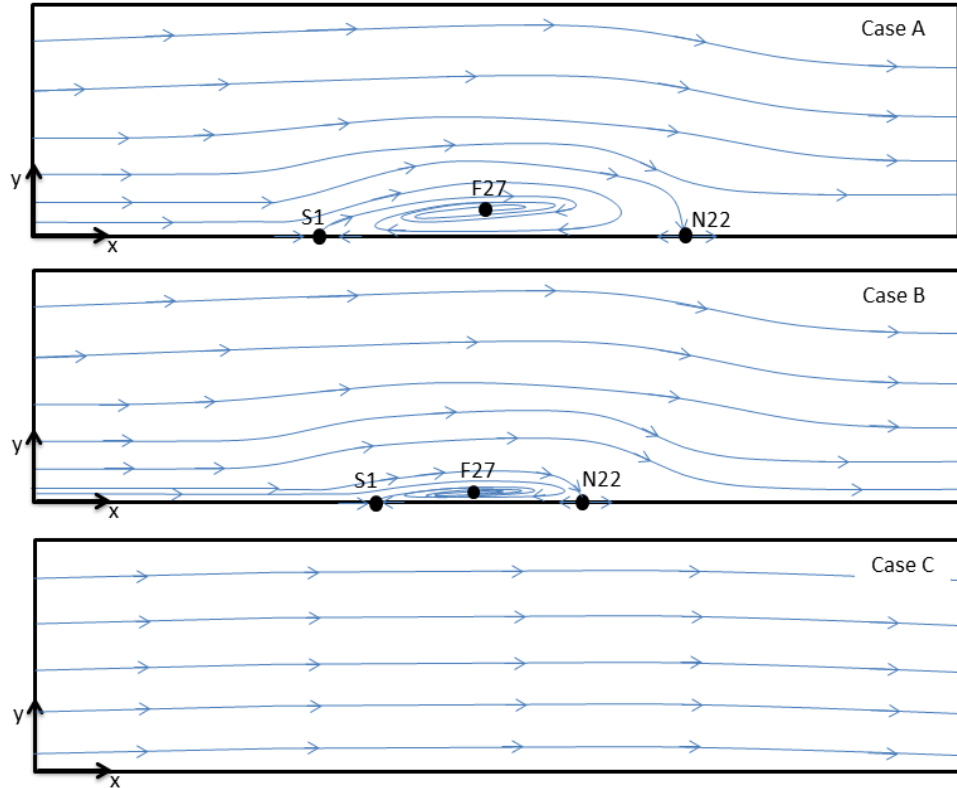


Figure 5.3 Streamwise slice of the centerline flow topology for Cases A, B, and C, highlighting the process leading to the inverse saddle node bifurcation that yields attached flow for Case C

In Figure 5.3, S1 and N22 are the same singular points identified in the surface topology for Case A, as shown in Figure 5.2; however, along this plane they are both half-saddle points. The “half” distinction is due to their being joined with the ramp surface, while node N22 is now technically a saddle point<sup>5</sup> since flow enters on one axis (the freestream) and departs along another (the ramp surface). This proposed topology satisfies the summation rule (Equation 5.3) for a streamwise slice with two half-saddle points and

---

<sup>5</sup> Node N22 is technically a saddle point in the three-dimensional sense (in fluid flows there are no sources or sinks due to continuity), as the flow enters from above along the y-axis, and departs along the x-z-plane; however, when viewed in x-z-plane it is considered a node for topological analysis. For more information on three-dimensional singular points see [87,88].

one node in the form of a focus. While the formation of a center instead of a focus is possible, this is not likely in practice, as it is a singular case rooted in the limit of two-dimensional separation and would present an example of an unstable saddle-point-to-saddle-point connection. As for stability, F27 must be stable and spiral inward as drawn above. Physically, it consists of spanwise vorticity, created by the shearing at the wall. The flow, separating from the surface via S1, travels along an inward spiraling plane and out through the central vortex core, F27, that is likely twisted to form a horseshoe vortex terminating downstream.

Also depicted in Figure 5.3 is the variation in centerline flow with ceiling configuration. Although it cannot happen in situ, lowering the ceiling from Case B to C, causes S1 and N22 to undergo an inverse saddle-node bifurcation, eliminating F27 and with it the separation region. Here the bifurcation parameter can be thought of as the wind tunnel ceiling position (i.e. the streamwise pressure gradient).

With this picture in mind, attention is now given to the other major flow features shown in Figure 5.2 as they depart from the surface. This will be examined from the perspective of the larger-scale separation case, Case A. As mentioned earlier, foci F2 and F12 detach from the surface and advect downstream. These foci possess the same sign of rotation as the freestream singular point vortex, F27, as it wraps around and advects downstream, indicating a high likelihood of the vortex cores intertwining and eventually merging with one another. Figure 5.4 illustrates what this would look like for Case A. As these spiraling vortical structures travel downstream, their impact on the surface must be consistent with the surface flow patterns seen earlier. In its wrapping around, the central foci, F27, depicted in Figure 5.4, leaves surface flow lines that emanate from N22. These

lines travel 1) upstream toward S1, 2) obliquely toward F2, S3, F5, F12, S13, and F15 as the central separation structure undergoes a 90 degree bend, and 3) in crossflow toward S11 and S21. This pattern is clearly evident in the surface topography, Figure 4.1, and corresponding topology, Figure 5.2, shedding new light on these features.

In close relation to the developing flow depicted in Figure 5.4, another off-surface flow slice that can be examined and pieced together via topological arguments is the crossflow plane at reattachment. The topology map of Figure 5.2 shows the existence of five singular points along the reattachment line. The pattern of these singular points consists of alternating nodes of attachment and saddle points, i.e. N10, S11, N22, S21, and N20. It is worth pointing out that this pattern is reminiscent of two-dimensional flow, in which separation and reattachment occur along singular lines consisting of repeating patterns of alternating saddle points and nodes in the limit as their separation tends to zero (i.e. they are infinitesimally close to one another). While this limiting situation never actually occurs, flows that are typically considered two-dimensional contain this repeating pattern. Axisymmetric flows are an example of this [21,89]. The observation of this pattern here provides support to the earlier claim that the reattachment region is quasi-two-dimensional.

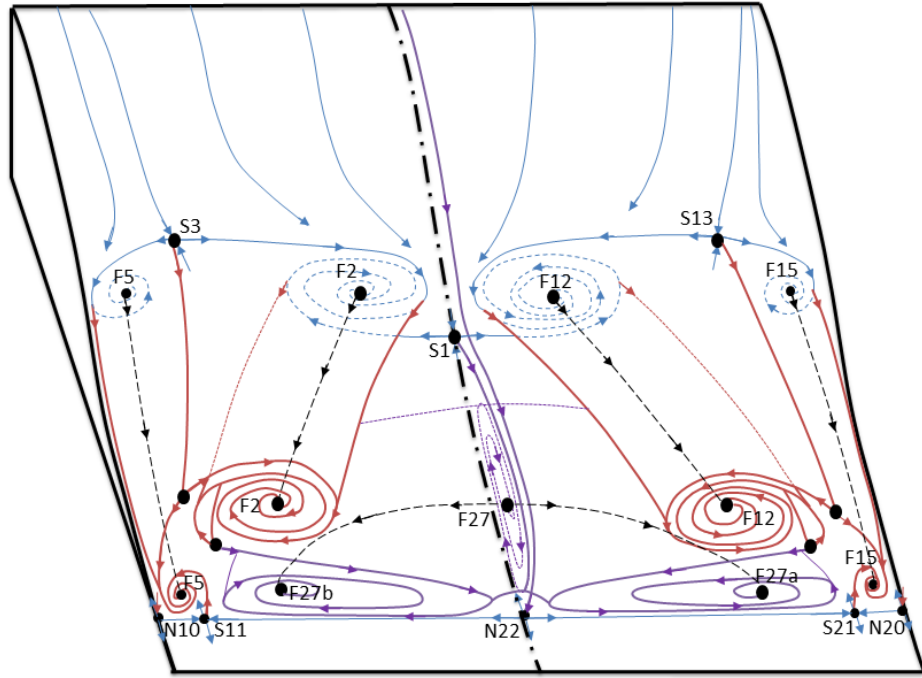


Figure 5.4 Illustration of the off-surface separating flow for Case A as it advects downstream with blue lines representing the surface flow, red lines representing the dividing line of separation as it departs from the surface, and purple lines representing the central separation region

Figure 5.5 (below) provides a sketch of what the streamline flow topology may look like in the crossflow reattachment plane. While there is no unique off-surface topology for a given surface topology, the large features (vortices/foci) that are prevalent in this flow are of interest. Figure 5.5 shows how the foci of Figure 5.4 are likely to be stretched or squeezed based on the surface topology at reattachment. To quantify this mean crossflow, select LDV measurements were acquired at the end of ramp,  $X = 0.9$  m, which is slightly downstream of reattachment. While the LDV system used in this study can only measure two components of velocity, overlapping measurements acquired at separate oblique angles allowed the mean crossflow component of velocity,  $W$ , to be determined. This procedure is outlined in Wicks et al. [90] and uses the same LDV system. However, due to

significant laser reflections and adverse optical effects associated with large incidence angles, only limited data could be collected at the two spanwise locations  $Z = -0.13$  m and  $Z = -0.26$  m. The centerline data shown in Figure 5.5.b only contains the mean  $V$ -component of velocity with the mean  $W$ -component assumed zero given the symmetry of the flow.

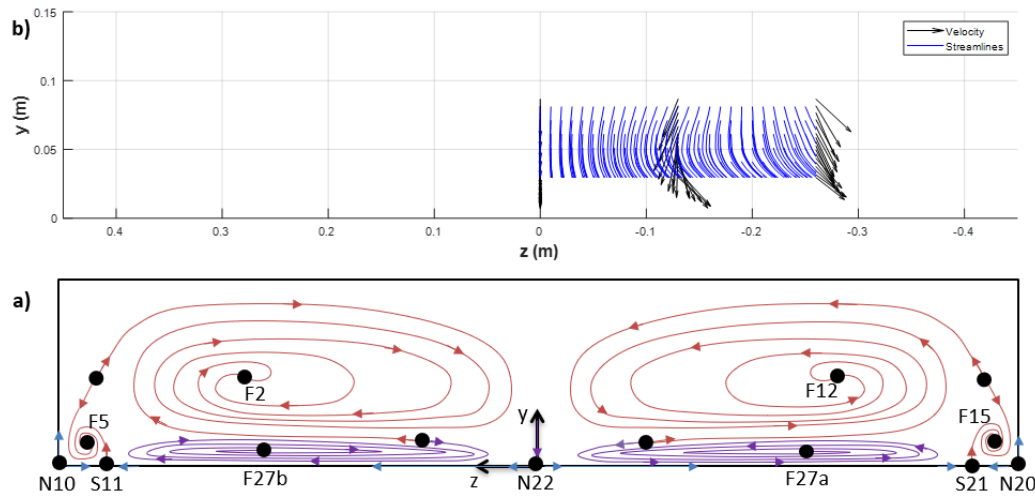


Figure 5.5 Sketch of the expected topology of the flow taken at reattachment (a), and mean velocity acquired via LDV at  $X = 0.9$  m highlighting crossflow (b). Note that in the given velocity data only the  $V$ -component was available at  $z = 0$ , with a symmetry assumption yielding  $W = 0$ .

Comparing the LDV data in the top portion of Figure 5.5 with the topology sketch in the lower portion, we see that the illustrated sketch is quite reasonable. The profiles at  $Z = -0.13$  m and  $Z = -0.26$  m are consistent and highlight the presence of the detached vortical structure F12. One should also keep in mind that the locations of the flow features in the sketch are only qualitative (the actual  $y$ -location is not known), so the features could be stretched or shifted. The vortex core of the recirculation region, F27a and F27b, is likely very near the ramp surface, below the available LDV data which starts 26 mm above the

surface. The magnitude of the crossflow velocity is highlighted more clearly in Figure 5.6. At the location nearest the wall, 26 mm above the surface, the crossflow velocity is still quite significant. At  $(X, Y, Z)^6 = (0.9 \text{ m}, 0.178 \text{ m}, -0.26 \text{ m})$  the velocity vector is  $(U, V, W) = (13.2 \text{ m/s}, -2.0 \text{ m/s}, -4.7 \text{ m/s})$  indicating the crossflow angle (the angle of the mean flow relative to downstream) is approximately 20 degrees, with the crossflow magnitude being approximately 35% of the streamwise flow. The data shown here support the off-surface flow field interpretation provided in Figure 5.5.a. However, they also indicate that, while the reattachment line is uniform and may be thought of as quasi-two-dimensional, there is significant crossflow observed on the surface that extends into the flow field, hence limiting the two-dimensionality assumption.

---

<sup>6</sup> At this streamwise location,  $Y = y + 0.152 \text{ [m]}$ , so for  $y = 0.026 \text{ m}$ ,  $Y = 0.178 \text{ m}$ .

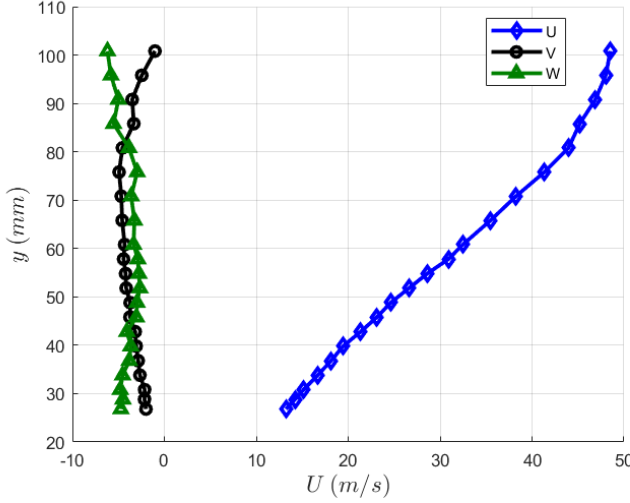


Figure 5.6 Mean flow profiles of the streamwise,  $U$ , wall-normal,  $V$ , and spanwise,  $W$ , components of velocity acquired at  $X = 0.9$  m and  $Z = -0.26$  m. Note that the wall-normal coordinate,  $y$ , is in local coordinates while the profile location is defined in global coordinates.

### 5.3 The Owl-Face Patterns

#### 5.3.1 The Four Types of Owl-Face Patterns

The commonality of the surface flow patterns observed in the experiments was discussed in the Chapter 4, with emphasis placed on the flow topography. The topological structure that provides the framework for this surface flow topography is even more ubiquitous. Looking at the core topological structure of Figure 5.2, the connection of S1-F2-S3-N22 and its symmetric side (S1-F12-S13-N22), a recognizable pattern can be identified. This pattern forms what is known as an owl-face pattern of the fourth kind. There are at least four types of owl-face patterns (referred to here as OFP) which are outlined in Perry and Hornung [91] and sketched here in Figure 5.7. The authors state that these patterns are created by vorticity departing from the wall and being carried into the freestream. Since the vorticity is highly concentrated along the vortex cores, the authors

claim that these surface patterns can be generated via an application of the Biot-Savart law with the bulk flow being largely predicted by the vortex cores. They go on to demonstrate this theory by recreating these patterns using the electromagnetic analogy, generating magnetic fields using current flowing through carefully positioned wires. Following this work, Chong and Perry [92] were able to numerically generate many of these OFPs using local Taylor series expansion solutions of the Navier-Stokes equations.

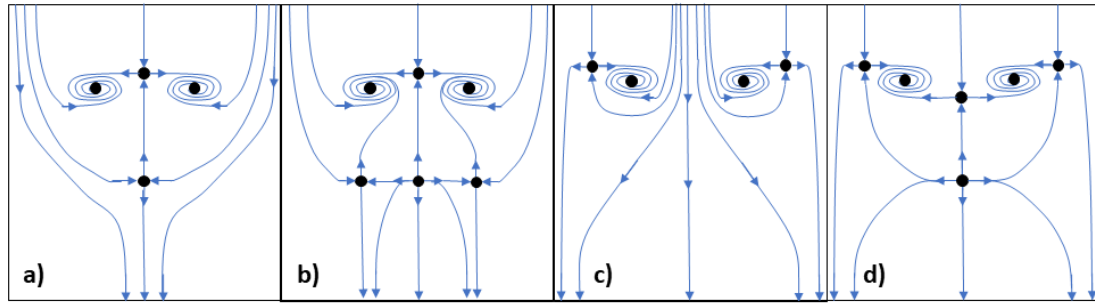


Figure 5.7 Topological structures of owl face patterns of the first (a), second (b), third (c), and fourth (d) kinds as defined by Perry and Hornung [91]

What is interesting about the OFPs is their apparent ubiquity in flows over both two- and three-dimensional geometries. While nicely labeled and classified by Perry and Hornung [91], the owl-face pattern was first identified by Fairlie [75] for its visual resemblance to an owl's face. He states that the owl structure, or some variation thereof, appears in flows from many different physical geometries ranging from bodies of revolution at incidence [his work], to nominally two-dimensional airfoils, shallow bell-shaped hills and nominally two-dimensional diffusers [the case here] and “seems to be one of the most commonly occurring structures to be found in three-dimensional separations” [75]. In addition to the physical geometries just listed, in the last chapter the core topological structure of a Stratford ramp flow was also linked to the OFPs [73], and a

literature search reveals that the OFPs have also been found in the wake of cylinders in shallow water [93] and flows over whale tubercles [94]. Even recent experimental work [25,40] conducted on three-dimensional hill shaped geometries aimed at CFD validation produced flow with OFPs of the first and second kind, although not identified as such.

It should also be recognized that the OFPs do not always occur in the isolated structures defined by Perry and Hornung [91]. In fact, re-examining Fairlie's work [75] in which he identified the owl structure, provides an example of this. The topography and topology provided by Fairlie, Figure 5.8, highlights the flow patterns he observed on a prolate spheroid at  $5^\circ$  angle of incidence. Looking closely, one can identify both OFPs of the first (flank) and fourth (leeward and windward) kinds. Figure 5.8.c also depicts the synthesized version of the topology, where the top and bottom saddle-node pair are the same, repeated for clarity.

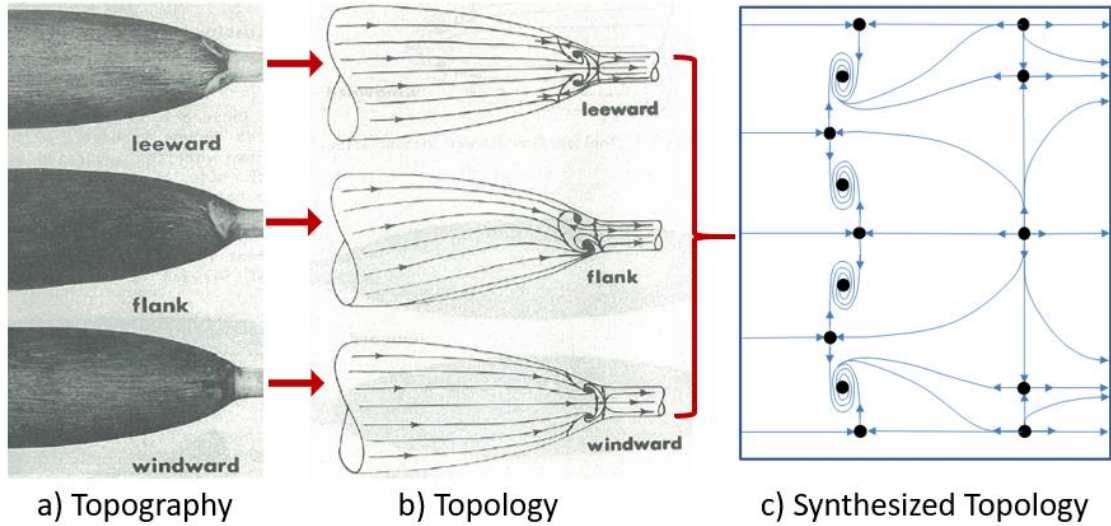


Figure 5.8 Synthesized version (c) of the topography (a) and topology (b) of the surface flow over Fairlie's [75] prolate spheroid at  $5^\circ$  angle of incidence

Another example of OFPs appearing as part of a larger structure can be identified in the experiments conducted by Wickens [95]. His work was conducted on a slender rectangular wing at  $20^\circ$  angle of attack. In fact, since this work was prior to Fairlie's, it may be one of the studies that Fairlie had in mind, although no formal citation was given. Tobak and Peake [96] later analyzed the topology of Wickens' slender wing with the hope of understanding the flow topology near the leading edge of slender delta wings. Their half-span topological analysis is shown in Figure 5.9.b. The redrawn "synthesized" topology, including the full span, is presented in Figure 5.9.c. In the synthesized form, it is evident that the central region forms the OFP of the first kind. Furthermore, both Fairlie's and Wickens' cases highlight that while individual OFPs can often be identified, they are often part of a larger, more generalized structure.

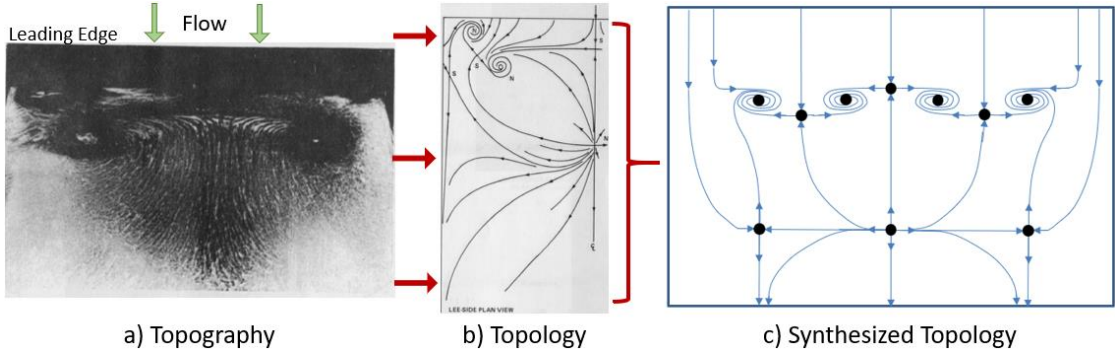


Figure 5.9 Synthesized version (c) of the topography (a) and topology (b) of the surface flow over the leeward side of Wickens' [95] slender rectangular wing at  $20^\circ$  angle of attack, with the topology interpretation of (b) taken from Tobak and Peake [96]

What it is important to note about these experimental studies is that they both occur at angles of incidence, which in the case of Fairlie [75] yielded asymmetric flow conditions, even though the geometry was axisymmetric. In addition to the streamwise APG, there was also a spanwise pressure gradient (due to the angle of incidence) that provided the driving force for the crossflow and ultimately the initial impetus for the formation of the three-dimensional separation via the OFPs. Analyzing the work of Gildersleeve and Rumsey [39] provides evidence that an angle of incidence, or some other perturbation, is necessary to produce separation via OFPs. They used an axisymmetric geometry, defined in Disotell and Rumsey [15], consisting of a 5<sup>th</sup> order polynomial defined similarly to the one used on the ND ramp geometry. Their experiments, which had no incidence angle, exhibited uniform two-dimensional separation. Only a few untripped cases, with slow tunnel startup conditions, provided the necessary conditions for the three-dimensional OFPs to form.

### 5.3.2 Simplified Surface Flow Topology

While many authors have recognized the OFPs in their own work, some to their own astonishment [93], few have tried to explain why this pattern forms so frequently. As

a steppingstone toward that goal, we will examine the OFPs in more detail to show that they are often part of a larger, simplistic structure. Since a topological map is only concerned with the connections between features, not their locations relative to one another, the map in Figure 5.2 can be drawn in a manner that is easier to visually interpret.<sup>7</sup> Figure 5.10 shows the same topological map as Figure 5.2, simplified to highlight the distinct separation and reattachment structures. This is equivalent to taking the map of Figure 5.2 and unfolding and stretching it out while maintaining all the connections between flow features. In other words, *the topology of Figure 5.10 is identical to that of Figure 5.2*. Only the topography has been changed. The figure clearly presents a repeating pattern of saddle points and foci for separation, as well as nodes and saddle points for reattachment. This repeating pattern, regardless of the number of saddle/foci and node/saddle pairs, we will label as a generalized owl-face pattern.

---

<sup>7</sup> As a caveat, this redrawing hinges on a proper interpretation of the connections between flow features, otherwise in the initial drawing is flawed, any error will be exaggerated.

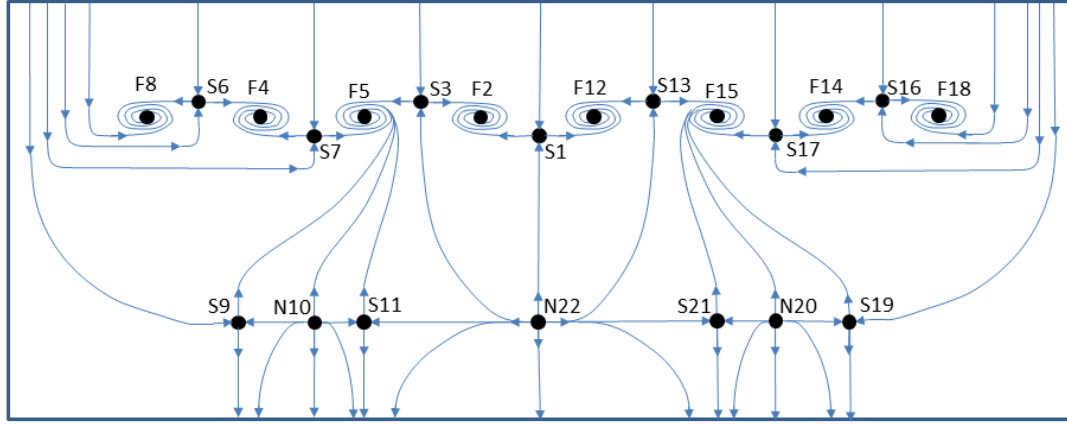


Figure 5.10 An equivalent redrawing of the topological map in Figure 5.2 highlighting the separation and reattachment regions which together form (what we label) a “generalized owl face pattern”

Using the method just described, topological maps for Cases B and C can be constructed, as shown in Figure 5.11 and Figure 5.12, respectively. As mentioned in the last chapter, the only topological difference between Cases A and B is the addition of node-saddle-point pairs on each side of the reattachment line, N24, S23, S25, and N26 in Figure 5.11. In terms of the generalized owl face pattern, this change has no real effect and the pattern of the core structure remains. What is really striking about the topological maps of Cases A and B is that the global line of separation can be unraveled so neatly and in such a simple manner! Thus, although the separation may be three-dimensional, its core structure is not complex. As for the attached flow case, Case C, its topology is the simplest of the three cases, featuring two owl-face patterns of the first kind with attached flow in between.

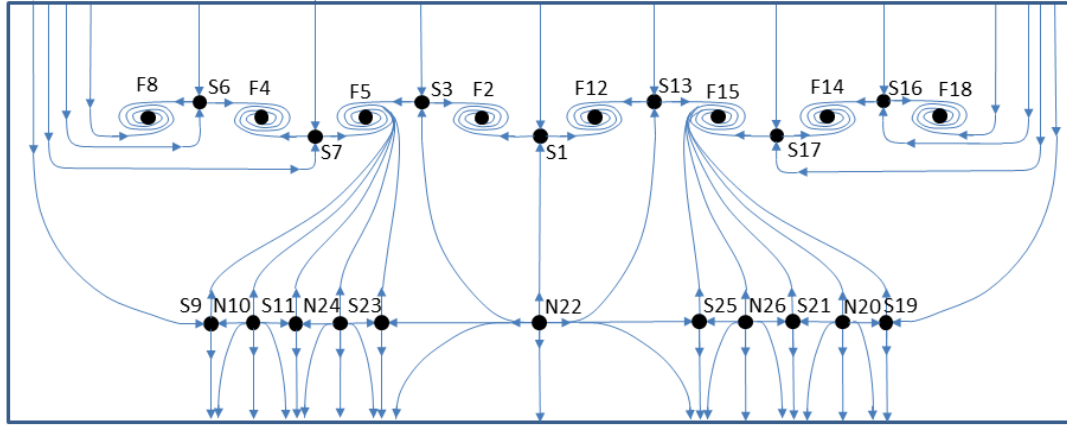


Figure 5.11 The topological map for Case B drawn in generic form highlighting the generalized owl face pattern. Note that the only differences between Case B and Case A are found on the reattachment line.

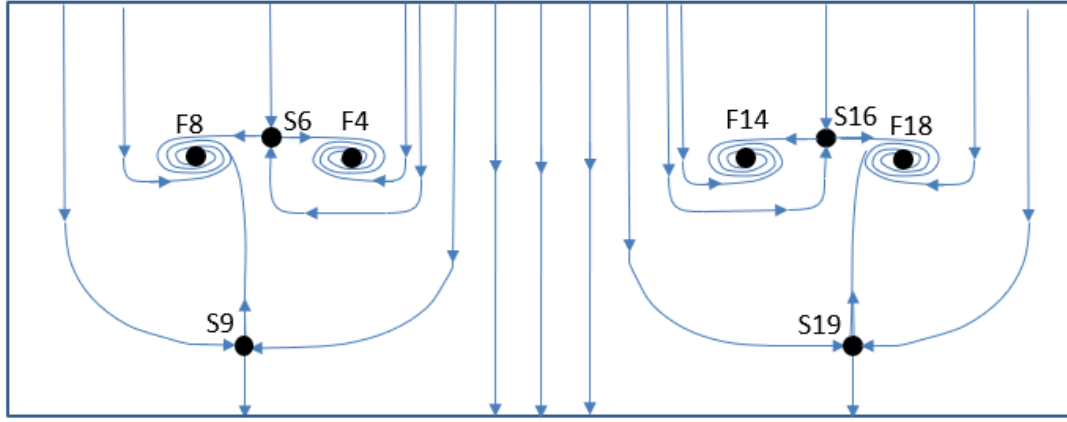


Figure 5.12 The topological map for Case C drawn in generic form highlighting the generalized owl face pattern, now broken to yield two distinct owl-face patterns of the first kind, see Figure 5.7.

All four of the OFPs listed by Perry and Hornung [91] can be identified in these generalized patterns by various inverse bifurcations or by only looking at select groupings, hence its generality. For example, let's examine Case A shown in Figure 5.10. The OFP of the fourth kind was already identified as the grouping of S1-F2-S3-N22 and its symmetric side S1-F12-S13-N22. Looking at this same grouping, the transition from the OFP of the fourth kind to that of the third kind could take place via an inverse saddle node bifurcation

of S1 and N22. The OFP of the second kind is a little harder to see as it would require at least two sets of inverse bifurcations. One possible way this pattern could form is the merger and elimination of F12-S13 and F2-S3 which would leave the connection of F5-S1-F15 with S11-N22-S21 forming the OFP of the second kind. While this may seem a little abstract, in a preliminary test utilizing passive flow control, discussed in the following chapter, the elimination of F12-S13 was observed, beginning the transition of the flow to an OFP of the second kind. Finally, the OFP of the first kind was already identified twice in Case C.

### 5.3.3 Surface Flow Topology Comparison

Just as the OFPs observed in Fairlie's [75] and Wickens' [95] studies were part of a larger structure, the OFP of the fourth kind observed in Case A is also part of a larger structure, shown above, which we have labelled the generalized OFP. Intriguingly, Figure 5.13 shows that the topology observed in Fairlie's [75] work is also contained within the structure of the generalized OFP observed for Case A. That is, S7-N10 and S17-N20 of Figure 5.10 would correspond to the top/bottom saddle-node pair shown in Figure 5.8. Furthermore, Figure 5.13, shows both the flow topologies of Case A and Fairlie's spheroid; the difference between these two flows likely corresponds to the difference in conditions occurring between the two-dimensional and axisymmetric geometries. In other words, the extra saddle-foci pairs and corresponding nodes observed on the ramp surface are a result of the sidewall boundary condition, whereas the central structures are purely a result of the remaining driving forces: pressure gradient and surface curvature. This stems from the fact that Fairlie's work was conducted on bodies of revolution at incidence, hence no sidewalls were present, only surface curvature and pressure gradient effects. Examining the topology

of the attached flow case, Case C in Figure 5.12, produces the same net result shown in Figure 5.13 when compared to the larger-scale separation case, Case A in Figure 5.10. Here, the difference in surface flow topology between these two cases also yields the exact same topological structure that forms on Fairlie's axisymmetric geometry, Figure 5.13. Again, this also suggests that the separation structures observed in the attached flow case, Case C, are a result of the sidewalls.

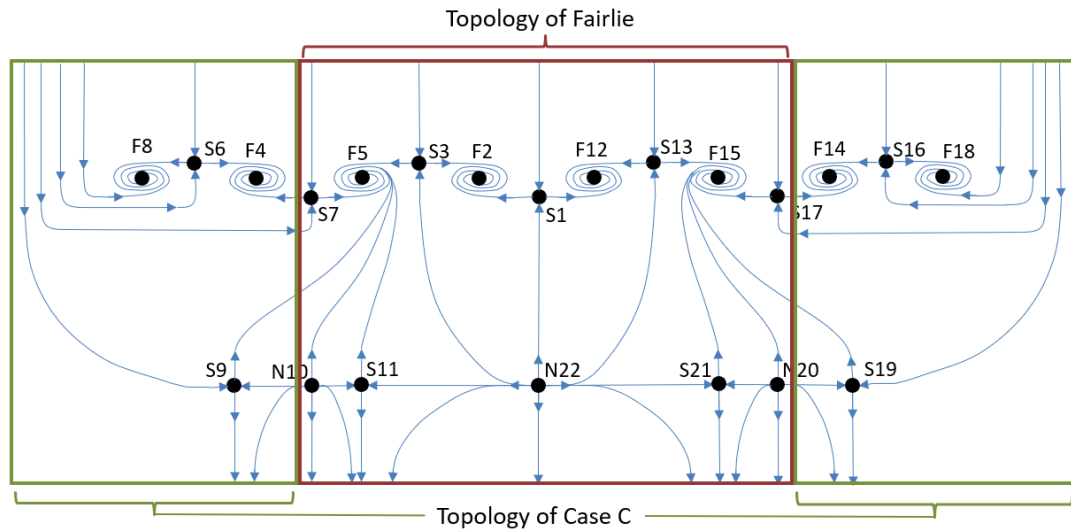


Figure 5.13 The surface topology map of Case A, Figure 5.10, highlighting the common topology of Fairlie's [75] spheroid, Figure 5.8, and the attached flow case, Case C, Figure 5.12

#### 5.4 Generalized Separation Structure

Thus far, evidence has been presented that suggests that the separation and reattachment structures occurring on the ramp are made up of repeating patterns of saddle points and foci for separation, alongside nodes and saddle points for reattachment, see Figure 5.10, Figure 5.11, and Figure 5.12. This simple, common structure warrants its own discussion here.

To reiterate, and expand upon a previous discussion, true two-dimensional flow separation does not exist in a three-dimensional world. What most researchers refer to when they speak of two-dimensional flow separation is a flow with homogeneous properties in the spanwise direction. Delery [77] explains that the topological form is a linear repeating pattern of saddle points and nodes whose proximity to one another increases with the extent of the two-dimensionality. Figure 5.14.a shows schematically what this two-dimensional separation structure would look like. Since there is a crossflow that alternates signs between adjacent nodes and saddle points, there is inevitably some non-homogeneity present, this is not truly two-dimensional.

As for three-dimensional separation, recent work by Surana et al. [97] mathematically identifies that “only four types of locally unique separation lines are possible in physical fluid flows: (S1) saddle-spiral<sup>8</sup> connections; (S2) saddle-node connections; (S3) saddle-limit cycle connections and (S4) limit cycles.” They go on to state that (S1) and (S2) are classified as closed separations and are often observed experimentally whereas (S3) and (S4) are open<sup>9</sup> type separations that are uncommon and have not been documented experimentally. Generally speaking, if separation occurs on a line originating from a saddle point, it is called a *global* line of separation or *closed* separation, whereas if it does not originate from a saddle point it is called a *local* line of separation, *open* separation or *crossflow* separation [70,86,98]. What was just labelled as two-dimensional separation in Figure 5.14-a is a repeating pattern of (S2) separation. Likewise, what has been observed experimentally in the three-dimensional separation work

---

<sup>8</sup> Here the authors use the terminology spiral instead of foci although they are one in the same.

<sup>9</sup> Surana et al. [97] note that as defined, their use of the term open separation “differ[s] from common examples of open separation in that they admit unique separation lines and surfaces”.

presented in this chapter is a repeating pattern of (S1) separation, see Figure 5.14-b. When combined with the reattachment structure, it is what was previously identified as the generalized owl-face pattern. While many researchers have identified (S1) separation, to the author's knowledge, no one has proposed this repeating chain of (S1) separation, see Figure 5.14-b, as a type of generic three-dimensional flow separation, as suggested here.

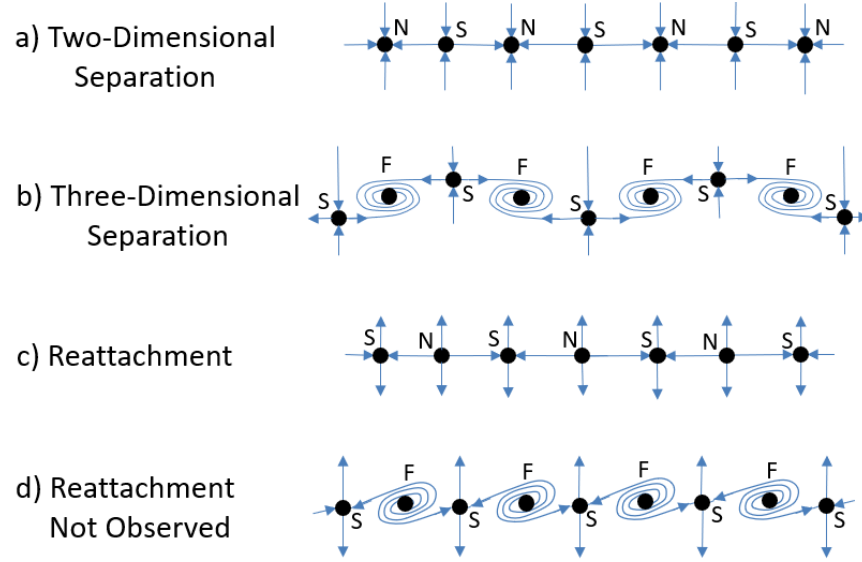


Figure 5.14 Illustration of generic separation and reattachment structures as repeating patterns of either saddle/node or saddle/foci pairs

The separation labeled as two-dimensional and three-dimensional in Figure 5.14 refers to the “structure”, or topology, of the separation and not purely to the “flow”, or topography, itself. What is meant by this is the following: suppose the spatial extent of the singular point features was reduced and the singular points themselves became collinear with one another as well as perpendicular to the mean flow, as in in Figure 5.14 above. From a global topography (zoomed out) view, there would be virtually no noticeable difference in the flow properties for the two-dimensional and three-dimensional topology

cases as both would be approximately homogeneous in spanwise extent. Now suppose the singular points fall out of line with one another; without the described collinearity, the flow becomes non-homogeneous regardless of whether the separation structure is two-dimensional or three-dimensional. This is depicted in Figure 5.15. In other words, flow separation can take on a relatively homogeneous or non-homogenous form regardless of the dimensionality of the flow topology structure; however, the two-dimensional form naturally adapts itself to a spanwise homogeneous flow, whereas the three-dimensional form naturally adapts itself to a spanwise non-homogeneous flow. The flow topology does not provide a physical explanation of what causes the flow to develop a given form, rather it provides a means of representing the forms that are observed and of designating other potential forms as either possible or impossible.

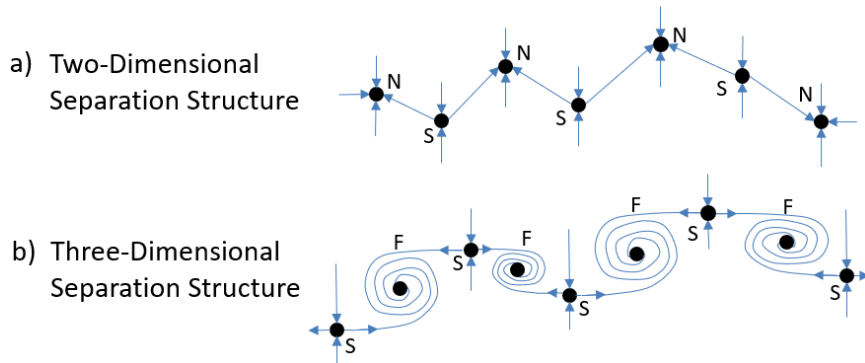


Figure 5.15 Example of a non-homogeneous flow for both the two-dimensional separation structure (a) and the three-dimensional separation structure (b)

While topologically analogous two-dimensional and three-dimensional separation structures appear in the flow, there are no topologically analogous reattachment structures. In all the flows examined in this work, the reattachment topology matched that of a two-dimensional flow; reattachment initiated at nodes and terminated into saddle points. A review of available literature reveals many examples of the same form of reattachment, with only Tobak and Peake [70] mentioning of foci of attachment. They state that these foci exist in flows with either rotation of the flow or the geometry. So why don't flows ever appear to reattach via unstable foci-saddle pairs? One intuitive answer is that vorticity is created in the shearing at the surface and transferred into the freestream and not vice versa. Attachment via an unstable focus would require a core of freestream streamwise vorticity to be bent towards and impact the surface, in a time-mean fashion, an event that is unlikely to occur in a non-rotating flow or geometry.

## 5.5 Realized Separation Structures

The generalized three-dimensional separation structure just presented provides the form that separation appears to take on; however, this is a repeating pattern, so it does not describe the exact number of “links in the separation chain.” For example, in the flow over Fairlie’s spheroid, four foci and four saddle points made up the separation line, see Figure 5.8, while in Cases A and B of the ND Ramp flow, eight foci and seven saddle points were connected to form the separation lines, see Figure 5.10 and Figure 5.11. Other combinations of saddle/foci pairs are possible topologically and the following example will highlight some cases that yield a reduced number of saddle/foci pairs.

Separation at the sidewall/surface junction is well recognized. The presence of the sidewall boundary layers, in conjunction with the ramp boundary layer, provides a

momentum deficit that, however small, naturally leads to flow separation at that point, provided a sufficient streamwise APG exists. Additionally, a simple spanwise pressure distribution with higher pressure near the sidewalls and lower pressure near the tunnel centerline could also be expected and explained due to this loss of momentum and early separation at the sidewall/ramp junction. While these effects would explain the separation structures at the sidewall/surface junction, see Figure 4.2, they don't explain why the additional large-scale, central vortical structures exist.

For example, Figure 5.16 shows illustrations of two possible separation patterns that agree well with the sidewall separation described above. To put these separation patterns in perspective, they can be combined with the typical reattachment pattern of nodes and saddle points to produce the surface flow topology maps shown in Figure 5.17. These maps are still the generalized owl-face patterns and contain the OFPs of the second and fourth kinds, as noted in Figure 5.17.

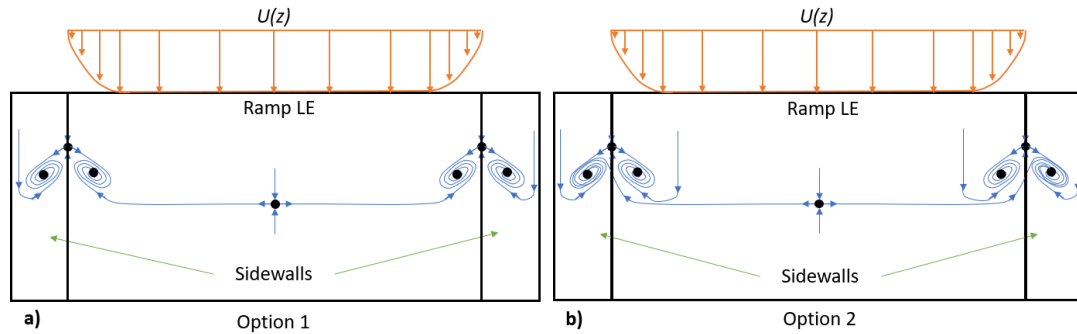


Figure 5.16 Examples of two possible separation patterns that agree well with what was shown about sidewall separation and contain the generalized owl-face patterns. Note, the sidewalls are shown laid flat as if bent from  $90^\circ$  to  $180^\circ$ .

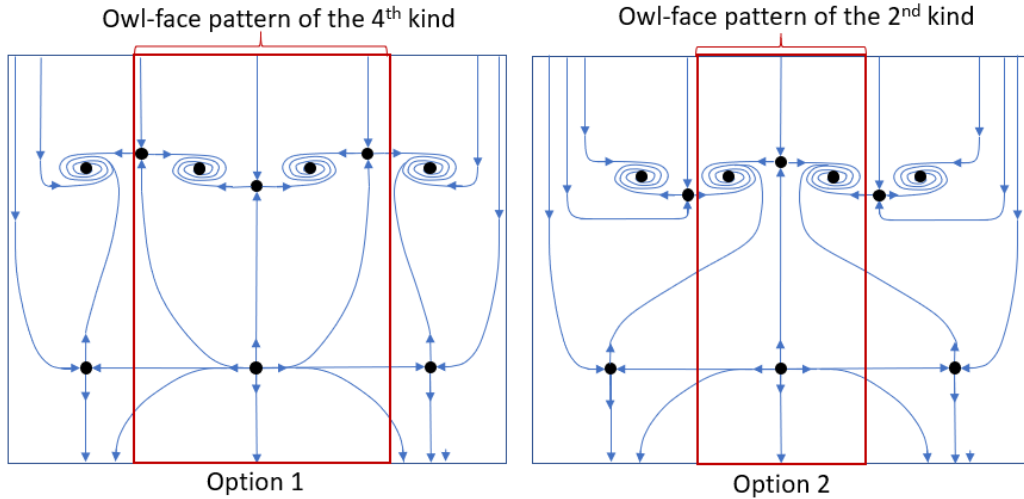


Figure 5.17 Example flow topologies with reattachment included for the separation patterns shown in Figure 5.16; Option 1 contains the OFP of the 4<sup>th</sup> kind and Option 2 the OFP of the 2<sup>nd</sup> kind

While artificial, these patterns are among the simplest examples of three-dimensional separation that could fit the given geometry and flow conditions, so the key question is *why don't we see separation taking one of these forms in experimental Case A or B?* In other words, *why do extra saddle/foci pairs form in the central region?* There must be some physical mechanism forcing the flow to take on extra saddle/foci pairs. At first thought, a likely suspect is the static pressure and/or pressure gradient distributions. The streamwise adverse pressure gradient is often identified as the primary agent dictating the streamwise location of separation, so it should likewise be expected that the spanwise pressure gradient will dictate the spanwise uniformity of the separation.

In his experimental work using a three-dimensional hill geometry undergoing flow separation, Tobak [99] showed that nodes of separation and attachment correspond to local surface pressure minima and maxima respectively, while saddle points represent a local surface pressure minima/maxima. Analyzing the spanwise pressure distribution over the central region of the ND Ramp, Figure 3.3, it is hard to confirm this for two reasons: (1)

the pressure distribution is quite uniform with only small spanwise variations present and (2) the spanwise pressure taps only extend over the central third of the ramp, with limited resolution, thereby preventing any comparative data near the sidewalls. However, even when high resolution, full width spanwise pressure measurements are available, the initial question, the cause of the formation of additional saddle/foci pairs, would not be answered. Tobak [99] goes on to state that “surface pressure extrema are not necessarily accompanied by singular points” indicating that they are a necessary, but not a sufficient, condition for the formation of singular points and that there must be an additional physical mechanism at work. Like the topology analysis, the pressure distribution is very useful, but is better thought of as descriptor than a cause. If this is the case, *what other physical mechanism(s) dictate(s) the number of saddle/foci pairs that form?* The likely answer comes from the geometric boundary conditions, in particular the streamwise surface curvature and its interaction with the ramp/sidewall juncture flow separation. These topics will be the focus of the next chapter.

## CHAPTER 6: STREAMWISE SURFACE CURVATURE AND SIDEWALL EFFECTS

The last two chapters describe the surface flow separation patterns and their topological interpretation. In all of this, however, there has been very little to explain why these patterns form and the physical mechanisms that produce them. This chapter will provide a cursory explanation of these topics by examining two geometric characteristics that have both been associated with the creation of vortical separation patterns, namely the ramp surface curvature and sidewall flow/separation condition.

The role of streamwise surface curvature will be analyzed and shown to generate secondary flow via centrifugal force. It is this secondary flow that is primarily responsible for producing the central vortical separation structures. While the curvature effect is important, it will be shown that the ramp/sidewall flow condition is at least of equal importance in dictating the overall flow separation topography. With slight modification to the ramp/sidewall juncture flow, the effect of surface curvature can either be enhanced or attenuated to change the surface flow topography. Supporting evidence will be presented based on the application of passive flow control to both the ramp surface and tunnel sidewalls. Here, surface flow visualization is the primary diagnostic tool, supported by select LDV measurements and a brief comparison to CFD data. Finally, it will be shown that (1) the sidewall/ramp juncture flow separation condition is highly coupled with the

centerline flow separation location and extent, and (2) both the location and uniformity of the central reattachment structure are insensitive to changes in the separation structure.

## 6.1 Surface Curvature and Sidewall Effects

Streamwise surface curvature inducing secondary flow in s-ducts is widely observed [100–103]. A typical explanation of the effect suggests that streamwise surface curvature introduces a centrifugal force that is directed radially outward from the center of curvature. Here the centrifugal force will be referenced on a per unit mass basis as,  $\frac{U^2}{R}$ , where  $U$  is the streamwise velocity and  $R$  is the streamwise radius of curvature. Since the streamwise velocity,  $U(y)$ , varies throughout the boundary layer, the effect of the centrifugal force is stronger near the upper edge of the boundary layer, where higher velocities are present, and lower near the ramp surface. This centrifugal force promotes thickening of the boundary layer, as it is stretched away from the surface and increases its susceptibility to the APG, inducing separation [102]. The outward fluid motion produced by the centrifugal force in the central region of the duct creates a secondary flow, directed outward along the centerline and downward along the sides, and effects the entire cross-section of the duct. Since the near surface flows have lower velocity magnitudes due to their boundary layers, they are not as strongly affected by the centrifugal force, so the opposing circulation necessitated by continuity is produced in these regions. An illustration of this secondary flow, and the resulting three-dimensional surface flow pattern, is shown in Figure 6.1.

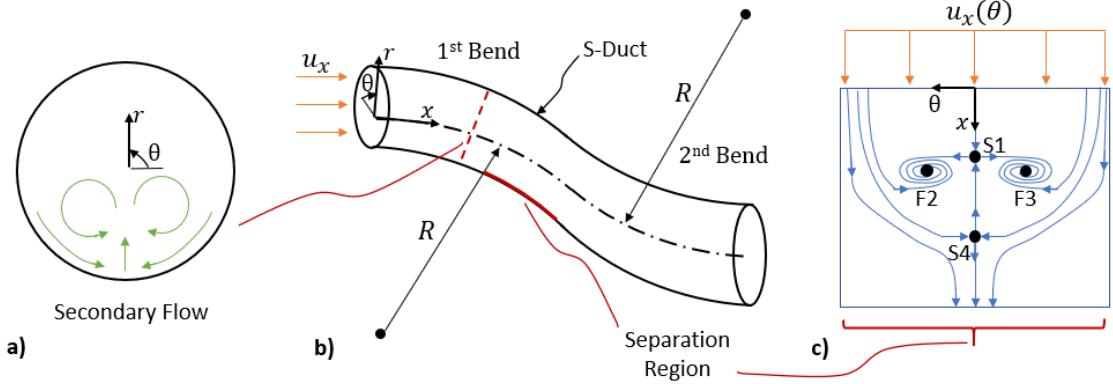


Figure 6.1 Illustration of secondary flow (a) generated in an s-duct (b) due to streamwise surface curvature and the resulting three-dimensional surface flow pattern in the form of the OFP of the first kind (c)

While common in s-ducts of circular cross-section, the three-dimensional surface flow separation pattern of the OFP of the first kind is also observed in s-ducts of other cross-sections [101]. For the ND ramp experiments, however, the expected flow field is different than that given above. Geometrically, it only possesses streamwise surface curvature, not spanwise curvature, which is common in s-ducts. Instead, it includes corners that connect the ramp to the tunnel sidewalls. An illustration of the expected secondary flow is given in Figure 6.2.a. Over the majority of the cross-section, the secondary flow should look similar to that of the s-duct; however, since the cross-section is rectangular, instead of circular, small opposing corner vortices are expected to form. The expected secondary flow is likely of very low magnitude. Additionally, this secondary flow should not exist upstream, as no three-dimensional flow effects were observed prior to the start of the ramp; rather, it is purely a result of streamwise surface curvature.

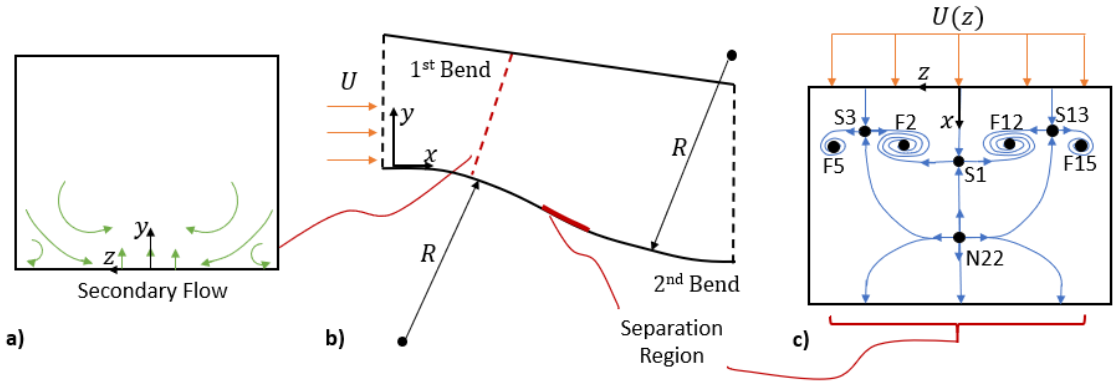


Figure 6.2 Illustration of expected secondary flow (a) generated over the ND Ramp (b) due to streamwise surface curvature and the resulting central three-dimensional surface flow pattern in the form of the OFP of the fourth kind (c)

The central<sup>10</sup> flow separation pattern for the ND ramp is shown in Figure 6.2.c. While the streamwise surface curvature of the ND Ramp is similar to that of s-ducts, the surface flow separation pattern is not. Instead, the central separation pattern is an OFP of the fourth kind, not the first kind, as depicted in Figure 6.1.c. Note that the primary difference between the two cases is that the central foci roll up in opposite directions.

To examine why s-ducts and the ND Ramp differ in their separation patterns and, more importantly, the role that streamwise surface curvature plays in the ND Ramp flow experiments, the streamwise surface curvature and mean flow fields will be quantitatively and qualitatively analyzed for both cross-sections. Figure 6.3 shows the streamwise radius of curvature<sup>11</sup>,  $R$ , for the ND Ramp and three typical s-duct studies [101–103]. Over the initial convex region, the s-ducts examined have constant radii,  $R = 1.02, 0.83$ , and  $0.45$  m, while the ND Ramp's, radius of curvature changes from infinity, at  $X = 0$  m, to values

<sup>10</sup> For clarity, the entire flow separation pattern is not shown here; see Figure 5.2 for a more complete picture.

<sup>11</sup> Note there is a discrepancy in the definition of streamwise radius of curvature as shown here. For the ND ramp,  $R$  is based on the lower surface while for the s-ducts it is typically based on the centerline axis.

similar to the s-ducts,  $R = 0.73$  m at  $X = 0.18$  m, and then back to infinity, at  $X = 0.45$  m. Thus, the s-ducts have roughly constant centrifugal forces over a given streamwise fetch while the ND Ramp centrifugal forces start and end at zero and peak in between. The result is similar for the concave curvature region, except that the radius of curvature, and hence centrifugal force, changes direction.

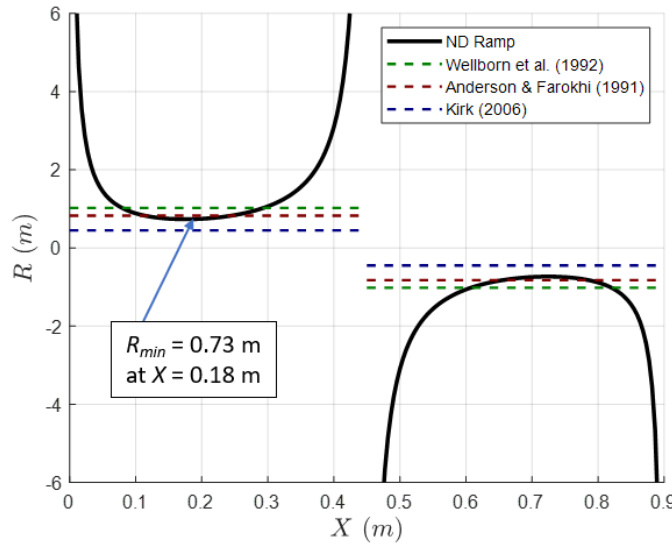


Figure 6.3 Radius of streamwise surface curvature comparison between the ND Ramp and three s-duct studies [101–103] with positive and negative values representing convex and concave curvature, respectively

It has already been established that the centrifugal force induces a secondary flow in s-ducts. This secondary flow, in conjunction with the mean flow, gives rise to the surface flow pattern presented in Figure 6.1.c. This argument assumes that the magnitude of secondary flow, and hence the  $u_\theta$ -component of velocity, is proportional to the centrifugal force,  $\frac{u_x^2}{R}$ . Over the duct surface, the secondary flow (inward directed crossflow), will increase from zero to roughly a constant magnitude. The streamwise mean flow near the

surface,  $u_x(\theta)$ , is homogeneous in  $\theta$ , as the initial boundary layer is uniform around the circular cross-section. Farther downstream,  $u_x(\theta)$  will change slightly. It will be strengthened away from the duct center due to the increased momentum being entrained from above and down the sides by the secondary flow, while the near center flow will be reduced by the APG and eventually separate.

The gradients in streamwise and azimuthal mean flow result in opposing regions of wall-normal vorticity,  $\omega_r$ , that lead to the eventual roll-up of opposing foci of separation when separation occurs. Together, these two foci produce the “eyes” of the OFP of the first kind. Figure 6.4 illustrates this process on one side of the centerline as it results in clockwise-oriented, wall-normal vorticity and leads to a focus of separation, F3, as shown in Figure 6.1.c. Note that Figure 6.4 also shows that regardless of streamwise position the wall-normal vorticity has the same sign of rotation. Following the same logic on the other side of the centerline (not shown here) yields a counterclockwise-oriented focus of separation, F2, as shown in Figure 6.1.c.

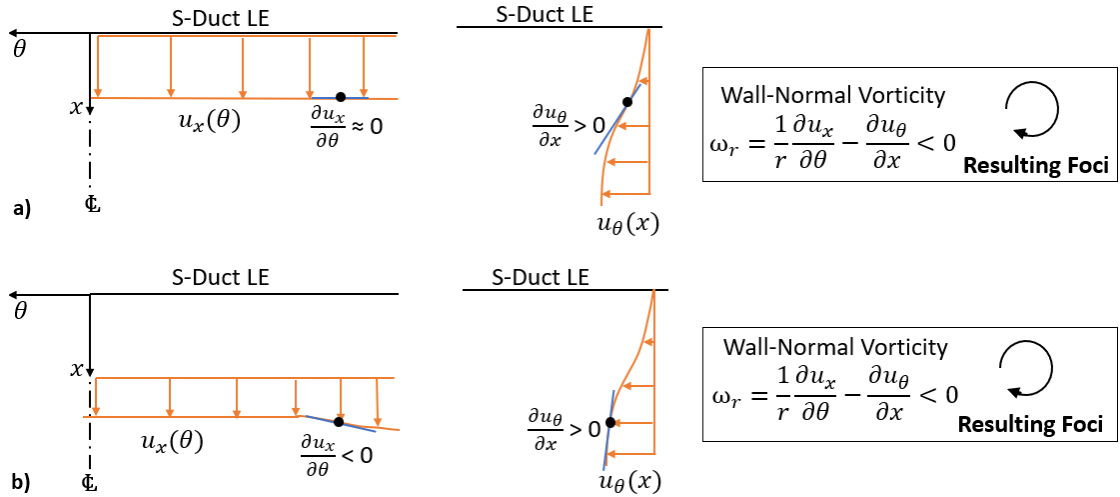


Figure 6.4 Qualitative analysis of the  $u_x(\theta)$  and  $u_\theta(x)$  mean velocity profiles in an s-duct of circular cross-section and the resulting wall-normal vorticity,  $\omega_r$ , that leads to the formation of the foci of separation. Here the flow in (a) is representative of the start of the duct,  $x = 0$ , and the flow in (b) is representative of a location further downstream but prior to separation.

For the ND Ramp, both the imposed centrifugal force and the near-surface mean flow are more complex than that of an s-duct. First, we will analyze the flow between the centerline and the sidewall separation. As in the case of the s-duct, the centrifugal force,  $\frac{U^2}{R}$ , initially increases, albeit at a slower rate, causing the inward directed crossflow,  $W$ , to increase as well; however, the surface curvature peaks at  $X = 0.18$  m, see Figure 6.3, and subsequently decreases, likely causing the induced inward directed crossflow to peak and then decrease as well. This peak and decline of the centrifugal force could begin at  $X = 0.18$  m but is more likely to occur slightly downstream, depending on the response time of the flow. Since the duct has a rectangular cross-section, the secondary flow that generates the inward crossflow also generates lower magnitude outward crossflow, given the secondary corner flow near the ramp/sidewall juncture, see Figure 6.2.a. Note that the secondary flow, or crossflow, analyzed here is only that induced by centrifugal forces and

is likely of low magnitude. The sidewall/ramp juncture separation will produce its own crossflow, which is likely to be of a greater magnitude.

As this secondary flow is developing, the near-surface streamwise mean flow,  $U(z)$ , is roughly constant over the majority of the span but reduces to zero at the sidewall due to the ramp/sidewall juncture, unlike the mean flow of the s-duct. Further downstream, this trend in the streamwise mean velocity is the same only reduced in magnitude, due to the APG, as the flow approaches separation. These mean flow gradients generate wall-normal vorticity,  $\omega_y$ , which influences the flow to spiral in one direction over another when separation occurs. Figure 6.5 illustrates this process on the outer loop side of the tunnel centerline for two streamwise locations, both of which are downstream of the ramp leading edge and prior to separation.

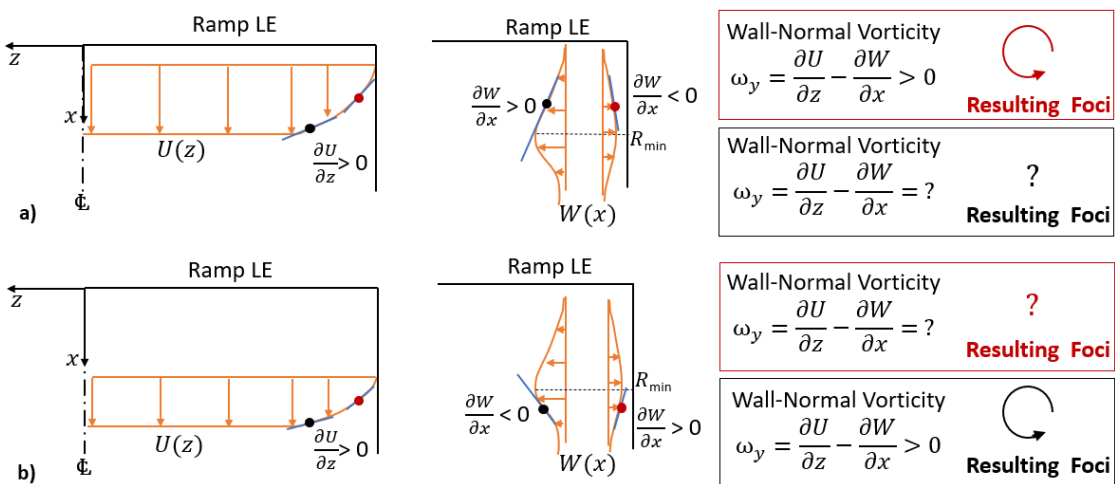


Figure 6.5 Qualitative analysis of the  $U(z)$  and  $W(x)$  mean velocity profiles over the ND Ramp at two different streamwise locations (a) and (b), and the wall-normal vorticity,  $\omega_y$ , causing the formation of the central foci when separation occurs

There are two regions to be analyzed in Figure 6.5, the central region with inward directed induced crossflow (the black circles) and the near wall region with outward directed induced crossflow (the red circles). These two regions have opposite crossflow gradients which switch signs some distance after the centrifugal force peaks. The near wall region initially has positive wall-normal vorticity that would likely reduce in magnitude and possibly change sign further downstream; however, sidewall/ramp juncture separation tends to form far enough upstream that the positive wall-normal vorticity still dictates the direction in which the focus spirals. The wall-normal vorticity in the more central region is initially weak because of opposing velocity gradients. Further downstream, however, the wall-normal vorticity becomes positive as the previously-increasing centrifugal force weakens. Since the central flow separates farther downstream, it will spiral into a positive, counterclockwise-oriented focus of separation as dictated by the wall-normal vorticity at that location. Following the same logic on the near wall side of the tunnel centerline yields a clockwise-oriented focus of separation. These two central foci, F2 and F12 in Figure 6.2.c, form the “eyes” of the OFP of the fourth kind.

The analysis in Figure 6.5 did not consider the presence of the sidewall separation. While the analysis suggests that sidewall separation is not required for foci F2 and F12 to form when the central flow separates, as has already been noted, the sidewall will separate before the central region does. It could be argued that the wall-normal vorticity generated is shed via the sidewall separation foci as they have the same sign of rotation. While the sidewall separation will change the flow field, even with this separation there is still strong wall-normal vorticity present in the central region of the flow that promotes the flow to adopt additional foci, i.e. F2 and F12, when separation occurs.

To illustrate this for the outer loop side of the wind tunnel, first assume the separation takes the simplistic structure presented in the last chapter and shown in Figure 6.6.a. The central near surface streamwise mean flow,  $U(z)$ , still has a positive gradient as the flow approaches and passes through separation. The near surface crossflow,  $W$ , is still initially inwardly directed due to the centrifugal force; however, it must drastically change direction and be directed toward the sidewall to roll-up into the sidewall separation focus. This gradient in the crossflow in combination with the gradient in the mean flow, shown in Figure 6.6.b, introduces additional positive, wall-normal vorticity which promotes the flow to adopt the additional counterclockwise-oriented foci of separation observed in the central region, represented by the red circle.

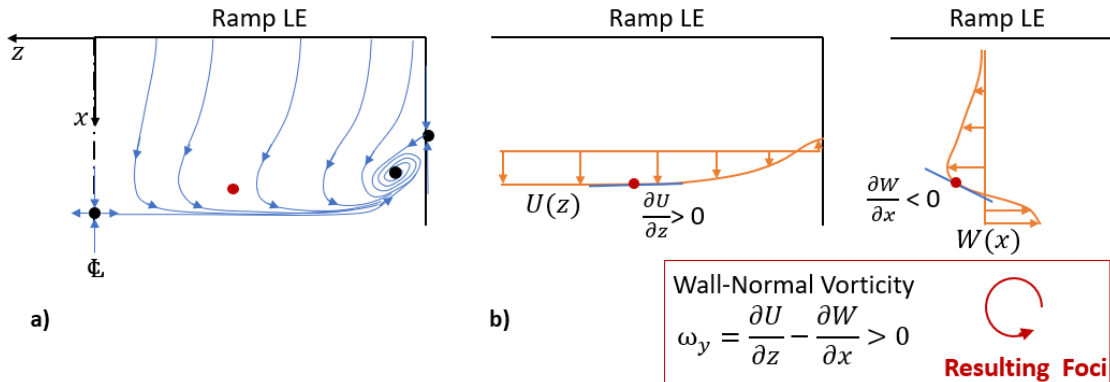


Figure 6.6 Qualitative analysis of the  $U(z)$  and  $W(x)$  mean velocity profiles over the ND Ramp (b) with the presence of sidewall separation (a) leading to the generation of wall-normal vorticity,  $\omega_y$ , and the likely formation of foci of separation in the central region

The off-surface flow development is also consistent with the centrifugal forces created via surface curvature. Over the convex portion of the ramp, the centrifugal force acts to direct the centerline flow outward in a direction wall-normal from the surface. Its magnitude (per unit mass) is plotted in Figure 6.7.a and is calculated from the centerline wall-normal LDV profiles, which will be presented in the following chapter. Since the boundary layer is thin initially, where the radius of curvature is decreasing, the centrifugal force is significant over the majority of the wall-normal extent; however, the flow is also subjected to a FPG which acts to inhibit separation. A little farther downstream, the streamwise pressure gradient switches from favorable to adverse, around  $X = 0.14$  m. While the APG increases and begins to peak, indicating separation is approaching, the centrifugal force is decreasing and begins to change signs as the flow transitions from the convex to concave portions of the ramp. The central separation initiates just after the centrifugal force changes sign from being directed outwardly to inwardly, thereby reversing the direction of the induced secondary flow from being directed toward the centerline to being directed away from it and promoting the flow to separate via the counter-rotating vortical separation structures, F2 and F12.

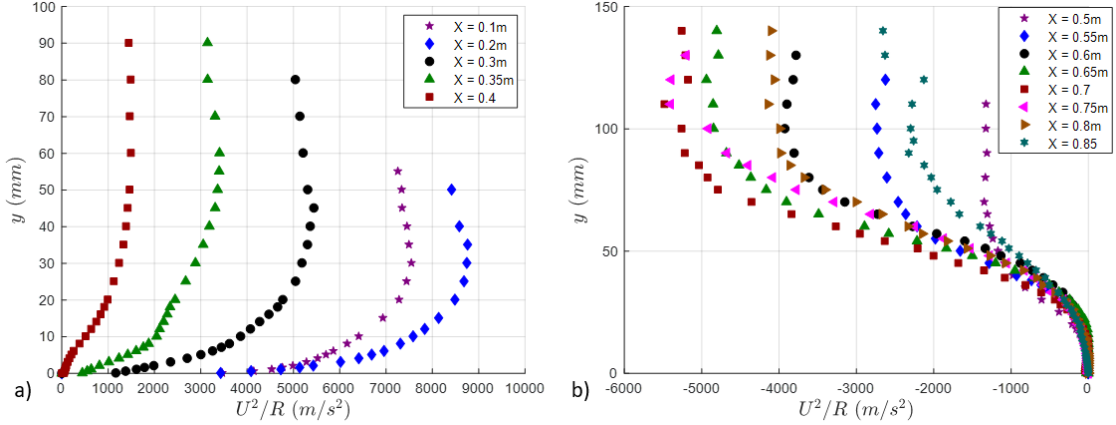


Figure 6.7 Centrifugal force per unit mass induced by streamwise surface curvature along the centerline of the ND Ramp over the convex (a) and concave (b) regions

Figure 6.7.b shows the centrifugal force over the concave region of the ramp where the centerline separation exists. Since the flow is separated in this region, the streamwise velocity magnitudes near the surface are very low and unaffected by the centrifugal force. Away from the surface, above the separation region, where the streamwise velocity magnitudes are larger, the centrifugal force still influences the flow. It acts to draw in freestream, high momentum fluid from above. Since the height of the separation region is lower in the central portion of the ramp and increases toward the sidewalls, the downward centrifugal force acts non-uniformly on the flow with a larger effect in the center and a smaller effect toward the sidewalls. The net result is two regions of streamwise vorticity of opposite signs. This shows excellent agreement with both the off-surface flow topology of foci F2 and F12, presented in the last chapter and repeated here in Figure 6.8.a, and the cross-sectional contours of streamwise mean velocity and vorticity of the DNS Stratford ramp simulations of Zhang and Fasel [54].

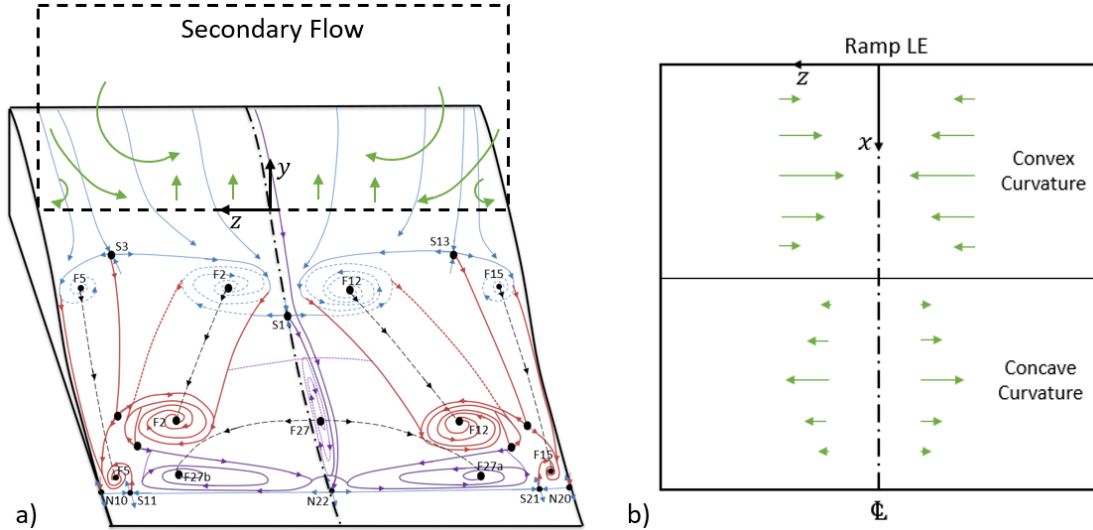


Figure 6.8 Cross-section view of the expected secondary flow generated due to the centrifugal force over the convex surface of the ramp imposed on the off-surface flow topology (a) and a top view of the expected near surface secondary flow generated due to centrifugal forces over the convex and concave regions of the ramp surface (b)

The expected secondary flow in Figure 6.2.a is imposed over the off-surface flow topology in Figure 6.8.a. There is excellent agreement between the topology presented in the last chapter and the induced secondary flow. In fact, saddle points S3 and S13 appear to be the result of the induced corner flows—a characteristic of the cross-section being rectangular instead of circular. Figure 6.8.b shows the expected near-surface flow induced via the centrifugal forces over the convex and concave regions of the ramp. Over the convex portion of the ramp the force is significant both above and near the surface, while over the concave portion of the ramp the force is only significant above the centerline separation region, F27.

This analysis explains why the central foci of separation tend to roll-up in the counter-rotating pattern that has been observed. While streamwise surface curvature has an important role in this formation, ultimately *both the roles of surface curvature and the sidewall/ramp juncture flow dictate how and when the separation patterns form*. In fact,

the role of surface curvature is likely second to that of the sidewall/ramp juncture flow. Evidence of this will be provided through a series of tests utilizing passive flow control, applied to the ramp juncture and sidewall, that are shown to modify the central separation structures. Throughout these experiments, the ramp surface curvature does not change and only minor changes occur to the centrifugal force via a changing boundary layer. Nevertheless, the alteration of the sidewall/ramp juncture flow is enough to either overcome or enhance the surface curvature effect. Either change will alter the separation flow topography and have dramatic effects on the centerline location of separation and reattachment.

## 6.2 Passive Flow Control Experiments

While the global flow separation pattern described in Chapter 4 was highly repeatable, provided the test conditions remained unchanged, it was only through repeated experiments that the idea that flow is very sensitive to physical perturbations first arose. For example, when slight modifications were made to the test section, i.e. a test section window was sealed more effectively, small discrepancies were sometimes observed in the surface flow patterns. This led to the further examination of the sensitivity effect via the application of passive flow control devices. Typically, studies utilizing flow control on similar geometries have focused on delaying separation or reducing its extent; however, in this case, passive flow control is employed purely as diagnostic tool to study the relationship between the sidewall or sidewall/ramp juncture flow and the central flow separation location and structures. Since flow control is not a focus of the current investigation, its discussion will be kept to a minimum.

Two methods of passive flow control tests will be briefly presented and discussed. The first method seeks to explicitly control the sidewall/ramp juncture separation structures and highlights how individual vortical structures (foci) can be greatly enhanced or attenuated by diverting higher momentum fluid into or away from them. It also demonstrates that enhancing the sidewall/ramp juncture flow induces the centerline flow to separate farther upstream. The second method aims to control only the sidewall boundary layers in order to study their interaction with both the secondary flow induced via centrifugal forces and the central flow separation along the ramp. While the presence of vortical separation structures observed on the ramp is not a result of a particularly undesirable sidewall flow condition, their form (topographical and even topological) is, in effect, modulated by the sidewall flow. In other words, adversely or favorably altering the sidewall flow condition does not change the fundamental separation topological structure of a repeating pattern of saddle/foci pairs (the generalized OFP), but it does change how many saddle/foci pairs form, and their respective signs of rotation, spatial extents, and locations relative to one another.

### 6.2.1 Ramp Application

A series of single tab-style vortex generators (VGs) was first applied just upstream of the sidewall separation at both corners of the ramp. This setup stemmed from the work of Meyer et al. [104] who applied this type of VG to both an airfoil and a compressor cascade. The authors state that the single vortex generator functions under two mechanisms: (1) creating a nozzle like flow directed into the corner and (2) introducing longitudinal vorticity that acts to entrain freestream momentum into the separating region.

The device is a simple tab made from thin sheet metal and secured to the ramp surface via double-sided adhesive. The study by Meyer et al. [104] used a VG height scaled on the airfoil chord, which was not applicable here. Their case is distinctly different from that of the ramp/sidewall junction because the ramp trailing edge smoothly transitions to a flat plate. Furthermore, the ramp also has a much thicker incoming boundary layer. Because of these differing conditions, a range of three different single tab VG sizes was employed on the ramp, starting from a height of 16 mm and reducing down to a height of about 1.2 mm (see Figure 6.9). All tab heights were fully contained within the local boundary layer, which was 25-30 mm thick.

Figure 6.9 shows the tab VGs as well as a schematic of their placement with respect to the ramp leading edge and wind tunnel sidewall. Note that while only one side is shown below, VGs were installed in pairs with one on each side of the ramp. Table 6.1 gives the parameters for the three sizes of tab VGs and the adhesive strip, which was also solely tested, as well as their respective locations relative to the sidewall and ramp leading edge.

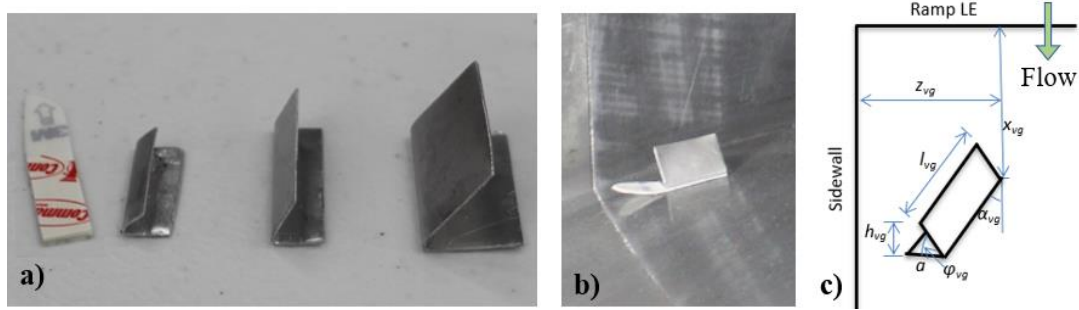


Figure 6.9 Tab-style vortex generators (VGs) used on the ramp surface, highlighting the Large, Medium, and Small VGs that were tested as well as the adhesive strip (a), the Large VG installed on the ramp (b), and a schematic of the VG placement with respect to the sidewall and ramp leading edge (c)

TABLE 6.1  
TAB-STYLE VORTEX GENERATOR PARAMETERS

<b>Tab VG</b>	<b>φ<sub>vg</sub> [°]</b>	<b>α<sub>vg</sub> [°]</b>	<b>a [mm]</b>	<b>l<sub>vg</sub> [mm]</b>	<b>h<sub>vg</sub> [mm]</b>	<b>z<sub>vg</sub> [mm]</b>	<b>x<sub>vg</sub> [mm]</b>
Large	55	14	15.2	25.4	16	50	177.8
Medium	55	14	8	25.4	10	50	177.8
Small	55	14	8	20	6	50	177.8
Adhesive	N/A	14	8	20	1.2	50	177.8

The large vortex generator has a profound effect on the overall flow field, see Figure 6.10. On the far side of the flow field, Figure 6.10.b1, the topology does not appear to have changed; instead, F5 occurs further down the ramp and increased in spatial extent, whereas and the central vortical structure, F2, has reduced its spatial extent. However, the flow is now clearly asymmetrical. On the near side, Figure 6.10.b2, the central vortical structure, F12, has merged with S13, causing the central separation region, S1, to move upstream thereby producing earlier centerline separation. One possible explanation for the asymmetry of the controlled flow is that it is the amplification of a slight asymmetry in the

baseline flow. For example, the tab VG on the far side (tunnel inner loop) is placed between the flow leading into S3 and the sidewall, see orange dashed line in Figure 6.10.a1, so the tab enhances the flow being directed from S3 into F5. On the near side (tunnel outer loop) the flow leading into S13 is between the tab and the sidewall, see orange dashed line in Figure 6.10.a2, so that the tab opposes the flow being directed from S13 to F12 and instead directs the flow to F15. Essentially, the tab VGs end up on opposite sides of the dividing streamlines heading into S3 and S13. It is also worth noting that these changes in the separation topology occur without significant changes in sidewall separation.

The off-surface extent of this earlier separation was later tested, this time employing LDV to acquire a single profile in the central separation region, both with and without the large tab VGs applied. The results, as shown in Figure 6.11, highlight the dramatic loss of momentum in the central region of the ramp when the tabs are installed. This loss of momentum, while largest in the near wall region, extends through the entire boundary layer, indicating a significant change to the flow field. This global change in the central region in response to such a small device located near the wall is quite remarkable and emphasizes the sensitivity of the entire flow separation to the sidewall/ramp juncture condition.

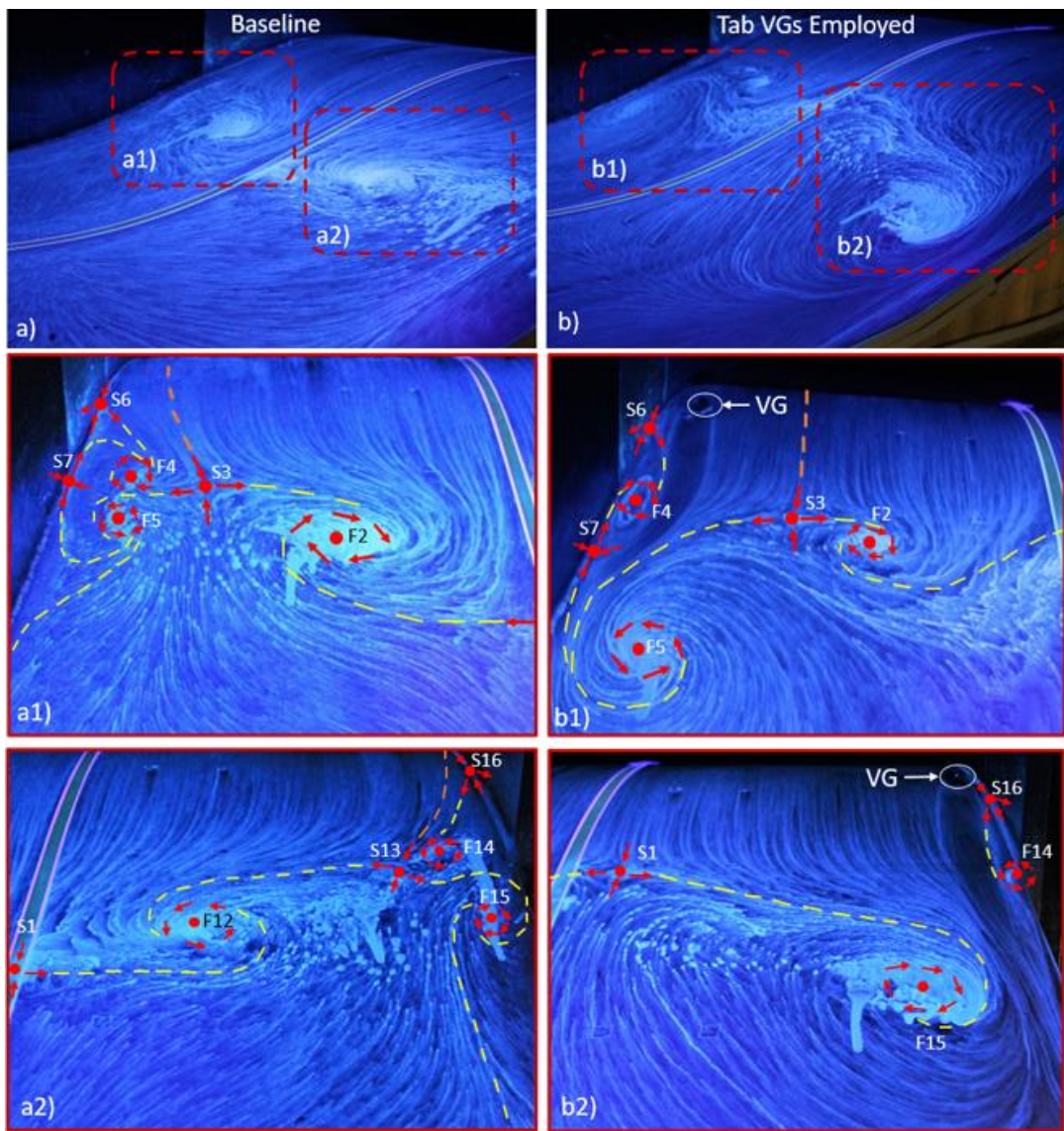


Figure 6.10 Surface flow visualization showing the ability to manipulate the flow structures using the large single tab-style vortex generators (b) compared to the baseline flow (a)

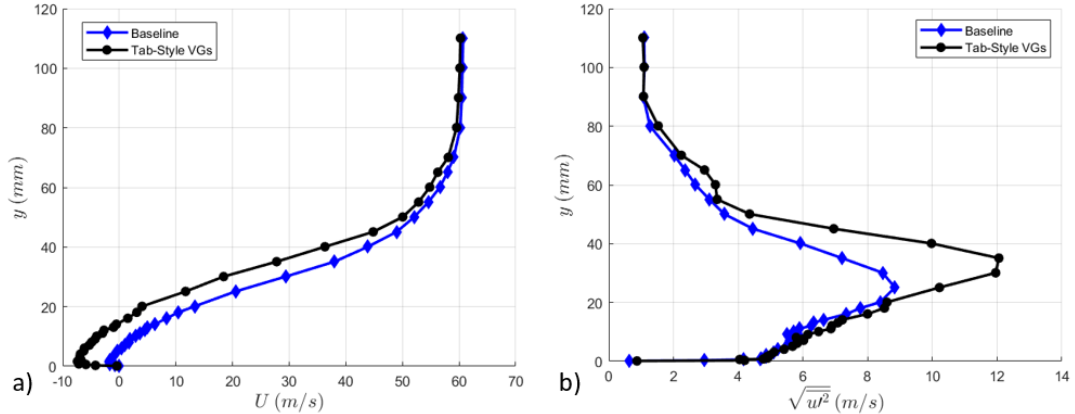


Figure 6.11 Boundary layer profile (a) and turbulent shear stress (b) comparison of large tab-style VGs to the baseline flow for a wall-normal profile located at  $X = 0.5$  m and  $Z = -0.1$  m

That the tabs produce flow that separates earlier should perhaps be expected. The tabs serve to divert freestream momentum into the near wall region, essentially extracting energy from the inner flow structures and transferring it to the near wall region. Reducing the tab height should reduce this energy transfer effect. Figure 6.12 shows the baseline and surface flow visualization corresponding to the three smaller tab heights listed in Table 6.1, with special emphasis placed on the centerline separation and reattachment locations. Surprisingly, even the small VGs, those which protrude only 25% of the boundary layer thickness, have a significant effect on the flow. Only the sole application of the adhesive strips maintains the baseline separation topology. In fact, the small perturbation of the strips slightly improves the symmetry of saddle points S3 and S13. All of this goes to show that the separation structures can be quite easily manipulated via the application of passive control devices.

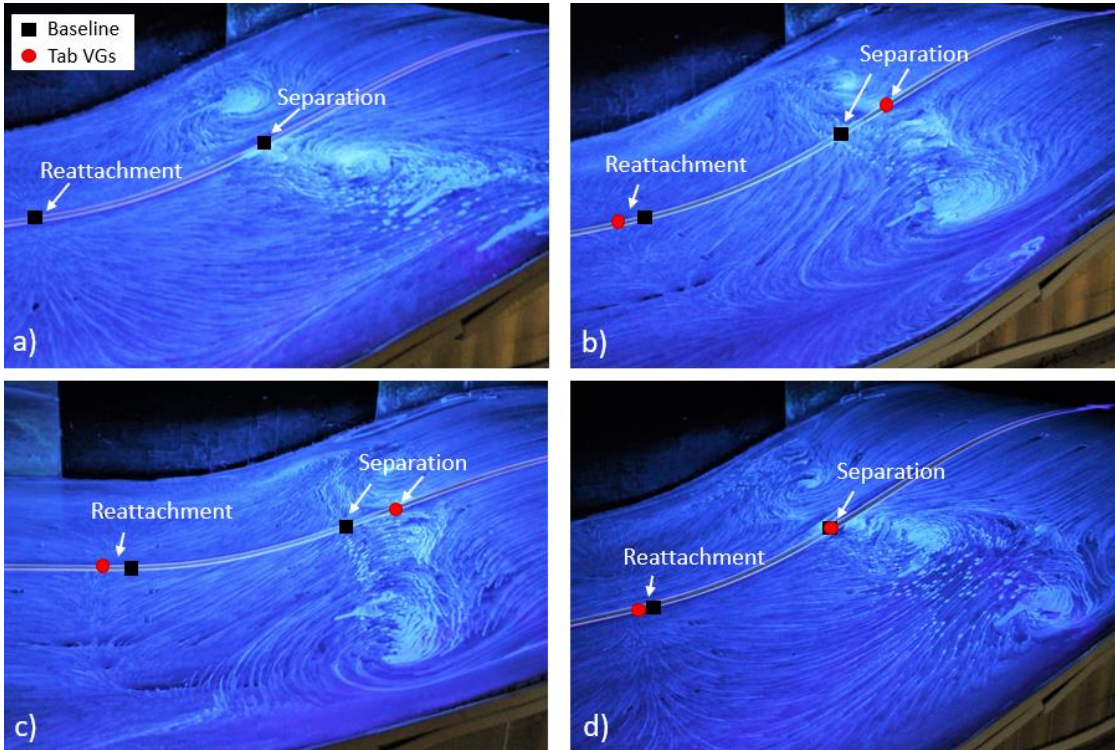


Figure 6.12 Surface flow visualization comparison for the baseline (a) medium (b), small (c), and adhesive strip (d) tab-style VGs placed near the sidewall/ramp juncture on each side of the ramp with the centerline separation and reattachment locations noted in red circles and baseline separation and reattachment locations noted in black squares

On the other hand, the reattachment structure and location are not very sensitive to the separation structure. While the direction of the flow moving along the reattachment line changes with the changing flow separation structure, the location and uniformity of the line is not significantly affected. What this first study hints at, and what will continue to be shown, is that while the separation structures can be manipulated via enhancing one and attenuating another, the common topological pattern remains. Like links in a chain, the singular points in the repeating pattern of saddle points and foci can be twisted about, change the sign of rotation, and even merge with one another, but the separation chain is still there.

### 6.2.2 Sidewall Application

The second method of passive flow control that was explored applied co-rotating VGs to both wind tunnel sidewalls just upstream of the ramp leading edge. These produced co-rotating streamwise vorticity. Co-rotating VGs are more robust in their placement and use because they can be somewhat insensitive to blade size, orientation, spacing and lateral flow, and because of their streamwise persistence [105,106]. These will be the focus of this work; however, small counter-rotating VGs as well as v-shaped boundary layer trips were also employed, and the results will be briefly given for comparative purposes. Figure 6.13 highlights the four different flow control devices installed on the wind tunnel inner loop sidewall, and Table 6.2 gives the respective geometric configuration parameters. Here  $X_{LE}$  is the distance upstream from the ramp leading edge to the start of the flow control device,  $h$  is the device height,  $l$  is the device length,  $\beta$  is the alignment angle with respect to the freestream, and  $\Delta$  is the distance between adjacent devices.

TABLE 6.2  
SIDEWALL FLOW CONTROL DEVICE PARAMETERS

<b>Configuration</b>	<b><math>X_{LE}</math> [mm]</b>	<b><math>h</math> [mm]</b>	<b><math>l</math> [mm]</b>	<b><math>\beta</math> [°]</b>	<b><math>\Delta</math> [mm]</b>
Angled Up	152	22.2	44.3	18	88.6
Angled Down	152	22.2	44.3	18	88.6
V-Shaped	102	22	10.8	26.6	24.5
Delta	90	13.1	78.8	14	47

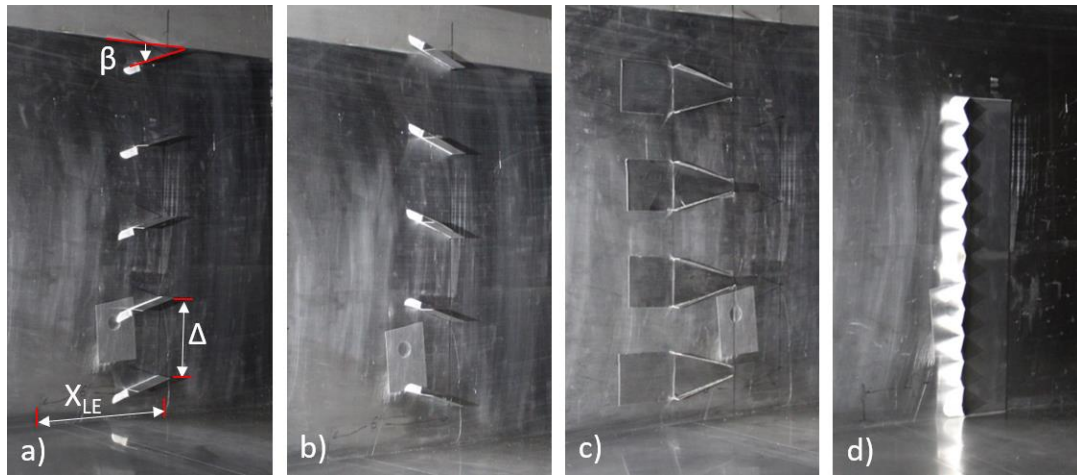


Figure 6.13 Sidewall flow control devices including: co-rotating VGs angled down (a), co-rotating VGs angled up (b), counter-rotating delta VGs (c), and v-shaped boundary layer trip (d), all applied upstream of the ramp leading edge

There were two different arrangements for the co-rotating VGs; angled upward and away from the ramp or angled downward towards the ramp. Changing the VG angle equates to changing both the sign of the freestream vorticity generated and the path the vortices follow. This is illustrated in Figure 6.14. Angling the VGs upward will generate counterclockwise vortices, when viewed looking downstream, and these, with their mirrored image, will induce the vortices to travel up and toward(s) the wall. On the other hand, angling the VGs downward will generate clockwise vortices, which, with their mirrored image will induce the vortices to travel down and away from the wall and onto the ramp surface. Essentially, these two modes of applying the sidewall VGs act to either direct the sidewall boundary layer flow down onto the ramp (downward angled VGs shown in Figure 6.14.b) or up and away from the ramp (upward angled VGs shown in Figure 6.14.a). It is also important to point out that this induced sidewall flow should either act to enhance (downward angled VGs) or suppress (upward angled VGs) the secondary flow generated via surface curvature.

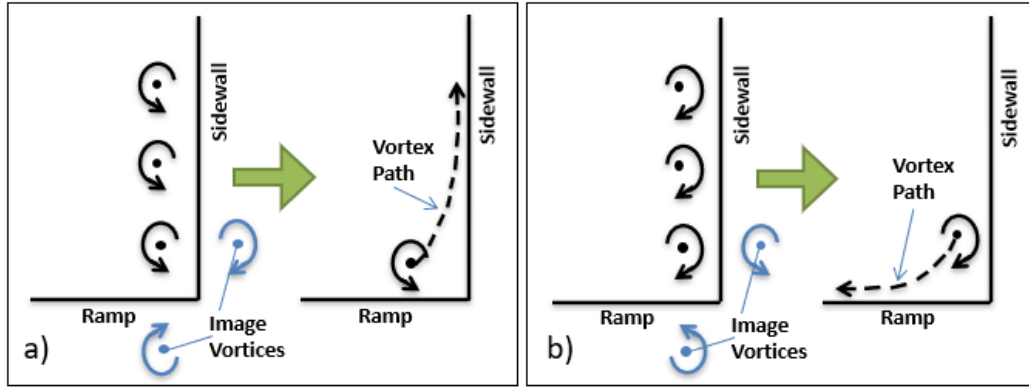


Figure 6.14 Illustration of the vortex path induced by the vortex image for co-rotating vortex generators angled up (a), and angled down (b) with both views oriented looking downstream

Figure 6.15 shows the surface flow pattern for the downward angled VGs. At first sight, the flow pattern looks remarkably different from the baseline. The separation structure appears to have taken on a dual-sided, elongated “g” shape, with the central and sidewall vortical structures appearing in one combined grouping on either side of the tunnel centerline. However, upon closer inspection, the separation topology is not that different from the baseline case—although the singular points are tightly woven together. The downward angled VGs have essentially forced the sidewall flow onto the ramp surface, thereby reducing any sidewall separation to that stemming from the VGs themselves. Additionally, the VGs enhance the secondary flow induced by the centrifugal forces over the convex portion of the ramp. Comparison of the controlled flow in Figure 6.15 with the secondary flow, Figure 6.8.a, shows good agreement even though the topological connection between flow features has changed.

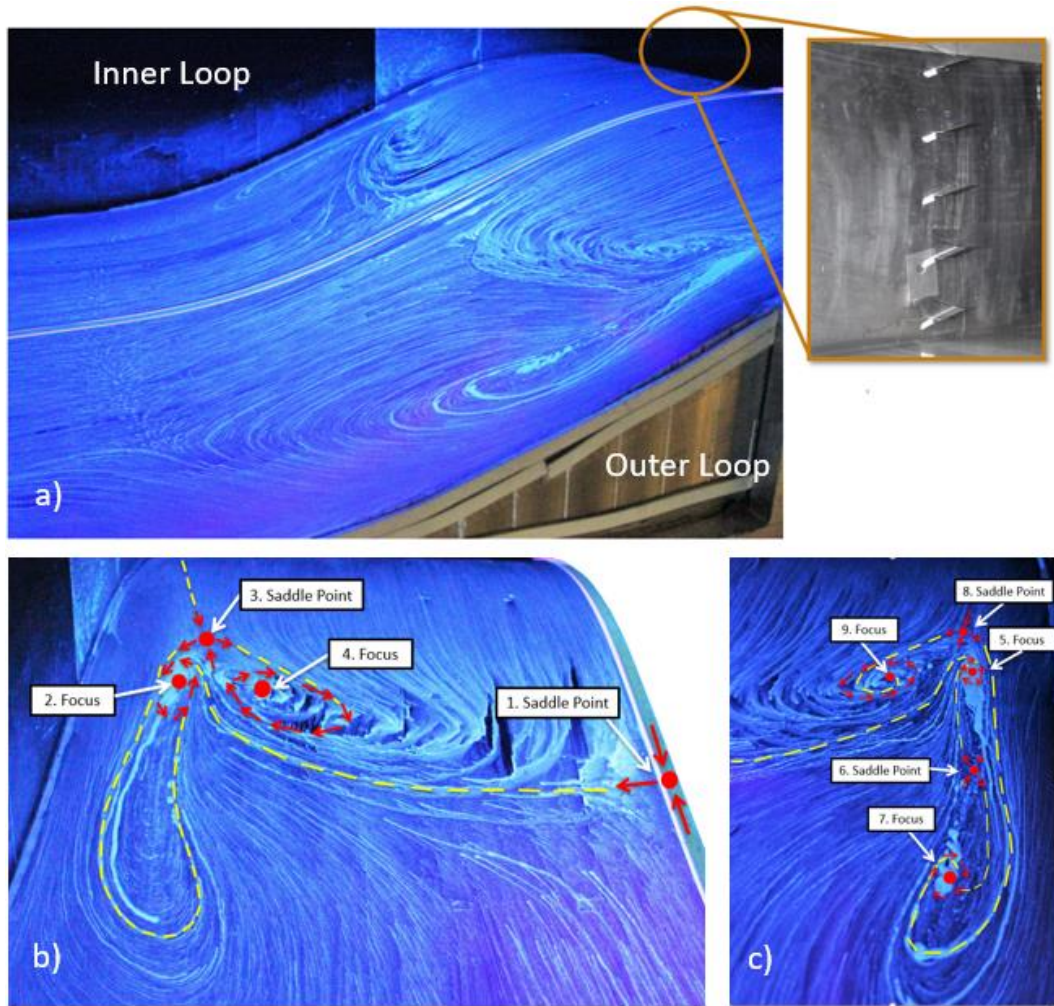


Figure 6.15 Surface flow pattern for sidewall flow VGs angled down, including overview (a) close up views highlighting the singular points on the inner loop (b) and outer loop (c) sides. Note the extra pair of singular points, S6 and F7, present on the outer loop side (c), but not on the inner loop side (b).

Figure 6.15.b and Figure 6.15.c provide close-up views of the surface flow highlighting the singular points. Here the flow topology appears to be asymmetric with the equivalent of S6 and F7, shown on the wind tunnel outer loop side Figure 6.15.c, missing from the wind tunnel inner loop side, Figure 6.15.b. This difference prompted further investigation via repeated wind tunnel tests with select tests utilizing the multiple dye oil-film surface flow visualization discussed in Chapter 4. The repeated tests, shown in

Appendix E.1, indicate that the asymmetry of the topology pattern shown in Figure 6.15 often remains but may switch sides or become symmetric with the elimination of S6 and F7 on the outer loop side. Even when variations in the topology are present, from a global perspective, the surface flow pattern does not change significantly between cases. These changes were often small and usually only noticeable by close inspection.

Before examining this surface topology further, attention will be given to the complementary case with the co-rotating VGs angled up. While tilting the sidewall VGs downward acted to contract the flow field onto the ramp, enhancing the induced secondary flow, tilting the sidewall VGs upward had the opposite effect, pulling the central flow toward the sidewalls, thereby opposing the induced secondary flow. Figure 6.16 shows the surface flow pattern for the upward angled VGs. It is apparent from the images that the primary vortical structures are now the sidewall separation structures themselves. When the sidewall flow is directed upward, the momentum-starved sidewall/ramp juncture is likely prone to have an increased spatial separation footprint (the extent of the flow spiraling into the foci is increased), which in turn, absorbs the streamwise vorticity in the flow and mitigates the need for additional foci to form in the central region of the ramp. However, the absorption is still not fully realized as an extra pair of singular points, F5 and S6, appear in the central region of the ramp on the wind tunnel outer loop side, see Figure 6.16.c. Interestingly, this asymmetric pair of flow features was only present occasionally. Nonetheless, it is included here (1) to draw attention to the role of surface curvature as it promotes the flow to develop foci of separation in the central region of the ramp, and (2) to highlight the topological variations (which are not always symmetric) in the stable flow states that do exist.

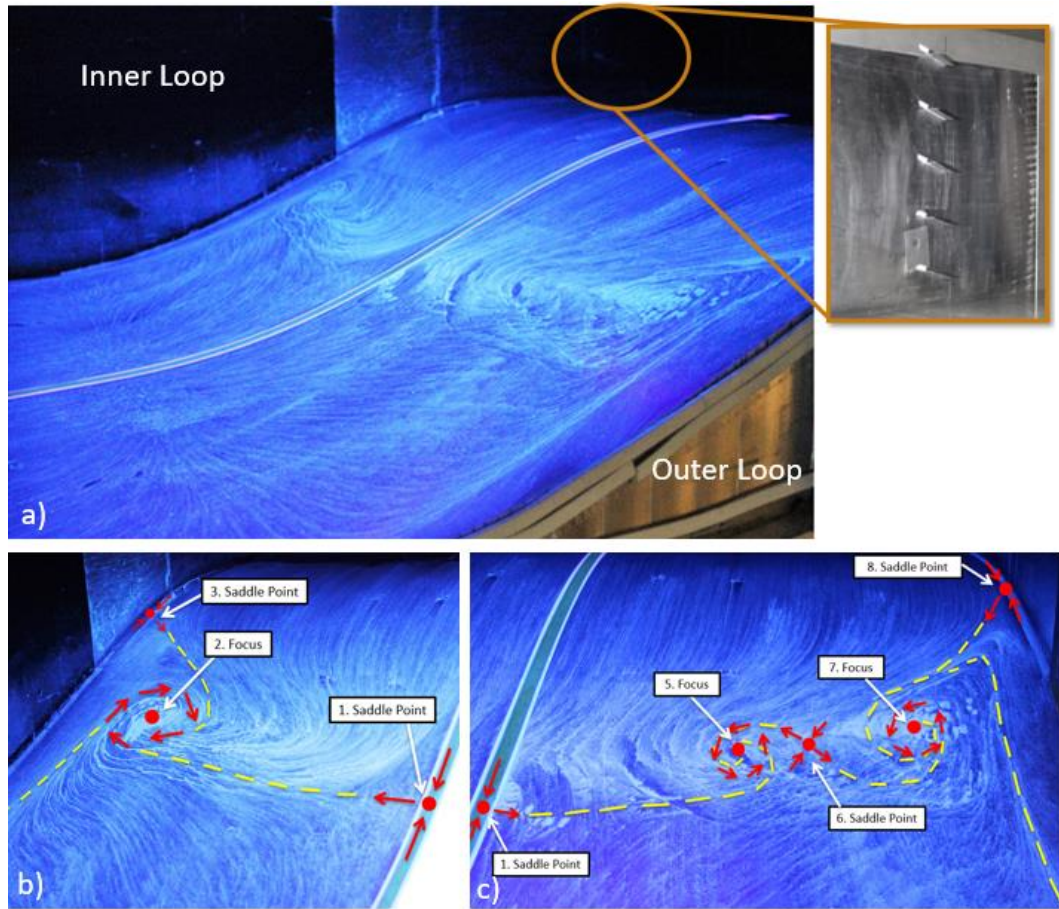


Figure 6.16 Surface flow pattern for sidewall flow VGs angled up including overview (a) and close up views highlighting the singular points on the inner loop (b) and outer loop (c) sides. Note the extra pair of singular points, F5 and S6, present on the outer loop side (c) but not on the inner loop side (b).

A case in which the central foci do not appear in the flow is shown in Figure 6.17. This run, conducted using the multiple dye method, highlights just how uniform the flow can become in the central region. The overall symmetry is very good and shows nearly the limit of uniformity that can be achieved without using boundary layer suction. Even when the effects of the secondary flow have been minimized, one can still see the initial formation of two new separation structures, saddle/foci pairs, highlighted in the figure. While not yet fully formed in a time mean sense, it is apparent that the flow “wants” to

take on the additional vortical separation structures that are now absent in the central region of the ramp. The evidence suggests that if the near sidewall structures were further reduced, these new central structures would grow.

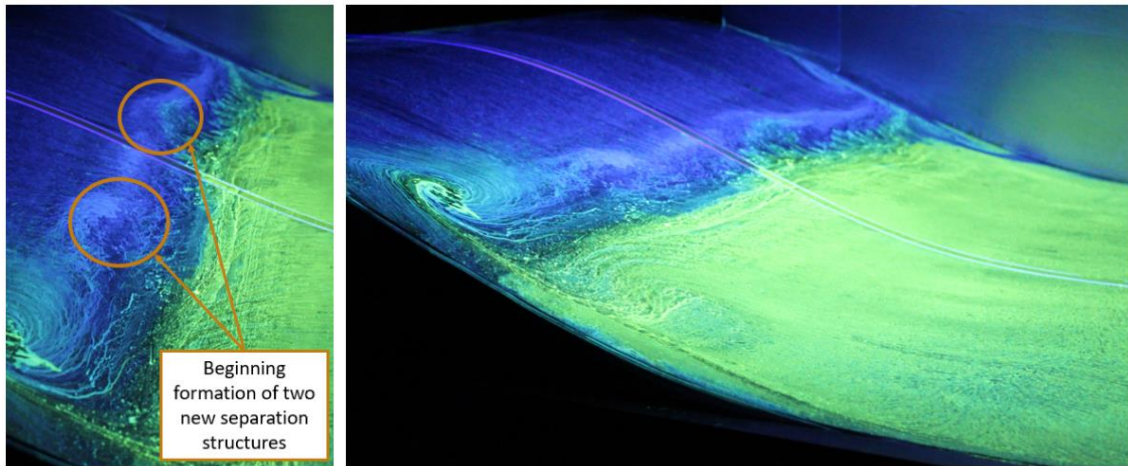


Figure 6.17 Images of the surface flow pattern using the multiple dye method with upward angled VGs installed on the sidewalls, highlighting that while there is increased uniformity of the flow in the separation region, two new separation structures are beginning to form

Figure 6.18 shows the surface flow topology resulting from the sidewall application of both downward and upward facing VGs. Here the flow topologies are drawn in the asymmetric forms first observed. In comparison to the baseline case, repeated in Figure 6.18.c, some of the signs of rotation of the foci have changed, and the symmetry and number of pairs may vary; however, the basic repeating pattern of saddle points and foci remains—providing additional support for the identification of the generalized owl-face pattern presented in the last chapter. The simplicity of this pattern is quite beautiful. Whether the flow is forced onto the ramp by the downward angled VGs or stretched towards the sidewalls by upward facing VGs, the simple core topological structure remains. Moreover, the topological structures observed in Figure 6.18, except for the additional

asymmetric saddle/foci pair, are remarkably similar to those presented in Figure 5.17, the simplest realizable cases.

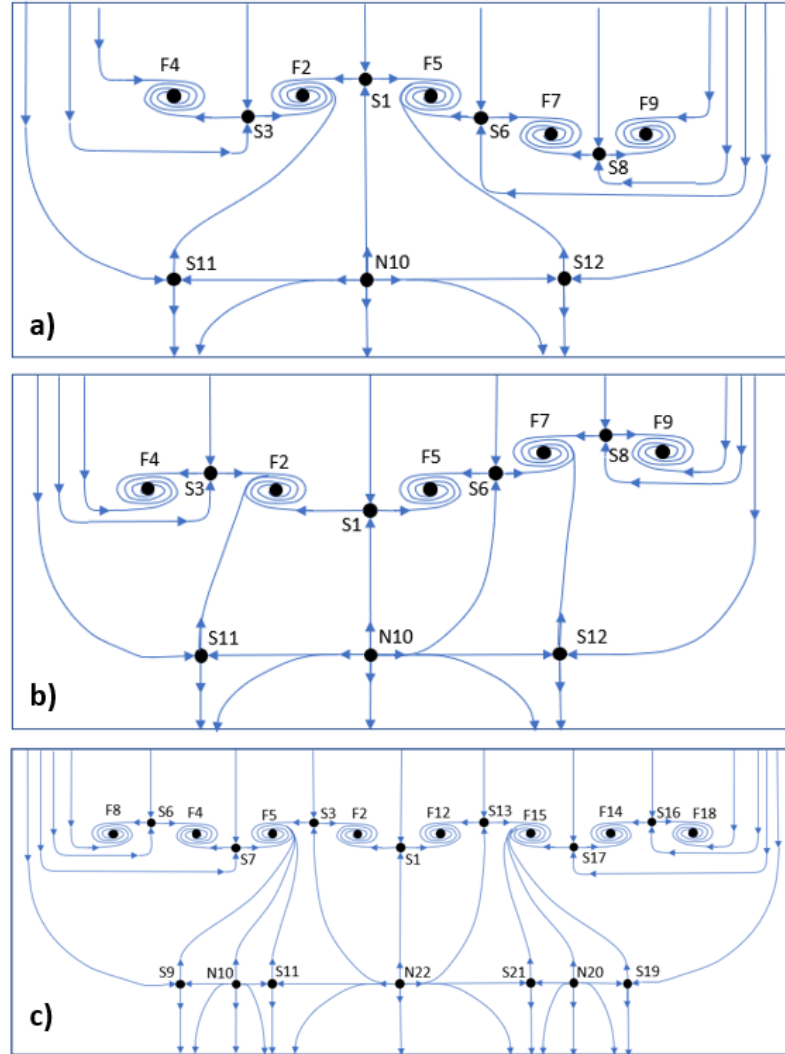


Figure 6.18 Sketches of the surface flow topology resulting from the sidewall application of downward (a) and upward (b) facing VGs and of the baseline flow (c)

While co-rotating VGs can cause the sidewall flow to interact with the induced secondary flow, altering the separation structure and location, similar results can be achieved using other flow control methods. Of the methods examined, arguably, the counter-rotating Delta VGs were the best at reducing the sidewall/ramp juncture separation. On the other hand, the v-shaped boundary layer trip caused massive separation at the sidewall/ramp juncture (as would be expected). Figure 6.19 gives the surface flow visualization images for these two tests. The focus of these images is to highlight the centerline separation extent and compare it to the baseline flow, not discuss the details of the flow topology.

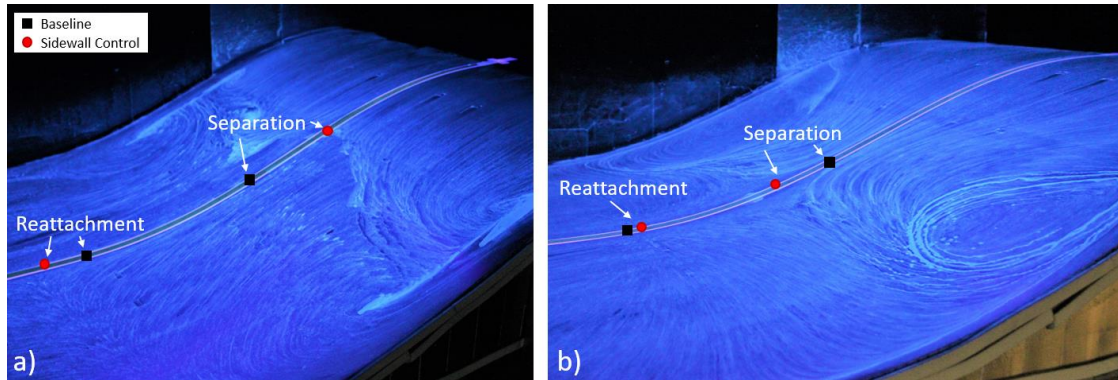


Figure 6.19 Surface flow visualization for the application of counter-rotating delta VGs (a) and v-shaped boundary layer trip (b) highlighting the extreme difference in centerline separation extent

Ironically, by reducing the extent of the sidewall separation, Figure 6.19.a, the extent of the centerline flow separation is significantly increased. In contrast, the induction of massive separation in the sidewall boundary layers dramatically decreases the extent of centerline flow separation, see Figure 6.19.b. As in the case of the large tab VGs installed near the sidewall/ramp juncture, if freestream energy is transferred to the sidewall flow,

the centerline flow has a harder time staying attached. Likewise, causing the sidewall flow to massively separate forces the flow toward the ramp centerline, in turn delaying its separation. This inverse relationship between the sidewall separation and the centerline separation has important implications for typical flow control studies which seek to delay flow separation as well as for CFD validation studies.

### 6.2.3 Summary

Table 6.3 shows the centerline separation and reattachment locations for the baseline and all the passive flow control tests discussed in this chapter. The measurements are based on the surface flow visualization, which, when compared to the LDV measurements presented in the next chapter, are slightly biased towards the prediction of later separation and reattachment. Thus, while somewhat qualitative, the data are useful for comparison between cases. For the baseline flow, the centerline separation extent (the separation location subtracted from the reattachment location) is 0.31 m. For both the large tab VGs and the counter-rotating delta VGs, the centerline separation occurs earlier, around  $X = 0.42$  m, and the reattachment occurs later, around 0.93m and 0.94 m, yielding a separation extent of 0.51 m and 0.52 m for the large tab VGs and the counter-rotating delta VGs, respectively. This is a 68% increase in separation extent as compared to the baseline. On the other hand, the v-shaped boundary layer trip delays centerline separation to  $X = 0.64$  m and produces early reattachment at  $X = 0.86$  m, yielding a separation extent of only 0.22 m, a 30% reduction in separation extent as compared to the baseline. It is thus demonstrated that *the flow over the ramp geometry cannot be treated as a separate entity from the wind tunnel sidewall flow; they are highly coupled because the pressure gradient, surface curvature and crossflow determine the separation topography.*

TABLE 6.3  
CENTERLINE SEPARATION EXTENT

Test Name	VG Location	Separation [m]	Reattachment [m]	Extent [m]
Baseline	N/A	0.58	0.89	0.31
Large	Ramp	0.42	0.93	0.51
Medium	Ramp	0.50	0.92	0.42
Small	Ramp	0.50	0.93	0.43
Adhesive	Ramp	0.58	0.90	0.32
Angled Up	Sidewall	0.58	0.89	0.31
Angled Down	Sidewall	0.53	0.93	0.40
V-Shaped	Sidewall	0.64	0.86	0.22
Delta	Sidewall	0.42	0.94	0.52

One must also note the effect of flow control on reattachment structure and location. In all the cases using passive flow control, while the separation topography changed significantly from the baseline, the reattachment did not. From Table 6.3 we see that for the extreme cases, the variation in centerline separation location is 24% of the ramp length, while the variation in centerline reattachment location is only 9% of the ramp length. *The reattachment location and its spanwise uniformity are not highly dependent on the separation location and form.*

### 6.3 Preliminary CFD Comparison

Finally, many of the experimental results just shown are also observed in preliminary CFD simulations. The computational runs were conducted courtesy of Chris Rumsey at NASA Langley Research Center and utilize the SA-RC-QRC model in FUN3D. Figure 6.20.a shows surface skin friction lines and pressure coefficients for a flat top,  $0^\circ$ , ceiling configuration, which is slightly higher than that which was used for Case A ( $\alpha = 3.2^\circ$ ). The preliminary CFD looks very similar to the v-shaped boundary layer tripped flow

control case, Figure 6.19.b. Both show (1) the sidewall/ramp juncture separation forming much farther upstream and covering a much larger spatial extent than was depicted in the baseline surface flow visualization and (2) small regions of centerline separation. The simulation results are only preliminary and may not be grid-converged; also the ceiling geometry is slightly different and they did not include the measured inflow boundary layer conditions recorded on the ramp and sidewall. Given these caveats, it is impossible to draw any conclusions, but it is likely that the sidewall/ramp juncture separation is sensitive to the turbulence model, grid, and inflow conditions. Future CFD efforts could explore these effects in more detail.

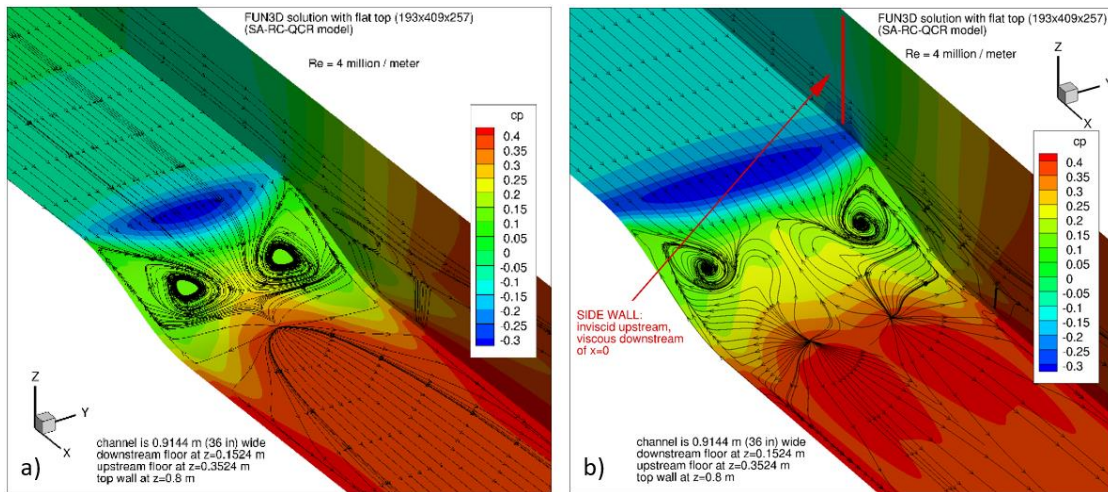


Figure 6.20 Preliminary CFD conducted in FUN3D with the SA-RC-QRC model for a baseline flat ceiling configuration (a) and for this formation with an inviscid condition upstream and viscous condition starting at the ramp leading edge (b). Figures courtesy of Chris Rumsey.

The simulation was repeated, this time employing an inviscid sidewall condition upstream of the ramp leading edge. The idea was that by “turning on” the viscous condition at the start of the ramp, the application of sidewall splitter plates could be crudely and quickly simulated. This also drastically reduces the sidewall boundary layer thickness prior to the sidewall/junction flow separation. While the simulation is crude, it shows that the centerline separation and reattachment locations move upstream and downstream, respectively. While the topology of the surface flow is not the same, nor should it be expected to be the same, a comparison can be drawn to the counter-rotating delta VG experiments shown in Figure 6.19.a. Both reduce the sidewall separation, which in turn causes the centerline flow to separate further upstream and reattach further downstream, giving rise to a large increase in the centerline separation extent. These preliminary simulations leave us to concluded that *accurately simulating this flow requires that the sidewall/ramp juncture boundary layer separation be accurately captured, as it appears to significantly influence the central ramp flow.*

## CHAPTER 7: FLOW FIELD DEVELOPMENT

This chapter presents the quantitative off-surface flow measurements for Cases A, B, and C, which were acquired via LDV and constitute the bulk of the experimental data set collected. In light of the three-dimensional surface flow, boundary layer profiles were acquired at 19 streamwise locations and 3 spanwise locations. These profiles include both streamwise and wall-normal mean velocity and turbulent normal and shear stresses. The complete data set is provided on the NASA Langley Research Center Turbulence Modeling Resource webpage [1].

First, using the near-wall portion of this experimental data, the flow separation and reattachment are documented and analyzed, both in the mean and unsteady forms common to turbulent boundary layer separation. Next, a comparison is made between the various states of the separation process and the pressure and pressure gradient distributions. Finally, these comparisons are shown to exhibit very good correlation both with the experimental data of the ND Ramp cases and other similar flow separation studies, indicating the utility of high-resolution streamwise pressure data to predict flow separation.

### 7.1 Overview of Flow Field Measurements

The following off-surface flow field measurements were acquired via LDV and emphasize the streamwise development of the mean flow and turbulent stresses. However,

due to the three-dimensionality of the surface flow patterns, multiple off-center profiles were utilized to capture the degree of spanwise variation in the flow. Three different spanwise measurements locations are presented; one on the centerline,  $Z = 0$  m, and two off-center locations,  $Z = -0.13$  m and  $Z = -0.26$  m, which can equivalently be written as  $Z/S = 0$ ,  $Z/S = -0.14$ , and  $Z/S = -0.28$ , respectively, where the span,  $S$ , is 0.914 m (3 ft). These profile locations, and their relation to the surface flow of Case A, are shown depicted as red dashed lines in Figure 7.1. Note that the off-center locations are selected such that they capture the spanwise variation in the flow produced by the primary vortical structures, yet still remain in the central region, thereby avoiding the sidewall separation structures.

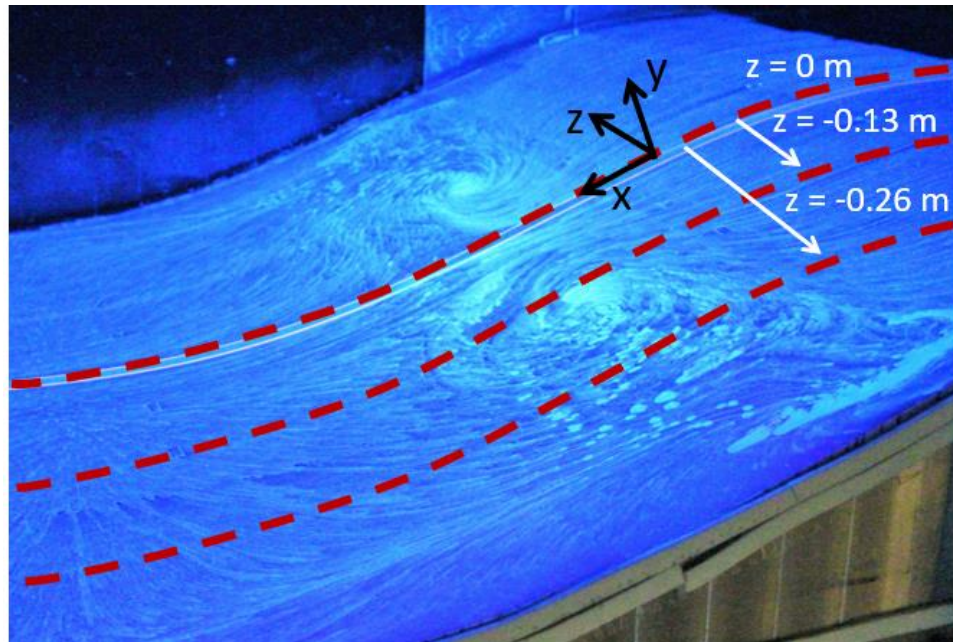


Figure 7.1 Sketch providing the local coordinate system and three spanwise locations of the LDV measurements overlaid on the surface flow visualization of Case A

Wall-normal boundary layer profiles acquired via 2-component LDV, capture the streamwise development of the flow. Local wall-normal profiles were selected instead of tunnel-normal coordinates to better capture the physics of the developing flow. However, for ease of utilization and comparison with standard CFD codes, all of the wall-normal profiles are also provided in the global coordinate system (see section 2.3 for details on the coordinate systems). This was achieved via tensor rotation of the mean and turbulent stresses, the details of which are provided in Appendix D.5. The acquired wall-normal profiles begin on the boundary layer development plate 0.56 meters upstream of the ramp,<sup>12</sup> with one other streamwise location,  $X = -0.28$  m, selected before the start of the ramp. Along the ramp, profiles were acquired every 10 cm until  $X = 0.3$  m, at which point the increment decreased to every 5 cm through the last location documented,  $X = 0.95$  m. Note that the location of each profile is designated by its surface starting position in the tunnel X-coordinate, with  $X = 0$  m and  $X = 0.9$  m corresponding to the start and end of the ramp respectively. To provide a sense of scale, Figure 7.2 both highlights the location of the streamwise LDV profiles, and provides the spanwise-averaged extent of the boundary layer and separation region for all three test cases.

---

<sup>12</sup> This location was initially selected to document the incoming flow; however, as discussed in Chapter 3, the initial condition location was moved further upstream due to geometric constraints.

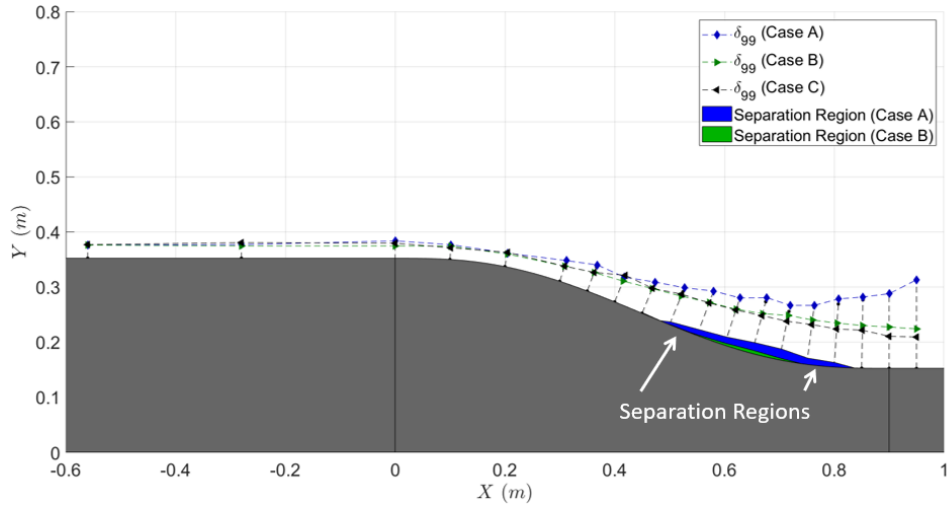


Figure 7.2 Spanwise average boundary layer growth and separation regions for all three test cases highlighting the 19 streamwise locations of the wall-normal LDV profiles, the local coordinates, the ramp geometry, and the global coordinates

## 7.2 Mean Flow Development

### 7.2.1 Case A – Larger-Scale Separation

The streamwise evolution of the mean flow is shown in Figure 7.3 below. All three spanwise locations are included in the figure. The center profiles are marked with blue diamonds, the mid-span profiles black circles, and the near-sidewall profiles green triangles. Initially, over the boundary layer development plate, the profiles exhibit the shape factor characteristics of zero pressure gradient turbulent boundary layers,  $H \approx 1.3 - 1.4$ , and are uniform in spanwise extent. The first noticeable spanwise deviation in the profiles occurs at around  $X = 0.1$  m with the center profile showing signs of acceleration, caused by the FPG, greater than that of the off-center profiles. Between  $X = 0.2$  m and  $X = 0.3$  m, the pressure gradient becomes adverse and the signs of spanwise deviation in the flow become apparent. From this point onward, the outer (off-center) profiles have a

progressively larger velocity deficit, in both streamwise and spanwise extent, compared to the centerline profile. Around  $X \approx 0.45$  m, the outer profile separates, in the mean sense, followed by the middle profile and the center profile by  $X \approx 0.55$  m. This confirms what was shown in the surface flow visualization: the separation region is rather three-dimensional. Additionally, the extent of the flow three-dimensionality is not localized to the surface either. Rather, the largest discrepancy is observed in the middle of the boundary layer.

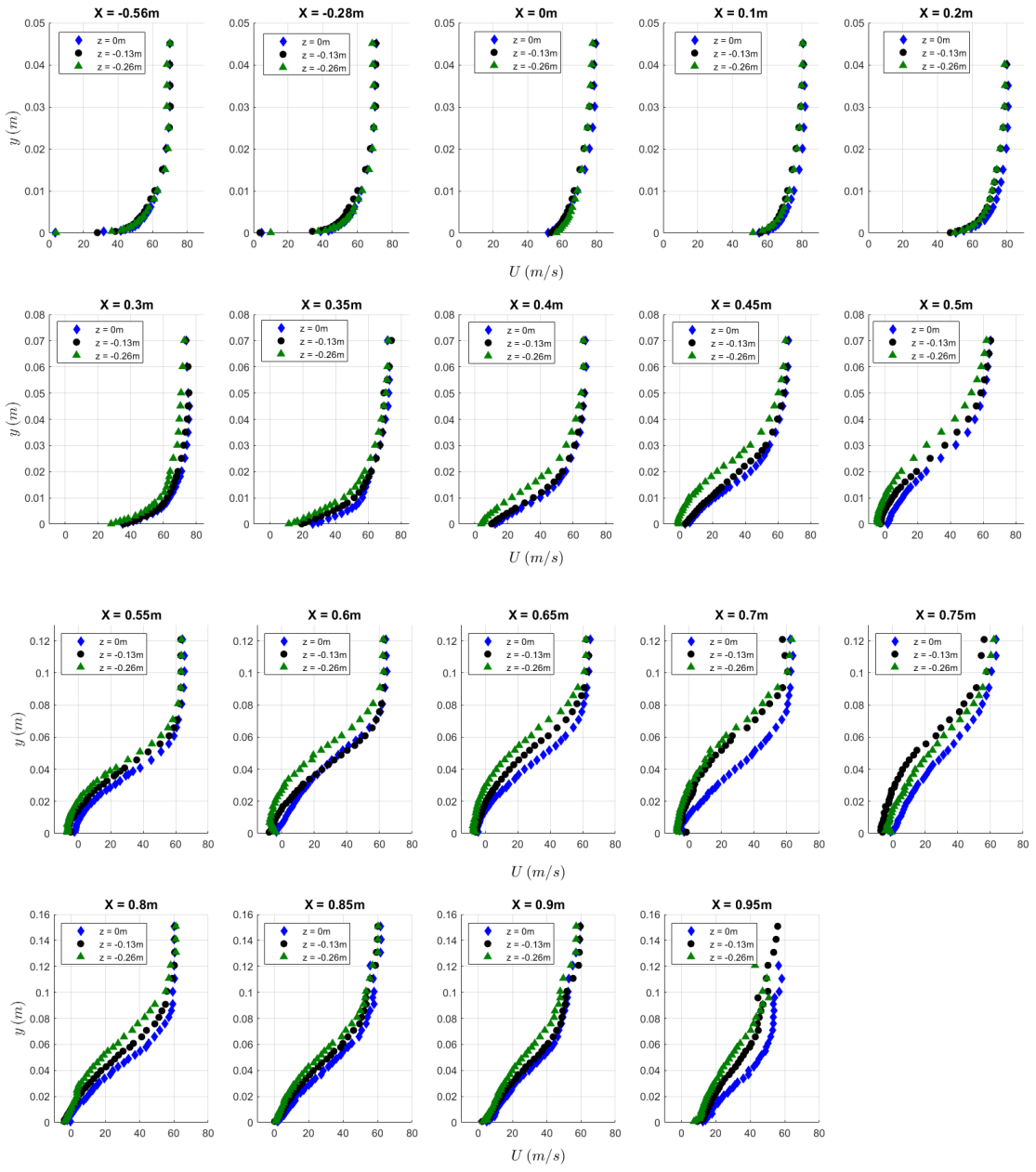


Figure 7.3 Evolution of wall-normal profiles for Case A showing spanwise variation in streamwise mean velocity,  $U$ , for flow starting on the boundary layer development plate,  $X = -0.56$  m, and continuing along the ramp through separation, reattachment, and recovery,  $X = 0.95$  m

As is typical for an adverse pressure gradient turbulent boundary layer, the mean profiles become inflectional, with the location of the outer inflection point moving away from the wall with downstream progression. This becomes noticeable at  $X \approx 0.4$  m and continues throughout the region documented here. The inflectional nature of the mean flow gives rise to an inviscid instability, which in turn leads to the formation of an embedded shear layer that roughly tracks the development of the outer inflection point, to be discussed in greater detail in the following chapter. Downstream of the separation region, as the surface flow visualization suggests, the near-wall flow becomes more uniform; by the time the flow reattaches,  $X \approx 0.85$  m, there is very little spanwise variation present in the reattachment location. However, this is only true near the surface, as the middle of the boundary layer profiles still shows strong variation with span. Furthermore, downstream of reattachment, recovery of the flow is evident; a new internal boundary layer begins to form and slowly propagates outward as the influence of the wall becomes stronger.

In the reattachment and recovery region of the flow, the edge of the boundary layer resembles that of a shear layer or wake. The development of the wall-normal component of mean velocity as well as of the turbulent stresses demonstrates more clearly that this is the case. This “secondary” shear layer first appears in the outer profile at  $X = 0.8$  m, but by  $X = 0.85$  m, it is apparent at all three spanwise locations—growing with streamwise development. While the cause of this phenomenon is not immediately apparent, and is possibly an experimental artifact, it occurs near the expected location of the eye of the streamwise vortical structure, F12, see Figure 5.5. Figure 5.5 and Figure 5.6 show that there is still significant crossflow velocity here and that it varies with wall-normal height, indicating that this secondary shear layer is not two-dimensional.

The off-surface flow structures presented in Chapter 5 and the curvature induced secondary flow presented in Chapter 6 provide some explanation for the spanwise variation in the mean flow that is present throughout its development. The cross-sectional sketch of the expected flow near reattachment, Figure 5.5, highlights the presence of streamwise vorticity that would tend to push the centerline flow downward and the outer flow upward. This would strengthen the centerline mean velocity profile,  $Z = 0$  m, transferring the high momentum fluid from the freestream towards the surface and attenuating the outer mean velocity profiles,  $Z = -0.13$  m and  $Z = -0.26$  m, by transferring near-wall low momentum fluid away from the surface. The observed mean profiles of Figure 7.3 affirm this explanation.

The streamwise development of the wall-normal component of mean velocity,  $V$ , is shown in Figure 7.4. Along the development plate, the velocity is uniform in both height and span. The first spanwise deviation in the flow occurs at  $X = 0.2$  m, where velocity increases in the outer profile; however, the inner profiles quickly follow suit and there remains only minor spanwise variation throughout the rest of the flow evolution. While the presence of a strong upper inflection point was expected and observed in the streamwise mean profiles, it is also observed at the same locations in many of the wall-normal mean velocity profiles. However, the presence of a peak in  $\frac{dV}{dy}$  does not have an equivalent meaning to  $\frac{dU}{dy}$  in terms of its generation of spanwise vorticity. Here it is primarily attributed to the mean flow not fully following the local wall-normal coordinate system in which the data was collected.

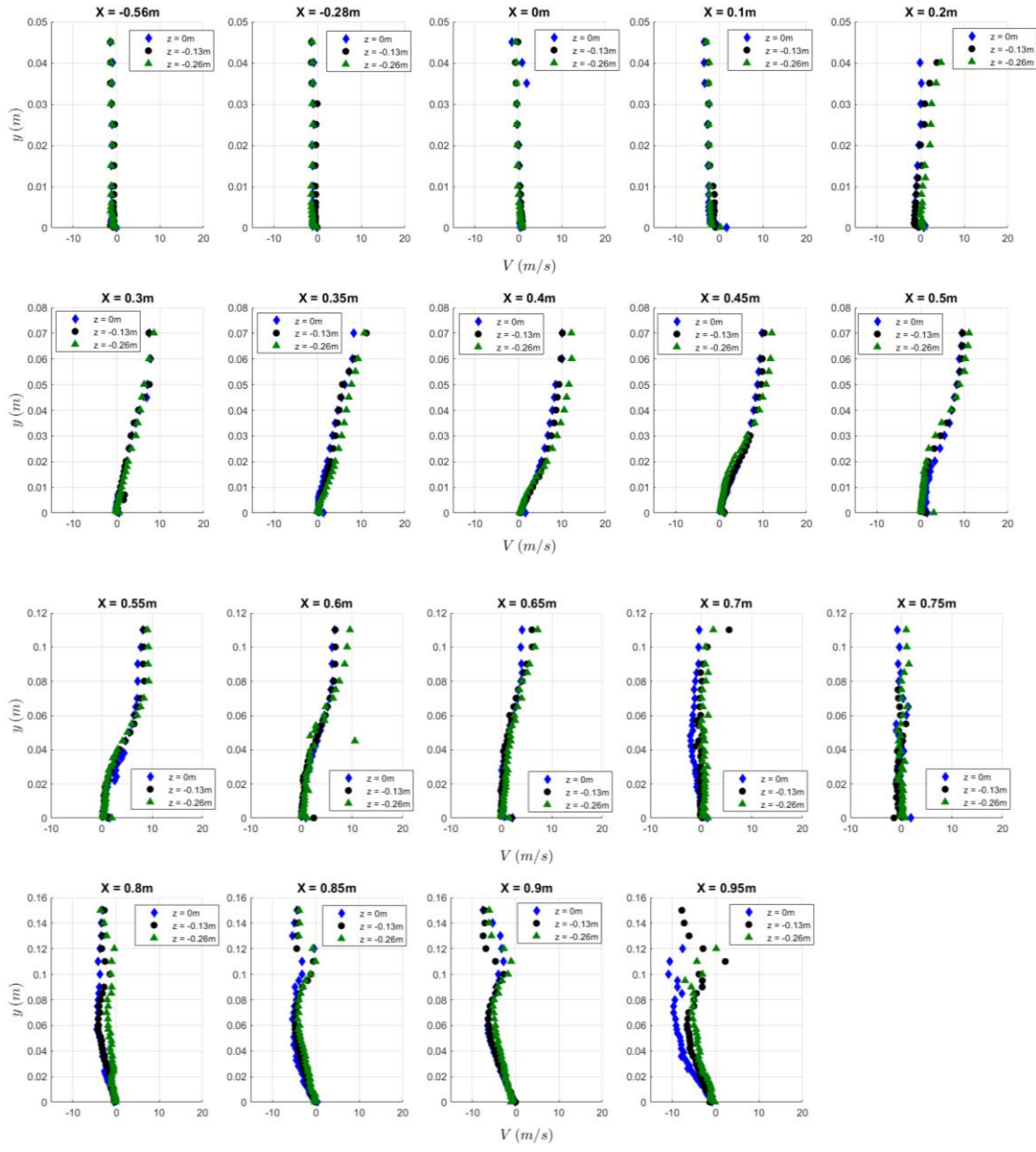


Figure 7.4 Evolution of wall-normal profiles for Case A showing: spanwise variation of wall-normal mean velocity,  $V$ , for flow starting on the boundary layer development plate,  $X = -0.56$  m, and continuing along the ramp through separation, reattachment, and recovery,  $X = 0.95$  m

### 7.2.2 Case B – Smaller-Scale Separation

The evolution of the streamwise mean velocity,  $U$ , profiles for the smaller-scale separation case, Case B, is presented in Figure 7.5. Like the flow in the larger-scale separation case, Case A, the flow is spanwise uniform along the development plate and at the start of the ramp, while the first signs of spanwise deviation occur farther down the ramp at  $X \approx 0.4$  m. Unlike those of Case A, the two center profiles,  $Z = 0$  m and  $Z = -0.13$  m, show excellent agreement over the majority of their streamwise development and it is only the outer profile,  $Z = -0.26$  m, that exhibits a velocity deficit, a deficit smaller than that of Case A. This trend continues through reattachment,  $X \approx 0.75$  m, after which the uniformity inverts; the middle profile,  $Z = -0.13$  m, recovers at a slower rate and becomes uniform with the outer profile,  $Z = -0.26$  m, all of this while the velocity deficit in the central region of the boundary layer lessens. As in Case A, the formation of a pronounced outer inflection point is observed beginning at  $X \approx 0.4$  m and continues throughout the separation and documented recovery regions.

Figure 7.6 highlights the wall-normal component of mean velocity,  $V$ , for Case B, which shows good spanwise uniformity over the entire flow development. The secondary shear layer, or wake, that was observed in the upper recovery region for Case A is now only slightly noticeable, primarily in the outer profile at  $Z = -0.26$  m from  $X \approx 0.8$  m – 0.85 m and could easily go unnoticed, if not looked for.

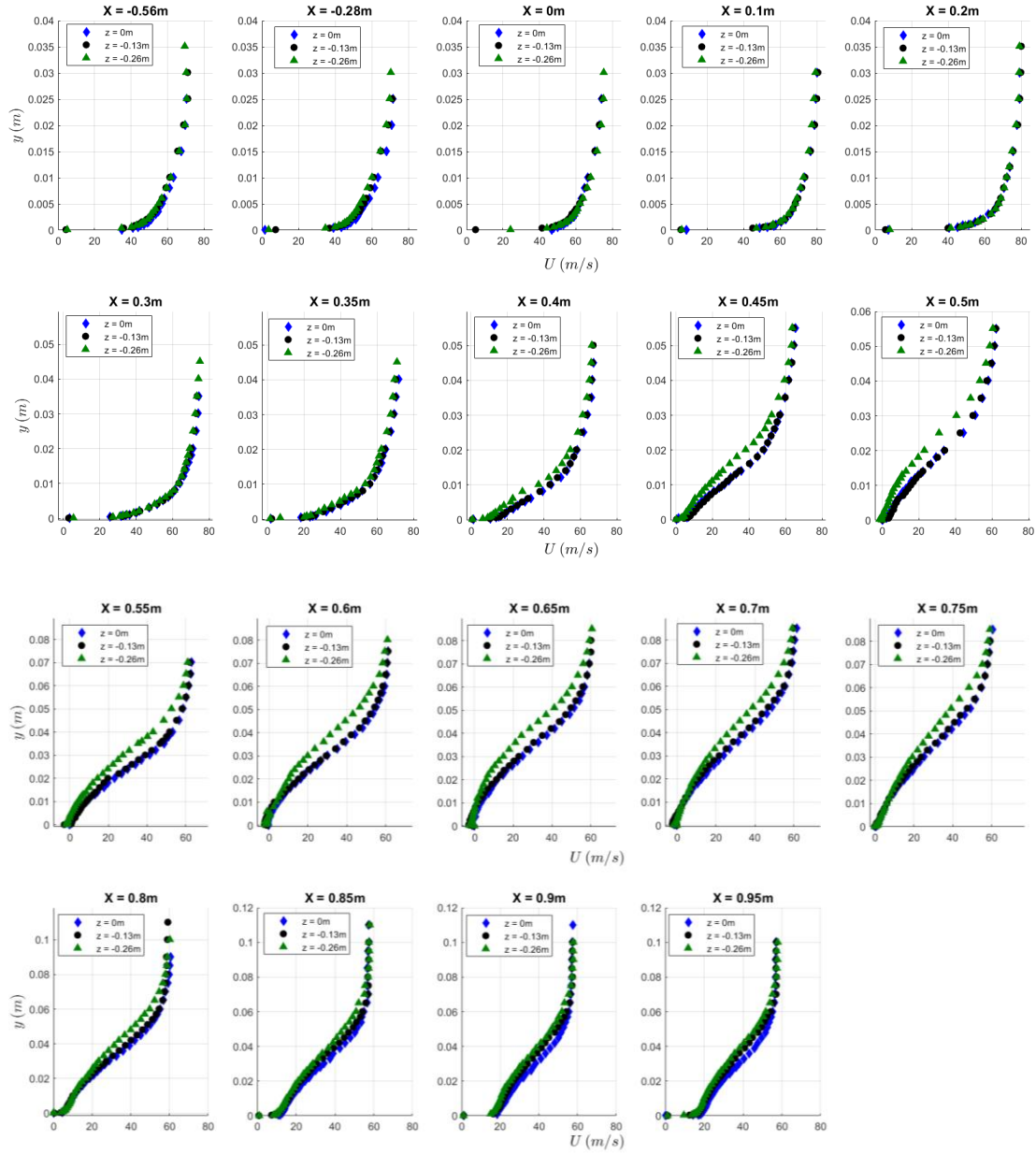


Figure 7.5 Evolution of wall-normal profiles for Case B showing spanwise variation of streamwise mean velocity,  $U$ , for flow starting on the boundary layer development plate,  $X = -0.56$  m, and continuing along the ramp through separation, reattachment, and recovery,  $X = 0.95$  m

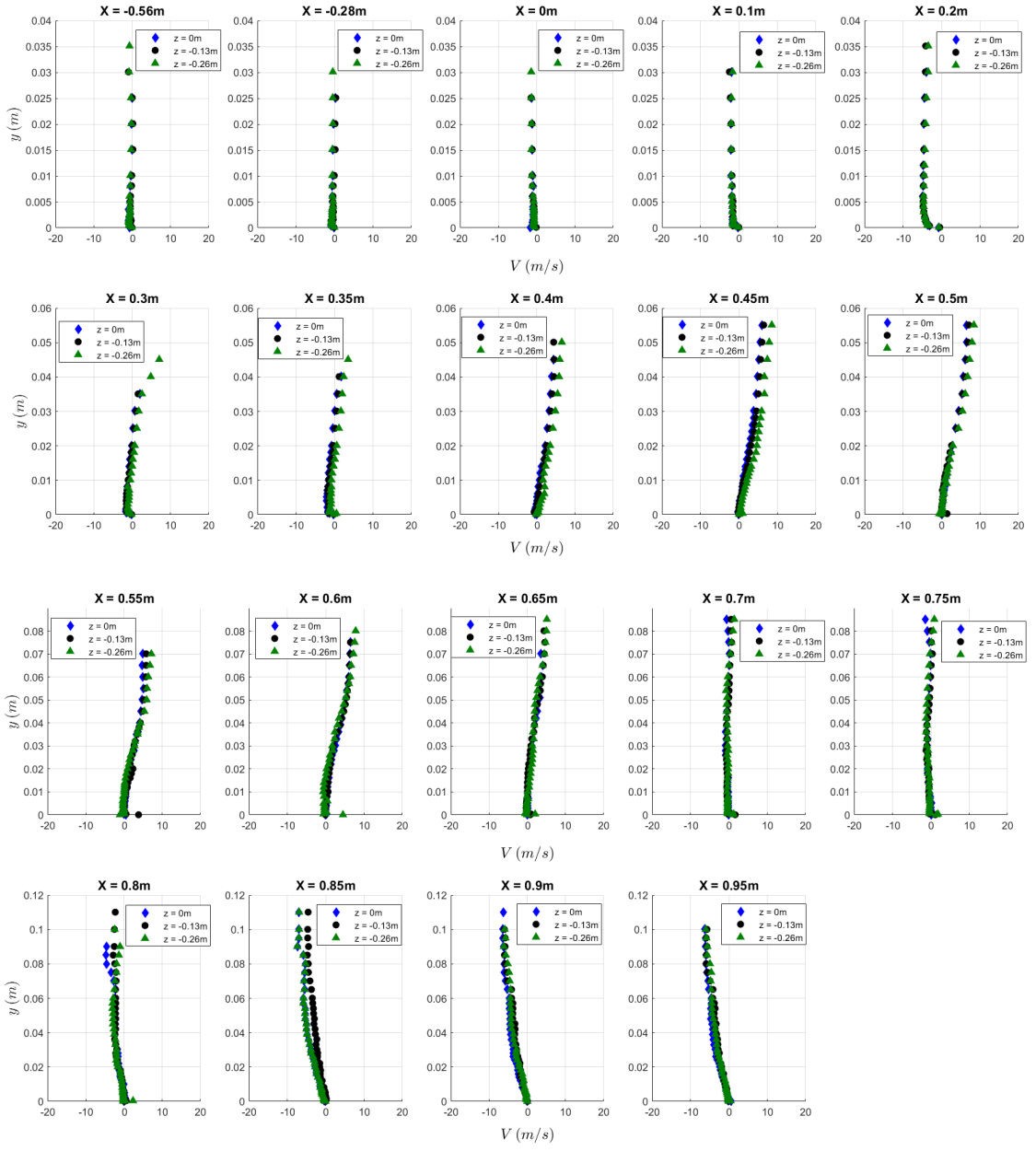


Figure 7.6 Evolution of wall-normal profiles for Case B showing spanwise variation of wall-normal mean velocity,  $V$ , for flow starting on the boundary layer development plate,  $X = -0.56$  m, and continuing along the ramp through separation, reattachment, and recovery,  $X = 0.95$  m

### 7.2.3 Case C – Attached Flow

The evolution of the streamwise component of the mean flow,  $U$ , for the attached flow case, Case C, is shown in Figure 7.7. Overall, the flow development in the middle and outer regions of the boundary layer is very similar to that of the other two cases. Since the flow remains attached, the near-wall region must deviate. The spanwise uniformity of the flow lasts until  $X \approx 0.5$  m, after which, unlike the profiles of Case B, the outer two profiles,  $Z = -0.13$  m and  $Z = -0.26$  m, show excellent uniformity while the centerline,  $Z = 0$  m, exhibits a fuller profile. This non-uniformity begins to vanish downstream of  $X \approx 0.8$  m, the profiles showing good spanwise agreement at the last measurement station,  $X \approx 0.95$  m. Furthermore, it should be noted, that while the flow for Case C does not separate in the mean sense, instantaneous back flow does occur, which indicates that the flow is undergoing unsteady separation. This will be discussed in greater detail later in the chapter.

As was observed for Cases A and B, there is little variation in the wall-normal component of the mean velocity,  $V$ , for Case C, see Figure 7.8. The variation at  $X \approx 0.65$  m is the only variation present. This variation is explained by the realignment of the LDV probe between the acquisition of the different spanwise data set locations. The wall-normal velocity is so low that any slight discrepancy in the wall-normal angle alignment is amplified by the addition of the streamwise component of velocity. This is not a flow feature but rather an experimental artifact of the data collection process that uniquely occurred for the profiles at this location. Finally, the secondary shear layer, or wake, observed in Cases A and B is not observed here; this would be expected given the elimination of the primary flow separation structures.

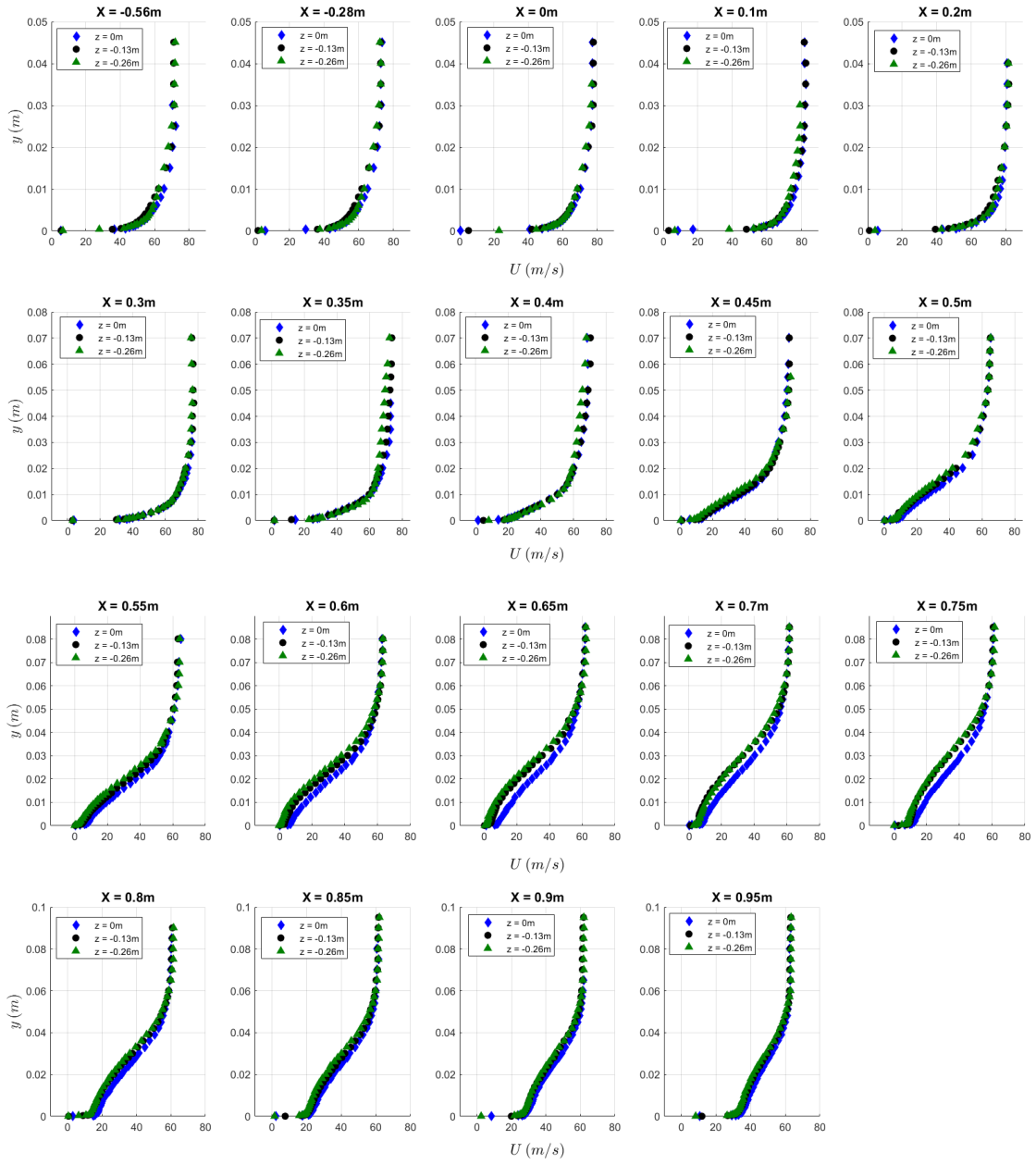


Figure 7.7 Evolution of wall-normal profiles for Case C showing spanwise variation of streamwise mean velocity,  $U$ , for flow starting on the boundary layer development plate,  $X = -0.56$  m, and continuing along the ramp through separation, reattachment, and recovery,  $X = 0.95$  m

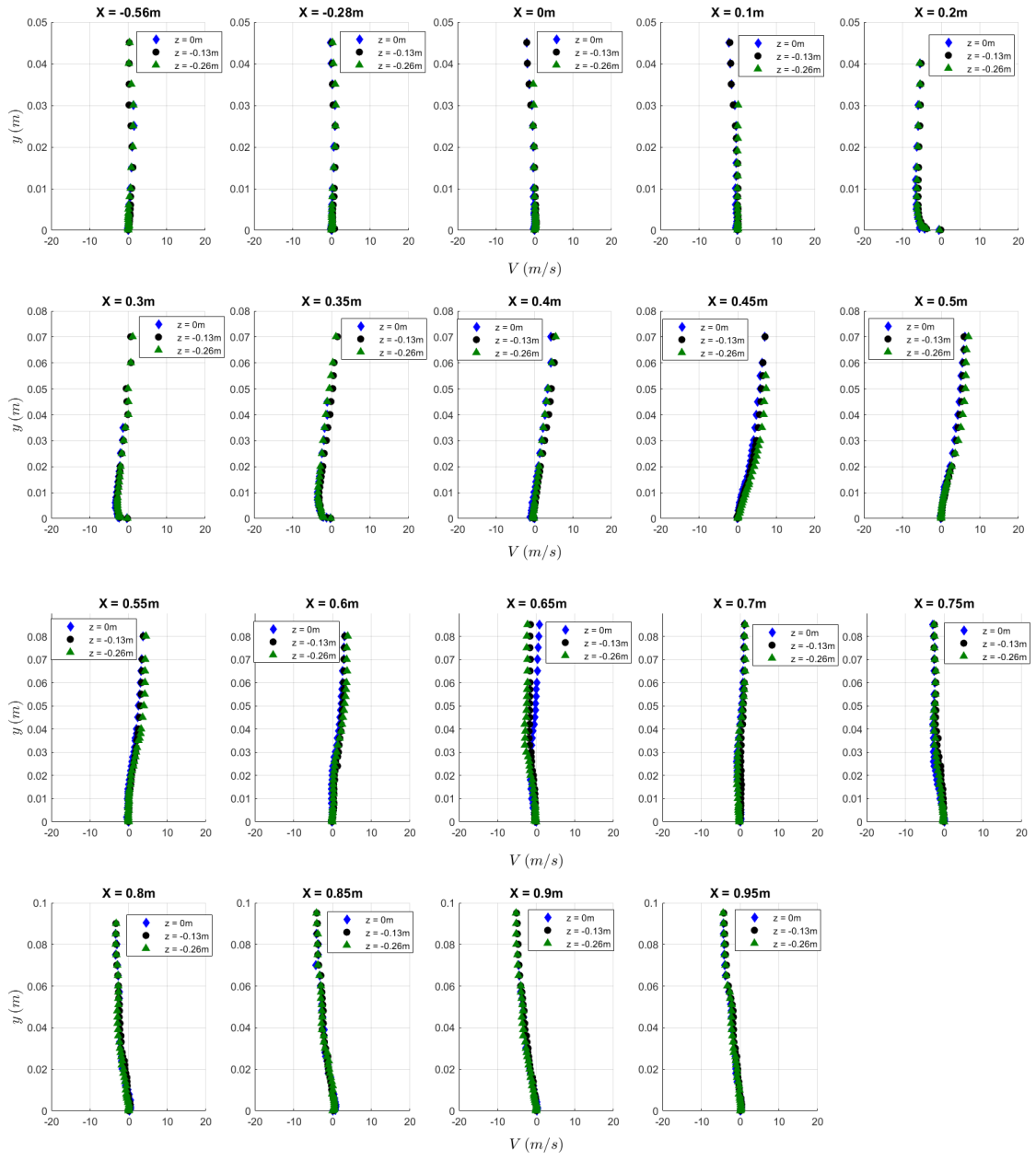


Figure 7.8 Evolution of wall-normal profiles for Case C showing spanwise variation of wall-normal mean velocity,  $V$ , for flow starting on the boundary layer development plate,  $X = -0.56$  m, and continuing along the ramp through separation, reattachment, and recovery,  $X = 0.95$  m

### 7.3 Turbulent Stress Development

The streamwise development of the Reynolds stresses, both normal and shear, is presented here. The data are taken from the same set used for the mean flow development and its presentation will follow the same streamwise and spanwise locations. In order to better compare the spanwise variation in the data, the stresses are plotted in raw form, not scaled by height. The boundary layer height is a somewhat ambiguous<sup>13</sup> quantity because it is difficult to accurately calculate and it loses meaning in a separated flow; therefore, scaling by its height may introduce additional error.

#### 7.3.1 Case A – Larger-Scale Separation

Figure 7.9 presents the streamwise development of the turbulent normal stresses. The figure legend is the same as that for the mean flow; however, solid symbols represent the streamwise normal stress,  $\overline{u'u'}$ , and open symbols represent the wall-normal component,  $\overline{v'v'}$ . Likewise, Figure 7.10 presents the streamwise development of the turbulent shear stress, plotted separately for clarity. On the boundary layer development plate, the near wall peak in the normal and shear stresses is readily apparent. Farther along the ramp, when the pressure gradient becomes adverse,  $X \approx 0.2$  m, the effect of the near wall peak diminishes and the outer peak in the turbulent stresses slowly grows in magnitude and moves away from the wall, demonstrating classic behavior of turbulent APG boundary layer flows. The development of this outer turbulence peak is associated with the embedded shear layer which forms due to the inflectional streamwise mean flow profiles.

---

<sup>13</sup> The boundary layer is an asymptotic quantity that can vary significantly due to uncertainty in the streamwise mean velocity. Due to low particle seeding concentrations near the edge of the boundary layer the number of data samples is low, leading to increased uncertainty.

As in the mean flow, the turbulent stresses begin to show slight spanwise variation around  $X = 0.1$  m, which becomes more apparent shortly after the APG forms. Along the streamwise development, the general trend is that the central profile,  $Z = 0$  m, experiences the smallest turbulence stresses and the outer profile,  $Z = -0.26$  m, the largest. Interestingly, the wall-normal location where this disparity is observed is in the middle of the boundary layer, predominately above the stress peak, while the inner layer, near the location where the surface flow visualization showed three-dimensional effects, remains quite uniform across the measured span. The secondary shear layer, or wake, forming in the upper region of the boundary layer near reattachment, is quite visible from the turbulent stress profiles. Note that, due to low sample size, the centerline data for  $X = 0.95$  m is not plotted as the turbulent statistics did not converge sufficiently.

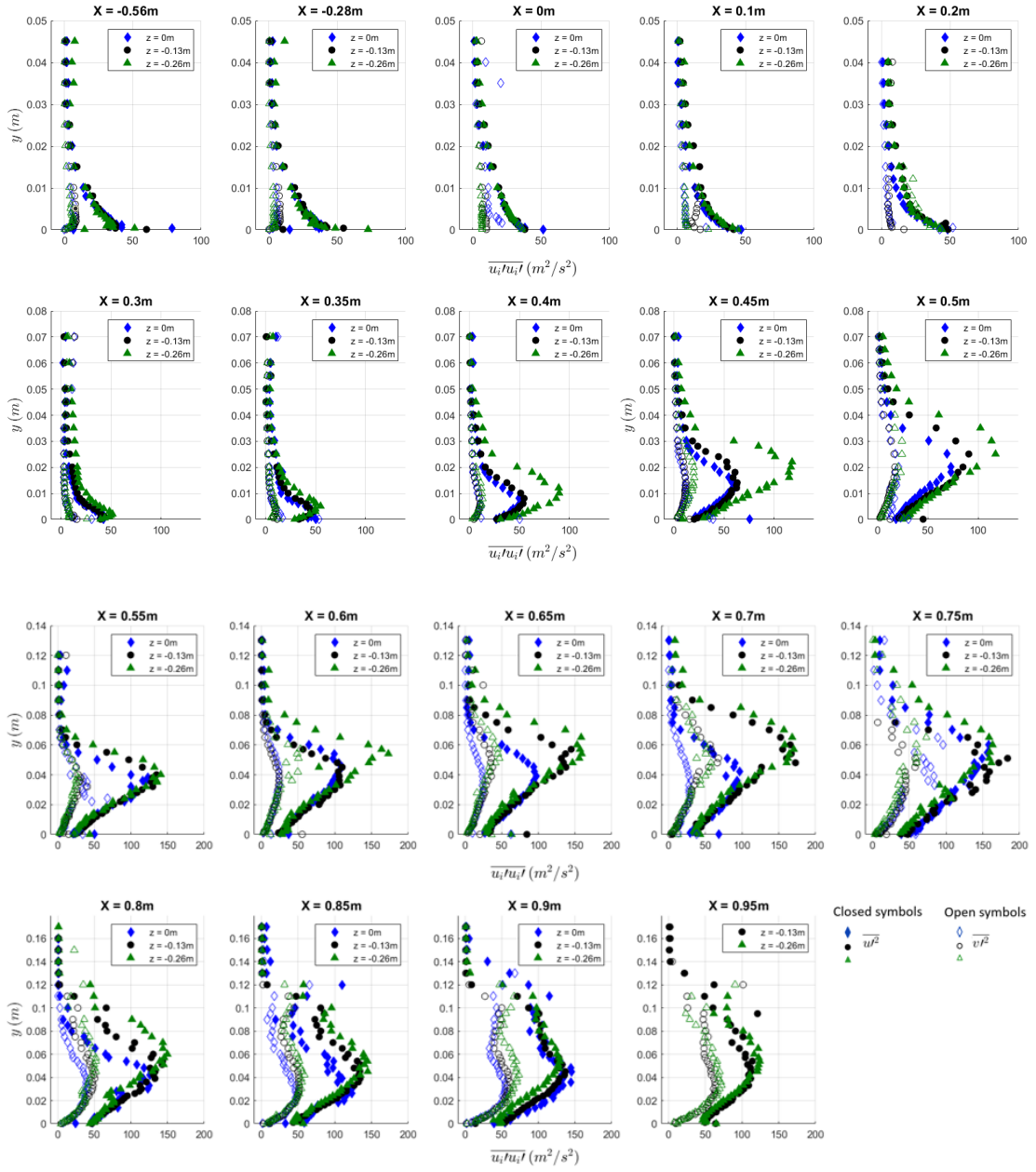


Figure 7.9 Streamwise development of the turbulent normal stresses for Case A with solid symbols corresponding to the streamwise component,  $\overline{u'u'}$ , and open symbols corresponding to the wall-normal component,  $\overline{v'v'}$

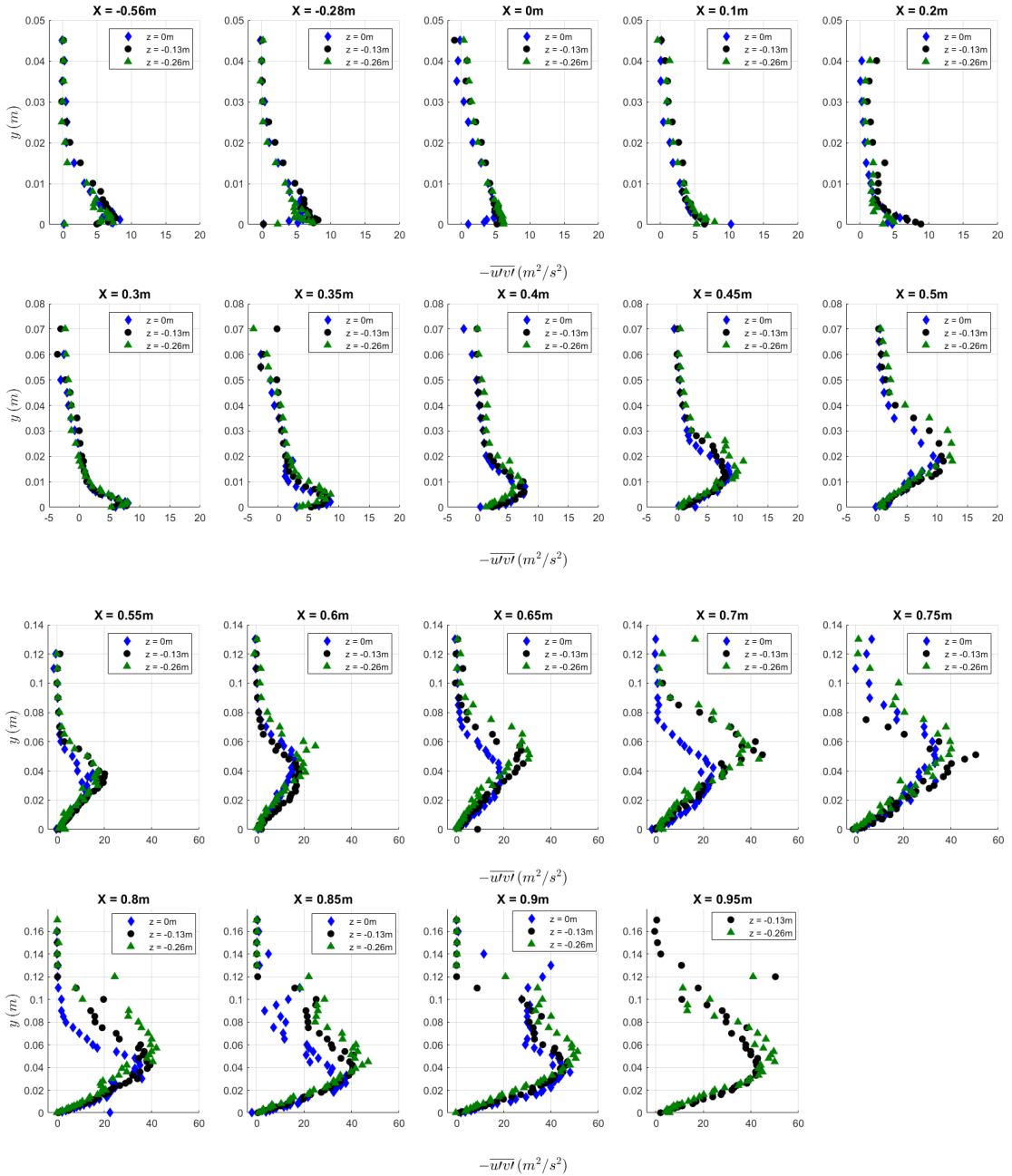


Figure 7.10 Streamwise development of the turbulent shear stresses for Case A at multiple spanwise locations

### 7.3.2 Case B – Smaller-Scale Separation

The streamwise development of the turbulent normal and shear stresses for the smaller-scale separation case, Case B, is shown in Figure 7.11 and Figure 7.12, respectively. Since the APG of Case B is very similar to that of Case A, just less severe, the development of the flow and turbulent stresses is likewise similar. The turbulent stresses develop a strong outer peak, with the onset of the APG, increase in magnitude, and initially move away from the wall. There is much improvement in the flow uniformity compared to Case A, with the two central spanwise locations,  $Z = 0$  m and  $Z = -0.13$  m, exhibiting excellent agreement over the majority of the streamwise flow development. Only the outer,  $Z = -0.26$  m, profiles show higher turbulence levels. However, in general, the turbulent stress levels are around 20% - 35% lower in magnitude than Case A and peak about 25% closer to the wall.

As was observed in the mean flow, the secondary shear layer, or wake, that was clearly visible for Case A is only slightly noticeable, primarily in the outer profile at  $Z = -0.26$  m, from  $X \approx 0.8$  m – 0.85 m, and could easily go unnoticed, if not looked for.

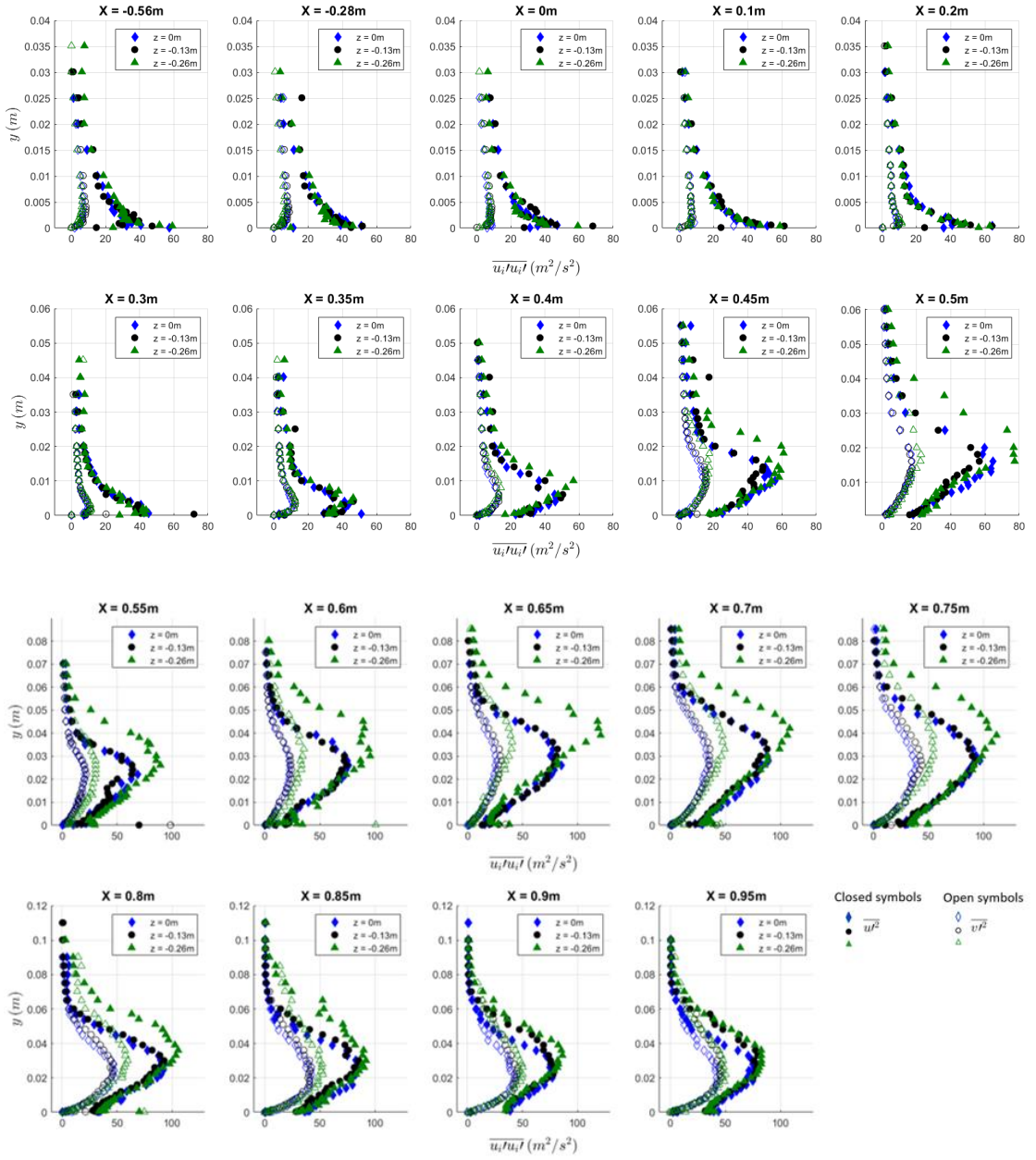


Figure 7.11 Streamwise development of the turbulent normal stresses for Case B with solid symbols corresponding to the streamwise component,  $\overline{u'u'}$ , and open symbols corresponding to the wall-normal component,  $\overline{v'v'}$

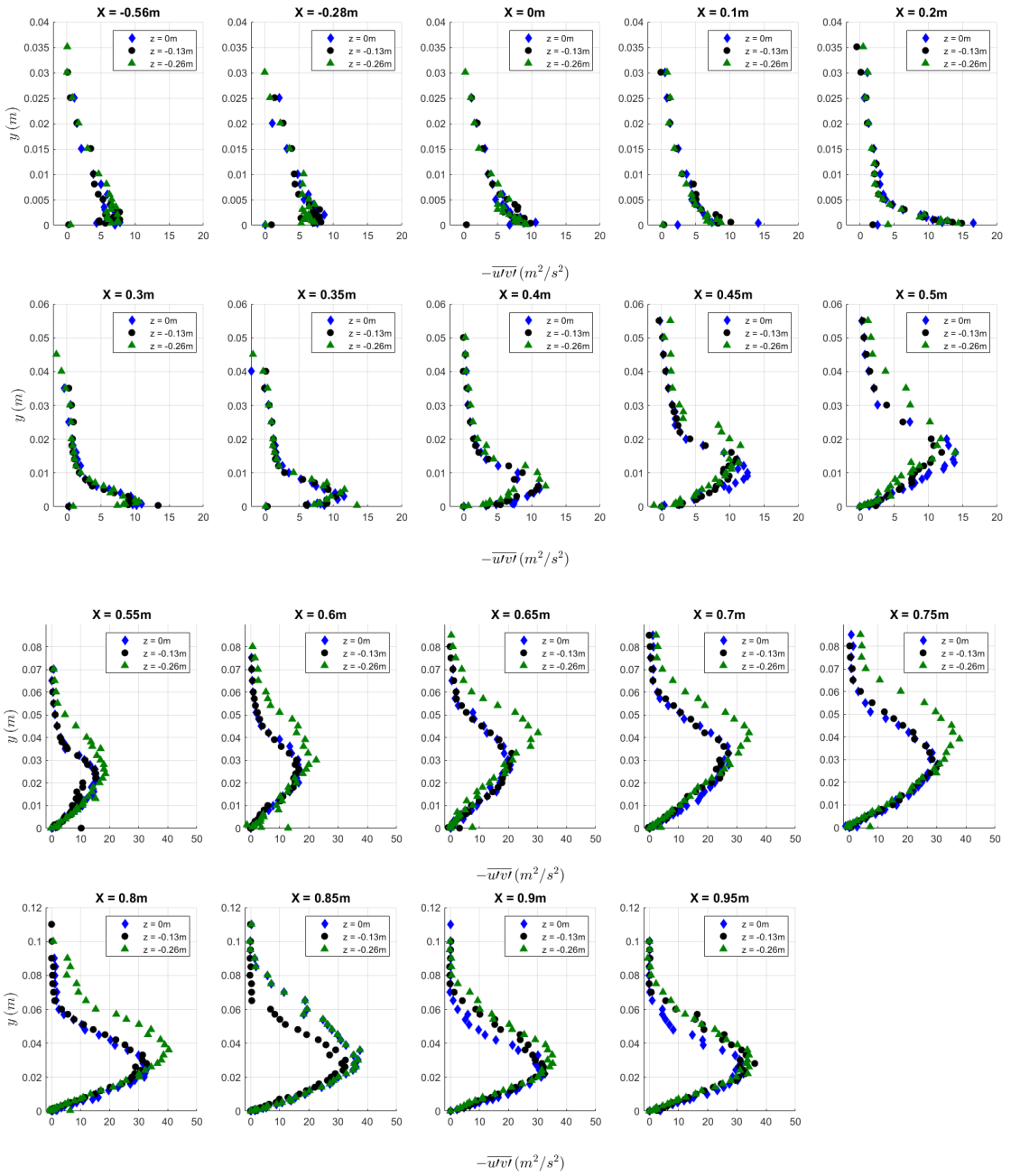


Figure 7.12 Streamwise development of the turbulent shear stresses for Case B at multiple spanwise locations

### 7.3.3 Case C – Attached Flow

The streamwise development of the turbulent normal and shear stresses for the attached flow case, Case C, is shown in Figure 7.13 and Figure 7.14, respectively. The global trends for this attached flow case are the same as for the two separation cases, with two notable differences: (1) the spanwise uniformity of the turbulent stresses is very good over the majority of the streamwise development and (2) the overall turbulent stress levels are around 30% - 35% lower in magnitude than those in Case B, and 45% - 55% lower in magnitude than those in Case A.

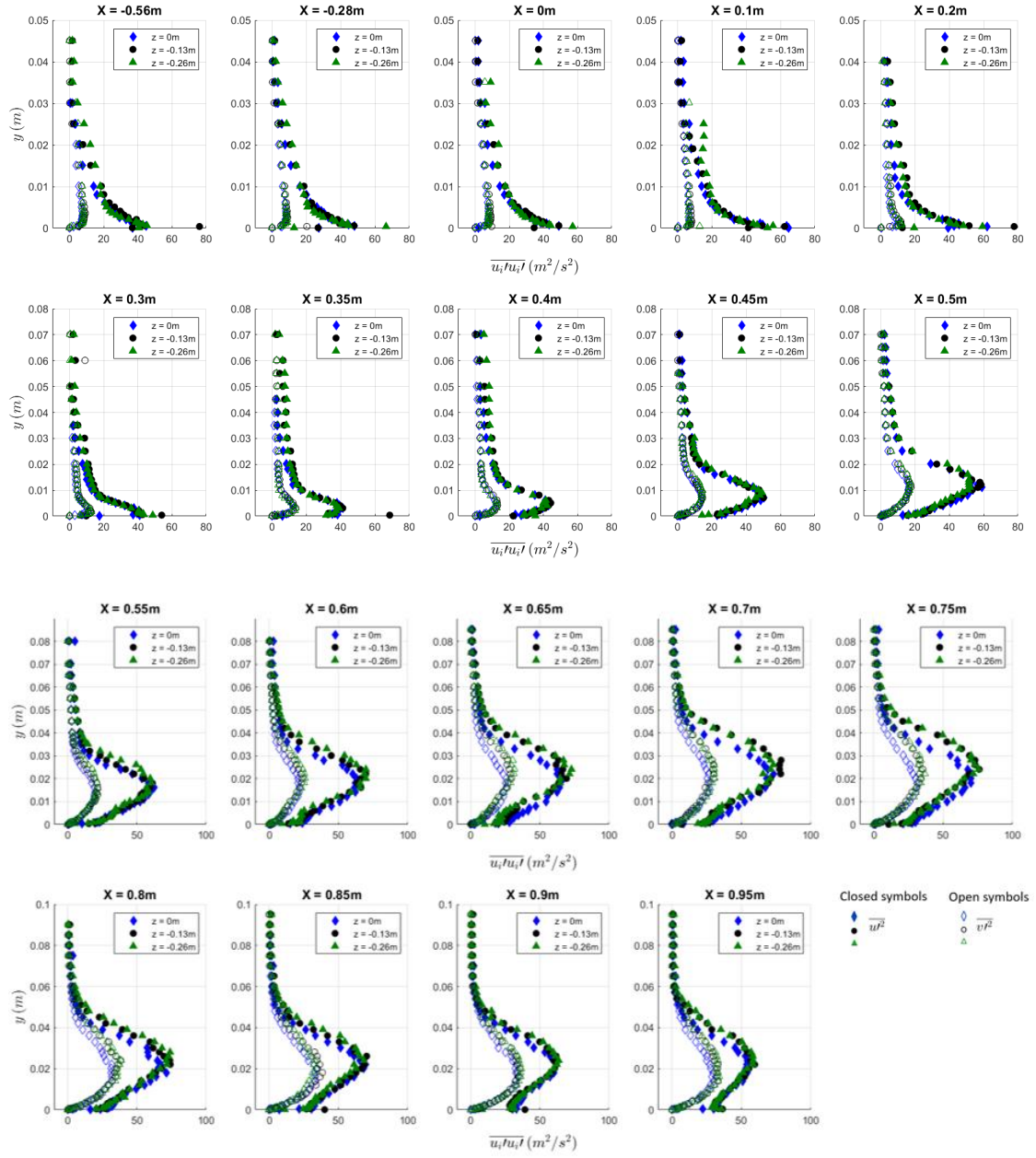


Figure 7.13 Streamwise development of the turbulent normal stresses for Case C with solid symbols corresponding to the streamwise component,  $\overline{u'u'}$ , and open symbols corresponding to the wall-normal component,  $\overline{v'v'}$

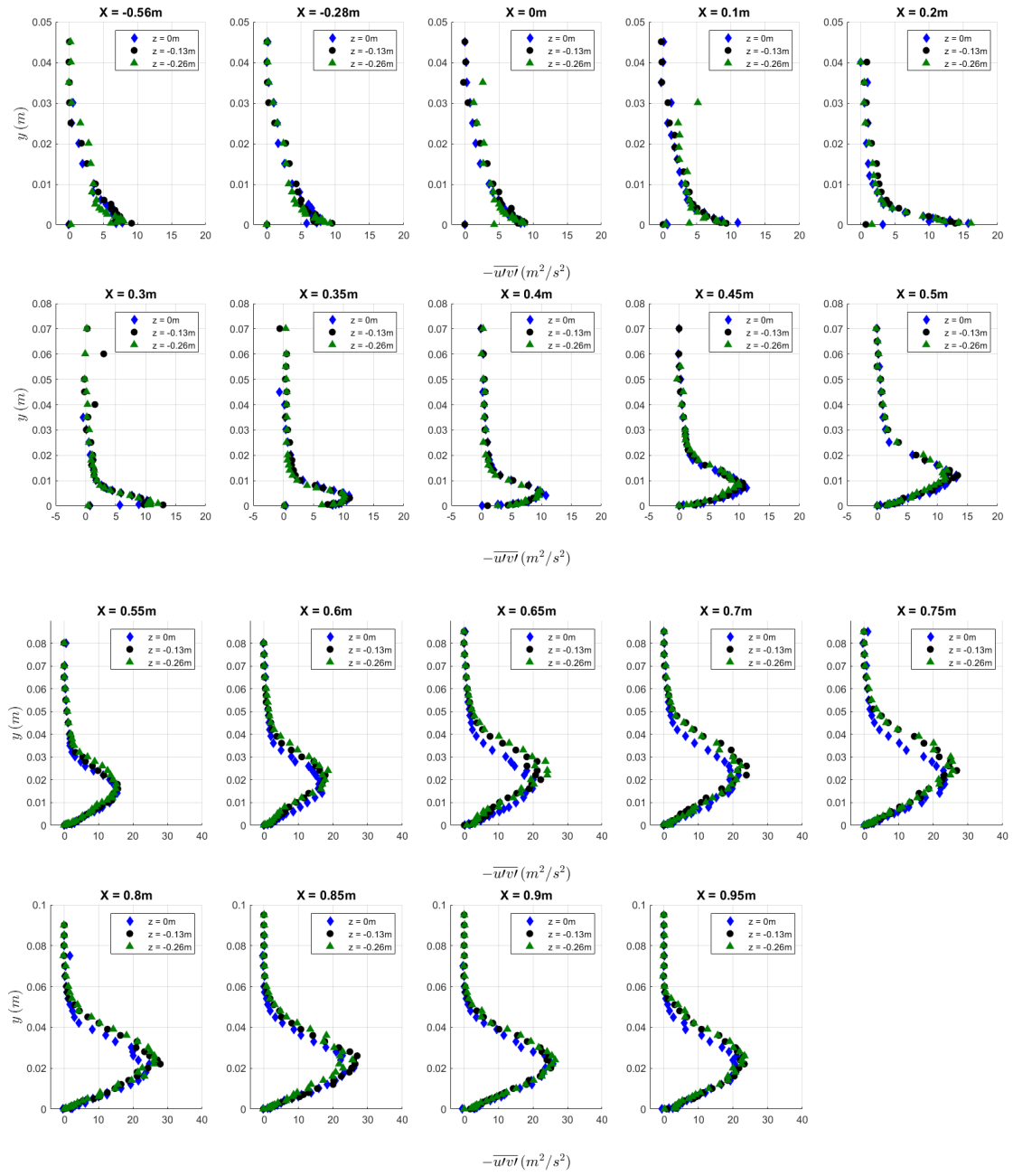


Figure 7.14 Streamwise development of the turbulent shear stresses for Case C at multiple spanwise locations

## 7.4 Separation Extent

While Chapter 4 analyzed the flow separation and reattachment topography using numerous surface flow visualization studies, this section describes the same flow separation and reattachment cases from a quantitative perspective. Thus far, flow separation has been treated in its true three-dimensional form. Here, each streamwise data set will be treated as if the flow were two-dimensional. The three-dimensionality will only be captured via the difference between these two-dimensional LDV data sets.

In order to unify the understanding of turbulent flow separation, and provide a good groundwork, Simpson [107] and other participants at the Colloquium on Turbulent Flow Separation [108] proposed a set of terminology for two-dimensional steady flow separation. While the flow examined here is only quasi two-dimensional at best and the steadiness is still in question, the proposed terminology, taken from Simpson [107], will still be useful for comparison purposes:

- A. *Detachment*—the location where the boundary layer flow leaves the wall; the locus of points where the limiting streamline [in a time mean sense] of the flow leaves the surface.
- B. *Reattachment*—locus of points where the limiting streamline of the time-averaged flow rejoins the surface.
- C. *Separation*—the total process consisting of detachment, recirculation, flow free-shear layer, and, in cases not involving a free wake, reattachment.
- D. *Stall*—zone of recirculating fluid created by pressure forces.
- E. *Stalled Fluid*—fluid with reverse or low velocity within a recirculating zone.

Throughout this dissertation, the term “separation” was used to signify the same thing as “detachment”, as defined above. The distinction between these terms will only be made in the remainder of this chapter.

While the proposed terminology defines separation as the entire process of detachment and reattachment, detachment itself is a process. Simpson [107] states that detachment cannot simply be viewed as “vanishing surface shearing stress or flow reversal.” Instead, he lays out another method of looking at the separation process nearest the surface from the perspective of the time-mean fraction of the time the flow moves downstream,  $\gamma_p$ . Here  $\gamma_p = 1$  corresponds to all the flow being directed downstream, and  $\gamma_p = 0$  corresponds to all the flow being directed upstream. The first sign of flow reversal,  $\gamma_p = 0.99$ , corresponds to incipient detachment (ID), flow reversal 20% of the time,  $\gamma_p = 0.8$ , corresponds to intermittent transitory detachment (ITD), and flow reversal 50% of the time,  $\gamma_p = 0.5$ , corresponds to transitory detachment (TD), which is the same as detachment (D) if the probability distribution is Gaussian. While this method captures much of the unsteadiness of the detachment process, Simpson [107] warns that it is a necessary but insufficient variable to describe the flow behavior; “it represents only the fraction of a streamwise velocity probability distribution that is positive.”

The flow separation process will first be examined in terms of the mean flow detachment and reattachment (what is often simply reported as the separation region), after which the unsteadiness will be examined based upon the fraction of time the flow moves downstream,  $\gamma_p$ . Mean flow detachment and reattachment were calculated using a linear interpolation between sequential boundary layer profiles as follows

$$X_{det} = X_i + (U_{det} - U_i) \frac{X_{i+1} - X_i}{U_{i+1} - U_i} \quad (7.1)$$

where  $X_i$  is the global X-coordinate, i.e.  $X_i = 0.45$  m,  $X_{i+1} = 0.5$  m, etc., and  $U_i$  is the streamwise mean flow near the surface, i.e.  $U_i = U(X_i, y \approx 0)$ , and  $X_{det}$  is the detachment location at  $U_{det} = 0$ .

Mean flow detachment and reattachment locations for Cases A and B, calculated using equation (7.1), are given in Table 7.1. Spanwise variations in detachment location range from  $X = 0.53$  m to  $X = 0.44$  m for Case A and from  $X = 0.56$  m to  $X = 0.49$  m for Case B, while variations in reattachment location only range from  $X = 0.82$  m to  $X = 0.84$  m for Case A and from  $X = 0.73$  m to  $X = 0.75$  m for Case B. As a percentage of the ramp length ( $L = 0.9$  m), over the spanwise region measured, the spanwise spatial variation in detachment location was 10% for Case A and 8% for Case B, whereas the variation in reattachment location was only 2% for both Cases A and B. This confirms what was already observed in the flow visualization, that the smaller-scale separation case, Case B, experiences an improvement in the spanwise uniformity of the detachment region. Furthermore, in all cases, reattachment is essentially spanwise uniform. The extent of the streamwise separation region, from detachment to reattachment, can be given in terms of a percentage of the ramp length, with all measurements taken along the X-axis, for each spanwise location. Separation extents range from 32% to 44% with the mean extent over this span being 39% for Case A. Similarly, for Case B, the separation extents range from 19% to 30% with the mean extent over this range being 24%.

TABLE 7.1  
MEAN FLOW DETACHMENT AND REATTACHMENT

Location [m]	Case A			Case B		
	X <sub>Det</sub> [m]	X <sub>Reatt</sub> [m]	Extent [%]	X <sub>Det</sub> [m]	X <sub>Reatt</sub> [m]	Extent [%]
Z = 0	0.53	0.82	32	0.56	0.73	19
Z = -0.13	0.48	0.84	40	0.55	0.75	22
Z = -0.26	0.44	0.84	44	0.49	0.76	30

The method of determining detachment and reattachment just discussed interpolates the mean velocity data. It assumes that detachment, while possibly a function of span, occurs at a single streamwise location. To show that this is not the case, and that detachment is indeed a process evolving in the streamwise direction, the fraction of time the flow moves downstream,  $\gamma_p$ , must be examined. Here  $\gamma_p$  is calculated as

$$\gamma_p \equiv \frac{\sum_{j=1}^N \Delta T_{(u_j > 0)}}{\sum_{j=1}^N \Delta T_{(u_j)}} \quad (7.2)$$

where  $u_j$  is the instantaneous streamwise velocity measurement of the data set,  $N$  is the number of samples and  $\Delta T$  is the transit time of a valid burst. The fraction of downstream flow defined here,  $\gamma_p$ , is based upon the number of samples headed downstream instead of the fraction of time the flow moves downstream. For a uniform sampling rate, this would be identical to the fraction of samples headed downstream; however, the sampling rate of LDV cannot be controlled by the user, but is instead a function of the frequency of valid bursts, as defined by the flow processor.

Figure 7.15 shows the various states of detachment, as a function of the streamwise and spanwise extent, for Cases A, B, and C. The data used is from LDV measurements

taken approximately 0.5 mm off the surface, corresponding to approximately 1% of the local boundary layer thickness. For Case A, incipient detachment first occurs at  $X = 0.35$  m for the outer,  $Z = -0.26$  m, profile and  $X = 0.41$  m for the centerline,  $Z = 0$  m, profile. As the flow progresses downstream, intermittent transitory detachment and transitory detachment follow with the three-dimensionality of the detachment process that is apparent from the offset between data sets. For Case B, incipient detachment occurs at almost the exact same location as for Case A; however, transitory detachment occurs farther downstream, corresponding to an approximate 30% increase in the extent of the detachment process. For both Cases A and B, transitory detachment is approximately the same as detachment as seen in Table 7.1. Case C, while fully attached in the mean, undergoes both incipient detachment, and intermittent transitory detachment, and comes just short of reaching transitory detachment. Here incipient detachment is mildly delayed compared to Cases A and B.

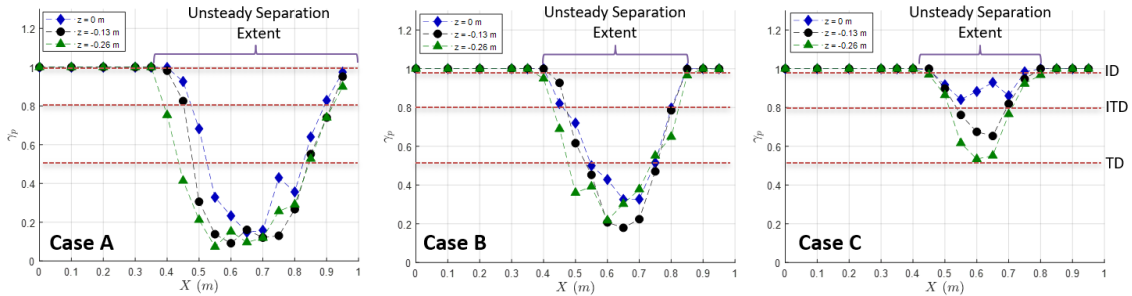


Figure 7.15 Fraction of downstream flow,  $\gamma_p$ , just above the surface for Case A, B, and C, with red dashed lines highlighting incipient detachment (ID),  $\gamma_p = 0.99$ , intermittent transitory detachment (ITD),  $\gamma_p = 0.8$ , and transitory detachment (TD),  $\gamma_p = 0.5$

While the spanwise averaged mean separation extent was shown to be approximately 39% for Case A and 24% for Case B, this only tells part of the story. The unsteady separation extent, roughly the streamwise extent over which  $\gamma_p < 1$ , is much larger than its mean counterpart, roughly twice the size, as highlighted in Figure 7.15. It is also apparent that  $\gamma_p$  never drops to zero in the separation zone, indicating that there is no location with backflow present at all times. This should not be surprising as other TBL flow separation experiments [109,110] exhibited similar phenomena with  $\gamma_p$  never reaching zero.

Since the streamwise pressure gradient is often thought of as the driver of the flow, and ultimately provides the sufficient condition for it to separate, it is not surprising that it can be analyzed to predict detachment and reattachment. Studies by Simpson et al. [109] and Alving and Fernholz [111] conducted on reportedly-two-dimensional turbulent boundary layer separation noted that detachment occurs at a local minimum in the streamwise pressure gradient. This is likely true in this experiment as well and can be seen in Figure 7.16 (a1-c1), which highlights the streamwise pressure gradient and centerline detachment locations for Case A, B, and C. Furthermore, the subsequent local maximum in streamwise pressure gradient seemingly corresponds to reattachment. While reattachment did not occur or was not documented by Simpson et al. [109], in the work of Alving and Fernholz [111], reattachment also appears to be in close proximity to the local maximum in streamwise pressure gradient (although not identified by the authors).

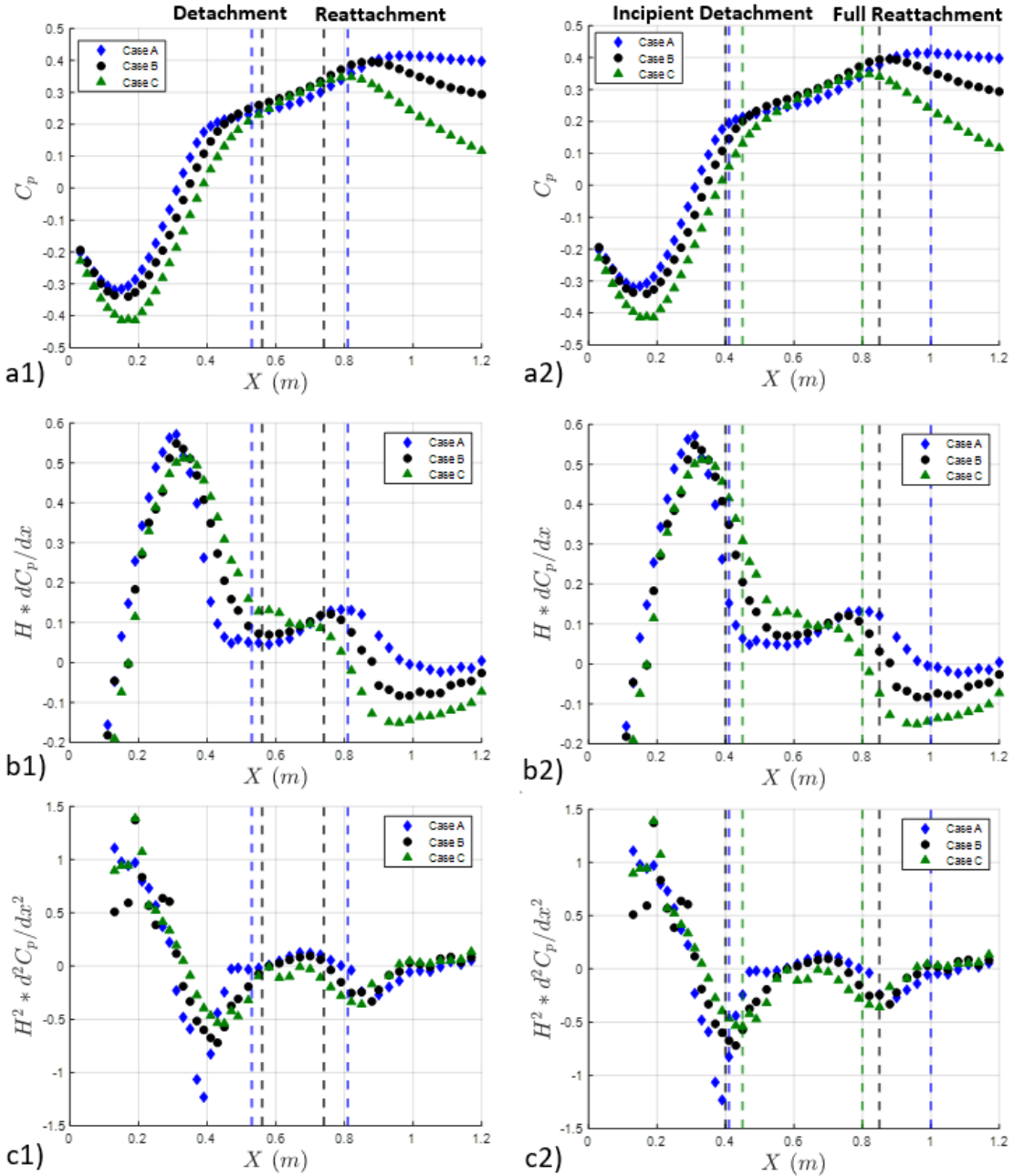


Figure 7.16 Streamwise pressure (a) and pressure gradient (b) and (c) distributions for Cases A, B, and C. Detachment and reattachment locations, corresponding to  $\gamma_p = 0.5$ , are highlighted by vertical dashed lines for (a1)-(c1) while incipient detachment and full reattachment locations corresponding to  $\gamma_p = 0.99$  and  $\gamma_p = 1$  are highlighted by vertical dashed lines for (a2)-(c2), respectively. Note the ramp height,  $H$ , is used to non-dimensionalize the pressure gradient distributions.

The streamwise pressure distribution not only governs the detachment and reattachment of the mean flow but also the whole detachment and reattachment process. Incipient detachment for the three test cases corresponds well with the local minimum in  $\frac{d^2C_p}{dx^2}$ , whereas the flow transitions to fully attached,  $\gamma_p = 1$ , just as the pressure gradient switches from mildly adverse to mildly favorable, which is also where  $C_p$  peaks. This can be seen in Figure 7.16 (a2)-(c2) where the dashed lines correspond to the locations of incipient detachment and full reattachment for Cases A, B, and C. These conclusions about correlations between the pressure distribution (and gradient distributions) and the degree of detachment, while derived from this work, also show excellent agreement with the experimental studies of both Alving and Fernholz [111] and Debien et al. [46], the latter of which examined both salient and smooth edge ramps. While no claims will be made on its general universality, it is apparent that for the type of work examined here the pressure distribution alone with adequate spatial resolution would be enough to accurately determine the various detachment and reattachment locations.

## CHAPTER 8: SCALING THE FLOW DEVELOPMENT

This chapter examines the streamwise development of the mean flow and turbulent stresses with the intent to provide a set of scaling parameters. As the savvy reader may expect, given 1) the flow three-dimensionality, 2) the variation in streamwise pressure gradient and surface curvature, and 3) separation of the flow in Cases A and B, and the attached flow for Case C, providing a set of universal scaling parameters that accurately captures the flow development is rather unlikely, if not impossible. While this may be the case, much can still be learned by examining the regions and variables where the flow can be scaled and where it cannot, and why these scalings either capture, or fail to capture, the relevant physics governing the developing flow. The primary scaling considered here is that utilizing embedded shear layer parameters first proposed by Schatzman and Thomas [56]. Somewhat surprisingly, the parameters provided by this approach will be shown to scale the mean flow development remarkably well. Adequately scaling the turbulent stresses turns out to be the greatest challenge, hence, much of this chapter examines the turbulent normal and shear stress development. Emphasis is placed on the role that streamwise surface curvature plays in its direct effect on the flow, via the radial pressure gradient, and its effect on the coordinate system in which the flow development is examined.

## 8.1 Review of Scaling APG Flows

Many smooth-body APG flow studies [26,50,56,112,113] have investigated scaling the streamwise development of both mean flow and turbulence quantities. While quite a few approaches have been employed, the two basic patterns utilize parameters based on more traditional outer/external variables or treat the flow as a shear layer—a type of “mid variable” scaling<sup>14</sup>. Scalings based on the former are more likely to be compatible with FPG and ZPG flows, while scalings based on the latter are more likely to be compatible with separated flows and will be examined here.

It is thought that the inflectional instability that forms in turbulent APG flows dominates the local flow physics and gives rise to an outer turbulence peak whose magnitude grows with streamwise distance and whose wall-normal location tracks the mean profile inflection point [50,56]. The strong inflectional nature of the mean flow profiles and its alignment with the peak turbulent stresses give these flows the strong resemblance to traditional shear layers which has been exploited to develop scaling parameters. This can take various forms; for example, Song and Eaton [28] scaled the wall-normal height of the boundary layer profiles off of the mean profile inflection point, while Stella, Mazellier, and Kourta [113] used the momentum thickness. Both approaches work well at collapsing the profiles for Reynolds number variation and do a decent job of accounting for the movement of the turbulence peak away from the surface. However, the outer variable scaling, in the case of Stella et al. [113], and the mixed outer- and inflection-point velocity scaling of Song and Eaton [28] did not account for the variation in magnitude

---

<sup>14</sup> Here the term “mid variable” is used since the outer mean profile inflection point, on which these scalings are based, is usually located near the middle of the boundary layer.

of the turbulent stresses associated with streamwise development. While both of these cases examined separated flows, prior to these studies, somewhat similar, albeit different, scalings were employed by Elsberry et al. [50] on attached TBL APG flows on the verge of separation. They successfully scale both the wall-normal and magnitude variation of the mean the turbulent stress profiles, but utilize different parameters for each, which included the Reynolds number, thus indicating that the flow was not in equilibrium.

More direct applications of mixing/shear layer parameter scaling to separated flows have also been employed. Flow separation experiments on a backward facing step by Jovic [23] followed by LES simulations on a rounded, backward facing step by Dandois, Garnier, and Sagaut [114] both employed the same similarity scaling of the flow-field development via common mixing layer parameters. Jovic [23] acknowledged that while the embedded shear layer cannot be expected to match that of a self-similar mixing layer, his findings showed good qualitative agreement between the cases. The mean flow profiles exhibited good collapse, while the turbulent stress profiles only collapsed in the wall-normal direction and, instead, varied in magnitude, indicating that the flow had not yet achieved self-similarity.

While the aforementioned studies have utilized shear layer scaling parameters to scale separated flows, and some have even commented on the similarity of features between attached flows and shear layers, Schatzman and Thomas [56] appear to be the first to employ shear layer scaling parameters on an attached, spatially varying flow (which also happened to be temporally varying). Analyzing quadrant 2 and quadrant 4 Reynolds stress components, they noticed that these took on common values where both the Reynolds stress peaked and the outer mean profile inflection point was located. This led them to

postulate that an embedded shear layer was the driver for the turbulent APG flow development. In addition to applying embedded shear layer scaling (referred to here as ESLS) to their own experiments with great success, they examined its universality by applying the scaling to the TBL APG flows of Marusic and Perry [115] as well as those compiled by Coles and Hirst [116] from the AFOSR-IFP-Stanford Conference. In all the cases examined, the ESLS did a remarkable job of collapsing the data sets, including both wall-normal mean and turbulent stress profiles.

Recently, Peterson, Vukasinovic, and Glezer [112,117] applied the ESLS of Schatzman and Thomas [56] to both a diffusing duct [117] and a wall-mounted airfoil [112]. Their experimental work transitioned back to smooth-body separating flows, but also expanded the application of ESLS to flows directly controlled by active flow control. They not only successfully scaled the mean flow using the standard ESLS, but also modified the scaling parameters to account for both the inviscidly unstable outer mean profile inflection point and the stable inner inflection point, which improved the collapse of the near wall data. While the collapse of the mean profiles was very robust, they did not experience the same success with the turbulent stress profiles; instead, they [112] state that “at present, there is no evidence that the Reynolds stresses can be scaled in the same manner [as the mean flow] and accordingly it cannot be argued that details of the flow dynamics are equivalent.”

An important question that arises from the studies utilizing ESLS parameters is why the parameters appear to scale the turbulent stresses well in some cases, i.e. the work of Schatzman and Thomas [56], but not in others, i.e. the work of Peterson et al. [112,117]. What physical mechanism causes this disparity and how can it be accounted for? In this

chapter, we will revisit the ESLS of Schatzman and Thomas [56] by applying it to both an attached turbulent APG flow and a separated turbulent APG flow that develop over the same ramp geometry. The focus here will be to analyze the role of surface curvature. Our work, like that of Peterson et al. [112,117] is conducted on a geometry that experiences streamwise surface curvature, whereas the experiments of Schatzman and Thomas [56], and the additional data sets they analyzed, were conducted on flows developing over geometries without surface curvature.

In Chapter 6 the role of streamwise surface curvature in generating secondary flow was discussed and shown to agree well with the observed surface flow visualization patterns. Likewise, this chapter will demonstrate that streamwise surface curvature also has an important impact on the development of the turbulent stresses. Here we will explore the development of the turbulent stresses, the application of embedded shear layer scaling, and the corresponding role that surface curvature and coordinate system orientation has on the scaling. It will be shown that *the turbulent shear stresses streamwise growth is highly dependent on the coordinate system reference frame, while the turbulent normal stresses streamwise growth exhibits only mild dependence on reference frame.*

## 8.2 Shear Layer Growth Rate and Scaling Applicability

The scaling proposed by Schatzman and Thomas [56] involving free shear layer parameters is illustrated in Figure 8.1. The length scale used is the embedded shear layer vorticity thickness defined as

$$\delta_\omega(x) \equiv \frac{U_d}{\left(\frac{dU}{dy}\right)_{IP}} \quad (8.1)$$

where the subscript IP denotes the quantity is to be evaluated at the outer inflection point, which is inviscidly unstable according to the Rayleigh-Fjørtoft theorem. The velocity is scaled by the velocity defect at the inflection point,

$$U_d \equiv U_e - U_{IP} \quad (8.2)$$

Using these parameters, the scaled wall-normal coordinate is given by

$$\eta \equiv \frac{y - y_{IP}}{\delta_\omega} \quad (8.3)$$

and the scaled mean velocity is given by

$$U^* \equiv \frac{U_e - U}{U_d} \quad (8.4)$$

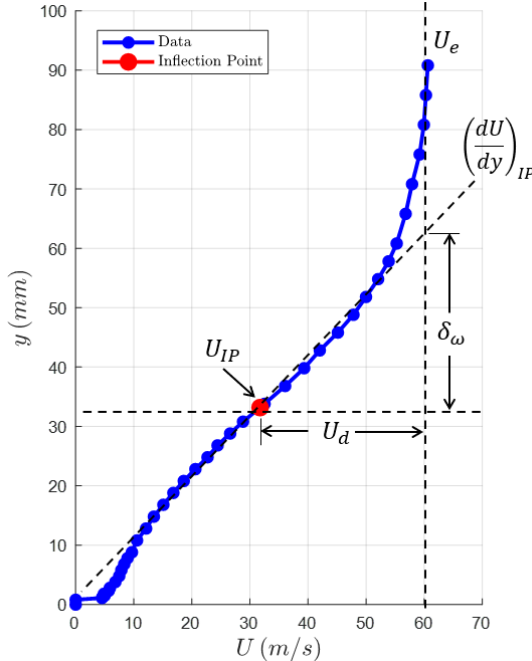


Figure 8.1 Illustration of embedded shear layer scaling parameters for an inflectional mean velocity profile

The growth rate of the vorticity thickness is a good indicator of the applicability of shear layer scaling. Bell and Mehta [118] note that for mixing layers, a linear growth rate is a necessary but insufficient condition for achieving self-similarity. Using the streamwise mean velocity data, presented in the last chapter, the vorticity thickness was calculated for all inflectional mean velocity profiles, and is presented in Figure 8.2. For the three cases, this typically occurs downstream of  $X = 0.4$  m. The plotted data includes all three separation cases (A, B and C) and all three spanwise locations discussed in the previous chapter. Linear growth rates for each separation case are estimated from spanwise averaged curve fits and given in the figure legend. While there is obvious scatter in the data, it is apparent that the flow three-dimensionality near separation is dominated by the two-dimensional shear layer instability, yielding a quasi-two-dimensional flow. Initially, the

growth rate is approximately linear, with Cases B and C having a common value of  $\frac{d\delta_\omega}{dx} \approx 0.03$ , and Case A having a higher value of  $\frac{d\delta_\omega}{dx} \approx 0.054$ . For Cases B and C, it is apparent that the growth rate does not persist past  $X = 0.8$  m and  $X = 0.75$  m, respectively. This change in growth rate occurs because the streamwise pressure gradient switches from adverse to favorable just downstream of these locations, as observed in Figure 7.16 of the previous chapter. Any scaling of the flow should only be attempted in this linear vorticity thickness growth rate region.

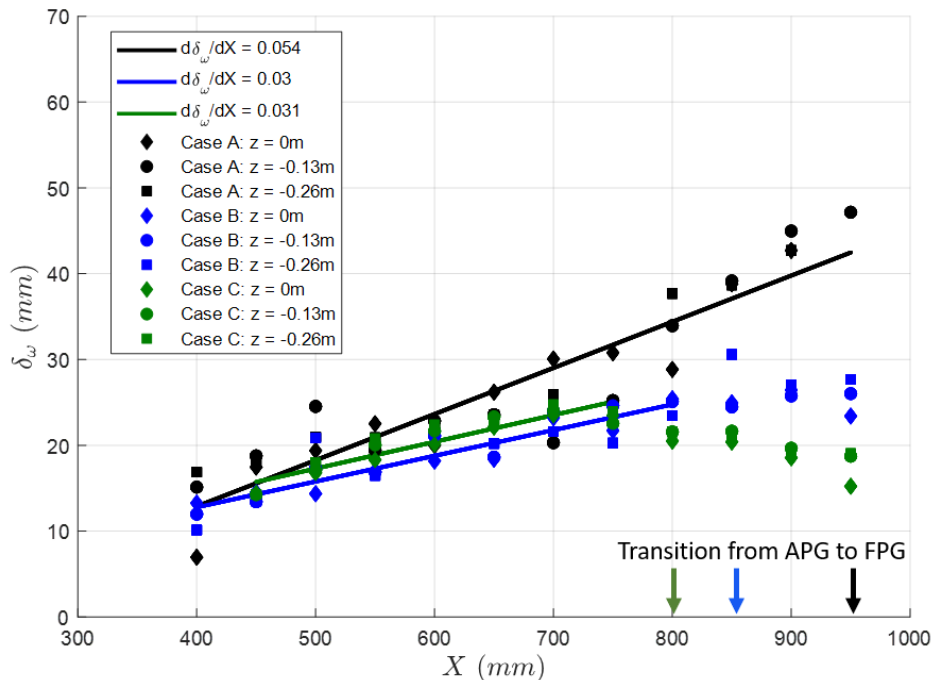


Figure 8.2 Vorticity thickness growth rates for Cases A, B, and C highlighting an initial uniform growth rate for Cases B and C and higher growth rate for Case A. Note that the solid lines are spanwise-averaged linear curve fits.

The vorticity thickness growth rates presented in Figure 8.2 are much lower than those of typical turbulent mixing layers. In their work on turbulent mixing layers, Browand and Troutt [119] showed a universal linear growth-rate of  $\frac{d\theta}{dx} = 0.034\lambda$  which they stated was equivalent to  $\frac{d\delta_\omega}{dx} = 0.17\lambda$  where  $\lambda$  is the speed ratio of the two layers and is equal to  $\lambda \approx 1$  for a boundary layer. Cherry, Hillier, and Latour [120] showed that the vorticity thickness growth rate appeared to be universal with a value of  $\frac{d\delta_\omega}{dx} = 0.17$ , which is significantly larger than that observed in the current set of experiments. This discrepancy comes from the definition of the vorticity thickness. Schatzman and Thomas [56] use the velocity defect to define the vorticity thickness whereas in shear layers the velocity difference,  $U_{\text{high}} - U_{\text{low}}$ , is typically used. For the case of a boundary layer, the velocity difference would predominately be the external velocity,  $U_e$ , with the addition of any small reverse flow velocity. This alternate vorticity thickness definition is given below.

$$\delta_{\omega_{\text{alt}}}(x) \equiv \frac{U_e}{\left(\frac{dU}{dy}\right)_{IP}} \quad (8.5)$$

The vorticity thickness growth calculated using this alternate definition is shown in Figure 8.3, and the growth rates come out to be  $\frac{d\delta_{\omega_{\text{alt}}}}{dx} = 0.11$ ,  $\frac{d\delta_{\omega_{\text{alt}}}}{dx} = 0.083$ , and  $\frac{d\delta_{\omega_{\text{alt}}}}{dx} = 0.087$  for Cases A, B, and C, respectively. These values are much closer to those typically found in shear layers. The generalized momentum thickness,  $\theta_{SL}$ , is another parameter that is frequently used to analyze flow development. It is defined as:

$$\theta_{SL}(x) \equiv \int_{y_{min}}^{\infty} \frac{U(x, y) - U_{min}(x)}{U_{\infty}(x) - U_{min}(x)} \left( 1 - \frac{U(x, y) - U_{min}(x)}{U_{\infty}(x) - U_{min}(x)} \right) dy, \quad (8.6)$$

and is shown in Figure 8.4. It also exhibits a linear growth rate that is slightly lower than that of a typical shear layer.

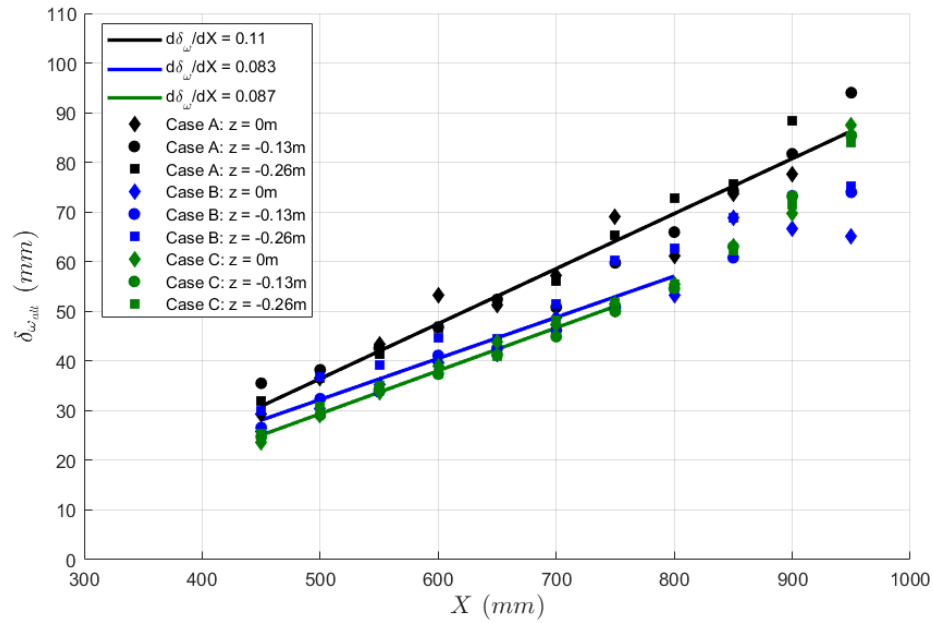


Figure 8.3 Modified vorticity thickness growth rate for Cases A, B, and C with the solid lines giving the spanwise averaged linear curve fits

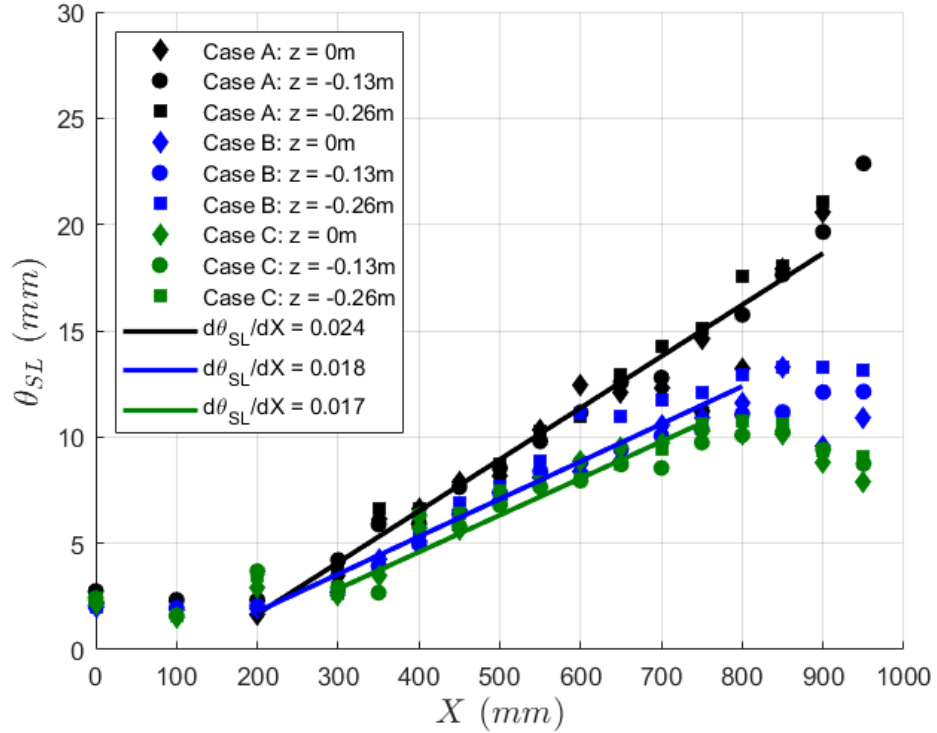


Figure 8.4 Generalized momentum thickness growth rates for Cases A, B and C, with the solid lines giving the spanwise averaged linear curve fits

The flow observed in this experiment has many similar features to that of Schatzman and Thomas [56], including a vorticity thickness that grows linearly in the streamwise direction and at roughly the same rate as the local boundary layer thickness, with  $\delta_\omega/\delta = \text{const.} \approx 0.3$ , included in Appendix F.1. This suggests that embedded shear layer scaling would also be applicable to this experimental data set. The flow examined by Schatzman and Thomas [56] was an attached APG flow, so Case C is the most comparable case. However, to examine how the scaling applies for separated flows, as it should since it was developed for a shear layer, Case B will also be considered. Cases B and C experience similar boundary layer and vorticity thickness growth rates, which should allow a more direct comparison between separated and attached flow cases. Thus, the remainder of this chapter will only discuss these two test cases, focusing on the regions with

inflectional mean velocity profiles and developing in the APG region. This will include profiles from  $X = 0.4\text{-}0.8$  m for Case B and from  $X = 0.45\text{-}0.75$  m for Case C. Additionally, while many of the trends are maintained for the off-center spanwise locations, for clarity, the analysis will be restricted to the centerline data.

### 8.3 Outer Variable Scaling

In order to gauge how well ESLS parameters scale the flow development, the mean velocity and turbulent normal and shear stress profiles are shown using conventional outer variable scaling in Figure 8.5 and Figure 8.6, respectively. As would be expected, the collapse of the data is far from ideal due to the nonequilibrium APG. The mean flow profiles strongly show the effect of the APG, even for attached flow Case C, and are far from equilibrium. Keep in mind that for Case B the data include mean velocity profiles upstream of, throughout, and downstream of separation. The turbulent stress data in the near wall and freestream regions collapse well. However, in the central boundary layer region, there is a clear outward growth in the peak turbulent stress and an increase in magnitude with streamwise development.

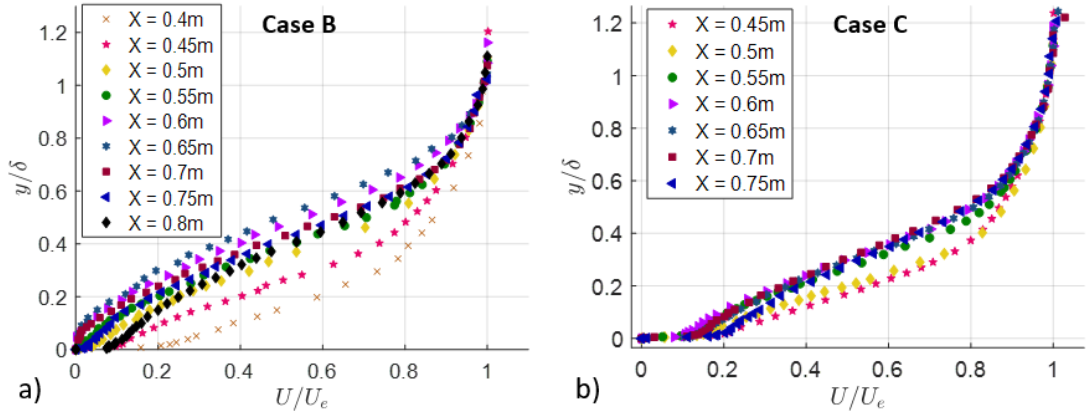


Figure 8.5 Conventional outer variable scaling of the mean flow of the centerline data for Case B (a) and Case C (b)

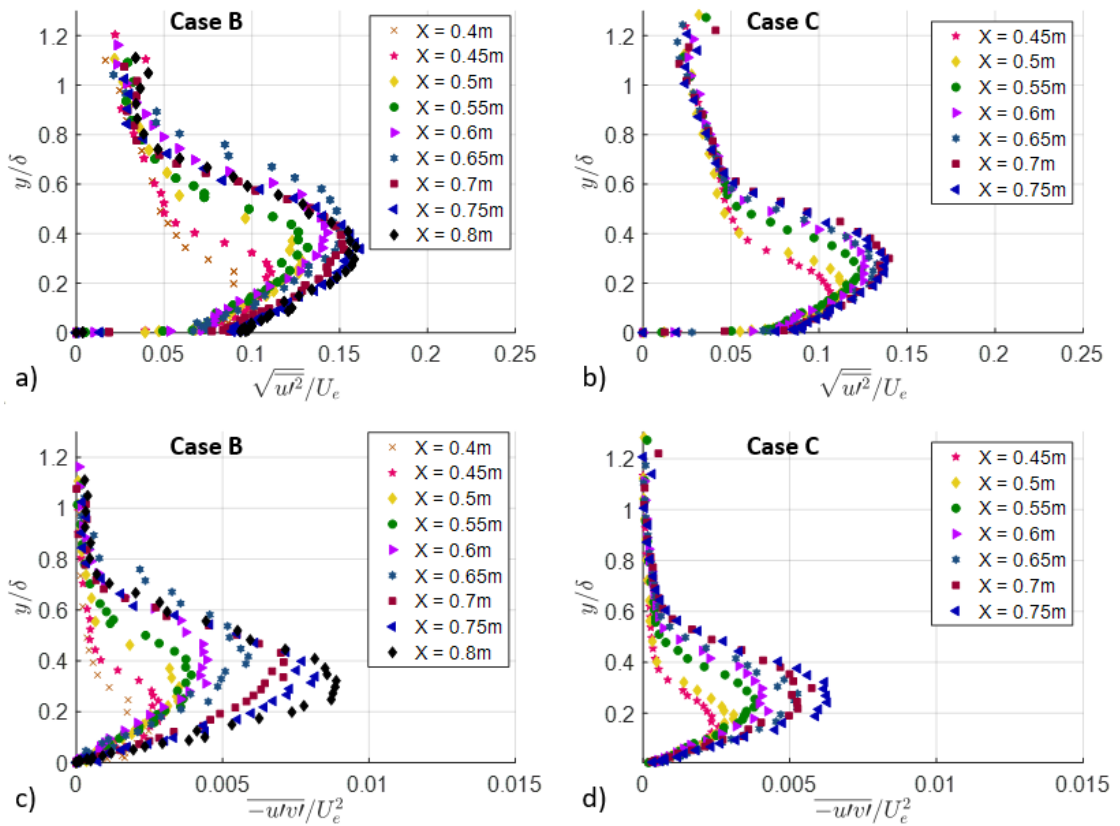


Figure 8.6 Conventional outer variable scaling of the turbulent normal, (a) and (b) and shear, (c) and (d), stresses of the centerline data for Case B, (a) and (c), and Case C, (b) and (d)

## 8.4 Embedded Shear Layer Scaling

While conventional outer variables scale the mean flow development rather poorly, applying embedded shear layer scaling actually scales it quite well. Figure 8.7 shows the same mean flow profiles given in Figure 8.5, now scaled using ESLS parameters. The result is quite remarkable, as the data obviously exhibit a good collapse indicating that, away from the surface the embedded free shear layer dominates the local flow physics. Over most of the boundary layer, the scaled mean velocity profiles are well approximated by the functional form

$$U^* = 1 - \tanh(\eta) \quad (8.7)$$

In the near wall region, the no-slip or separation conditions cause the data to deviate from this functional form, yet the individual collapse is still good. While the profiles shown in Figure 8.7 only include centerline data, the off-center profiles, as well as those occurring downstream where the pressure gradient changes, also exhibit fairly good collapse and are included in Appendix F.2.

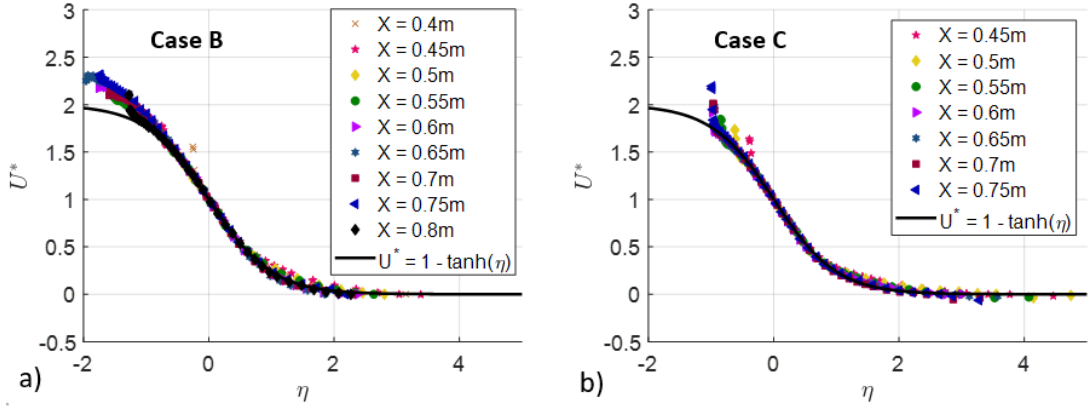


Figure 8.7 Embedded shear layer scaling of the inflectional mean velocity profiles of the centerline data for Case B (a) and Case C (b)

When the embedded shear layer scaling is applied to the turbulent normal and shear stresses there is significant variation in the magnitude of the scaled stresses, as shown in Figure 8.8. For the normal stress,  $\sqrt{\overline{u'^2}}$ , the variation in magnitude appears to be centered around the peak value of  $\sqrt{\overline{u'^2}}_{peak}/U_d \approx 0.21$ , which was the constant peak value observed in the non-curvature APG data sets analyzed by Schatzman and Thomas [56]. As for the turbulent shear stress,  $-\overline{u'v'}$ , the trend is the same and the scaled magnitude varies with streamwise location. Note that while Figure 8.8 only shows the centerline profiles, the off-span profiles exhibited similar trends. Furthermore, for both stress components there is a subtle variation in the scaled wall-normal coordinate of the stress peaks. This is shown by the black dashed lines in Figure 8.8 that deviate from the horizontal line,  $\eta = 0$ , corresponding to the wall-normal location of the outer inflection point. Hence, there are two streamwise development variation trends that need to be examined. First, the variation in the wall-normal peak location, i.e. why  $\eta(X)$  varies from zero, will be analyzed. Next, the increase in scaled stress magnitude with streamwise development, i.e. why the defect velocity fails to account for the increasing stresses, will be analyzed.

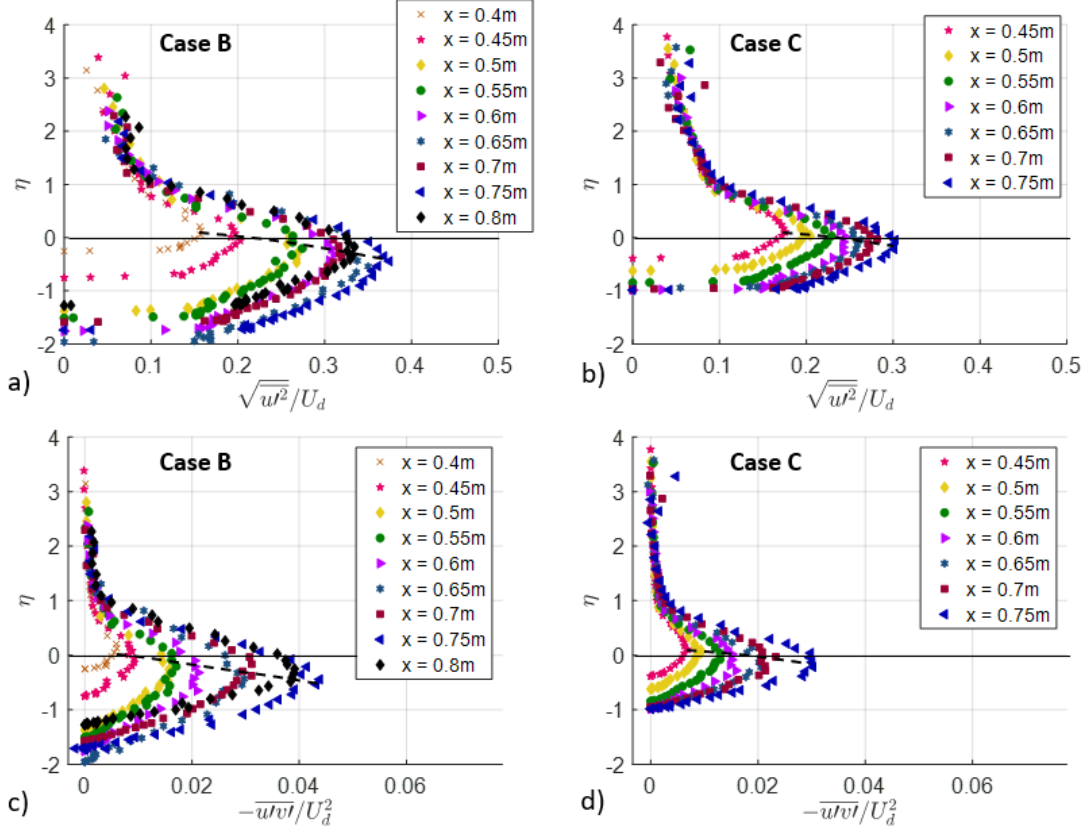


Figure 8.8 Embedded shear layer scaling of the turbulent normal, (a) and (b), and shear, (c) and (d), stresses of the centerline data for Case B, (a) and (c), and Case C, (b) and (d). Note the black dashed lines show the deviation of the peak turbulent stresses from  $\eta = 0$ .

### 8.5 Accounting for the Wall-Normal Variation in Stress Peak

The subtle variation in the scaled wall-normal coordinate indicates that the turbulence peak is not precisely tracking the inflection point of the mean profile ( $\eta = 0$ ), as would be expected. This can be shown even more clearly by plotting the wall-normal locations of the peak turbulent normal stress,  $y_{uu_p}$ , and outer mean profile inflection point,  $y_{IP}$ , in Figure 8.9. Note that the turbulent shear stress (not shown here) follows the same peak wall-normal location as the turbulent normal stress. Initially, the wall-normal location of the peak normal stress appears to closely follow that of the mean profile inflection point,

however its subsequent movement away from the wall does not match that of the inflection point and the disparity widens with streamwise distance. For Case B, Figure 8.9.a, this trend continues throughout the separation region; however, after the flow reattaches, the disparity narrows. For the attached flow of Case C, Figure 8.9.b, the widening trend continues.

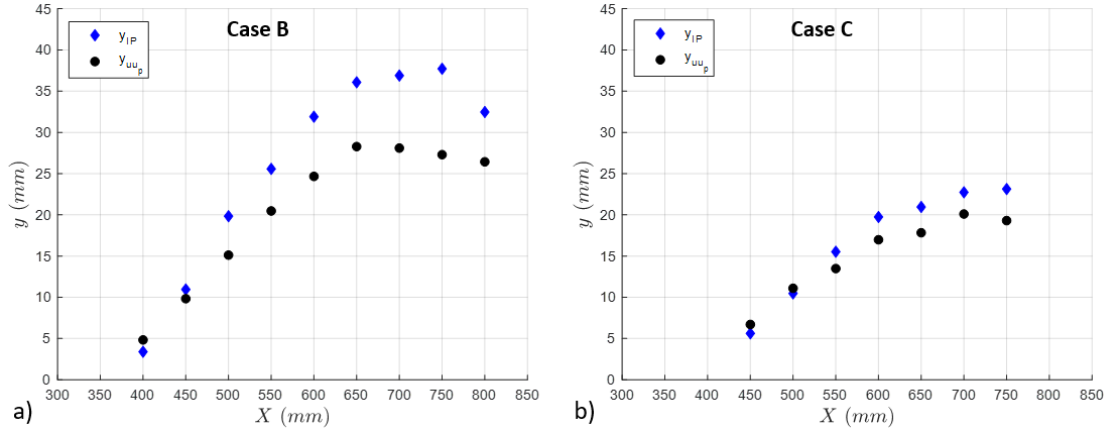


Figure 8.9 Wall-normal growth of the location of the peak turbulent normal stress and upper mean profile inflection point for the centerline data for Case B (a) and Case C (b)

The deviation of the peak turbulent stresses from the mean profile inflection point has also been observed in other similar experiments. In their study of a separating, reattaching, and recovering turbulent boundary layer developing over a rounded backward facing step, Song and Eaton [28] scaled the turbulent normal and shear stresses using the mean profile inflection point. They noticed that the profiles collapsed well among themselves and that both the stress peaks and inflection point locations were not dependent on Reynolds number. While they did not point out the extent of the deviation of the stress peak from the inflection point, examine its streamwise variation, or draw much attention

to it, analysis of their data [28] shows that most of it falls into the range of  $y_{uu_p}/y_{IP} \approx 0.7 - 0.8$ , where  $y_{uu_p}$  is location of the peak turbulent normal stress and  $y_{IP}$  is the outer mean profile inflection point location.

In order to better analyze the physical mechanism causing the peak turbulent stresses' movement away from the mean profile inflection point, the data of Figure 8.9 is replotted as the ratio of peak normal stress location over the mean profile inflection point location,  $y_{uu_p}/y_{IP}$ , as a function of streamwise development and is shown in Figure 8.10.a. This plot more clearly reveals that initially the peak stress location is above the mean profile inflection point. Around  $X = 0.45\text{-}0.5$  m, the peak stress location drops below the inflection point, and then around  $X = 0.55$  m, it stabilizes to a ratio of approximately 0.82, which is similar to that of Song and Eaton [28]. This switch in location of the peak stress from above to below the inflection point at  $X = 0.45$  m occurs right as the ramp surface curvature changes from convex to concave, indicating that the deviation is the result of surface curvature. Furthermore, the trend is the same regardless of whether the flow is separated or attached. The coincidence of the inflection point and peak normal stress around  $X = 0.45$  m, where there is no surface curvature, demonstrates support for the argument that the developing outer turbulence peak is associated with the inflectional instability of the mean flow, and it only deviates due to some physical effect that we expect is the result of surface curvature.

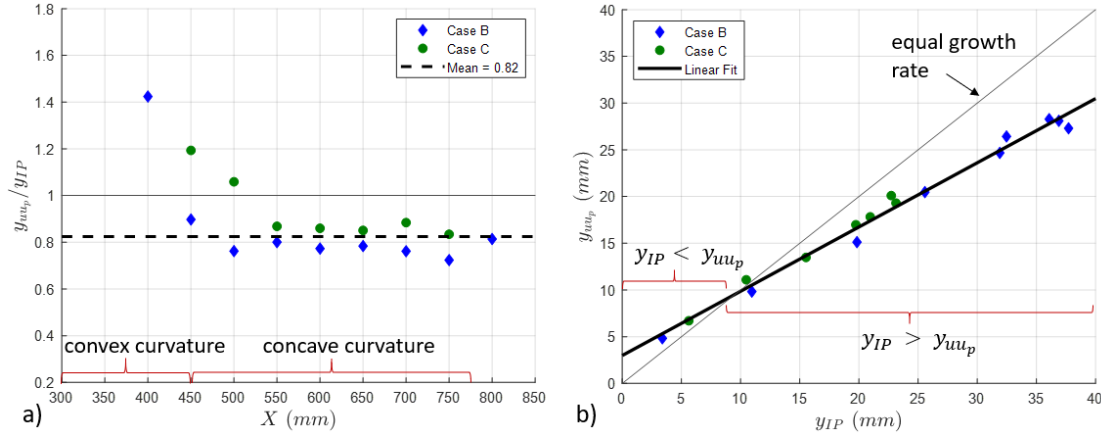


Figure 8.10 Plots showing the centerline peak turbulent normal stress location as it falls below the mean profile inflection point location and stabilizes around 0.82 (a), and the centerline peak turbulent normal stress location versus the mean profile inflection point location showing constant proportional growth for both cases (b)

As was shown in Chapter 6, the centrifugal force produced by the streamwise surface curvature likely generates secondary flow that is directed outward and inward along the convex and concave regions of the ramp, respectively. This may lead to wall-normal transport of the turbulent stresses and their deviation from the mean profile inflection point, as has been observed. Another way of examining the deviation of the turbulent normal stress peak from the mean profile inflection point is shown in Figure 8.10.b, which plots the peak turbulent normal stress location against the mean profile inflection point location. The peak turbulent normal stress location grows at a rate proportional to the inflection point location. This growth rate is the same for Cases B and C and is shown by the common linear fit. The intersection of the linear fit line with the directly proportional, equal growth rate line occurs just after the flow transitions from convex to concave curvature, again, highlighting the influence of surface curvature.

## 8.6 Modified Embedded Shear Layer Scaling

The wall-normal deviation of the peak stresses from the mean profile inflection point implies that any scaling of the turbulent stress profiles based upon the inflection point location will be in error. This error can be accounted for by adjusting the scaling variable  $\eta$  to track the stress peak location instead of the mean profile inflection point. The modified scaling variables are shown in Figure 8.11 and designated with a subscript ‘p’ which denotes that the scaling is based off the wall-normal location of the peak turbulent stress value. Note that for most of the profiles, the stress peak is below the inflection point, because most of the inflectional profiles occur over the concave curvature region. This not only changes the wall normal scaling,  $\eta_p$ , but also increases the modified defect velocity,  $U_{dp}$ , and vorticity thickness,  $\delta_{op}$ .

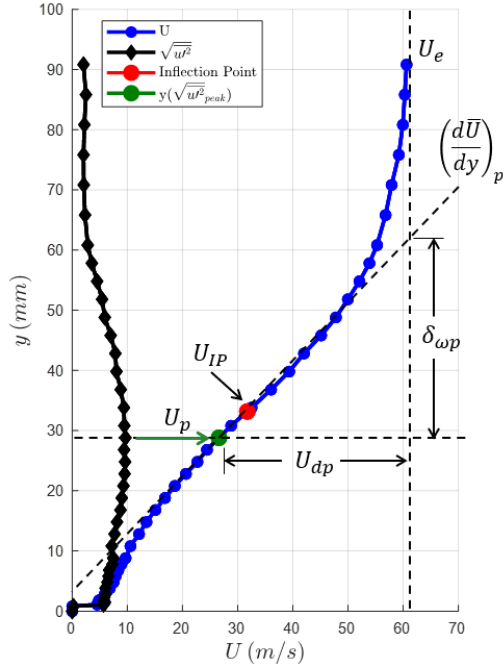


Figure 8.11 Illustration of the modified embedded shear layer scaling parameters for an inflectional mean velocity profile

While the modified scaling is employed to better scale the turbulent stress profiles, it should first be examined in its application to the mean flow profiles, Figure 8.12. Surprisingly, the modified parameters do a very good job of scaling the mean flow—perhaps slightly better than the original scaling parameters. In the near wall region, the collapse of the mean flow data is better than that shown in Figure 8.7, while in the outer profile region, it is slightly worse. This slight change in the quality of the fit makes sense because the location the scaling is based around, originally the mean profile inflection point and now the peak stress location, moves closer to the wall. Regarding this modified scaling, keep in mind that length and velocity scales are typically based on the mean profile and then applied to the turbulent stresses. This modified scaling operates somewhat out of

order, using scaling parameters that originate in the turbulent stress profile but are then actually defined by the mean velocity profile.

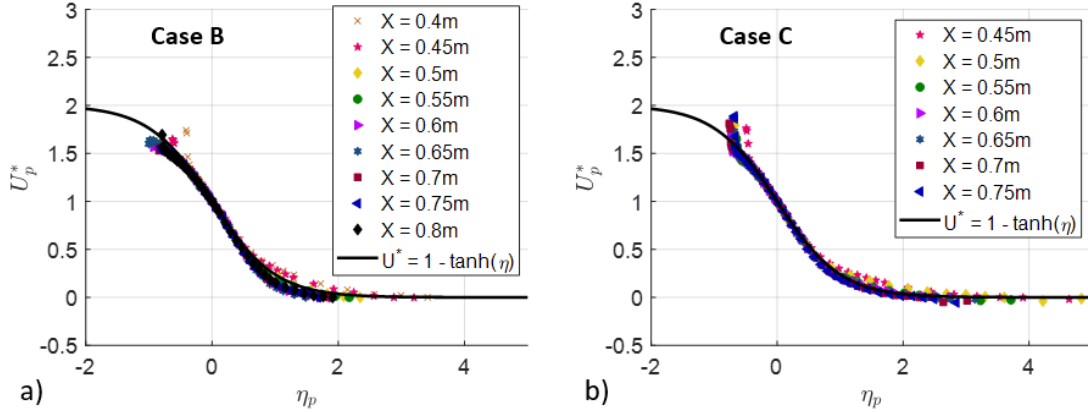


Figure 8.12 Modified embedded shear layer scaling of the inflectional mean velocity profiles for Case B (a) and Case C (b) for all spanwise locations

As for the scaled turbulent normal and shear stresses, shown in Figure 8.13, not only does the wall-normal coordinate collapse (as it now must by definition), but the slight change in the location on which the scaling is based has also altered the defect velocity,  $U_{dp}$ , so as to produce a tighter collapse in magnitude—still centered near the peak value of  $\sqrt{u'^2}_{peak}/U_d \approx 0.21$  as highlighted in the figure. While the collapse is significantly better than the original scaling, there is still variation in the turbulent stress magnitudes which appears to increase with streamwise development.

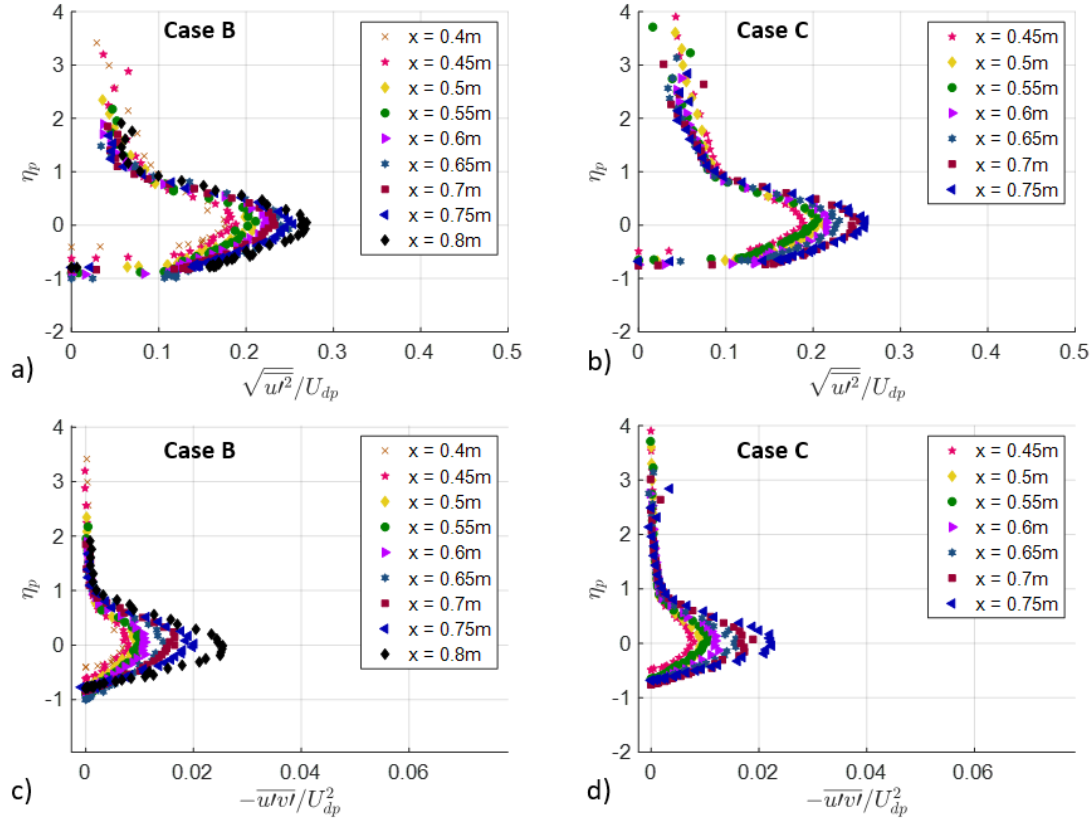


Figure 8.13 Modified embedded shear layer scaling of the turbulent normal, (a) and (b), and shear, (c) and (d), stresses of the centerline data for Case B, (a) and (c), and Case C, (b) and (d)

## 8.7 Streamwise Surface Curvature Effects

The growth in magnitude of the turbulent stresses, shown in Figure 8.13, is likely the result of streamwise surface curvature. The significance of surface curvature in a given flow is usually expressed as the ratio of the local boundary layer thickness to the local radius of curvature and is shown in Figure 8.14. Here, convex curvature is denoted as positive and concave curvature as negative. The leading edge of the ramp exhibits zero curvature followed by a region of convex curvature from  $X = 0$  m to  $X = 0.45$  m and concave curvature from  $X = 0.45$  m to  $X = 0.9$  m. The halfway point,  $X = 0.45$  m, exhibits zero curvature as do the trailing edge and all locations downstream. Figure 8.14 shows that

in the convex region, the local boundary layer thickness approaches 3.3% of the radius of curvature, while in the concave region downstream it surpasses 11%, due to the thickening of the separated boundary layer—both values are significant.

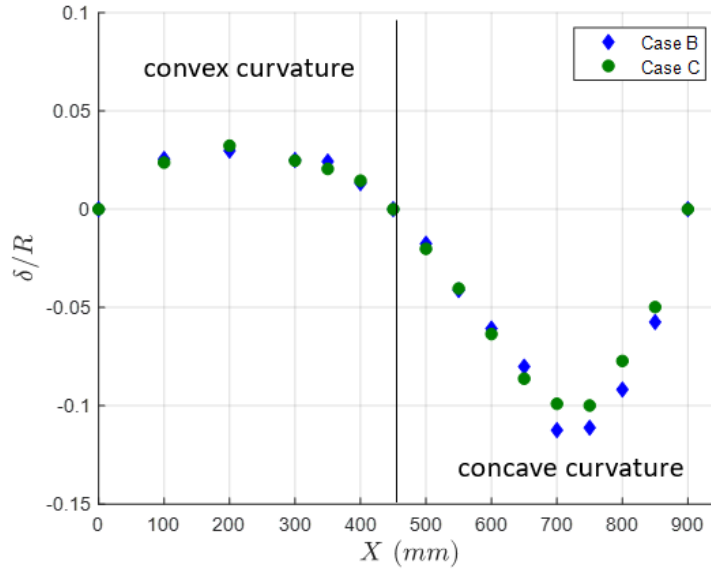


Figure 8.14 The significance of surface curvature along the ramp plotted as the ratio of local boundary layer thickness to local radius of curvature with convex curvature being positive and concave curvature negative

The effect of surface curvature on turbulent boundary layers has received much attention throughout the years. Many have conducted studies on concave curvature [121,122], convex curvature, [123–125] and both [126,127]. For flows involving mild convex curvature, with  $\delta/R > 1\%$ , turbulent stresses have been shown to be suppressed below plane flow values [123,124] and suppressed in their diffusion away from the wall [127]. On the other hand, for flows involving concave curvature, a type of longitudinal vortices are reported to be generated that, in conjunction with the curvature, change the turbulence structure and increase turbulent stress values away from the wall [121,122].

These and other effects are discussed in a review of the subject by Patel and Sotiropoulos [128], who also summarize four generally recognized and uncontested statements regarding curvature effects, which they state as:

1. The effects of curvature (on the turbulence) are nonlinear, being proportionately larger on mildly curved ( $\delta/R < 0.01$ , say) surfaces than on surfaces with moderate ( $\delta/R \sim 0.1$ ) or strong curvature ( $\delta/R \sim 1$ )
2. The effects of convex and concave curvatures are opposite and asymmetric
3. A turbulent flow responds to convex curvature faster than to concave curvature
4. A turbulent flow recovers slower from convex curvature than from a concave curvature

This summary regards curvature, without considering pressure gradient effects.

While some of these studies have considered regions containing a mild pressure gradient, over the majority of their streamwise development, the pressure variation was subtle, largely removing its effect. Moreover, many suggest that the effects of pressure gradients are more prominent than those of surface curvature and hence would dominate the flow [128]; however, this is not necessarily the case.

A joint university study reported by Cullen et al. [129] compared a smooth-body APG flow developing over a curved ramp geometry to that developing over a flat plate geometry. The study found that for the flat plate, both the mean and turbulence intensity profiles collapsed when scaled using local freestream velocity and momentum thickness, whereas for the curved ramp geometry, only the mean profiles collapsed. Instead, the turbulence intensity only scaled in the wall-normal direction with the peak magnitude growing with downstream extent. The authors attribute this difference to the “concave curvature causing a lack of equilibrium in the boundary layer” and remark that this is

noteworthy evidence “that concave surface curvature, generally considered as being secondary to a strong adverse pressure gradient, plays a very significant role in a flow approaching separation” [129].

Although the aforementioned studies are for boundary layers, the impact of surface curvature on the turbulent stresses behaves in much the same way for curved shear/mixing layers [130–132]. Plesniak, Mehta, and Johnston [130], for example, showed that stable curvature can reduce the turbulent stresses by as much as twice that of similar unstable curvature, with the straight layer value laying in-between. Note that surface curvature is considered stable if the radial gradient of angular momentum is positive [131]; this equates to convex curvature for a boundary layer. Likewise, surface curvature is considered unstable if the radial gradient of angular momentum is negative; this equates to concave curvature for a boundary layer. The similar influence of curvature on the turbulent stress development in boundary and shear layers implies that it is insignificant whether the flow is attached or separated. This is also supported by the similar trends in turbulent stress development for the separated flow Case B and attached flow Case C.

The effects of surface curvature described in this brief review are very similar to those observed in the ND ramp experiments. Before discussing how these effects manifest themselves in the ND ramp experiments, it is instructive to provide a comparison of the original and modified ESLS peak stress growth rates as a function of streamwise extent, Figure 8.15. Notice that with the modified scaling there is excellent agreement for Cases B and C, as they both take on common growth rates and initial turbulent stress values. The linear curve fits are shown in Figure 8.15.b as the solid blue and green lines for the turbulent normal and shear stresses, respectively. This is not the case for the original scaling, where

Case B has both higher growth rates and higher initial turbulent stress values than Case C. Here, the linear curve fits are shown in Figure 8.15.a as the solid lines for Case B and dashed lines for Case C, with the turbulent normal and shear stresses distinguished by blue and green lines, respectively. The linear fits' commonality for the modified scaling provide another reason why accounting for the turbulent stress peaks deviation from the mean profile inflection point is necessary to properly scale the flow and understand its development.

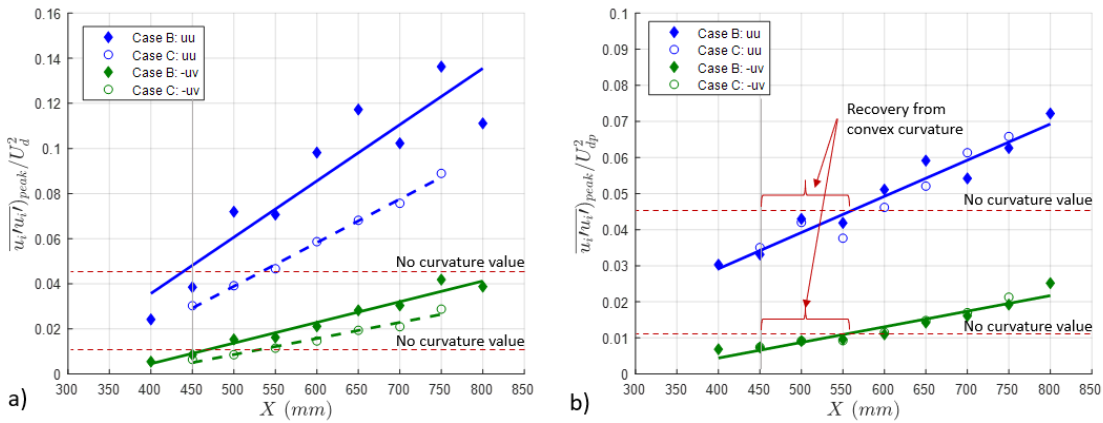


Figure 8.15 Streamwise growth of the peak turbulent normal and shear stresses scaled using both original (a) and modified (b) embedded shear layer scaling with linear fit(s) applied to each data set

For either defect velocity scaling, in general, the turbulent normal and shear stress profiles that have attenuated magnitudes, compared to similarly scaled flow developing over a straight geometry, occur over the convex region (which is stabilizing), whereas those that exhibit increased magnitudes occur over the concave region (which is unstable). Here the reference values<sup>15</sup> are  $\overline{u'u'})_{peak}/U_d^2 \approx 0.044$  for the normal stress and  $\overline{u'v'})_{peak}/U_d^2 \approx 0.011$  for the shear stress, which are the values known to collapse the flat plate APG BL data from Schatzman and Thomas [56] and are shown as horizontal red dashed lines in Figure 8.15. Note that now, for consistency, the streamwise normal stress is defined as  $\overline{u'u'})_{peak}/U_{dp}^2$ , which is the square of that shown Figure 8.13.a-b. The slow recovery from convex curvature and slow response to concave curvature can also be seen in Figure 8.15. For example, Figure 8.15.b shows that both the normal and shear turbulent stress peak magnitudes surpass the reference values around  $X = 0.55m$ , which is downstream from where the curvature becomes concave. For the original scaling, the trend is not as clear. In Figure 8.15.a, the turbulent stresses for Case C show a delayed response time while those of Case B do not.

The shear layer experiments of Plesniak, Mehta, and Johnston [130] showed that the application of a constant curvature either magnifies or attenuates the turbulent stresses to a constant value once similarity is reached. For the ramp flow experiments, the curvature is continuously changing, so it should not be expected to reach a state of similarity. This, in combination with the delayed response time, makes any direct correlation between the

---

<sup>15</sup> Note that the reference values in Figure 8.15.b are given in terms of  $U_{dp}$ , not  $U_d$ , so a direct comparison to the reference flat plate data (where  $U_d$  is used) is likely to deviate slightly, as is observed.

turbulent stress magnitudes and the local ramp curvature rather difficult. The time scales of the mean flow (see Appendix F.3) are much smaller than those of the turbulent stresses, hence the mean flow is able to respond to the ramp curvature much faster than the turbulent stresses are able to. Overall, this provides evidence that the ramp surface curvature is the primary factor causing the turbulent normal stresses to be out of equilibrium with the mean flow when scaled using embedded shear layer parameters, original or modified.

If the growth of the peak turbulent stresses can properly be accounted for, and a set of scaling parameters presented, how well could they collapse the stress profiles? Figure 8.16 answers this question by showing the same turbulent normal and shear stress profiles presented in Figure 8.13, now scaled with both the modified ESLS and the stress magnitudes that have been scaled by the stress peaks shown in Figure 8.15.b. All of the profiles exhibit excellent collapse. This normalization implies that the shapes of turbulent stress profiles do not change significantly and that if the stress peak growth can be accounted for, a scaling may exist. It should be emphasized that the results of Figure 8.16 do not provide a set of generic scaling parameters in and of themselves, rather, they show that it may be possible to scale the flow.

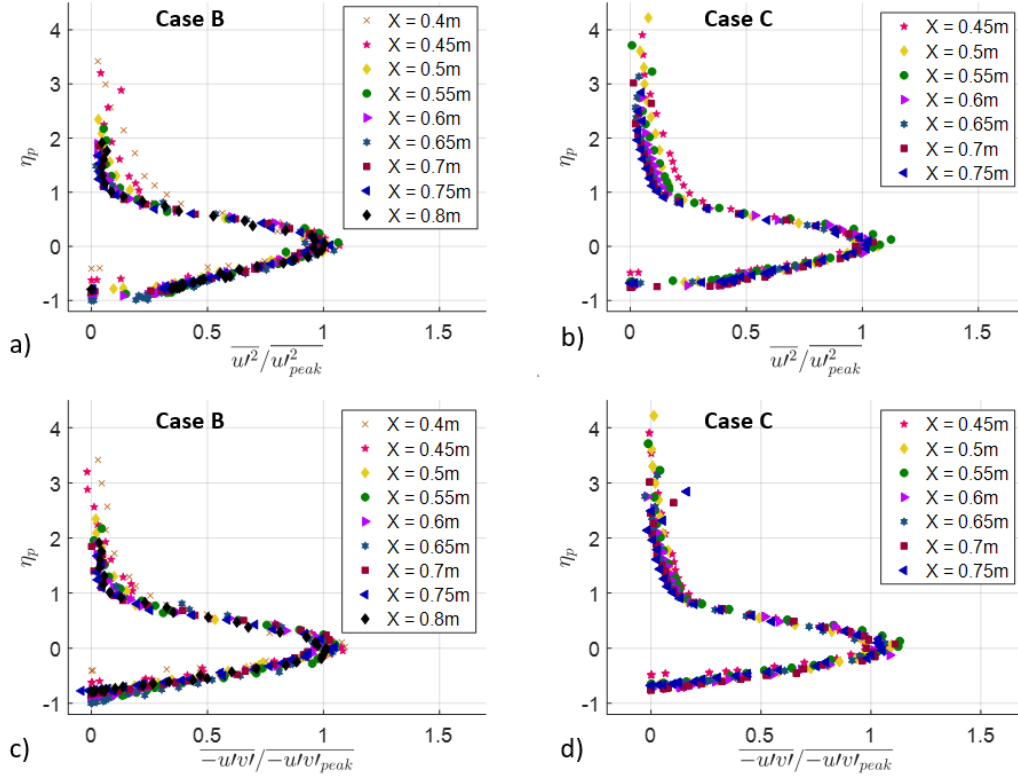


Figure 8.16 Modified embedded shear layer scaling and peak stress normalization of the turbulent normal, (a) and (b), and shear, (c) and (d), stresses of the centerline data for Case B, (a) and (c), and Case C, (b) and (d)

## 8.8 Coordinate Rotation for Reynolds Shear Stress

Thus far, the mean and turbulent stresses have been examined in a wall-normal coordinate system. This captures the physics of a developing boundary layer that is tracking the local wall curvature. However, this should really be thought of as the mean flow tracking the local wall curvature because the time scales of the mean flow are smaller than those of the turbulence stresses. Furthermore, it was noted above that a flow is slower to respond to concave curvature and slower to recover from convex curvature. Since the flow over the ramp rapidly transitions from a region of convex to concave curvature, it was hypothesized that the turbulent shear stresses may not be tracking the wall and may be, in effect, frozen. This result would not be observable in the streamwise variation of the wall-

normal profiles, as the turbulent shear stress is highly dependent on the coordinate system in which it is calculated, i.e. it is not invariant to coordinate rotation. While the turbulent normal stresses are also dependent on the coordinate system, they are only mildly dependent, as will be shown below.

While the data were collected in a locally wall-normal coordinate system, it is of interest to recalculate the turbulent shear stresses from the concave regions ( $0.45 \text{ m} < X < 0.9 \text{ m}$ ) in a reference coordinate system aligned with that of  $X = 0.45 \text{ m}$ . This coordinate system was chosen because it corresponds to the location between convex and concave surface curvature on the ramp. This process can be conducted in two ways: (1) by rotating the coordinate system before calculating the turbulent shear stress correlation, which requires reprocessing the original time series of data, or (2) by using a second order tensor transformation, equation (8.8), on the existing turbulent shear stresses to rotate the coordinate system through the angle  $\theta$ , which utilizes the normal stresses.

$$\overline{u'v'} = \frac{1}{2} [\overline{(v'v')}_l - \overline{(u'u')}_l] \sin(2\theta) + \overline{(u'v')}_l \cos(2\theta) \quad (8.8)$$

In equation (8.8), the subscript ‘*l*’ corresponds to a value in the original local coordinate system and  $\theta$  is the angle of rotation to the new system aligned wall-normal with  $X = 0.45 \text{ m}$ . Both methods were utilized and are in full agreement with one another. Using the first method, shown in Figure 8.17.a, one can see how the rotation of the coordinate system at a single point changes the u-v scatter plot such that the shear stress correlation is weakened. This can also be seen for an entire profile in Figure 8.17.b. For example, this figure shows the original turbulent shear stress profile for Case B at  $X = 0.6 \text{ m}$  and  $X = 0.45 \text{ m}$  and the

turbulent shear stress at  $X = 0.6$  m rotated so that its coordinate system matches that of  $X = 0.45$  m. While the profile has widened in its wall-normal extent, remarkably, the magnitudes of the peaks are in good agreement.

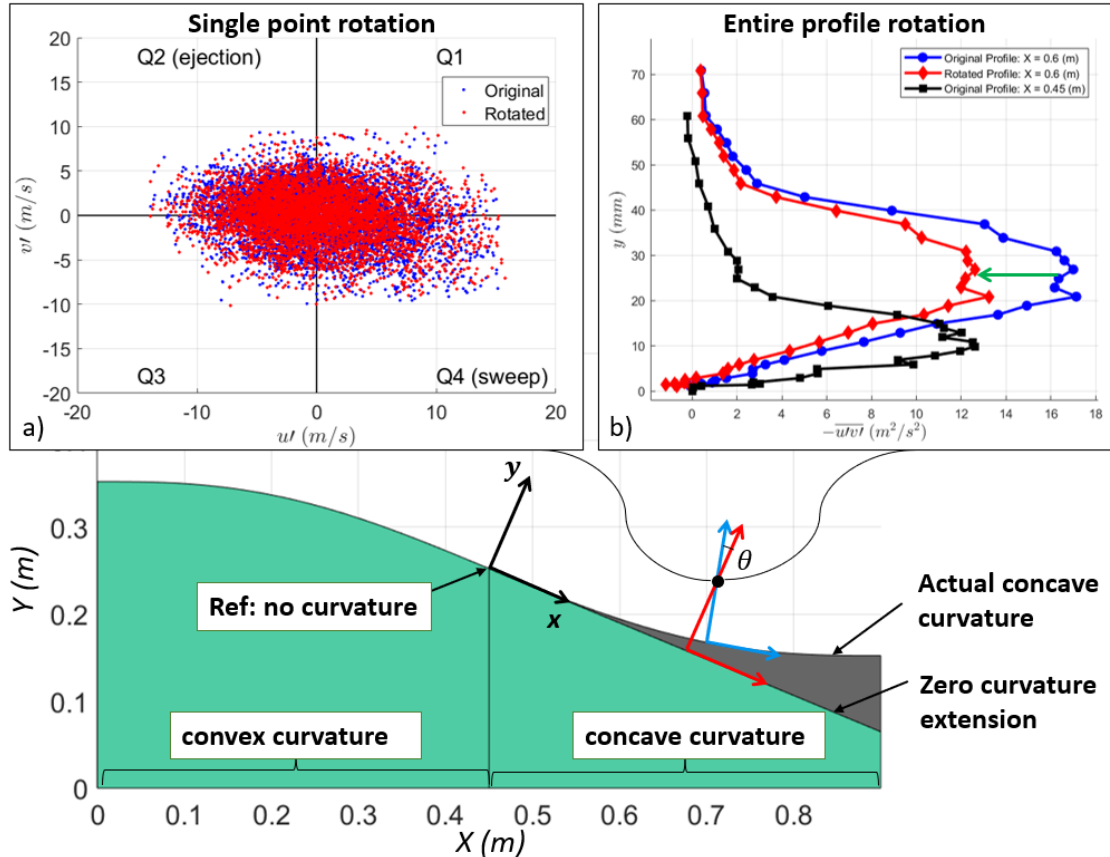


Figure 8.17 Illustration of the rotated turbulent shear stress correlation for a single point (a) and for an entire profile (b). Part (c) shows the original turbulent shear stress at  $X = 0.6$  m and  $X = 0.45$  m and the turbulent shear stress at  $X = 0.6$  m rotated so that its coordinate system matches that of  $X = 0.45$  m.

Repeating this process for all centerline profiles ranging from  $X = 0.45$  m to  $X = 0.8$  m, shown in Figure 8.18.a-b, yields the same remarkable result—the magnitude of peak turbulent shear stress in each case remains constant, see Figure 8.18.c-d. This seems to imply that the turbulent shear stress is not tracking the wall in the concave region but instead is being advected downstream, seemingly unaware that the wall is curving up toward it. Another way to picture this is to imagine that the ramp surface, tangent at  $X = 0.45$ , extends linearly downstream instead of curving up into the flow. This is shown as the zero-curvature extension in Figure 8.17. In this hypothetical scenario, the coordinate system of the flow does not rotate counterclockwise (as a local wall-normal coordinate system would) in the streamwise development, but instead remains constant. This is what the turbulent shear stresses seem to experience, and the farther away the flow is from the wall, the less likely it is to sense the ramp curvature. Figure 8.18.c and Figure 8.18.d show that in the near-wall region, the rotated turbulent shear stresses are reduced enough to change signs. While this change of signs could be due to reversed flow, it is more feasible that the flow is tracking the wall here and the rotation over predicts reality.

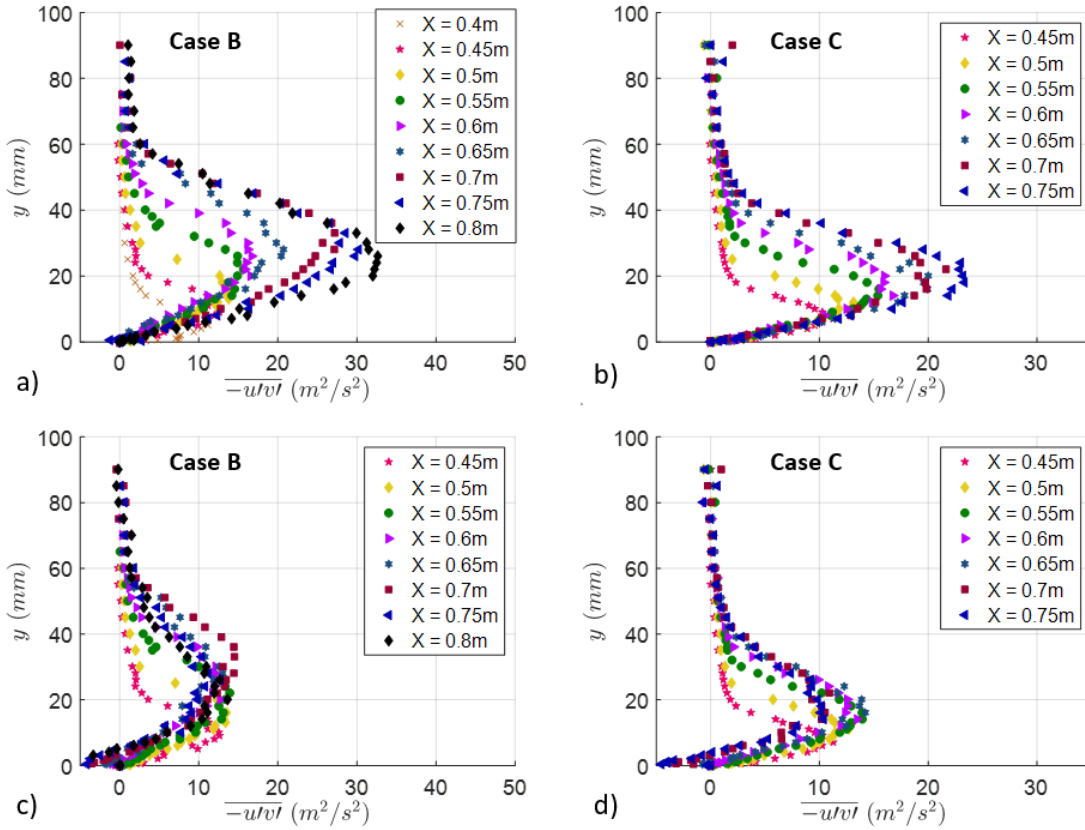


Figure 8.18 Comparison of unscaled turbulent shear stresses, (a) and (b), and unscaled turbulent shear stresses now rotated to wall-normal reference frame at  $X = 0.45$  m, (c) and (d)

Since the modified embedded shear layer scaling adequately scaled the wall-normal coordinate of the turbulent stresses, it is applied again here. This time, the turbulent shear stresses were first rotated and then scaled with the modified defect velocity,  $U_{dp}^2$ . The result, shown in Figure 8.19, is a set of neatly collapsed profiles with a peak value of approximately  $-\overline{u'v'})_{peak}/U_{dp}^2 \approx 0.009$ , which is slightly less than the value of  $-\overline{u'v'})_{peak}/U_d^2 \approx 0.011$ , which was observed in the cases without surface curvature. As mentioned before, this small difference is likely present because the modified defect velocity,  $U_{dp}$ , is slightly larger than the original defect velocity,  $U_d$ , since the turbulent

stress peak lies below the mean profile inflection point. Even with this small difference, the magnitudes still exhibit very good collapse among themselves.

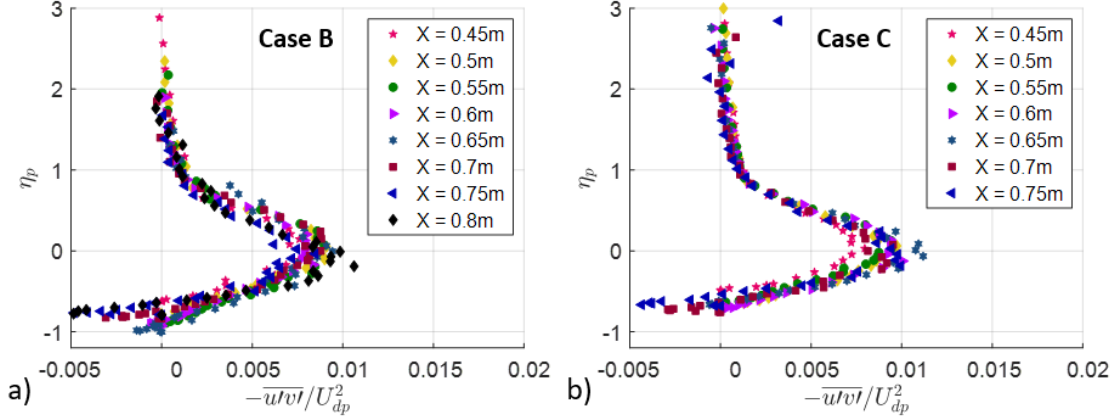


Figure 8.19 Turbulent shear stress profiles rotated to the  $X = 0.45$  m wall-normal reference frame and scaled using the modified embedded shear layer scaling for Case B (a) and Case C (b)

As alluded to earlier, the rotation of the coordinate system that was just applied will not work with the turbulent normal stresses, as they are only mildly dependent on the coordinate system orientation. To show this, the data from Figure 8.15, which gives the peak turbulent normal and shear stresses, are replotted in Figure 8.20 and now include the peak stresses rotated to the  $X = 0.45$  m wall-normal reference frame. Examining the modified ESLS in Figure 8.20.b, we see that the scaled peak turbulent shear stresses, once rotated, change from having a positive streamwise growth rate, solid green line, to an approximately-zero growth rate, the solid black line. This is what was observed as a constant turbulent shear stress peak in Figure 8.18.c-d and Figure 8.19. The scaled peak turbulent normal stresses, however, undergo almost no change in growth rate after rotating their reference frame, as the solid blue and red lines indicate. What this implies is that destabilizing streamwise curvature (which is concave in the cases examined here) acts to

enhance the turbulent normal stresses. It is not simply a rotation of the reference frame that produces the higher stress values.

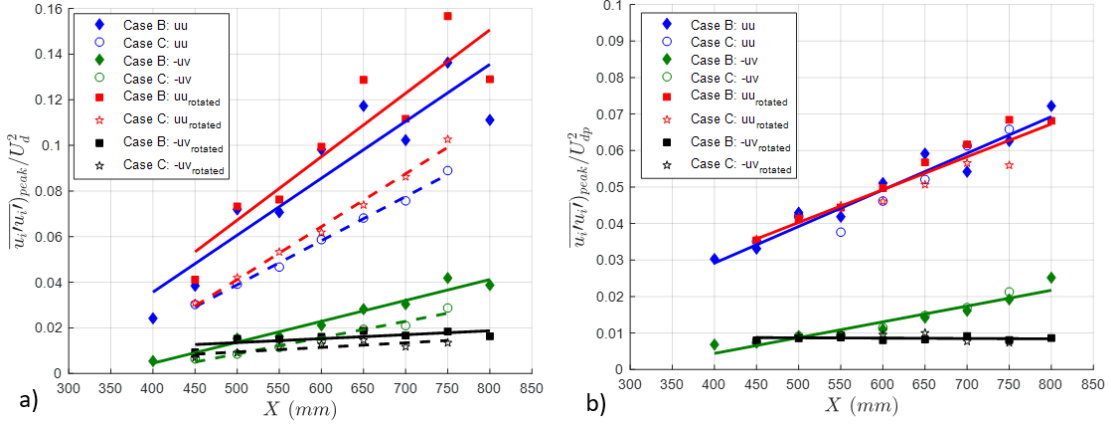


Figure 8.20 Comparison of peak turbulent normal and shear stresses with that of those rotated to the  $X = 0.45$  m wall-normal reference frame and scaled using both original (a) and modified (b) embedded shear layer scaling with linear fits applied to each data set

While it was just shown that the peak turbulent normal and shear stresses behave differently when analyzed in the locally wall-normal and fixed (rotated to  $X = 0.45$  m) coordinated systems, the physical mechanism for this is still not fully understood. One possible way to examine this further is to analyze the turbulent kinetic energy (TKE) production. In tensor notation, production of TKE, per unit mass, is defined as

$$Production = -\bar{u}_i' \bar{u}_j' \frac{1}{2} \left( \frac{\partial U_i}{\partial x_j} + \frac{\partial U_j}{\partial x_i} \right). \quad (8.9)$$

Assuming the flow is two-dimensional and that  $\frac{\partial V}{\partial X}$  is small, equation (8.9) can be simplified to:

$$Production = -\overline{u'v'} \frac{\partial U}{\partial y} + (\overline{u'u'} - \overline{v'v'}) \frac{\partial V}{\partial y} \quad (8.10)$$

and plotted for the centerline data from Cases B and C, Figure 8.21. Once the shear layer develops, the magnitude of outer peak production does not change significantly; this location is also roughly where the destabilizing curvature begins. This can be more clearly seen in Figure 8.22. Around this transition,  $X = 0.45$  m, the peak production rapidly moves away from the wall and widens. The widening of the production profile is known to be caused by destabilizing curvature [131]. Furthermore, in the separation region for Case B, the production appears to be constant.

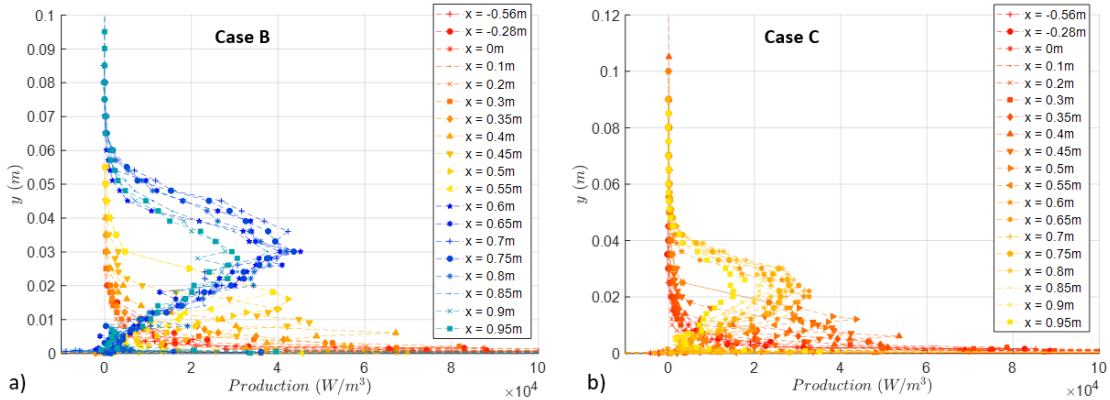


Figure 8.21 Streamwise development of TKE production for Case B (a) and Case C (b) showing that once the shear layer develops, the outer production peak does not change significantly

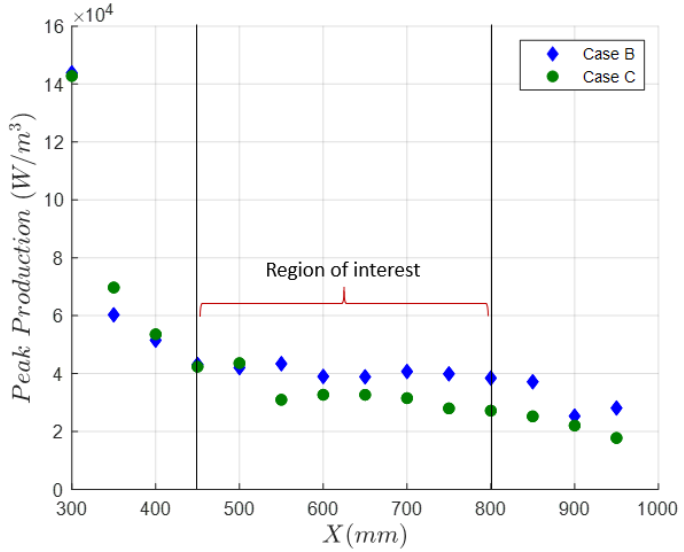


Figure 8.22 Peak TKE production appears to be roughly constant from  $0.45 \text{ m} < X < 0.8 \text{ m}$

While the peak production is roughly constant from  $0.45 \text{ m} < X < 0.8 \text{ m}$ , the turbulent normal and shear stress peaks, shown in Figure 8.15, grow linearly. Comparing these turbulent stress growth rates to equation (8.10) implies that the mean flow gradients must relax to yield a constant production. In the rotated reference frame, the turbulent peak shear stress is constant. This means that, roughly speaking, the turbulent shear production, the first term on the right hand side of equation (8.10), is decreasing as the mean flow gradient relaxes. For TKE production to be constant, the normal production term must be growing at a greater rate in the rotated reference frame than in the wall-normal coordinate system. This is exactly what is observed. Figure 8.23 shows the difference in peak normal stresses, scaled using the modified defect velocity, for both the wall-normal coordinate system and the rotated coordinate system. In the rotated coordinate system, the growth rate is larger than that of the wall-normal coordinate system.

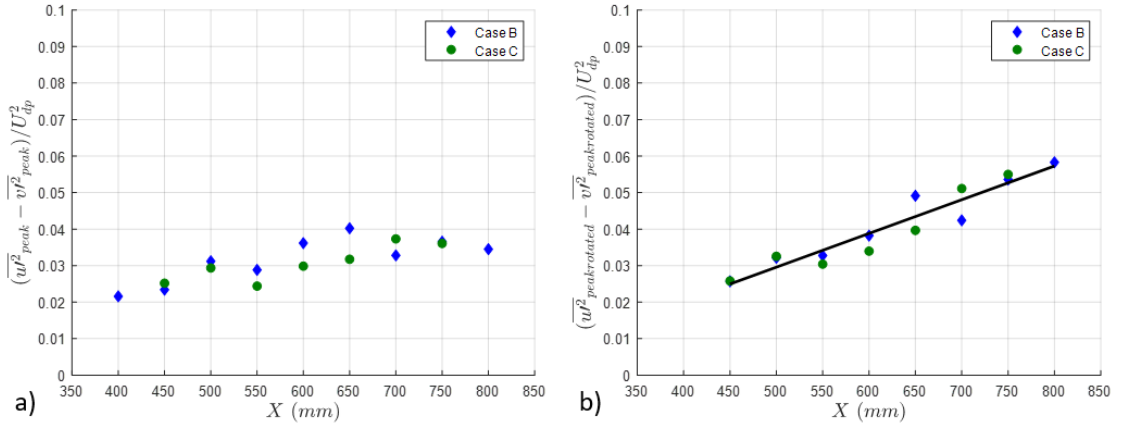


Figure 8.23 Growth of the scaled difference in peak normal stresses for the wall-normal coordinate system (a) and rotated coordinate system (b)

In conclusion, while the growth of the peak turbulent normal and shear stresses behaves differently in the wall-normal and rotated coordinate systems, the peak TKE production, which is a scalar quantity, appears to be constant. Rotation of the reference frame acts to increase either shear or normal production, while the other quantity subsequently decreases, and the overall production remains constant.

## CHAPTER 9: CONCLUSIONS AND RECOMMENDATIONS FOR FUTURE WORK

### 9.1 Conclusions

There is a clear need to expand the range, reliability, and applicability of CFD simulations and reduce the computational costs involved. Perhaps nowhere is this more evident than in the challenging prediction of turbulent smooth-body flow separation. As part of the turbulence modeling improvement and development process, the CFD Vision 2030 study [3] highlighted the need for additional benchmark experiments as a means of providing validation quality data sets. *The work of this dissertation is intended to satisfy this need by providing archival data sets containing the results from a series of smooth-body flow experiments. These document both separated and attached adverse pressure gradient flow, for the purpose of furthering CFD validation and turbulence model improvement.* Three test cases were examined: Case A, larger-scale separation and reattachment, Case B, smaller-scale separation and reattachment, and Case C, attached APG flow development. The use of a single ramp geometry for all three test cases was unique to these experiments. The geometry consisted of a two-dimensional, smooth, backward-facing ramp that is analytically defined in terms of a fifth-order polynomial.

The experiments were conducted at a unit Reynolds number of  $\text{Re} \approx 10^6/\text{m}$  ( $\text{Re}_0 \approx 10^4$ ), which is low enough to be accessible to various CFD methods, yet high enough to

accurately represent practical problems. Extensive inflow and boundary condition documentation—lacking in many earlier experiments—provides CFD users the necessary boundary conditions to numerically replicate the series of experiments. This included detailed documentation of the flexible ceiling geometry, hot-wire profiles of the incoming boundary layer on both the development plate and wind tunnel sidewalls, surface skin-friction measurements of both the incoming flow and the flow at the start and end of the ramp, surface streamwise and spanwise pressure measurements, and images the surface flow separation patterns. The complete data set and documentation is provided on the NASA Langley Research Center Turbulence Modeling Resource website [1].

While initially a two-dimensional flow separation was sought after, extensive surface oil-film flow visualization experiments showed that in the central region of the ramp, the flow separates via two counter-rotating vortical structures. A literature search revealed that, while this type of flow separation appears to be common for smooth backward-facing ramp geometries, there is very little detailed documentation and characterization of it. Of the studies [48,52,53,72] featuring similar separation patterns, almost all were focused on flow control applications. Only a brief discussion was given to the baseline surface flow, while the sidewall flow interaction was not examined at all. The surprising nature of this flow separation structure and the general lack of understanding of how, and if, the sidewall/ramp juncture flow separation contributes to the central separation introduced a second focus of this work—*the characterization of the smooth-body flow separation and reattachment surface topography and topology, including both its generic character and the influence of the sidewall/ramp juncture flow separation.*

Detailed surface flow visualization studies conducted on both the ramp surface and wind tunnel sidewalls showed, via topographical patterns, that the central vortical separation structures are distinct from the sidewall/ramp junction flow separation even though they are part of the same global line of separation. However, while this separation topography was three-dimensional for cases A and B, the reattachment topography was uniform in spanwise extent. The only significant deviation from two-dimensionality was a crossflow directed toward each sidewall, which LDV measurements showed was up to 35% of the streamwise mean flow. Furthermore, the separation patterns were very repeatable run-to-run, yet highly sensitive to imposed upstream geometric perturbations in the boundary layer.

A deeper investigation into the separation structure was conducted for Case A to reveal the flow topology. Using the singular points identified in the surface flow topography pattern, a surface flow topology map was proposed that presented a concise description of the surface flow field for both the ramp surface and wind tunnel sidewalls. It agreed with both the available singular-point data and the rules of topology. This surface flow topology map was extended to the off-surface flow to provide an illustration of both the separation and downstream advection of the central, counter-rotating vortical structures and the formation of the central separation region.

The three-dimensional flow separation topology takes on the owl-face pattern (OFP) of the fourth kind. The OFPs are some of the most common forms of flow separation and the simplest that occur for three-dimensional flows [75,91]. By analyzing the ramp flow cases, and the works of Fairlie [75] and Wickens [95], it was discovered that the OFPs are often part of a larger structure which are called the “generalized owl-face pattern”. The

generalized owl-face pattern is a simplistic surface flow topology structure, consisting of a repeating pattern of saddle-points (SP) and foci (F) for separation and nodes (N) and saddle-points for reattachment. While the ramp flow separation takes the form of the generalized owl-face pattern, the pattern itself does not define the number of connected singular points, which can vary, Figure 5.10. Topologically, a reduced separation structure consisting of fewer singular points is possible, yet it was not observed for either of the separation cases. This raised the question of what causes extra saddle/foci pairs to form in the central region?

Two aspects of the geometry, streamwise surface curvature and the sidewall/ramp junctures, were analyzed with the intent to explain the unique separation saddle point/foci pattern that was observed. Given the similarity to a circular s-duct, the centrifugal force generated by streamwise surface curvature appears to produce a small secondary “cross” flow. In s-ducts, this secondary flow is widely known to produce a separation structure consisting of two counter-rotating vortical structures, taking the form of the owl-face pattern of the first kind. This secondary flow forms differently in ducts of rectangular cross-section due to the sidewall/ramp junctures, which are not present in circular s-ducts. *The streamwise surface curvature induced secondary flow is influenced by the sidewall/ramp junctures, causing the additional saddle-foci pairs and the owl-face pattern of the fourth kind.* The occurrence of curvature induced secondary flows is consistent with the observed surface and proposed off-surface flow topology, including the central counter-rotating central vortical separation structures.

While streamwise surface curvature has an important role in the formation of the vortical separation pattern, ultimately the roles of both surface curvature and the

sidewall/ramp juncture flow dictate the formation of the surface separation patterns. A series of passive flow control experiments that involved perturbing the tunnel sidewalls were designed to examine the effects of the sidewall/ramp juncture and sidewall flows. Control devices were applied to alter the sidewall flow and produce a fluid motion, acting either in conjunction or opposition to the secondary flow that is generated via streamwise surface curvature. The control devices had a significant impact on the flow field. Those that opposed the curvature-induced secondary flow caused the primary vortical structures to shift toward the sidewalls, thereby producing a more spanwise uniform flow separation in the central region. On the other hand, those devices whose motion supported the curvature-induced secondary flow caused the sidewall vortical separation structures to move away from the sidewalls, toward the central region of the ramp. The passive flow control experiments demonstrated two additional points. First, *the sidewall/ramp juncture flow separation condition is highly coupled with the centerline flow separation location and extent*. The coupling is inverse such that with increasing sidewall separation extent there is decreasing centerline separation extent, and vice versa. Second, while the separation structure and location can be highly influenced by the control devices, *both the location and uniformity of the central reattachment structure are insensitive to changes in the separation structure.*

Extensive off-surface flow measurements, including both first and second order turbulence quantities, were taken using 2-component LDV. To capture the flow's three-dimensionality, three spanwise measurement planes were utilized. These consisted of the centerline,  $Z/S = 0$ , and two off-center planes,  $Z/S = -0.14$  and  $Z/S = -0.28$ , where the span,  $S$ , is 0.914 m (3 ft). In general, the greater the extent of separation, the more

prominent the three-dimensionality of the flow. For example, the attached flow, Case C, was the most spanwise uniform, while the larger-scale separation case, Case A, had the most variation between successive spanwise profiles. The streamwise development of the flow was characterized via LDV profiles acquired at 19 streamwise locations, extending from the inflow condition to beyond the ramp trailing edge, which was downstream of the reattachment location. Interpolating the near wall mean flow showed that for Case A the separation extent covered approximately 39% of the ramp's length, while for Case B it covered only around 24%. In both cases, *the separation regions exhibited significant spanwise variation that was almost solely due to the variation in separation location, as the reattachment location was very spanwise uniform.*

Analyzing the positive fraction of time in which the streamwise flow was directed downstream,  $\gamma_p$ , showed that the unsteady separation extent covered roughly twice the percentage of ramp length compared to the steady separation extent. Furthermore, Case C underwent unsteady separation, despite remaining fully attached in the time-mean sense. The mean and unsteady detachment and reattachment locations were also correlated to the pressure and pressure gradient distributions. For all three cases, *the pressure distribution alone with adequate spatial resolution is sufficient to accurately determine the various detachment and reattachment locations.* The detachment ( $\gamma_p = 0.5$ ) and reattachment ( $\gamma_p = 0.5$ ) locations correspond to local minima/maxima in the pressure gradient distribution, respectively. Similarly, the incipient detachment ( $\gamma_p = 0.99$ ) and full reattachment ( $\gamma_p = 1$ ) locations correspond to local minima in the second derivative of the pressure distribution and the pressure distribution local maxima, respectively.

Despite being three-dimensional, the streamwise mean flow develops in a characteristic fashion for adverse pressure gradient turbulent boundary layers. The mean flow profiles become inflectional with the associated inflectional instability (associated with the outer inflection point) resulting in the formation of an embedded shear layer. Similarly, the near-wall peaks of the turbulent normal and shear stresses diminish with streamwise development, while outer peaks begin to form, quickly grow in magnitude, and move away from the wall. It is widely thought that the peak turbulent stress's wall-normal location tracks that of the outer mean profile inflection point. This has led researchers [56] to successfully apply shear layer scaling to the inflectional mean velocity profiles and accompanying turbulent stress profiles. In the cases examined here, only the mean profiles scaled using the shear layer parameters, while the turbulent normal and shear stresses did not. It was shown that the peak turbulent stress's wall-normal location deviates from the mean profile inflection point. This deviation was attributed to wall-normal transport resulting from the streamwise-curvature induced secondary flow.

Modifying the shear layer scaling to track the turbulent stress peak, instead of the mean profile inflection point, improved the collapse of the profiles. Even the mean flow profiles, which were successfully scaled with the original set of parameters, exhibited good collapse. Still, there remained a magnitude variation for both scaled turbulent normal and shear stress profiles. In general, the stress magnitudes were attenuated and amplified over regions experiencing convex (stabilizing) and concave (de-stabilizing) streamwise surface curvature, respectively. This trend is consistent with flow studies published for both curved boundary layers and free shear layers.

Due to the slow response times, relative to the mean flow, experienced by the turbulent stresses transitioning from convex to concave curvature, it was hypothesized that the turbulent shear stresses were not tracking the local wall curvature over the concave region of the ramp. Applying a coordinate system rotation to these turbulent shear stress profiles confirmed that while the stress peaks widened due to turbulent transport and continued to move away from the surface, their magnitudes did not change. *In both cases analyzed, including attached and separated flow, the turbulent shear stress peaks did not increase in magnitude with streamwise development if analyzed in the fixed, no-curvature reference frame associated with the transition from convex to concave curvature.* This was not the case for the turbulent normal stresses, which were only mildly dependent on coordinate system orientation. Why the turbulent shear stresses appear to be frozen, but the turbulent normal stresses do not, is still not fully understood; however, the constant production term in the turbulent kinetic energy equation at least provides consistency in the results. When taken together, the results indicate that streamwise surface curvature not only influences the growth in magnitude of the turbulent stresses through physical mechanisms, but also through the coordinate system reference frame in which they are analyzed.

## 9.2 Future Work

The principal aim of this work was to develop a series of smooth-body flow separation experiments for the purpose of CFD validation. Initially, a series of two-dimensional flow experiments was sought after. However, it was quickly discovered that producing a two-dimensional flow, whether separated or attached yet near separation, is not trivial. Instead, two-dimensional flow separation is rather a limiting case of more

generic three-dimensional flow separation that is forced to be highly spanwise uniform. This raises the question—should future efforts aimed at CFD validation attempt to model two-dimensional or three-dimensional flows? In general, three potential paths exist: (1) continue studying the current (or similar) flows exhibiting three-dimensional separation over a two-dimensional geometry, (2) design a new series of two-dimensional flow separation experiments (likely requiring either a very high W/L aspect ratio or an axisymmetric geometry), or (3) refocus efforts toward a series of three-dimensional flow separation experiments occurring on a three-dimensional geometry.

Currently, paths (2) and (3) are under investigation [15,25,43] and seem to be the focus all future studies, seeing as path (1) was not even the original intent of the current study. Full three-dimensional flow separation experiments, path (3), should capture the underlying physics most accurately; however, they are also the most expensive and time-consuming to carry out, and revealing the underlying physics may be difficult. On the other hand, while two-dimensional flow separation, path (2), may be achievable through very careful design efforts, a word of caution should be given regarding its relevance. If a series of two-dimensional flow separation experiments are carried out and used for CFD validation and turbulence model improvement, what does this suggest about the scope of problems for which these CFD codes would be applicable, since most real engineering flows of practical nature do not behave in the manner of the validation case? This is not a suggestion to avoid the study of full three-dimensional or two-dimensional flows for CFD validation experiments, rather, it is to point out that the seemingly overlooked case of a three-dimensional flow developing over a two-dimensional geometry, path (1), has its own

unique qualities that complement the current and future studies of pure two-and-three-dimensional flows.

There is still much to learn regarding the nature of “quasi-two-dimensional” flows, path (1), and many lessons can be gleaned from this dissertation. Perhaps the most significant improvement to the current set of experiments would be the measurement of the spanwise flow statistics. While the current series of experiments employed two-component LDV for the acquisition of flow field data, future experiments would greatly benefit from the additional spanwise velocity measurements of a three-component LDV system. This would permit better characterization of the three-dimensionality of the flow. It would also allow the complete Reynolds stress tensor to be measured, a highly desirable quantity for CFD validation. Furthermore, while it was argued that streamwise surface curvature induces a small secondary flow that promotes the formation of the vortical separation structures, only limited spanwise flow measurements were acquired downstream of reattachment to verify this. Additional spanwise flow measurements would allow this small secondary flow to be measured, thereby providing a better indication of its importance in the separation process.

The application of traditional three-component LDV is quite challenging, especially in an experiment in which no optical access is available in either the wind tunnel floor or ceiling, as was the case in this study. While new compact, embedded three-component LDV systems exist, the focal lengths are too small for the systems to be mounted external to the test section and still measure the centerline flow. (These compact three-component LDV systems, however, are ideally suited to study the sidewall/ramp juncture flow—another area rich for study that was only touched upon in this work.)

Perhaps another, more feasible, option would be the application of highspeed planar PIV in the Y-Z crossflow plane. While presenting its own challenges, particularly the adequate seeding of the flow, highspeed cross-planar PIV would provide a means to accurately, quickly, and more fully, characterize the flow's three-dimensionality.

While developing a series of CFD validation experiments, the research and analysis presented in this dissertation suggests a multitude of possible research paths that are rich with opportunities. These include (1) studying the three-dimensional separation structures, their causal mechanisms and dependence on geometric aspect ratio, test section blockage ratio, streamwise surface curvature, inflow boundary layer thickness and surface roughness; (2) analyzing the sidewall/ramp juncture flow and the inverse relationship between sidewall separation and the ramp centerline separation, including how this relationship is dependent on the ramp aspect ratio, e.g., how wide (compared to its length and height) does the ramp have to be for the extent of the sidewall separation to be insignificant?; (3) investigating the turbulence stress transport and the disparity in scaling of the turbulent normal and shear stresses, e.g., would the coordinate rotation scaling proposed in Chapter 8 hold if the concave region of the ramp was changed to a flat section?; (4) studying the effects of surface curvature on the mean flow and turbulent stresses by using multiple ramps of constant curvature; and (5) investigating how the separation flow topology changes for a morphing ramp geometry.

### 9.3 Practical Considerations for Future Validation Experiments

Much has been learned throughout the process of designing and carrying out these experiments. Some of the lessons learned and other practical considerations that would be useful for the design of future CFD validation experiments are shared below. This is by no

means a complete list of all the difficulties that one may encounter. Rather, it consists of those most prominent in the experimental work conducted for this dissertation.

1. Upon comparing the aspect ratio of this ramp to that of ramps in similar studies, as well as CFD simulations featuring different ramp lengths, it was found that the flow separation topology itself is likely not dependent on the aspect ratio; however, the larger the width to length is,  $W/L \gg 1$ , the more spanwise uniform the flow is in the central region. This implies that if a spanwise uniform flow is desired (what is often considered to be two-dimensional flow) the width to length aspect ratio should be as large as possible. This high aspect ratio should also reduce the inverse coupling between the sidewall separation extent and the centerline separation extent. The wind tunnel blockage ratio must also be considered, as a test section with high blockage behaves more like a duct/channel flow. The ramp flow examined here featured a very high blockage ratio, approximately 49%. Since the effective cross-section is small, it promotes the development of a streamwise surface curvature induced secondary flow, which aids in the formation of the vortical separation structure. For a given test section, reducing the ramp length also reduces the height (assuming the L/H ratio is held constant), alleviating both the aspect ratio and blockage effects; however, the spatial resolution of the flow development and the effective diagnostic probe volume will be compromised.
2. Careful and thorough documentation of the surface flow patterns, including patterns approaching the sidewalls, is needed on all future studies. It is not enough to simply analyze the central region of a geometry to check for uniformity as this dissertation shows that the extent of the sidewall/ramp juncture flow separation is inversely, and strongly so, coupled to the centerline separation extent. Additionally, a great deal of qualitative information can be gained from examining the surface flow visualization patterns and creating topology maps.
3. The implementation of good particle seeding is quite challenging, especially in a wind tunnel of the size used in this work. Adequate particle seeding is necessary for both LDV and PIV techniques, which are used extensively as modern flow diagnostic techniques. In general, two approaches can be used successfully. For example, Todd Lowe's group [43] from Virginia Tech used CFD simulations to track the streamtube leaving a seeding probe installed upstream of the test section. This allowed them to use smaller amounts of precisely located seeding particles for their optical measurements. On the other hand, Jenkin's group [133] from NASA Langley used a Pea Soup fog machine to seed the entire tunnel. Important considerations are (1) health safety of the researchers inhaling these particles, (2) ease of cleanup (e.g. solubility of the seeding fluid), (3) quantity of particles being injected

into the flow (this is highly influential in the realizable data rates), and (4) the influence on the flow field of probe wakes or jets used to deploy particles.

4. Surface coatings on the geometry are important in two ways: (1) to reduce laser reflections (for LDV and PIV) and allow flow measurements to be acquired very near the surface (this is important for comparison with CFD), and (2) to allow OFI measurements to be acquired. These coatings will likely be very different, thus requiring the removal of one coating and installation of another for each diagnostic technique. The need for these coatings stems from the fact that most model geometries are either machined from 6061 aluminum or printed from additive manufacturing materials such as ABS due to their low cost, machinability, and relatively light weight. Aluminum, however, has very poor surface qualities for both laser reflections and OFI fringe pattern visibility, and ABS is likely not much better.
5. Pressure taps should be employed along the entire span, including areas bordering the sidewalls. To the author's knowledge peripheral taps are rarely employed, however they would better inform the researcher as to the spanwise uniformity of the flow. Furthermore, maintaining the high spatial resolution measurements in the streamwise direction is also recommended. These measurements not only provide better comparison opportunities for CFD, but also allow the detachment and reattachment process to be further studied by comparison to the pressure and pressure gradient distributions.
6. To ensure experimental repeatability despite multiple tear-downs/set-ups having to occur in a shared facility, permanent boundary layer probes should be installed on the boundary layer development plate and each sidewall to record (and alert the experimentalist) of any changes that have occurred in the inflow boundary layer thickness or shape. This data collection should be automated, if possible, and conducted frequently and, at minimum, each time the test setup is newly installed. Several data sets from this experiment had to be thrown out when it was discovered that abnormalities in the sidewall boundary layer thickness occurred. For example, in one case measurements showed a substantially thicker boundary layer on one side of the test section than on the other side, which was believed to be the result of a slight off-set in the test section that occurred on certain installations.

APPENDIX A:  
EXPERIMENTAL GEOMETRY

A.1 Additional Experimental Geometry Images

Figure A.1 presents some of the relevant dimensions of the ramp and boundary layer development plate via a CAD drawing.

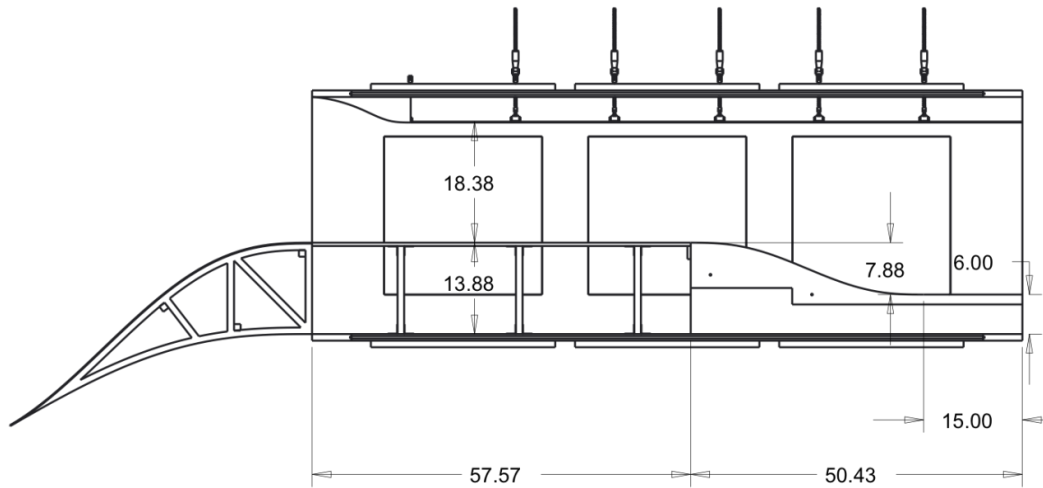


Figure A.1 Schematic drawing of the test section and model geometry including dimensions in inches

## A.2 Ramp Model Geometry

The ramp model, shown in Figure A.2, extends the entire width of the test section. It was fabricated in three spanwise sections, each machined in-house from two aluminum blocks, toleranced within 0.025 mm (0.001 in), then welded together. The three sections were bolted together, and its surface given a polished finish so that the seams are undetectable. Note that in addition to the contoured section of the ramp, there is a flat section downstream of the ramp that has a length of 0.381 m (15.0 in). This is manufactured as part of the ramp model and provides the flow with a recovery region prior to entering the wind tunnel diffuser. The tubulations and tubing are shown in Figure A.3. The ramp is placed 0.152 m (6in) above the test section floor to allow optical access along its downstream side. To provide this offset, a supporting structure was fabricated out of aluminum and is shown in Figure A.4.



Figure A.2 Photographs of the top (a) and bottom (b) assembled ramp model just after polishing showing the three separate sections bolted together

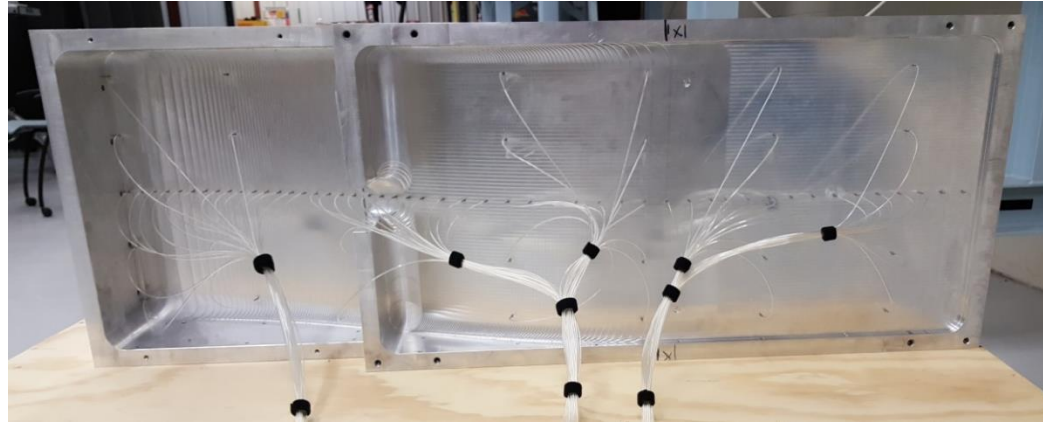


Figure A.3 Underside view of the central section of the ramp model showing pressure tubulations and tubing



Figure A.4 Supporting structure for ramp model that provides the necessary 0.152 m (6 in) of vertical offset required for optical access to the recovery region

### A.3 Internal Inlet Contour

The internal inlet contour, shown in Figure A.5, is a removable wind tunnel contraction insert, fabricated with a zero derivative end condition to smoothly bring the flow from the wind tunnel inlet contraction up to the leading edge of the flat boundary layer development plate. It consists of two symmetrical inserts each installed on the lower

surface of the wind tunnel contraction and bolted to each other and the legs of the boundary layer development plate. Each frame is constructed from aluminum and covered with a 6.35 mm (0.25 in) flexible plastic sheet. Once installed, aluminum foil ducting tape is used to completely seal all internal edges to prevent the front edge from lifting up and allowing airflow to pass underneath the boundary layer development plate. Figure A.5.b shows an in-process photograph of the ducting tape being installed.

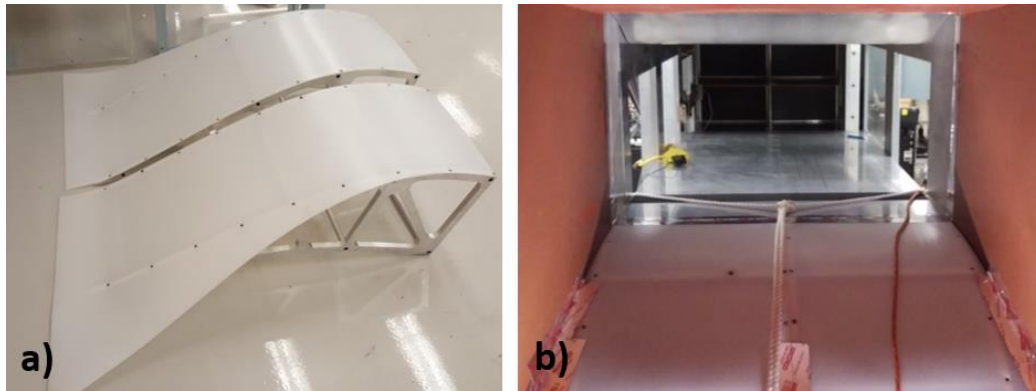


Figure A.5 Internal inlet contour sections outside (a) and installed in the wind tunnel contraction (b)

#### A.4 Turbulent Boundary Layer (TBL) Development Plate

The boundary layer development plate, shown in Figure A.6, spans the full 0.914 m (3 ft) width of the test section, is 1.462 m (57.57 in) in streamwise length and its top surface is lifted 0.352 m (13.88 in) off of the test section floor. It is constructed from 19.1 mm (0.75 in) thick aluminum plating, see Figure A.6.c, and secured to the test section floor via 18 steel legs to prevent aeroelastic vibrations, see Figure A.6.b. To ensure the incoming boundary layer was turbulent, it was tripped with a 101.6 mm (4 in) wide strip of distributed sand grain roughness with an average roughness element size of 46  $\mu\text{m}$ , mounted 1.2 m (47.2 in) upstream of the ramp leading edge, as shown in Figure A.6.a and Figure A.6.d.

The plate also contains a streamwise array of static pressure taps (1) in order to characterize the upstream boundary layer pressure gradient conditions. As will be described below, the streamwise pressure gradient can be controlled by a flexible top wall insert.

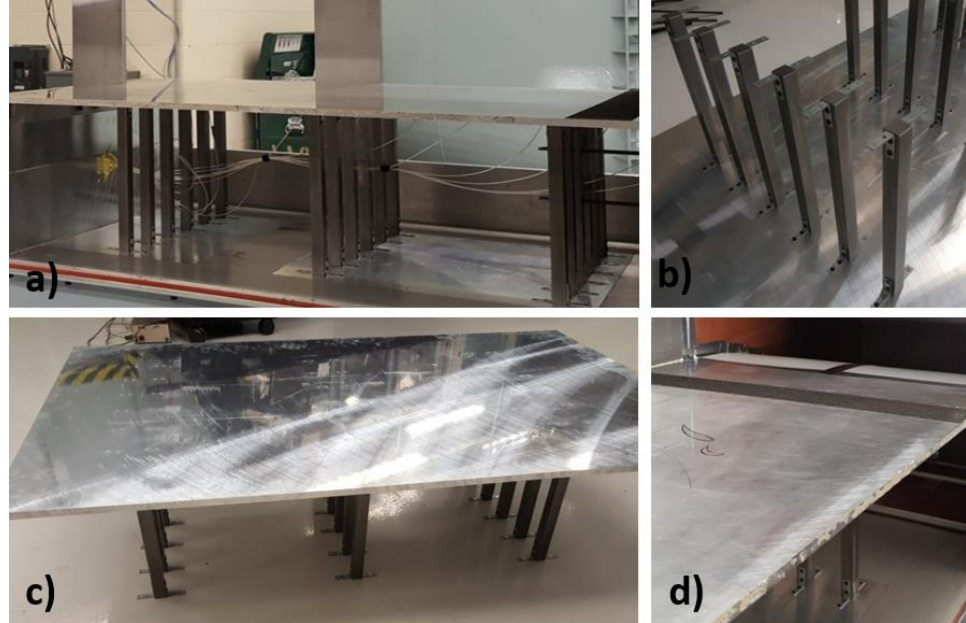


Figure A.6 Views of the boundary layer development plate during the installation process highlighting the aluminum plate (c), the steel support legs (b), and the tripping roughness element (a) and (d)

#### A.5 Flexible Top Wall Insert / Turnbuckle Assembly

To adjust the streamwise APG over the ramp surface and thereby achieve each of the desired archival benchmark flow cases, a flexible tunnel top wall assembly was designed and installed in the test section. Figure A.7 shows a schematic of the flexible upper wall assembly and the associated multiple turnbuckle system that is used to adjust the ceiling contour. The flexible ceiling was constructed from 10-gauge aluminum sheet metal (0.102 in) and is nominally mounted 9.86 cm (3.88 in) below the test section ceiling. The top three windows of the test section were removed, and were replaced with three

aluminum blanks, with the turnbuckle assemblies integrated into them as shown in Figure A.7. At the test section inlet, the top wall inlet contour smoothly transitions the flow to the flexible ceiling. It also serves to prevent any flow from passing between the top of the test section and flexible ceiling. The ceiling is nominally positioned 0.46 m above the boundary layer development plate. Adjustments to this nominal position allow the pressure gradient on the boundary layer development plate to vary from initially mildly favorable (due to the both top and bottom internal inlet contractions) to approximately ZPG. Over the convex ramp surface, the adjustment of the turnbuckles allows the desired APG to be imposed on the ramp TBL.

For each APG TBL case the wall contour was carefully measured. To do this the three panels on the test section ceiling that house the turnbuckle adjustment mechanisms also were equipped with access holes for accurately measuring the position of the ceiling. There are 23 holes down the centerline of the test section with holes on each side at five streamwise positions in order to verify spanwise uniformity of the ceiling position. In order to record the flexible ceiling location, a pair of digital calipers is used as a depth gauge to go through each hole to measure the distance between the panel top surface and the flexible ceiling top surface. This measurement is repeated for each of the 33 holes in the tunnel ceiling. Once these measurements are recorded, the holes are sealed in order to prevent any airflow through them. Figure A.8 Schematic top view of test section ceiling showing locations for measuring the position of the flexible ceiling contour shows the hole positions for each of the three ceiling panels. The number of measurement holes is greatest for the third panel which is located over the convex ramp where wall curvature is greatest.

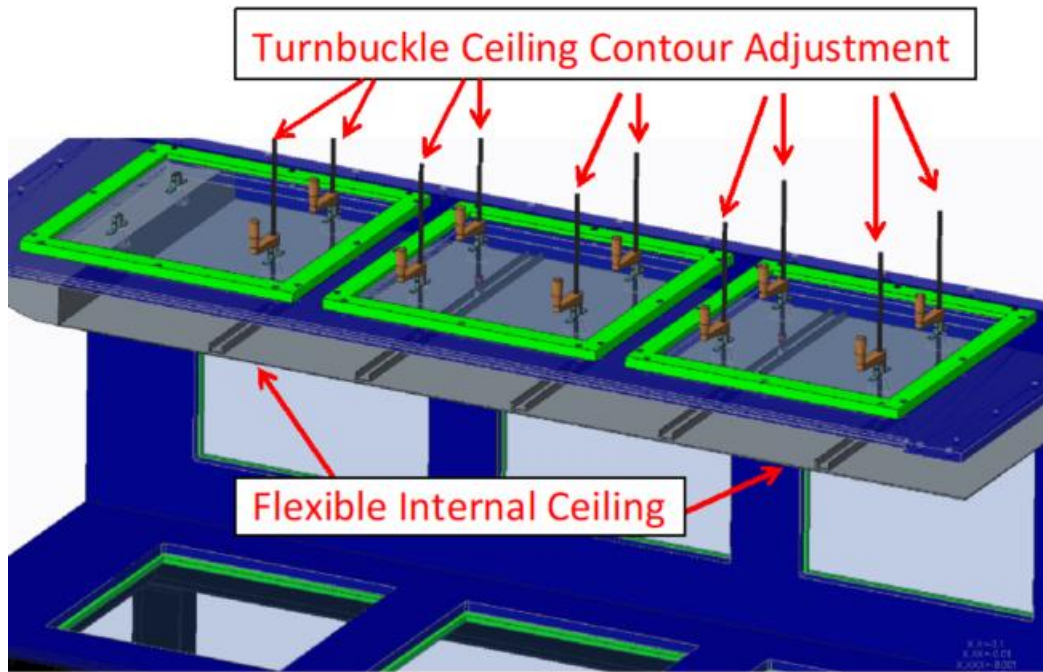


Figure A.7 Model of the flexible top wall insert and turnbuckle assembly viewed from the wind tunnel inner loop side

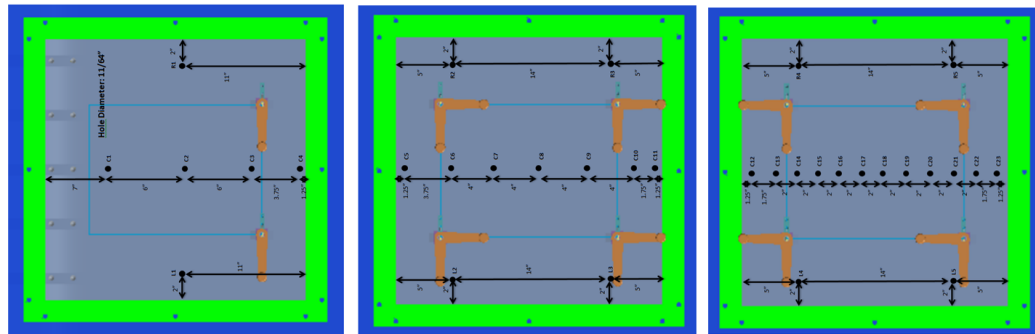


Figure A.8 Schematic top view of test section ceiling showing locations for measuring the position of the flexible ceiling contour. Note sections 1, 2, and 3 are shown from left to right.

The ceiling position measurements were repeated prior to each test entry or with the changing of separation test cases. Table A.1-Table A.3 provide the ceiling position measurements, converted to the global coordinate system, for each of these instances. Included in these tables is the mean ceiling position and the estimated uncertainty. The combined standard uncertainty of  $Y$  is a combination of the random uncertainty,  $s_Y$ , and the systematic standard uncertainty,  $b_Y$ .

$$u_Y = [ b_Y^2 + s_Y^2 ]^{1/2} \quad (A.1)$$

The random uncertainty,  $s_Y$ , is related to the variance as follows:

$$s_Y = \sqrt{\frac{Var(Y)}{N}} \quad (A.2)$$

where  $N$  is the number of times the ceiling configuration was repositioned and measured (4 times for Case A). The systematic uncertainty was divided into three components, the caliper uncertainty,  $b_c$ , taken as 0.025 mm (0.001 in), the sheet metal thickness uncertainty,  $b_t$ , taken as 0.127 mm (0.005 in), and the uncertainty of the machining of the test section,  $b_m$ , taken as 1.270 mm (0.050 in).

$$b_Y = [ b_c^2 + b_t^2 + b_m^2 ]^{1/2} \quad (A.3)$$

The expanded uncertainty is the combined standard uncertainty multiplied by the Student's t-table value,  $t_{v,p}$  where  $v$  is  $N - 1$  and  $p$  is the selected confidence interval. At 20:1 odds or  $p = 95\%$  confidence,  $t_{v,p} = 3.18$  for Case A. Using this analysis, the true value is expected to lie within:

$$Y_{mean} \pm t_{v,p} u_Y \quad (A.4)$$

where  $t_{v,p} u_Y$  is the expanded uncertainty or simply the 95% confidence intervals in this case. Note that for Cases C only two repeated measurement sets were taken, so instead of using this value, it was estimated to have the same random uncertainty as Case B.

TABLE A.1  
FLEXIBLE CEILING POSITION FOR CASE A

<b>Location</b>	<b>X (m)</b>	<b>Z (m)</b>	<b>Y<sub>1</sub> (m)</b>	<b>Y<sub>2</sub> (m)</b>	<b>Y<sub>3</sub> (m)</b>	<b>Y<sub>4</sub> (m)</b>	<b>Y<sub>mean</sub> (m)</b>	<b>Y<sub>CI_95%</sub> (m)</b>
Section 1								
L1	-0.853	0.254	0.818	0.818	0.818	0.818	0.818	0.004
R1	-0.853	-0.254	0.820	0.820	0.820	0.820	0.820	0.004
C1	-1.005	0.000	0.817	0.817	0.817	0.817	0.817	0.004
C2	-0.853	0.000	0.819	0.819	0.819	0.819	0.819	0.004
C3	-0.700	0.000	0.822	0.822	0.822	0.822	0.822	0.004
C4	-0.605	0.000	0.824	0.824	0.824	0.824	0.824	0.004
Section 2								
L2	-0.269	0.254	0.828	0.825	0.826	0.827	0.827	0.005
L3	0.087	0.254	0.822	0.818	0.819	0.821	0.820	0.005
R2	-0.269	-0.254	0.819	0.827	0.826	0.827	0.825	0.007
R3	0.087	-0.254	0.817	0.821	0.820	0.820	0.820	0.005
C5	-0.364	0.000	0.825	0.826	0.826	0.826	0.826	0.004
C6	-0.269	0.000	0.826	0.826	0.826	0.826	0.826	0.004
C7	-0.167	0.000	0.826	0.826	0.826	0.826	0.826	0.004
C8	-0.065	0.000	0.824	0.824	0.826	0.825	0.825	0.004
C9	0.036	0.000	0.822	0.821	0.823	0.823	0.822	0.004
C10	0.138	0.000	0.816	0.817	0.817	0.818	0.817	0.004
C11	0.182	0.000	0.814	0.814	0.815	0.816	0.815	0.004
Section 3								
L4	0.519	0.254	0.790	0.791	0.792	0.793	0.791	0.005
L5	0.875	0.254	0.769	0.770	0.771	0.771	0.770	0.004
R4	0.519	-0.254	0.795	0.795	0.794	0.794	0.794	0.004
R5	0.875	-0.254	0.772	0.769	0.772	0.772	0.771	0.005
C12	0.424	0.000	0.799	0.799	0.799	0.800	0.799	0.004
C13	0.468	0.000	0.796	0.796	0.796	0.797	0.796	0.004
C14	0.519	0.000	0.792	0.793	0.793	0.793	0.793	0.004
C15	0.570	0.000	0.789	0.790	0.790	0.790	0.790	0.004
C16	0.621	0.000	0.786	0.786	0.787	0.786	0.786	0.004
C17	0.671	0.000	0.783	0.783	0.784	0.783	0.783	0.004
C18	0.722	0.000	0.780	0.780	0.781	0.780	0.780	0.004
C19	0.773	0.000	0.777	0.777	0.778	0.777	0.777	0.004
C20	0.824	0.000	0.774	0.774	0.775	0.775	0.775	0.004
C21	0.875	0.000	0.771	0.771	0.772	0.771	0.771	0.004
C22	0.925	0.000	0.768	0.768	0.768	0.768	0.768	0.004
C23	0.970	0.000	0.766	0.765	0.764	0.766	0.765	0.004
End	1.281	0.000	0.749	0.749	0.749	0.749	0.749	0.004

TABLE A.2  
FLEXIBLE CEILING POSITION FOR CASE B

<b>Location</b>	<b>X (m)</b>	<b>Z (m)</b>	<b>Y<sub>1</sub> (m)</b>	<b>Y<sub>2</sub> (m)</b>	<b>Y<sub>3</sub> (m)</b>	<b>Y<sub>mean</sub> (m)</b>	<b>Y<sub>CI_95%</sub> (m)</b>
Section 1							
L1	-0.853	0.254	4.188	4.201	4.202	4.197	0.006
R1	-0.853	-0.254	4.132	4.140	4.132	4.135	0.006
C1	-1.005	0.000	4.280	4.250	4.250	4.260	0.006
C2	-0.853	0.000	4.148	4.154	4.151	4.151	0.006
C3	-0.700	0.000	4.300	4.043	4.043	4.129	0.006
C4	-0.605	0.000	3.966	3.986	3.981	3.978	0.006
Section 2							
L2	-0.269	0.254	3.778	3.855	3.845	3.826	0.008
L3	0.087	0.254	4.148	4.240	4.306	4.231	0.007
R2	-0.269	-0.254	3.877	3.854	3.855	3.862	0.006
R3	0.087	-0.254	4.226	4.271	4.252	4.250	0.006
C5	-0.364	0.000	3.848	3.868	3.921	3.879	0.006
C6	-0.269	0.000	3.828	3.855	3.892	3.858	0.006
C7	-0.167	0.000	3.853	3.884	3.918	3.885	0.006
C8	-0.065	0.000	3.928	3.977	3.992	3.966	0.006
C9	0.036	0.000	4.106	4.134	4.150	4.130	0.006
C10	0.138	0.000	4.404	4.418	4.455	4.426	0.006
C11	0.182	0.000	4.590	4.594	4.581	4.588	0.006
Section 3							
L4	0.519	0.254	6.214	6.155	6.192	6.187	0.006
L5	0.875	0.254	7.422	7.464	7.447	7.444	0.006
R4	0.519	-0.254	6.111	6.065	6.115	6.097	0.006
R5	0.875	-0.254	7.351	7.403	7.424	7.393	0.006
C12	0.424	0.000	5.722	5.714	5.736	5.724	0.006
C13	0.468	0.000	5.888	5.902	5.907	5.899	0.006
C14	0.519	0.000	6.109	6.103	6.094	6.102	0.006
C15	0.570	0.000	6.308	6.303	6.303	6.305	0.006
C16	0.621	0.000	6.497	6.477	6.536	6.503	0.006
C17	0.671	0.000	6.670	6.713	6.700	6.694	0.006
C18	0.722	0.000	6.850	6.865	6.889	6.868	0.006
C19	0.773	0.000	7.020	7.036	7.054	7.037	0.006
C20	0.824	0.000	7.182	7.212	7.235	7.210	0.006
C21	0.875	0.000	7.374	7.420	7.420	7.405	0.006
C22	0.925	0.000	7.586	7.650	7.626	7.621	0.006
C23	0.970	0.000	7.786	7.852	7.826	7.821	0.006
End	1.281	0.000	9.154	9.154	9.154	9.154	0.006

TABLE A.3  
FLEXIBLE CEILING POSITION FOR CASE C

<b>Location</b>	<b>X (m)</b>	<b>Z (m)</b>	<b>Y<sub>1</sub> (m)</b>	<b>Y<sub>2</sub> (m)</b>	<b>Y<sub>mean</sub> (m)</b>	<b>Y<sub>CI_95%</sub> (m)</b>
Section 1						
L1	-0.853	0.254	4.188	4.208	4.198	0.006
R1	-0.853	-0.254	4.132	4.138	4.135	0.006
C1	-1.005	0.000	4.248	4.257	4.253	0.006
C2	-0.853	0.000	4.148	4.154	4.151	0.006
C3	-0.700	0.000	4.011	4.046	4.029	0.006
C4	-0.605	0.000	3.950	3.981	3.966	0.006
Section 2						
L2	-0.269	0.254	3.817	3.859	3.838	0.006
L3	0.087	0.254	4.359	4.405	4.382	0.006
R2	-0.269	-0.254	3.867	3.839	3.853	0.006
R3	0.087	-0.254	4.347	4.339	4.343	0.006
C5	-0.364	0.000	3.906	3.913	3.910	0.006
C6	-0.269	0.000	3.832	3.886	3.859	0.006
C7	-0.167	0.000	3.879	3.831	3.855	0.006
C8	-0.065	0.000	3.946	3.954	3.950	0.006
C9	0.036	0.000	4.175	4.177	4.176	0.006
C10	0.138	0.000	4.589	4.646	4.618	0.006
C11	0.182	0.000	4.867	4.928	4.898	0.006
Section 3						
L4	0.519	0.254	7.119	7.091	7.105	0.006
L5	0.875	0.254	8.747	8.687	8.717	0.006
R4	0.519	-0.254	6.911	6.976	6.944	0.006
R5	0.875	-0.254	8.687	8.688	8.688	0.006
C12	0.424	0.000	6.400	6.523	6.462	0.006
C13	0.468	0.000	6.677	6.670	6.674	0.006
C14	0.519	0.000	6.965	6.988	6.977	0.006
C15	0.570	0.000	7.246	7.247	7.247	0.006
C16	0.621	0.000	7.509	7.491	7.500	0.006
C17	0.671	0.000	7.790	7.707	7.749	0.006
C18	0.722	0.000	7.973	7.931	7.952	0.006
C19	0.773	0.000	8.206	8.154	8.180	0.006
C20	0.824	0.000	8.453	8.371	8.412	0.006
C21	0.875	0.000	8.710	8.631	8.671	0.006
C22	0.925	0.000	8.976	8.993	8.985	0.006
C23	0.970	0.000	9.208	9.356	9.282	0.006
End	1.281	0.000	11.154	11.279	11.217	0.006

## A.6 Diffuser Transition

The end of the flexible internal ceiling is transitioned into the diffuser via a hinged assembly that provides a linear transition from the end of the flexible internal ceiling to the diffuser ceiling. This transition piece, shown in Figure A.9, was necessary on two accounts: (1) it provided additional structural rigidity that prevented vibration of the flexible ceiling, and (2) it eliminated feedback likely to occur via separated flow entering the cavity between the actual test section ceiling and the flexible internal sheet metal ceiling. Due to the fastener location on the diffuser ceiling being fixed, and the end of the flexible internal ceiling being dictated by the required ceiling configuration, the linear section of the hinged assembly had to be custom made for each ceiling configuration. This equated to the lower the ceiling configuration, the longer the linear portion of the hinged assembly.

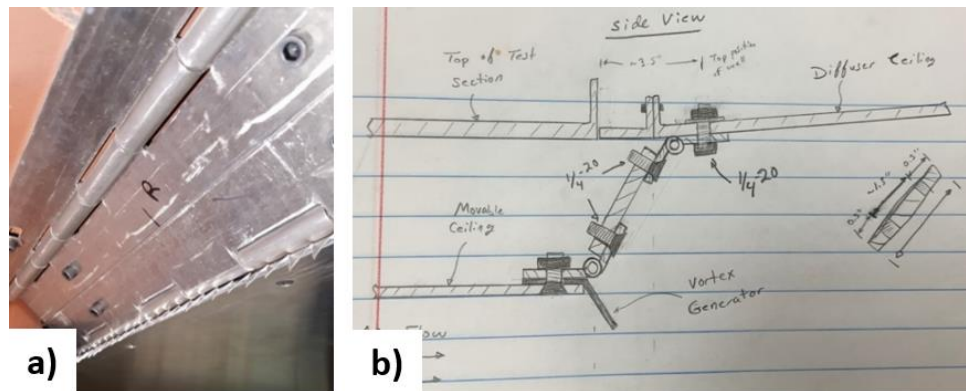


Figure A.9 Photograph (a) and schematic (b) of the diffuser hinged assembly transition piece

Due to the central cruciform in the diffuser, the hinged assembly was divided into two parts, one for each side of the cruciform. Each side of the hinged assembly consisted of two aluminum piano hinges, a linear section, and a streamwise vortex generator strip, see Figure A.10.a. Downstream of the ramp, on the lower part of the test section, the flow smoothly contours into the diffuser via removable inserts.

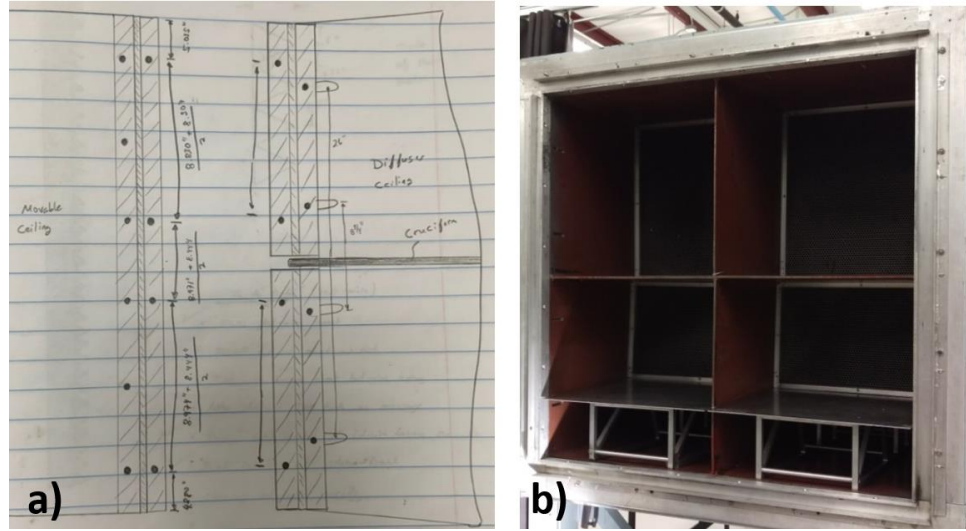


Figure A.10 Schematic top view of the piano hinge transition piece showing the diffuser cruciform (a), and photograph of the hexagonal grids installed in the diffuser (b)

In order to provide a pressure drop, and decouple the upstream and downstream flow, hexagonal mesh grids were installed approximately 0.51 m (20 in) downstream of the test section in each of the 4 sections of the diffuser, see Figure A.10.b. Each cell of the hexagonal grids was approximately 6.4 mm (0.25 in) in diameter and in total provided a blockage of approximately 21%.

## A.7 Adjustable Wind Tunnel Sidewall

A new test section sidewall, located on the wind tunnel outer loop (-Z axis) and not shown in Figure 2.4, with adjustable window positioning was fabricated to allow complete sidewall optical access at any streamwise location. This new sidewall is shown in Figure A.11.b and can be compared to the original sidewall, shown in Figure A.11.a. In the configuration shown in Figure A.11.b, the window locations for the two sidewalls are at similar streamwise positions; however, the new adjustable sidewall places the windows 51 mm (2.0 in) lower. This can be easily seen by comparing the different widths of the upper and lower crossbars Figure A.11.b. The new adjustable sidewall can also take on different window positions by repositioning the central supports, highlighted in yellow in Figure A.11.b, with additional supports and half windows being added as necessary. This setup allowed a special 0.5" thick plate glass window to be positioned anywhere in the central region of the sidewall, which in turn, allowed complete optical access over the ramp geometry, a necessity for the LDV measurements.

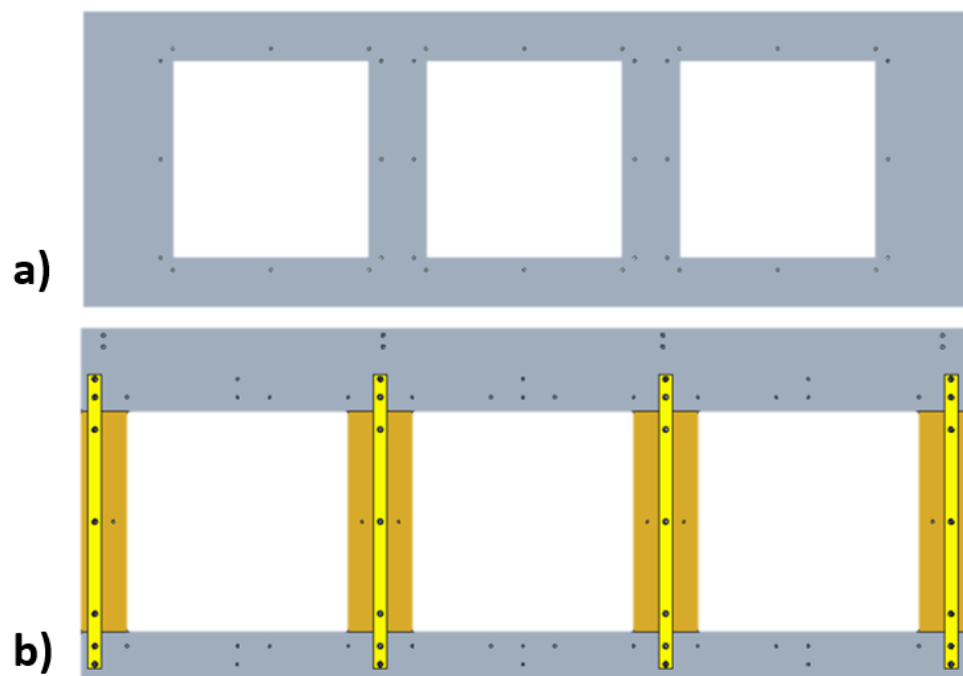


Figure A.11 Comparison of original test section sidewall (a) and new adjustable sidewall (b). Note that the new adjustable sidewall is positioned 51 mm lower and allows the central supports to be repositioned, as necessary.

## APPENDIX B: DIAGNOSTIC TECHNIQUES

### B.1 Surface Pressure Tap Locations

The surface pressure tap locations are provided in Table B.1 in the global coordinate system with units given in meters. Two columns of location data are provided, one for the centerline and one for the off centerline.

TABLE B.1  
SURFACE PRESSURE TAP LOCATIONS

Centerline			Off Centerline		
X (m)	Y (m)	Z (m)	X (m)	Y (m)	Z (m)
-1.4369	0.3524	0	0.03	0.3523	-0.168
-1.3099	0.3524	0	0.03	0.3523	-0.084
-1.1829	0.3524	0	0.03	0.3523	0.084
-1.0559	0.3524	0	0.03	0.3523	0.168
-0.9289	0.3524	0	0.21	0.3351	-0.168
-0.8019	0.3524	0	0.21	0.3351	-0.084
-0.6749	0.3524	0	0.21	0.3351	0.084
-0.5479	0.3524	0	0.21	0.3351	0.168
-0.4209	0.3524	0	0.39	0.2771	-0.168
-0.2939	0.3524	0	0.39	0.2771	-0.084
-0.1669	0.3524	0	0.39	0.2771	0.084
-0.0399	0.3524	0	0.39	0.2771	0.168
0.03	0.3523	0	0.61	0.1911	-0.168
0.05	0.3521	0	0.61	0.1911	-0.084
0.07	0.3516	0	0.61	0.1911	0.084
0.09	0.3507	0	0.61	0.1911	0.168
0.11	0.3494	0	0.79	0.1554	-0.168
0.13	0.3476	0	0.79	0.1554	-0.084
0.15	0.3453	0	0.79	0.1554	0.084
0.17	0.3425	0	0.79	0.1554	0.168
0.19	0.339	0	0.9599	0.1524	-0.168
0.21	0.3351	0	0.9599	0.1524	-0.084
0.23	0.3305	0	0.9599	0.1524	0.084
0.25	0.3254	0	0.9599	0.1524	0.168
0.27	0.3198	0	1.1397	0.1524	-0.168
0.29	0.3137	0	1.1397	0.1524	-0.084
0.31	0.3071	0	1.1397	0.1524	0.084
0.33	0.3001	0	1.1397	0.1524	0.168
0.35	0.2927	0			
0.37	0.285	0			

TABLE B.1 (CONTINUED)

<b>Centerline</b>		<b>Off Centerline</b>
0.39	0.2771	0
0.41	0.269	0
0.43	0.2607	0
0.45	0.2524	0
0.47	0.2441	0
0.49	0.2358	0
0.52	0.2237	0
0.55	0.2121	0
0.58	0.2012	0
0.61	0.1911	0
0.64	0.1821	0
0.67	0.1743	0
0.7	0.1677	0
0.73	0.1623	0
0.76	0.1583	0
0.79	0.1554	0
0.82	0.1536	0
0.85	0.1527	0
0.88	0.1524	0
0.8999	0.1524	0
0.9299	0.1524	0
0.9599	0.1524	0
0.9898	0.1524	0
1.0198	0.1524	0
1.0498	0.1524	0
1.0798	0.1524	0
1.1097	0.1524	0
1.1397	0.1524	0
1.1697	0.1524	0
1.1997	0.1524	0
1.2296	0.1524	0

## B.2 Oil-Film Interferometry Silicone Oil



Phone: 001 215 366-7860  
 Email: [info@clearcoproducts.com](mailto:info@clearcoproducts.com)

### Viscosity to Temperature Chart Clearco Pure Silicone Fluids

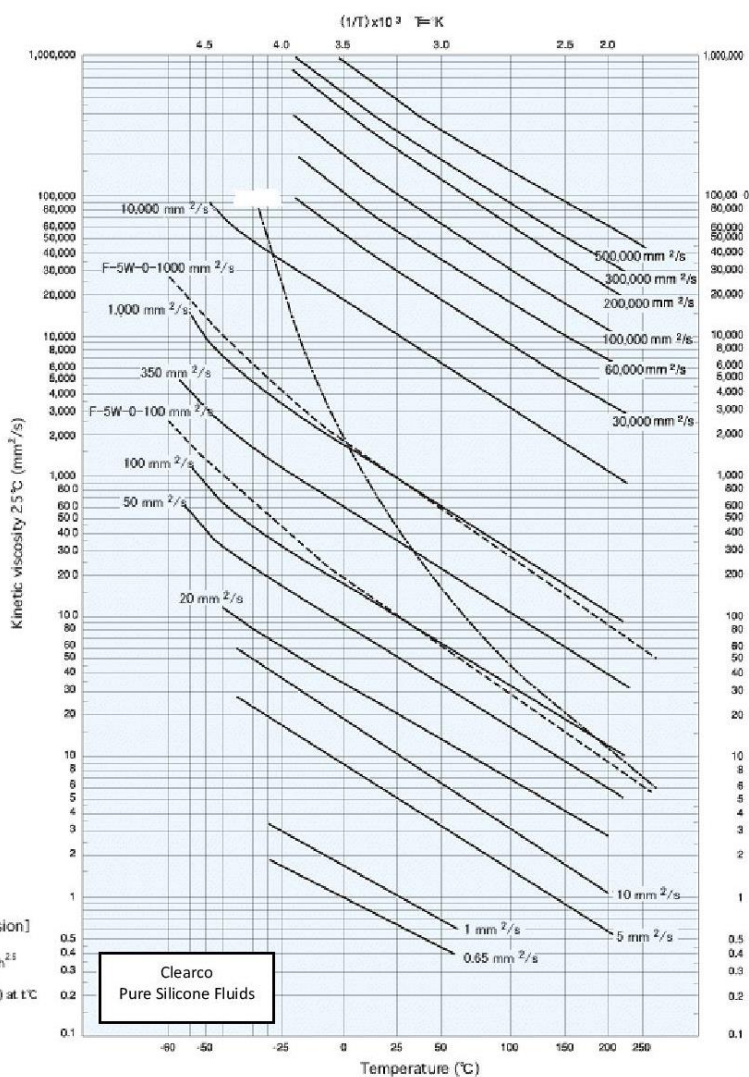


Figure B.1 Viscosity temperature dependence for Clearco pure silicone fluids

### B.3 Laser Doppler Velocimetry Particle Seeding

The bulk of the experiments are conducted non-intrusively using laser Doppler velocimetry (LDV) which requires the flow be seeded. Di-Ethyl-Hexyl-Sebacot (DEHS) particles of nominally 1-micron diameter were used to seed the flow. In order to minimize the required seeding volume, it was necessary to modify a section of the internal inlet contour to accept a seeding manifold so that localized seeding could be achieved. The internal inlet contour on the  $-z$  (spanwise) axis was modified by installing a manifold, shown in Figure B.2, that would allow wall-normal particle seeding at the required spanwise locations. The manifold consisted of eight flush-mounted tubes of 9.53 mm (3/8" in) diameter installed 0.24 m (9.5 in) upstream of the test section. Figure B.2.a shows the flush-mounted manifold from the top, airflow side. Internally, the tubes were paired off via a y-connector as shown in Figure B.2.b. This system was designed such that by supplying particles to one tube they would eventually exit the manifold straddling the spanwise location of the desired LDV profile. This allowed the seeding to be concentrated only where necessary for each run.

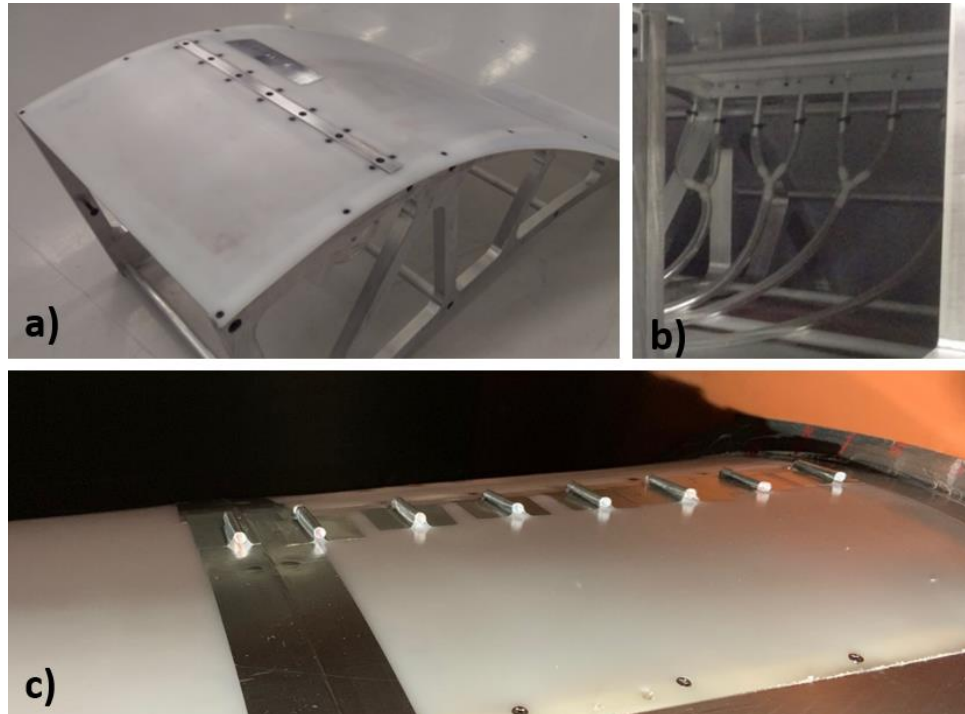


Figure B.2 Internal inlet contour modified with a particle seeding manifold to allow localized seeding of the upstream boundary layer highlighting the top view (a) internal view (b) and top view of additional modification for y-connectors (c)

An additional modification to the seeding manifold was made prior to making LDV measurements in the recovery region of Case B and all LDV data for Case C. This modification was necessary to keep LDV data acquisition at an acceptable rate and consisted of installing downstream facing straws in the manifold tube openings. Figure B.2.c shows the modified seeding manifold with the straws and can be compared to the original flush-mounted seeding manifold shown in Figure B.2.a. The downstream facing tubes increased the concentration of airborne seeding particle, which prior were collecting on the surface, significantly increasing the LDV data rate. While this modification acted as a physical obstruction in the flow, it occurred in the favorable pressure gradient region and

sufficiently far upstream to not adversely affect the experiment. This was determined by taking comparison LDV profiles downstream in the recovery region of Case B using both seeding manifolds with the difference being deemed negligible. In addition, hot-wire boundary layer profiles were taken upstream at  $X = -0.678$  m both with and without the modified seeding method installed. Figure B.3 shows the comparison profiles which agree quite well with one another, again, indicating a negligible difference in flow conditions for each seeding method. For more discussion on the particle seeding, see the LDV documentation.

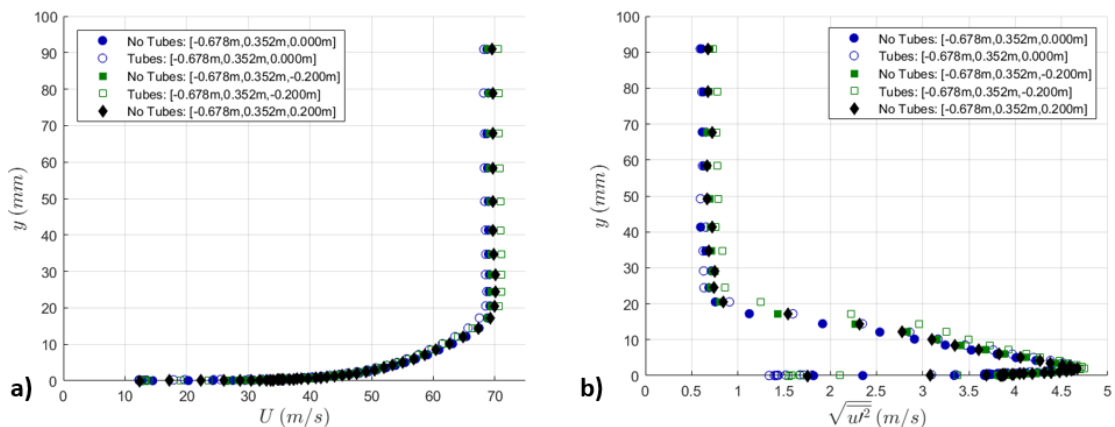


Figure B.3 Comparison of incoming mean flow (a) and turbulent stress (b) boundary layers both with and without the modified seeding tubes installed showing negligible difference in flow condition. Note that the profiles were taken using hot-wire anemometry for the C.

## APPENDIX C: OPERATING TEST CONDITIONS

The test conditions were recorded at least once per day and included, lab temperature, pressure, and relative humidity. These measurements, recorded in the archival data files, were made using a Fisher Scientific digital barometer model #14-650-118. Density, viscosity, freestream velocity, and Reynolds number were calculated using the procedures and equations outlined in this document. Additional measurements including, wind tunnel temperature and relative humidity were measured throughout the duration of several tests to characterize their typical variation, which is largely a function of the flexible ceiling position, (i.e. which separation case was being examined, and the run duration).

### C.1 Temperature

The wind tunnel temperature was recorded using a thermocouple located in the wind tunnel contraction. A typical temperature variation for Case C is shown in Figure C.1 and includes both tunnel and lab temperature. For reference, in the following figures each data point is taken approximately 15 minutes apart and the time is non-dimensionalized to yield a test duration that goes from 0 to 1 corresponding to the start and end of the test, respectively.

Due to the lowered flexible ceiling position, this case required the most power from the drive motor. This in combination with the significant tunnel test section blockage caused the chilled water-cooling system to not be able to fully maintain a constant temperature throughout each test. It was not uncommon for tunnel temperature to vary 5-15 °C throughout the duration of each run. A typical LDV test duration was 1-3 hours, and often the tests were closely spaced which prevented the tunnel temperature from returning to that of the lab before the start of the next test.

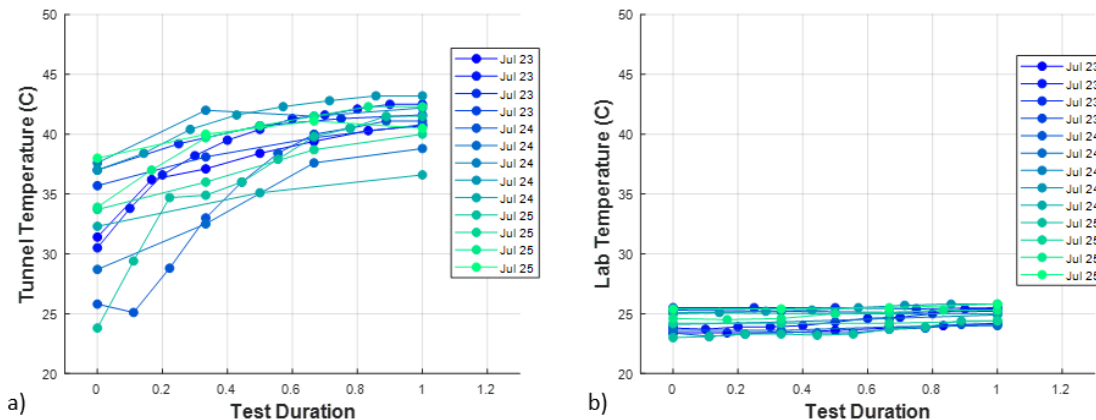


Figure C.1 A typical temperature variation for Case C showing both the tunnel temperature (a) and lab temperature (b). Each test is plotted over its duration which goes from start (0) to finish (1) with each data point being taken approximately 15 minutes apart.

A typical temperature variation for Case B is shown in Figure C.2 and includes both tunnel and lab temperature. Due to flexible ceiling being positioned higher up, the blockage was not as significant as in Case C, causing the typical temperature rise to be lower. For Case B the tunnel temp usually only varied by about 5 °C. For reference, the lab temperature is also shown to indicate that the tunnel temperature rise is not due to any sort of temperature variation in the lab.

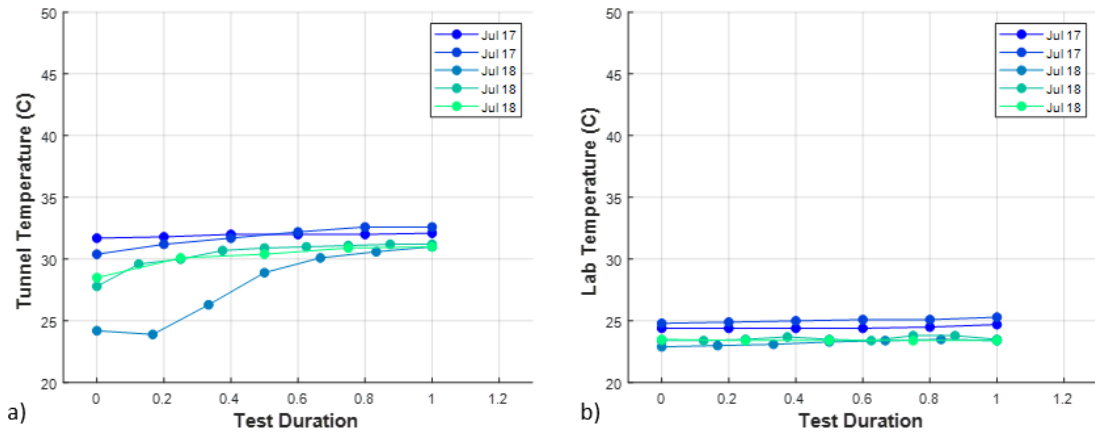


Figure C.2 A typical temperature variation for Case B showing both the tunnel temperature (a) and lab temperature (b). Each test is plotted over its duration which goes from start (0) to finish (1) with each data point being taken approximately 15 minutes apart.

A typical temperature variation for Case A is shown in Figure C.3 and includes both tunnel and lab temperature. Unlike Cases C and B, the higher position of the flexible ceiling reduced both the blockage and required drive motor input power. This allowed the chilled water-cooling system to do a decent job of maintaining the tunnel temperature throughout the duration of each test. Here the tunnel temp usually only varied by about 2 °C.

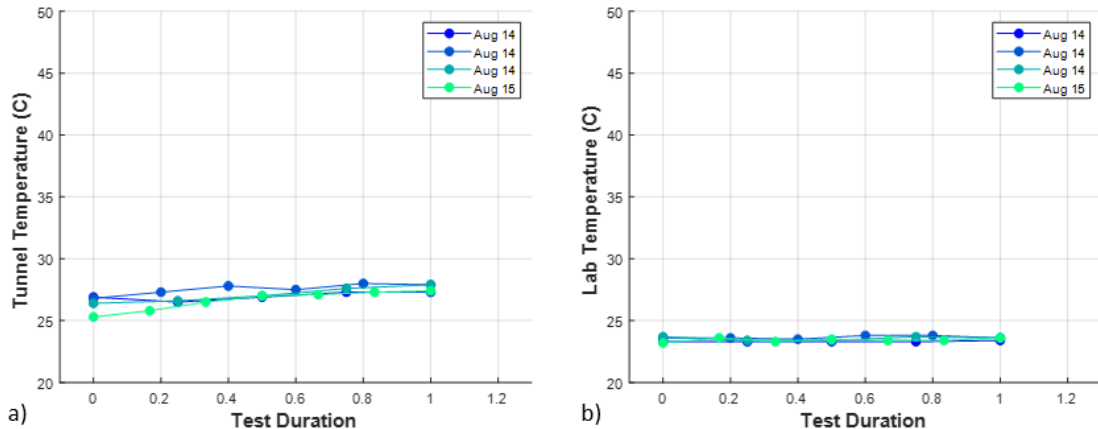


Figure C.3 A typical temperature variation for Case A showing both the tunnel temperature (a) and lab temperature (b). Each test is plotted over its duration which goes from start (0) to finish (1) with each data point being taken approximately 15 minutes apart.

## C.2 Pressure

Absolute pressure measurements of the laboratory environment were recorded at least once per day. From multiple measurements recorded over the period of the day, it is estimated the lab pressure may vary by about 1-2 hPa.

## C.3 Relative Humidity

Relative humidity was also recorded both in the wind tunnel and in the lab and typical variations for Cases, C, B, and A are shown below in Figure C.4-6. As was done for the temperature plots, here each data point is taken approximately 15 minutes apart and the test duration is non-dimensionalized to yield a test duration that goes from 0 to 1 which correspond to the start and end of the test, respectively. While the lab humidity may vary by about 5% during a test, the tunnel humidity for all cases start out high and quickly drop and stabilize to a value far below that in the lab.

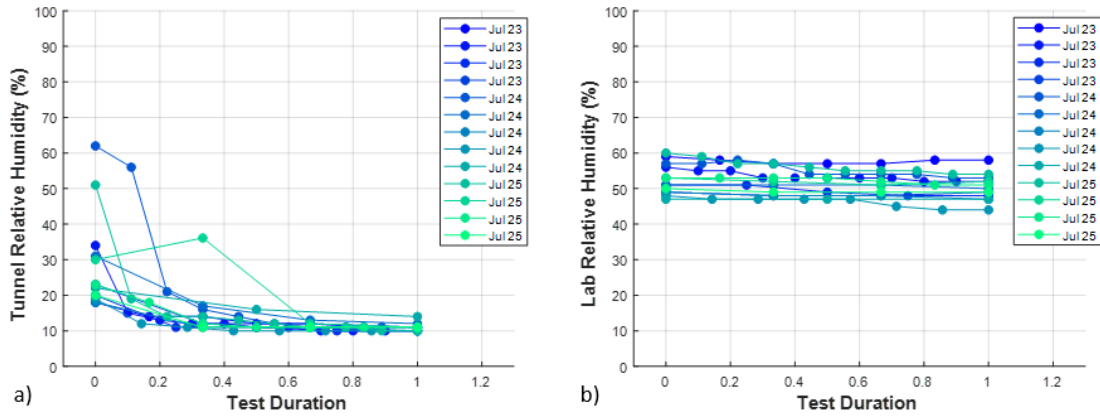


Figure C.4 A typical relative humidity variation for Case C showing both the tunnel humidity (a) and lab humidity (b). Each test is plotted over its duration which goes from start (0) to finish (1) with each data point being taken approximately 15 minutes apart.

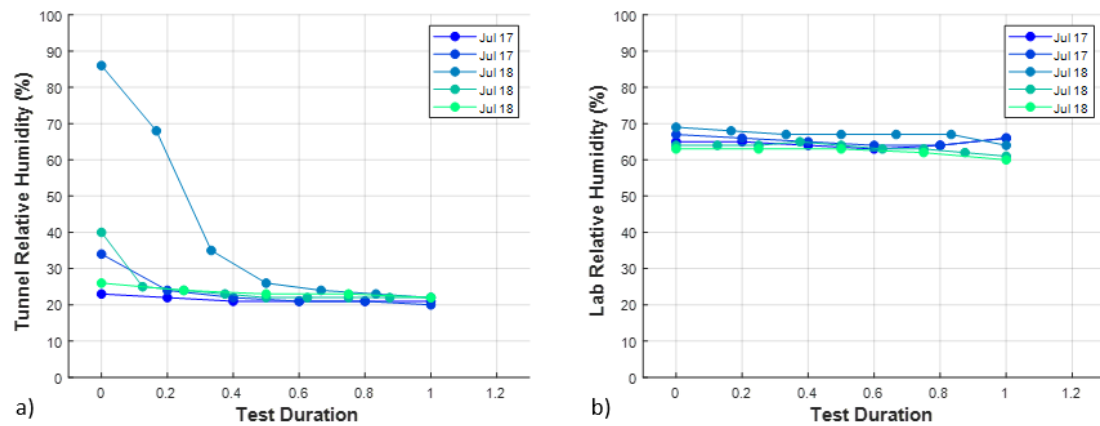


Figure C.5 A typical relative humidity variation for Case B showing both the tunnel humidity (a) and lab humidity (b). Each test is plotted over its duration which goes from start (0) to finish (1) with each data point being taken approximately 15 minutes apart.

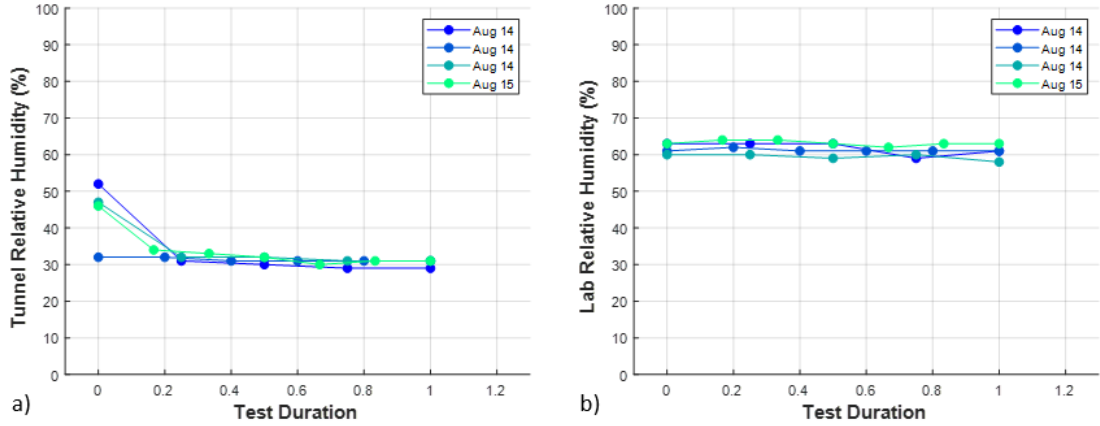


Figure C.6 A typical relative humidity variation for Case A showing both the tunnel humidity (a) and lab humidity (b). Each test is plotted over its duration which goes from start (0) to finish (1) with each data point being taken approximately 15 minutes apart.

#### C.4 Density

The density,  $\rho$  [kg/m<sup>3</sup>], was calculated as a function of pressure temperature and relative humidity using Jones's formula [57]

$$\rho = \frac{0.0034848}{T+273.15} (P - 0.0037960 * RH * P_s) \quad (C.5)$$

where  $P$  is the atmospheric pressure [Pa],  $T$  is the temperature [C],  $RH$  is the relative humidity [%], and  $P_s$  is the saturated water vapor pressure. Teten's formula was used to calculate the saturated water vapor pressure as

$$P_s = 611 \times 10^{\left(\frac{7.5T}{T+237.3}\right)} \quad (C.6)$$

## C.5 Viscosity

The dynamic viscosity was calculated using Sutherland's law [63] with three coefficients which has the form

$$\mu = \mu_0 \left( \frac{T}{T_0} \right)^{\frac{3}{2}} \left( \frac{T_0 + S}{T + S} \right) \quad (C.7)$$

where  $T$  is the temperature [K],  $\mu_0 = 1.7894 \times 10^{-5}$  [kg/(m\*s)] is a reference viscosity,  $T_0 = 273.11$  [K] is a reference temperature, and the Sutherland constant  $S = 110.56$  [K] is the effective temperature. The kinematic viscosity is related to the dynamic viscosity and density as

$$\nu = \frac{\mu}{\rho} \quad (C.8)$$

and has units of [m<sup>2</sup>/s].

## C.6 Freestream Velocity

A pitot-static tube located in the test section freestream at  $X = -0.97$  [m] and  $Y = 0.58$  [m] was used to measure dynamic pressure which was then converted to velocity and Mach number. Two built-in Setra model 270 absolute pressure transducers were used in conjunction with this pitot-static tube and recorded the total  $P_T$  and static pressure  $P_S$  respectively. The Mach number,  $M$ , was then determined as follows:

$$M = \sqrt{\frac{2(P_T - P_s)}{\gamma P_s}} \quad (C.9)$$

where  $\gamma = 1.4$  is the specific heat ratio of air. The wind tunnel freestream velocity was then primarily dictated by the Mach number, which was fixed at  $M = 0.2$ , and the temperature which varied as discussed previously. This relation can be written as:

$$U_\infty = M\sqrt{\gamma RT} \quad (C.10)$$

where  $R = 287.05$  [J/(kg\*K)] is the gas constant for air, and  $T$  is the air temperature [K]. The sensitivities of  $M$  with respect to each of the dependent values were obtained by partial differentiation.

$$\frac{\partial M}{\partial P_T} = \frac{1}{M\gamma P_S} \quad (C.11)$$

$$\frac{\partial M}{\partial P_S} = \frac{-P_T}{M\gamma P_S^2} \quad (C.12)$$

This gives the uncertainty of the Mach number,  $b_M$  as:

$$b_M = \left[ \left( \frac{\partial M}{\partial P_T} b_{P_T} \right)^2 + \left( \frac{\partial M}{\partial P_S} b_{P_S} \right)^2 \right]^{\frac{1}{2}} \quad (C.13)$$

where  $b_{P_T}$  and  $b_{P_S}$  are the uncertainties of the Setra pressure transducers given as 25 Pa. Since the Mach number,  $M$  is held constant at 0.2 throughout the duration of the tests, the freestream velocity must change in proportion to the local speed of sound. This inherently introduces uncertainty that may be accounted for by examining the relationship between

freestream velocity,  $U_\infty$ , Mach number,  $M$ , and temperature,  $T$ , using equation (6). The uncertainty in freestream velocity can be written as:

$$b_{U_\infty} = \left[ \left( \frac{\partial U_\infty}{\partial T} b_T \right)^2 + \left( \frac{\partial U_\infty}{\partial M} b_M \right)^2 \right]^{\frac{1}{2}} \quad (C.14)$$

or equivalently,

$$b_{U_\infty} = \left[ \left( \frac{M}{2} \sqrt{\frac{\gamma R}{T}} b_T \right)^2 + (\sqrt{\gamma R T} b_M)^2 \right]^{\frac{1}{2}} \quad (C.15)$$

where  $b_T$  is the uncertainty in temperature taken as half the estimated greatest change in temperature over the course of all the tests, as seen in Figure C.1-3. Using the estimates of temperature and temperature change from Figure C.1-3, as well as the uncertainty introduced from the two Setra pressure transducers, the estimated uncertainty in freestream velocity is given in Table 1.

TABLE C.1  
UNCERTAINTY ESTIMATES FOR CASES A, B AND C

	<b>Case A</b>	<b>Case B</b>	<b>Case C</b>
$T_{mean}$ [°C]	27	30	35
$U_\infty$ [m/s]	69.46	69.81	70.38
$b_T$ [°C]	1.5	3.5	9
$b_M$	0.0013	0.0013	0.0013
$b_{U_\infty}$ [m/s]	0.49	0.61	1.13

## C.7 Reynolds Number

The Reynolds number was based off the ramp height,  $H = 0.2$  [m], and is given as follows:

$$Re_H = \frac{U_\infty H}{\nu} \approx 8.4 \times 10^5 \quad (C.16)$$

where  $U_\infty$  is the freestream velocity recorded with the pitot tube and  $\nu$  is kinematic viscosity.

## APPENDIX D: UNCERTAINTY ANALYSIS

### D.1 Surface Pressure Uncertainty Analysis

The uncertainty analysis procedure followed the general guidelines laid out in the ASME PTC 19.1-2005 Test Uncertainty manual [134]. This section will outline the procedure used to calculate the uncertainty for the  $C_p$  measurements, both of which are reported in this document and on the NASA Langley Turbulence Modeling Resource website [14]. The combined standard uncertainty of  $C_p$  is a combination of the random uncertainty,  $s_{C_p}$ , and the systematic standard uncertainty,  $b_{C_p}$ .

$$u_{C_p} = \left[ b_{C_p}^2 + s_{C_p}^2 \right]^{\frac{1}{2}} \quad (D.17)$$

The functional dependence of the pressure coefficient on the measured gauge pressure and dynamic pressure is as follows:

$$C_p = f(\Delta P_i, q) \quad (D.18)$$

The sensitivities of  $C_p$  with respect to each of these dependent values were obtained by partial differentiation.

$$\frac{\partial C_p}{\partial \Delta P_i} = \frac{1}{q} \quad (D.19)$$

$$\frac{\partial C_p}{\partial q} = -\frac{\Delta P_i}{q^2} \quad (D.20)$$

The random uncertainty,  $s_{C_p}$ , is a function of the random uncertainties  $s_{\Delta P_i}$  and  $s_q$ ,

and were obtained from equations (D.18) and (D.19) as follows:

$$s_{C_p} = \left[ \left( \frac{\partial C_p}{\partial \Delta P_i} s_{\Delta P_i} \right)^2 + \left( \frac{\partial C_p}{\partial q} s_q \right)^2 \right]^{\frac{1}{2}} \quad (D.21)$$

or equivalently,

$$s_{C_p} = \frac{1}{|q|} \left[ s_{\Delta P_i}^2 + C_p^2 s_q^2 \right]^{\frac{1}{2}} \quad (D.22)$$

The random standard uncertainties  $s_{\Delta P_i}$  and  $s_q$  are related to the estimator variances as follows:

$$s_{\Delta P_i} = \sqrt{\frac{var_{\Delta P_i}}{N}} \quad (D.23)$$

$$s_q = \sqrt{\frac{var_q}{N}} \quad (D.24)$$

where  $N$  is the number of samples.

Propagation of the systematic uncertainties was done in a similar manner to that of the random uncertainties.

$$b_{C_p} = \left[ \left( \frac{\partial C_p}{\partial \Delta P_i} b_{\Delta P_i} \right)^2 + \left( \frac{\partial C_p}{\partial q} b_q \right)^2 \right]^{\frac{1}{2}} \quad (D.25)$$

or equivalently,

$$b_{C_p} = \frac{1}{|q|} \left[ b_{\Delta P_i}^2 + C_p^2 b_q^2 \right]^{\frac{1}{2}} = \frac{b_p}{|q|} \left[ 1 + C_p^2 \right]^{\frac{1}{2}} \quad (D.26)$$

Here the fact that the systematic uncertainty for the measured gauge pressure and dynamic pressure are the same,  $b_p$ , was used to simplify the equation. This fact is due to all pressure measurements being made with the same pressure transducer. The systematic uncertainty of the Scanivalve pressure transducer was divided into two components, the calibration uncertainty,  $b_{cal}$ , and the instrument uncertainty,  $b_{inst}$ .

$$b_p = [ b_{cal}^2 + b_{inst}^2 ]^{\frac{1}{2}} \quad (D.27)$$

The instrument uncertainty is that given with the pressure transducer, 0.3% of full-scale, with the full-scale range being 10 inches of water. Once converted to the metric system, this yields  $b_{inst} = \pm 7.47$  [Pa]. The calibration uncertainty is based off the linear regression used to convert the Scanivalve transducer output voltage to pressure. The calibration curve is shown in Figure 2.7 and the linear fit equation is:

$$P = 1205.207V + 45.5483 \quad (D.28)$$

where  $V$  is the transducer output in Volts and  $P$  is the respective pressure in Pascals. From this regression curve fit the uncertainty was calculated using the procedure outlined in section 8-6 of the ASME PTC 19.1-2005 Test Uncertainty manual [134]. The calibration uncertainty is dependent on the voltage and hence varies for each point. In general,  $b_{cal}$  is about 60-85% of  $b_{inst}$ .

The combined standard uncertainty was given in equation (D.17) and is a combination of the random uncertainty and the systematic standard uncertainty. Here it is repeated utilizing equations (D.21) and (D.25).

$$u_{C_p} = \frac{1}{|q|} \left[ b_p^2 (1 + C_p^2) + (s_{\Delta P_i}^2 + C_p^2 s_q^2) \right]^{\frac{1}{2}} \quad (D.29)$$

The expanded uncertainty is the combined standard uncertainty multiplied by the Student's t-table value,  $t_{v,p}$  where  $v$  is  $N - 1$  and  $p$  is the selected confidence interval. At 20:1 odds or  $p = 95\%$  confidence and assuming a large sample size,  $t_{v,p} = 1.96$ . Using this analysis, the true value is expected to lie within:

$$C_p \pm t_{v,p} u_{C_p} \quad (D.30)$$

where  $t_{v,p} u_U$  is the expanded uncertainty or simply the uncertainty of the quantity.

## D.2 Pitot-Tube Measurement Uncertainty Analysis

The uncertainty analysis procedure followed the general guidelines laid out in the ASME PTC 19.1-2005 Test Uncertainty manual [134]. This section will outline the procedure used to calculate the uncertainty for the sidewall boundary layer streamwise mean velocity,  $U$ , measurements which are reported in this document and on the NASA Langley Turbulence Modeling Resource website [14]. The combined standard uncertainty of  $U$  is a combination of the random uncertainty,  $s_U$ , and the systematic standard uncertainty,  $b_U$ .

$$u_U = [b_U^2 + s_U^2]^{1/2} \quad (D.31)$$

The functional dependence of the mean velocity on the measured pressure and density are as follows:

$$U = f(\Delta P, \rho) = \sqrt{\frac{2\Delta P}{\rho}} \quad (D.32)$$

The sensitivities of  $U$  with respect to each of these dependent values were obtained by partial differentiation.

$$\frac{\partial U}{\partial \Delta P} = \frac{1}{\sqrt{2\rho\Delta P}} \quad (D.33)$$

$$\frac{\partial U}{\partial \rho} = -\sqrt{\frac{\Delta P}{2\rho^3}} \quad (D.34)$$

The random uncertainty,  $s_U$ , is a function of the random uncertainty  $s_P$  and was obtained from equations (D.32) and (D.33) as follows:

$$s_U = \left[ \left( \frac{\partial U}{\partial \Delta P} s_P \right)^2 \right]^{\frac{1}{2}} \quad (D.35)$$

or equivalently,

$$s_U = \frac{1}{\sqrt{2\rho\Delta P}} S_P \quad (D.36)$$

The random standard uncertainty  $s_P$  is related to the estimator variance as follows:

$$s_P = \sqrt{\frac{var_P}{N}} \quad (D.37)$$

where  $N$  is the number of samples.

Propagation of the systematic uncertainties was done in a similar manner to that of the random uncertainties except here we need to consider the uncertainty due to the variation in freestream velocity with temperature. The freestream velocity is related to the temperature,  $T$ , via the definition of the Mach number,  $M$ , written as:

$$U = M\sqrt{\gamma RT} \quad (D.38)$$

where  $M$  is held constant at 0.2 throughout the duration of the tests. Including the sensitivity of this term, the systematic uncertainty can be written as:

$$b_U = \left[ \left( \frac{1}{k_P} \frac{\partial U}{\partial \Delta P} b_P \right)^2 + \left( \frac{1}{k_\rho} \frac{\partial U}{\partial \rho} b_\rho \right)^2 + \left( \frac{1}{k_T} \frac{\partial U}{\partial T} b_T \right)^2 \right]^{\frac{1}{2}} \quad (D.39)$$

or equivalently,

$$b_U = \left[ \frac{1}{2\rho P k_P} b_P^2 + \frac{P}{2\rho^3 k_\rho} b_\rho^2 + \frac{M^2 \gamma R}{4T k_T} b_T^2 \right]^{\frac{1}{2}} \quad (D.40)$$

where  $k_P$ ,  $k_\rho$ , and  $k_T$  are the coverage factors taken as  $\sqrt{3}$  while  $b_P$ ,  $b_\rho$ , and  $b_T$  are the systematic uncertainties in pressure, density, and temperature respectively. The systematic uncertainty of the density was estimated using:

$$b_\rho = \frac{|\rho_{start} - \rho_{end}|}{2} \quad (D.41)$$

where  $\rho_{start}$  and  $\rho_{end}$  are the respective densities calculated from the temperature variation from the start to end of the experiment. As was done for the pressure measurements, the systematic uncertainty of the Scanivalve pressure transducer was divided into two components, the calibration uncertainty,  $b_{cal}$ , and the instrument uncertainty,  $b_{inst}$ .

$$b_p = [b_{cal}^2 + b_{inst}^2]^{\frac{1}{2}} \quad (D.42)$$

The instrument uncertainty is that given with the pressure transducer, 0.3% of full-scale, with the full-scale range being 10 inches of water. Once converted to the metric system, this yields  $b_{inst} = \pm 7.4652$  [Pa]. The calibration uncertainty is based off the linear regression used to convert the Scanivalve transducer output voltage to pressure. The calibration curve is shown in Figure 1 and the linear fit equation is:

$$P = 1205.207 V + 45.5483 \quad (D.43)$$

where  $V$  is the transducer output in Volts and  $P$  is the respective pressure in Pascals. From this regression curve fit the uncertainty was calculated using the procedure outlined in section 8-6 of the ASME PTC 19.1-2005 Test Uncertainty manual [134]. The calibration uncertainty is dependent on the voltage and hence varies for each point. For the range used in these measurements  $b_{cal}$  is about 45-91% of  $b_{inst}$ . The temperature uncertainty is a combination of the variation in the temperature over the course of the run,  $\Delta T$ , and the uncertainty in the thermocouple,  $b_{TC}$ . This can be written as:

$$b_T = [\Delta T^2 + b_{TC}^2]^{1/2} \quad (D.44)$$

where  $b_{TC}$  is taken as 2 °C.

The combined standard uncertainty was given in equation (D.31) and is a combination of the random uncertainty and the systematic standard uncertainty. The expanded uncertainty is the combined standard uncertainty multiplied by the Student's t-table value,  $t_{v,p}$  where  $v$  is  $N - 1$  and  $p$  is the selected confidence interval. At 20:1 odds or

$p = 95\%$  confidence and assuming a large sample size,  $t_{v,p} = 1.96$ . Using this analysis, the true value is expected to lie within:

$$U \pm t_{v,p} u_U \quad (D.45)$$

where  $t_{v,p} u_U$  is the expanded uncertainty or simply the uncertainty of the quantity.

### D.3 Hot-Wire Anemometry Uncertainty Analysis

The uncertainty analysis procedure followed the general guidelines laid out in the ASME PTC 19.1-2005 Test Uncertainty manual [134] as well as a Dantec hot-wire measurement guide [135]. The combined standard uncertainty of  $U$  is a combination of the random uncertainty,  $s_U$ , and the systematic standard uncertainty,  $b_U$ .

$$u_U = [b_U^2 + s_U^2]^{\frac{1}{2}} \quad (D.46)$$

The random uncertainty,  $s_U$ , is related to the variance as follows:

$$s_U = \sqrt{\frac{\bar{u'^2}}{N}} \quad (D.47)$$

where  $N$  is the number of samples. The overall systematic standard uncertainty is the geometric sum of the individual systematic uncertainties written as:

$$b_U = \left[ \begin{array}{l} \left( \frac{1}{k_\theta} b_\theta \right)^2 + \left( \frac{1}{k_{fit}} b_{fit} \right)^2 + \left( \frac{1}{k_{cal}} b_{cal} \right)^2 + \left( \frac{1}{k_P} b_P \right)^2 + \dots \end{array} \right]^{\frac{1}{2}} \\ \left. \begin{array}{l} \left( \frac{1}{k_T} b_T \right)^2 + \left( \frac{1}{k_A} \frac{b_A}{D} \right)^2 + \left( \frac{1}{k_D} b_D \right)^2 \end{array} \right] \quad (D.48)$$

where  $k_i$  is the coverage factor of the input variance. The systematic uncertainty of the probe angular alignment was estimated using:

$$b_\theta = U(1 - \cos(\theta)) \quad (D.49)$$

where  $\theta$  is the probe angle with respect to freestream flow. Here,  $\theta$  is estimated to be aligned within  $\pm 3^\circ$ . Since the calibration curve fit implicitly defines  $U(E)$  calculating the systematic uncertainty in the fit required a backward approach as follows:

$$b_{fit} = \frac{b_E}{\frac{\partial E}{\partial U}} \quad (D.50)$$

where  $b_E$  is the estimated standard error in the voltage produced by using the curve fit for the velocity  $U$  (provided by using the polyval command in MATLAB) and  $\frac{\partial E}{\partial U}$  was calculated using equation (2.12).

The uncertainty in the calibration,  $b_{cal}$ , is a combination of two primary factors, 1) the accuracy with which the selected calibration flow speeds,  $M_i$  or  $U_i$ , are known, and 2) the deviation of flow from the pitot probe location to the hot-wire probe location during the calibration process, i.e. the freestream flow uniformity. The calibration speeds were set

by the wind tunnel controls and are measured by the two Setra pressure transducers. The uncertainty of the flow speeds is calculated from pressure via Bernoulli's equation and from the definition of Mach number given as:

$$M = \sqrt{\frac{2(P_T - P_S)}{\gamma P_S}} \quad (D.51)$$

where  $P_T$  and  $P_S$  are the local total and static pressure respectively, each measured with a Setra Model 270. The sensitivities of  $M$  with respect to each of the dependent values were obtained by partial differentiation.

$$\frac{\partial M}{\partial P_T} = \frac{1}{M\gamma P_S} \quad (D.52)$$

$$\frac{\partial M}{\partial P_S} = \frac{-P_T}{M\gamma P_S^2} \quad (D.53)$$

This gives the uncertainty of the calibration Mach numbers,  $b_{M_{cal}}$  as:

$$b_{M_{cal}} = \left[ \left( \frac{\partial M}{\partial P_T} b_{P_T} \right)^2 + \left( \frac{\partial M}{\partial P_S} b_{P_S} \right)^2 \right]^{\frac{1}{2}} \quad (D.54)$$

where  $b_{P_T}$  and  $b_{P_S}$  are the uncertainties of the Setra pressure transducers given as 25 Pa.

Using this information, the uncertainty in the calibration velocities can then be calculated using equations (D.54) and (2.9) as follows:

$$b_{U_{cal}} = \left[ \left( \frac{U}{M} b_{M_{cal}} \right)^2 + \left( \frac{U}{2T} \Delta T \right)^2 \right]^{\frac{1}{2}} \quad (D.55)$$

where  $\Delta T$  is the uncertainty of the temperature measurements taken as 2 °C. An example of the uncertainty in the calibration velocities is shown in the calibration plot, Figure 2.10. This uncertainty in the calibration velocity at a given voltage is equivalent to the uncertainty in the flow measurement for the same voltage. The uncertainty in the freestream flow uniformity from the hot-wire location to the pitot tube is likely to be significant, as the freestream velocity appears to vary location to location; however, this uncertainty has not been systematically addressed, hence it will not be considered here. If included, it would be geometrically added to the uncertainty in the calibration velocity as follows:

$$b_{cal} = \left[ (b_{U_{cal}})^2 + (b_{U_{uniformity}})^2 \right]^{\frac{1}{2}} \quad (D.56)$$

Changes in ambient pressure also produce an uncertainty in the result through their influence on density. Since the calibration velocity more formally represents a change in

mass flux,  $\rho U$ , the density enters the calibration equation. Hence, the calibration equation could be written as:

$$E(\rho, U) = f(\rho U) \quad (D.57)$$

The uncertainty caused by changes in ambient pressure can then be written as:

$$b_p = \frac{\partial U}{\partial E} \frac{\partial E}{\partial \rho} \frac{\partial \rho}{\partial P} \Delta P = \frac{U \Delta P}{P} \quad (D.58)$$

where  $\Delta P$  is the uncertainty or change in the ambient pressure during the calibration and test, estimated as 1 hPa.

While a temperature correction was applied to the calibration and data, there is still uncertainty in the measured temperature, and hence this should be considered as a source of uncertainty. This uncertainty in temperature comes from the fact that the hot-wire voltage is directly related to the heat transfer. To account for this, the voltage-velocity relation is first written in a form relating it to the convective heat transfer.

$$E(\rho, U, T_a) = (T_w - T_a) * f(\rho U) \quad (D.59)$$

This form of the equation is then used to determine the uncertainty caused by changes in temperature as:

$$b_T = \frac{\partial U}{\partial E} \frac{\partial E}{\partial T} \Delta T + \frac{\partial U}{\partial E} \frac{\partial E}{\partial \rho} \frac{\partial \rho}{\partial T} \Delta T = \frac{-f(\rho U) \Delta T}{(T_w - T_a) * f'(\rho U) \rho} + \frac{-U \Delta T}{T} \quad (D.60)$$

where the first term is due to convective heat transfer and the second term changes in density caused by temperature.

The uncertainty in the analog to digital conversion can be calculated as follows:

$$b_{\frac{A}{D}} = \frac{E_{AD}}{2^n} \frac{\partial U}{\partial E} \quad (D.61)$$

where  $E_{AD}$  is the A/D board input range taken as 20 V, and  $n$  is the resolution in bits taken as 16. Of the uncertainty sources examined, this one is the smallest in magnitude and could easily be neglected without changing the overall uncertainty result.

Another systematic uncertainty that arises is a drift in the anemometer voltage as the probe approaches the surface. This can be seen by taking a data set profile with no air flow, recording the voltages, and then running them through the calibration curve fit equation to give velocities. With no air flow the voltage should yield a velocity near zero, with only small deviations due to normal air circulation in the room/wind tunnel. What is seen, however, is that near the surface the indicated velocity is not zero and instead deviates substantially, as shown in Figure D.1.b. Once the probe is about  $y_{off} = 1.4$  mm off the surface, this variation is gone and only the expected small deviations remain with the voltage being roughly  $E_{cal} = E(0)$ .

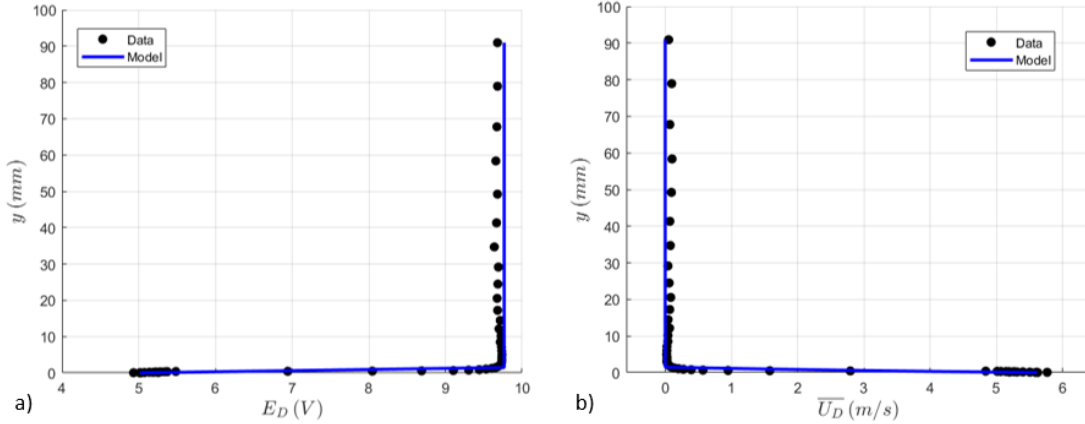


Figure D.1 Plot of drift voltage (a) and drift velocity (b) as functions of wall-normal height for a test with no air flow, i.e.  $M = 0$ . Note that near the surface the voltage (a) drifts causing an “artificial” velocity (b) to appear.

This near wall effect could be due to heat transfer and should be included in the uncertainty of the measurements. The drift in voltage was not nearly this substantial in most of the cases, so this example should be treated as the extreme case; however, the trend was the same. To account for this effect, instead of taking a no-flow profile before each test, the drift in voltage was recorded at the first point near the wall,  $E_{wall}$ , before the test was started. This was then fit to a linear function of voltage vs wall normal location that only extended  $y_{off} = 1.4$  mm off the surface with the remaining drift voltage being set to  $E_{cal}$ . In equation form this is written as:

$$E_D = \frac{E_{cal} - E_{wall}}{y_{off}} y + E_{wall} \quad (D.62)$$

where  $E_D$  is the drift voltage and is a function of the wall-normal location. The uncertainty that this produces in the velocity,  $b_D$ , is calculated by inputting the drift voltage into the

calibration curve fit equation (2.12) and solving by the bisection method to yield the drift velocity. This can be written as follows:

$$b_D = g(E_D) \quad (D.63)$$

This model is also shown in Figure D.1 and compares quite well to the observed data. Again, most profiles did not drift as far as 5 V and were instead in the 7-9 V range.

A list of the uncertainty sources just discussed, and their estimated magnitudes, are shown in Figure D.1. It should also be pointed out what sources of uncertainty were not considered here. As mentioned, the uniformity of the freestream flow is not known. Additionally, the effects of spatial averaging over the span of the hot-wire length likely influences the shape and magnitude of the variance profiles. This can be seen when the variance is written in the form of turbulence intensity. Hutchins et al. [67] provide a likely explanation for this phenomena in the attenuation of small scales due to a large viscous scaled wire length,  $l^+$ , approximately 271 here. For further discussion see Hutchins et al. [67].

TABLE D.1  
SYSTEMATIC UNCERTAINTY SOURCES

Uncertainty Source	Estimated Uncertainty	Coverage Factor	Remarks
Probe angular alignment: $\mathbf{b}_\theta$	$\pm 0.14\%$ of U	$\sqrt{3}$	Estimated uncertainty in alignment with streamwise flow direction.
Curve fit: $\mathbf{b}_{fit}$	$\pm 1\%$ of U	2	Estimated by using the standard error of the curve fit $E = f(U)$
Calibration: $\mathbf{b}_{cal}$	$\pm 1\%$ to $\pm 4\%$ of U	2	Only includes the uncertainty of the calibration points, not the freestream flow non-uniformity.
Temperature: $\mathbf{b}_T$	$\pm 1\%$ of U	$\sqrt{3}$	Estimated based off thermocouple uncertainty of $2^\circ\text{C}$ .
Ambient Pressure: $\mathbf{b}_P$	$\pm 0.1\%$ of U	$\sqrt{3}$	Estimated based off a 1 hPa change in ambient pressure during the calibration and test.
A/D Resolution: $\mathbf{b}_{\frac{A}{D}}$	$\pm 0.01\%$ of U	$\sqrt{3}$	For the NI DAQ with 16 bits of resolution and 20 V input range.
Voltage Drift: $\mathbf{b}_D$	$\pm 0\%$ to $\pm 5\%$ of U	$\sqrt{3}$	This uncertainty is only substantial near the surface and in most cases peaks around 2% of U.

An example of the elemental uncertainty of each of the systematic uncertainty components and the random uncertainty are shown as a function of the wall-normal profile point in the bar graph in Figure D.2. Here, the sum of each element is scaled to equal 100% to highlight the relative magnitude of each uncertainty source and the profile point starts at the wall (point 1) and continues into the freestream (point 48). In general, the uncertainties due to calibration, temperature, curve fit, and voltage drift are the most significant, with substantial variation across the boundary layer profile.

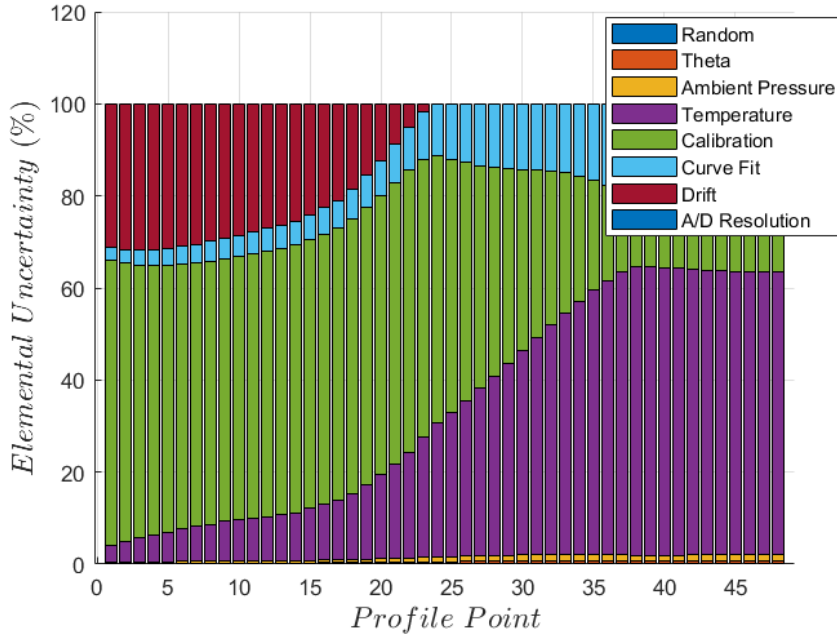


Figure D.2 Plot of the relative uncertainty due to each of the sources discussed as a function of the boundary layer height. Here the uncertainty of each source is written as a percentage of the total uncertainty at each point. Note that the profile point starts just off the surface, Profile Point 1, and continues into the freestream, Profile Point 48.

The combined standard uncertainty was given in equation (D.46) and is a combination of the random uncertainty and the systematic standard uncertainty. The expanded uncertainty is the combined standard uncertainty multiplied by the Student's t-table value,  $t_{v,p}$  where  $v$  is  $N - 1$  and  $p$  is the selected confidence interval. At 20:1 odds or  $p = 95\%$  confidence and assuming a large sample size,  $t_{v,p} = 1.96$ . Using this analysis, the true value is expected to lie within:

$$U \pm t_{v,p} u_U \quad (D.64)$$

where  $t_{v,p} u_U$  is the expanded uncertainty or simply the uncertainty of the quantity.

The uncertainty considered thus far is with respect to the mean velocity,  $U$ . It is assumed that the systematic uncertainties examined only effect the mean not the variance. Thus, the uncertainty of the variance is solely a function of the variance, the kurtosis, and the number of samples and can be written as:

$$u_{\overline{u'^2}} = \sqrt{\frac{\overline{u'^4} - \overline{u'^2}^2}{N}} \quad (D.65)$$

This yields the expanded uncertainty as:

$$\overline{u'^2} \pm t_{v,p} u_{\overline{u'^2}} \quad (D.66)$$

#### D.4 Oil-Film Interferometry Uncertainty Analysis

This section will outline the procedure used to calculate the uncertainty for the oil-film interferometry measurements reported. The uncertainty of  $C_f$  is a combination, via propagation, of the uncertainties of each of the parameters of  $C_f$ . The functional dependence of  $C_f$  is as follows:

$$C_f = f(\theta, \lambda, \Delta x, n, q_\infty(t), \mu(v_0, T(t))) \quad (D.67)$$

The sensitivities of  $C_f$  with respect to each of these dependent values were obtained by partial differentiation of equation (2.17). For ease of calculation, the integral in the denominator of equation (2.17) is defined as:

$$I = \int_0^{t_{run}} \frac{q_\infty(t)}{\mu(\nu_0, T(t))} dt \quad (D.68)$$

The uncertainty of  $C_f$  can then be written as:

$$\begin{aligned} u_{C_f} = & \left[ (\frac{\partial C_f}{\partial \theta} u_\theta)^2 + (\frac{\partial C_f}{\partial n} u_n)^2 + (\frac{\partial C_f}{\partial \Delta x} u_{\Delta x})^2 + (\frac{\partial C_f}{\partial I} \frac{\partial I}{\partial q_\infty} u_{q_\infty})^2 + \right. \\ & \left. \dots (\frac{\partial C_f}{\partial I} \frac{\partial I}{\partial \mu} \frac{\partial \mu}{\partial \nu_0} u_{\nu_0})^2 + (\frac{\partial C_f}{\partial I} \frac{\partial I}{\partial \mu} \frac{\partial \mu}{\partial T} u_T)^2 \right]^{\frac{1}{2}} \end{aligned} \quad (D.69)$$

The estimated uncertainties of each of the parameters in equation (D.69) is given below in Table D.2. Approximately 85% of the uncertainty of  $C_f$  is due to the uncertainty associated with the variation in the viscosity. This includes both the 5% manufacturer's reported uncertainty as well as its variation with temperature and the uncertainty therein. The uncertainty in  $C_f$  of each of the measurements is shown in Table 3.1 and is approximately 5-9% of the local reported nominal value.

TABLE D.2  
UNCERTAINTY SOURCES AND ESTIMATE VALUES

Uncertainty Source	Estimated Uncertainty	Remarks
Incident angle: $u_\theta$	$\pm 0.051$ (2.9°)	Primarily due to the geometry imposed small camera focal distance and the streamwise length of the interferogram region.
Fringe spacing: $u_{\Delta x}$	$\pm  \Delta x_1 - \Delta x_2 $	Taken as the magnitude of the difference between Fourier series fit results. This dominates the random uncertainty.
Oil viscosity: $u_{\nu_0}$	$\pm 5\%$ of $\nu_0$	Manufacturer's specification. Uncertainty could be reduced by viscometer calibration.
Temperature: $u_T$	$\pm 2$ °C	Estimated based off standard k-type thermocouple uncertainty.
Dynamic pressure: $u_{q_\infty}$	$\pm 0.3\%$ of FS	Full-scale range is 10 in H2O. This value was doubled to account for the calibration uncertainty which is of approximately equal magnitude.
Oil index of refraction: $u_n$	$\pm 0.002$	Manufacturer's specification.
Light wavelength: $u_\lambda$	Negligible	The two wavelengths from the sodium lamp 589 nm and 589.6 nm are so close together the uncertainty is very small.

### D.5 Laser Doppler Velocimetry Uncertainty Analysis

The LDV data presented in this dissertation were acquired over the period of approximately 17 months ranging from April 2018 to August 2019. For each test, the tunnel was warmed up and allowed to reach steady state before any LDV measurements were acquired. For each profile, the probe locations were preset in the BSA flow software and the data collection process was semi-automated. A typical profile took anywhere from 30 minutes to 3 hours to collect sufficient statistically converged data. The number of samples collected per probe location varied significantly due to a highly varying data rate throughout the flow measurement region. In many cases, multiple runs were acquired for

a profile and the results were then ensemble averaged. Dantec BSA Flow Software versions 4.10 and 6.5 were used to acquire and process the raw signal. The data output for each probe location consisted of a separate text file containing the row#, arrival time [ms], transit time [ms], and the instantaneous streamwise  $u$  [m/s] and wall-normal,  $v$  [m/s] velocity components for each sample.

#### D.5.1 Processing of Data:

The individual text files for each probe location were loaded into and processed in MATLAB. The mean velocities were calculated as follows:

$$\bar{U} = \frac{\sum_{j=1}^N u_j}{N} \quad (D.70)$$

$$\bar{V} = \frac{\sum_{j=1}^N v_j}{N} \quad (D.71)$$

where  $u_j$  and  $v_j$  is the instantaneous velocity measurement of the data set and  $N$  is the number of samples. The variance is calculated as follows:

$$\overline{u'^2} = \frac{\sum_{j=1}^N |u_j - \bar{U}|^2}{N - 1} \quad (D.72)$$

$$\overline{v'^2} = \frac{\sum_{j=1}^N |v_j - \bar{V}|^2}{N - 1} \quad (D.73)$$

and the covariance as:

$$\overline{u'v'} = \frac{\sum_{j=1}^N (u_j - \bar{U})(v_j - \bar{V})}{N - 1} \quad (D.74)$$

Using these statistical quantities, the raw data was then filtered to remove any samples outside of three standard deviations from the mean, to minimize errors as suggested by DeGraaff and Eaton [136], and new statistical quantities were calculated to replace those acquired using the raw data. All these quantities are local ones calculated directly from the filtered time series data. To determine the coordinate locations and the statistical quantities in the global coordinate system, a rotation must be applied to the local data. In the general sense, this is shown in Figure D.1 where a coordinate system  $(x,y,z)$  is rotated to a reference frame  $(x_{ref},y_{ref},z_{ref})$ . The angle of the local coordinate system is  $\alpha$  and the angle of the reference coordinate system is  $\theta_{ref}$ . Together their difference gives the required rotation angle to rotate a vector in the  $(x,y,z)$  frame to one in the  $(x_{ref},y_{ref},z_{ref})$  frame.

$$\theta = \theta_{ref} - \alpha \quad (D.75)$$

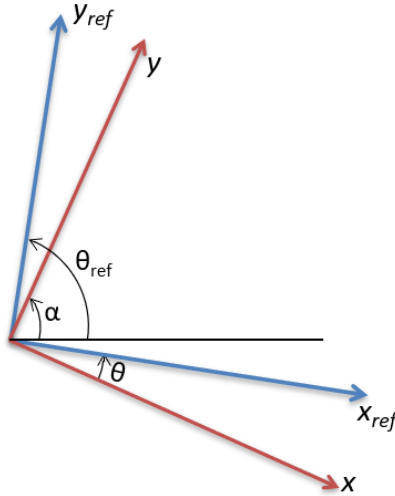


Figure D.3 Local and reference coordinate system relations

In this case, the reference coordinate system is the global one and  $\theta_{ref} = \pi/2$ . The angle of the local coordinate system,  $\alpha$ , is calculated from the normal line of the ramp as follows:

$$\alpha(X) = \text{atan}\left(\frac{-1}{5a_4X^4 + 4a_3X^3 + 3a_2X^2}\right) \quad (D.76)$$

where the coefficients are given in terms of the ramp length,  $L = 0.9$  m, the ramp height,  $H = 0.2$  m and defined as:

$$a_2 = -10H/L^3, \quad a_3 = 15H/L^4, \quad a_4 = -6H/L^5 \quad (D.77)$$

Note that  $\alpha$  is a function of  $X$  and for each rotation, the starting  $X$ -location of the profile,  $X_p$ , must be used to calculate  $\alpha$ . Here the rotation consists of rotating the local quantities in the  $(x,y,z)$  coordinate system through the angle  $\theta$  to the global coordinate system  $(X,Y,Z)$ .

First the local  $(x,y,z)$  coordinates were rotated to the global coordinate system using the a first order tensor rotation

$$X_G = R^T \cdot X_L + X_{offset} \quad (D.78)$$

where  $X_G$  is the coordinate vector in the global coordinates and  $X_L$  is the coordinate vector in the local coordinates and  $X_{offset}$  is the translation of the origin. Here  $X_G$ ,  $X_L$  and  $X_{offset}$  are defined as

$$X_G = \begin{bmatrix} X \\ Y \\ Z \end{bmatrix} \quad \text{and} \quad X_L = \begin{bmatrix} x \\ y \\ z \end{bmatrix} \quad \text{and} \quad X_{offset} = \begin{bmatrix} X_p \\ f(X_p) \\ 0 \end{bmatrix} \quad (D.79)$$

and  $R$  is the rotation matrix defined as

$$R = \begin{bmatrix} \cos(\theta) & -\sin(\theta) & 0 \\ \sin(\theta) & \cos(\theta) & 0 \\ 0 & 0 & 1 \end{bmatrix} \quad (D.80)$$

The mean velocities were then calculated in the global coordinate system using a similar first order tensor rotation defined as follows:

$$U_G = R^T \cdot U_L \quad (D.81)$$

where  $U_G$  is the mean velocity vector in the global coordinates and  $U_L$  is the mean velocity vector in the local coordinates. Here  $U_G$  and  $U_L$  are defined as:

$$U_G = \begin{bmatrix} U_{global} \\ V_{global} \\ 0 \end{bmatrix} \quad \text{and} \quad U_L = \begin{bmatrix} U_{local} \\ V_{local} \\ 0 \end{bmatrix} \quad (D.82)$$

Finally, the stresses were calculated in the global coordinate system using a second order tensor rotation defined as

$$T_G = R^T \cdot T_L \quad (D.83)$$

where  $T$  is the Reynolds stress tensor defined as follows:

$$T = \begin{bmatrix} \overline{u'^2} & \overline{u'v'} & 0 \\ \overline{u'v'} & \overline{v'^2} & 0 \\ 0 & 0 & 0 \end{bmatrix} \quad (D.84)$$

and the subscripts  $L$  and  $G$  refer to the local and global coordinate systems, respectively.

### D.5.2 Uncertainty Analysis:

The uncertainty analysis procedure followed the general guidelines laid out in the ASME PTC 19.1-2005 Test Uncertainty manual [134]. First the uncertainty of the statistical quantities in the local coordinate system will be presented followed by that of the global coordinate system.

### D.5.2.1 Uncertainty Analysis – Local Values

#### D.5.2.1.1 Random Uncertainty

Random standard uncertainties were calculated based off the guidelines of Benedict and Gould [137] as they apply to data fitting any probability distribution and not just the normal distribution. The random standard uncertainties are related to the estimator variances as follows:

$$s_{\bar{U}} = \sqrt{\frac{\bar{u}'^2}{N}} \quad (D.85)$$

$$s_{\bar{V}} = \sqrt{\frac{\bar{v}'^2}{N}} \quad (D.86)$$

$$s_{\bar{u}'^2} = \sqrt{\frac{\bar{u}'^4 - \bar{u}'^2}{N}} \quad (D.87)$$

$$s_{\bar{v}'^2} = \sqrt{\frac{\bar{v}'^4 - \bar{v}'^2}{N}} \quad (D.88)$$

$$s_{\bar{u}'\bar{v}'} = \sqrt{\frac{\bar{u}'^2\bar{v}'^2 - (\bar{u}'\bar{v}')^2}{N}} \quad (D.89)$$

This next part documents how the systematic uncertainties were accounted for.

#### D.5.2.1.2 Filtering Uncertainty

The first systematic uncertainty accounted for is that due to filtering the raw data as suggested by DeGraaff and Eaton [136]. A filtering uncertainty was based on the

difference between the raw variables and the filtered ones. This uncertainty is nonsymmetric, so the procedure outlined in section 8-2 of the ASME PTC 19.1-2005 Test Uncertainty manual [134] was followed. The systematic standard uncertainty is written as:

$$b_{\bar{U}_f} = \frac{\bar{U}_{raw} - \bar{U}}{2} \quad (D.90)$$

$$b_{\bar{V}_f} = \frac{\bar{V}_{raw} - \bar{V}}{2} \quad (D.91)$$

$$b_{\bar{u'^2}_f} = \frac{\bar{u'^2}_{raw} - \bar{u'^2}}{2} \quad (D.92)$$

$$b_{\bar{v'^2}_f} = \frac{\bar{v'^2}_{raw} - \bar{v'^2}}{2} \quad (D.93)$$

$$b_{\bar{u'v'}_f} = \frac{\bar{u'v'}_{raw} - \bar{u'v'}}{2} \quad (D.94)$$

where the coverage factor was taken as  $k_f = \sqrt{3}$ . The offset of each of the measurements

is defined as follows:

$$q_{\bar{U}_f} = \frac{\bar{U}_{raw} - \bar{U}}{2} \quad (D.95)$$

$$q_{\bar{V}_f} = \frac{\bar{V}_{raw} - \bar{V}}{2} \quad (D.96)$$

$$q_{\bar{u'^2}_f} = \frac{\bar{u'^2}_{raw} - \bar{u'^2}}{2} \quad (D.97)$$

$$q_{\bar{v'^2}_f} = \frac{\bar{v'^2}_{raw} - \bar{v'^2}}{2} \quad (D.98)$$

$$q_{\overline{u'v'}_f} = \frac{\overline{u'v'}_{raw} - \overline{u'v'}}{2} \quad (D.99)$$

#### D.5.2.1.3 Temperature Variation Uncertainty

The temperature varies throughout the duration of each run thereby changing the local speed of sound. Since the Mach number,  $M$  is held constant at 0.2 throughout the duration of the tests, the freestream velocity must change in proportion to the local changes in the speed of sound. This introduces uncertainty that may be accounted for by examining the relationship between freestream velocity,  $U$ , and temperature,  $T$ , via the definition of the Mach number,  $M$ , written as:

$$\bar{U} = M\sqrt{\gamma RT} \quad (D.100)$$

The sensitivity of this term can be written as:

$$\frac{\partial \bar{U}}{\partial T} = \frac{M}{2} \sqrt{\frac{\gamma R}{T}} \quad (D.101)$$

or equivalently,

$$b_{\overline{U_T}} = \frac{\partial U}{\partial T} b_T = \frac{M}{2} \sqrt{\frac{\gamma R}{T}} b_T \quad (D.102)$$

where  $b_T$  is the uncertainty in temperature taken as half the estimated greatest change in temperature over the course of all the tests. Similarly, the wall-normal component of velocity,  $V$ , would be affected by the changing temperature. Here we estimate its uncertainty as follows:

$$b_{\bar{V}_T} = \frac{\bar{V}}{\bar{U}} \frac{\partial \bar{U}}{\partial T} b_T = \frac{\bar{V}}{\bar{U}} \frac{M}{2} \sqrt{\frac{\gamma R}{T}} b_T \quad (D.103)$$

#### D.5.2.1.4 Calibration Uncertainty

The uncertainties listed so far are all dependent on the experiment, i.e. the number of samples, the type of post-process filtering, and the temperature variation during the test. Excluding these uncertainties, there is still a calibration uncertainty inherent with the LDV hardware and software, (i.e. how based on the inherent accuracy of the system). A typical method to calibrate LDV systems is to use a small wire on the edge of a rotating disk. The LDV probe volume is set coincident to the edge of the disk and a burst is detected each time the wire breaks the probe volume. By accurately knowing the diameters of the wire and disk and the rotation rate, the LDV system uncertainty can be estimated. Results from a NIST calibration on a similar Dantec Dynamics LDV system was used to estimate the calibration uncertainty. The uncertainty is taken from [138] and given as a function of velocity and is applied here to both LDV components as:

$$b_{\bar{U}_c}(\bar{U}) = \sqrt{(0.0032\bar{U})^2 + (0.0018)^2} \quad (D.104)$$

$$b_{\bar{V}_c}(\bar{V}) = \sqrt{(0.0032\bar{V})^2 + (0.0018)^2} \quad (D.105)$$

Again, this calibration uncertainty is only an estimate based on a similar calibration procedure.

#### D.5.2.1.5 Instrument Uncertainty

There is inherent uncertainty associated with the settings of the LDV flow processer, dubbed here as the instrument uncertainty. These settings include sensitivity, signal gain, signal to noise ratio, velocity span etc. With the most stringent settings, in theory, the instrument uncertainty should approach zero; however, frequently these settings had to be adjusted to off-ideal values as the data rate would otherwise fall to zero. There is no standard procedure for quantifying this uncertainty and our attempts would be speculative at best. Here we only acknowledge the existence of this uncertainty component but do not include it in the analysis.

#### D.5.2.1.6 Velocity Bias Uncertainty

Another source that introduces uncertainty into the measurement is that stemming from velocity bias. DeGraaff and Eaton [136] describe velocity bias as, “assuming the particles are uniformly distributed in the fluid, the likelihood of a particle passing through the measurement volume is proportional to the fluid velocity”. Weighting methods exist to compensate for this bias, but they are only viable in high data rate scenarios, which is not the case here. In low data rate scenarios there is no consensus on the best approach to quantify the velocity bias [139]. The Dantec reference manual [140] states that if the samples are statistically independent then weighting methods are unnecessary as the

standard weighting of 1/N is sufficient. Here we acknowledge the velocity bias uncertainty, which is likely to be quite small in this case, but do not attempt to account for it in this analysis.

#### D.5.2.1.7 Validation Bias Uncertainty

Also known as filter bias, validation bias is “the tendency of real systems to have a measurement efficiency that is dependent on the speed of the measured particle” [139]. There is no universal approach to handle validation bias as it is too system dependent. Again, this uncertainty is simply acknowledged but not accounted for here.

#### D.5.2.1.8 Systematic Standard Uncertainty

The systematic standard uncertainty is a combination of all the individual systematic uncertainties and coverage factors and is calculated as follows:

$$b_{\bar{U}} = \left[ \left( \frac{1}{k_f} b_{\bar{U}_f} \right)^2 + \left( \frac{1}{k_c} b_{\bar{U}_c} \right)^2 + \left( \frac{1}{k_T} b_{\bar{U}_T} \right)^2 \right]^{\frac{1}{2}} \quad (D.106)$$

$$b_{\bar{V}} = \left[ \left( \frac{1}{k_f} b_{\bar{V}_f} \right)^2 + \left( \frac{1}{k_c} b_{\bar{V}_c} \right)^2 + \left( \frac{1}{k_T} b_{\bar{V}_T} \right)^2 \right]^{\frac{1}{2}} \quad (D.107)$$

$$b_{\bar{u'^2}} = \left[ \left( \frac{1}{k_f} b_{\bar{u'^2}_f} \right)^2 \right]^{\frac{1}{2}} \quad (D.108)$$

$$b_{\bar{v'^2}} = \left[ \left( \frac{1}{k_f} b_{\bar{v'^2}_f} \right)^2 \right]^{\frac{1}{2}} \quad (D.109)$$

$$b_{\bar{u}'\bar{v}'} = \left[ \left( \frac{1}{k_f} b_{\bar{u}'\bar{v}'_f} \right)^2 \right]^{\frac{1}{2}} \quad (D.110)$$

Unless otherwise specified, the distributions were not assumed to be known so the coverage factors were taken as  $k = \sqrt{3}$ .

#### D.5.2.1.9 Combined and Expanded Uncertainties

The combined standard uncertainty is a combination of the random uncertainty and the systematic standard uncertainty.

$$x_{\bar{U}} = [ b_{\bar{U}}^2 + s_{\bar{U}}^2 ]^{\frac{1}{2}} \quad (D.111)$$

$$x_{\bar{V}} = [ b_{\bar{V}}^2 + s_{\bar{V}}^2 ]^{\frac{1}{2}} \quad (D.112)$$

$$x_{\bar{u}'^2} = [ b_{\bar{u}'^2}^2 + s_{\bar{u}'^2}^2 ]^{\frac{1}{2}} \quad (D.113)$$

$$x_{\bar{v}'^2} = [ b_{\bar{v}'^2}^2 + s_{\bar{v}'^2}^2 ]^{\frac{1}{2}} \quad (D.114)$$

$$x_{\bar{u}'\bar{v}'} = [ b_{\bar{u}'\bar{v}'}^2 + s_{\bar{u}'\bar{v}'}^2 ]^{\frac{1}{2}} \quad (D.115)$$

The expanded uncertainty is the combined standard uncertainty multiplied by the Student's t-table value,  $t_{v,p}$  where  $v$  is  $N - 1$  and  $p$  is the selected confidence interval. At 20:1 odds or  $p = 95\%$  confidence and assuming a large sample size,  $t_{v,p} = 1.96$ . For all of the reported values,  $t_{v,p}$  was calculated based off of the actual number of samples in the

data set and hence in some cases was larger than 1.96. Using this analysis, the 95% confidence intervals are:

$$\bar{U}_{95} = \pm t_{v,p} x_{\bar{U}} \quad (D.116)$$

$$\bar{V}_{95} = \pm t_{v,p} x_{\bar{V}} \quad (D.117)$$

$$\overline{u'^2}_{95} = \pm t_{v,p} x_{\overline{u'^2}} \quad (D.118)$$

$$\overline{v'^2}_{95} = \pm t_{v,p} x_{\overline{v'^2}} \quad (D.119)$$

$$\overline{u'v'}_{95} = \pm t_{v,p} x_{\overline{u'v'}} \quad (D.120)$$

where  $t_{v,p} x_i$  is the expanded uncertainty. The final asymmetric 95% confidence intervals can then be written as:

$$\bar{U}_{lower\ limit} = \bar{U} + q_{\bar{U}_f} - \bar{U}_{95} \quad (D.121)$$

$$\bar{U}_{upper\ limit} = \bar{U} + q_{\bar{U}_f} + \bar{U}_{95} \quad (D.122)$$

$$\bar{V}_{lower\ limit} = \bar{V} + q_{\bar{V}_f} - \bar{V}_{95} \quad (D.123)$$

$$\bar{V}_{upper\ limit} = \bar{V} + q_{\bar{V}_f} + \bar{V}_{95} \quad (D.124)$$

$$\overline{u'^2}_{lower\ limit} = \overline{u'^2} + q_{\overline{u'^2}_f} - \overline{u'^2}_{95} \quad (D.125)$$

$$\overline{u'^2}_{upper\ limit} = \overline{u'^2} + q_{\overline{u'^2}_f} + \overline{u'^2}_{95} \quad (D.126)$$

$$\overline{v'^2}_{lower\ limit} = \overline{v'^2} + q_{\overline{v'^2}_f} - \overline{v'^2}_{95} \quad (D.127)$$

$$\overline{v'^2}_{upper\ limit} = \overline{v'^2} + q_{\overline{v'^2}_f} + \overline{v'^2}_{95} \quad (D.128)$$

$$\overline{u'v'}_{lower\ limit} = \overline{u'v'} + q_{\overline{u'v'}_f} - \overline{u'v'}_{95} \quad (D.129)$$

$$\overline{u'v'}_{upper\ limit} = \overline{u'v'} + q_{\overline{u'v'}_f} + \overline{u'v'}_{95} \quad (D.130)$$

where the  $q_i$ 's are the offset given by equations (D.95-D.99).

#### D.5.2.2 Uncertainty Analysis – Global Values:

For the global coordinate system, Section 7 of the ASME PTC 19.1-2005 Test Uncertainty manual [134] was followed to propagate the uncertainties calculated for the local coordinate system into the global coordinate system. The functional dependence of the mean and turbulence quantities in the global coordinate system on those acquired in the local coordinate system is as follows:

$$\overline{U}_G = f(\overline{U}_L, \overline{V}_L) \quad (D.131)$$

$$\overline{V}_G = f(\overline{U}_L, \overline{V}_L) \quad (D.132)$$

$$\overline{u'^2}_G = f(\overline{u'^2}_L, \overline{v'^2}_L, \overline{u'v'_L}) \quad (D.133)$$

$$\overline{v'^2}_G = f(\overline{u'^2}_L, \overline{v'^2}_L, \overline{u'v'_L}) \quad (D.134)$$

$$\overline{u'v'_G} = f(\overline{u'^2}_L, \overline{v'^2}_L, \overline{u'v'_L}) \quad (D.135)$$

The sensitivities of each global value with respect to its dependent local values may be obtained by partial differentiation. For example, the sensitivities of Eq. (D.81) are

$$\frac{\partial \overline{U}_G}{\partial \overline{U}_L} = \frac{\partial}{\partial U_L} (R^T \cdot U_L) = R_{11}^T \quad (D.136)$$

$$\frac{\partial \overline{U}_G}{\partial \overline{V}_L} = \frac{\partial}{\partial V_L} (R^T \cdot U_L) = R_{12}^T \quad (D.137)$$

where Eq. (D. 131) is used. Similar results are obtained for Eqs. (D. 132-D. 135).

Using the sensitivities, the random uncertainties are:

$$S_{\overline{U}_G} = [(R_{11}^T S_{\overline{U}_L})^2 + (R_{12}^T S_{\overline{V}_L})^2]^{\frac{1}{2}} \quad (D. 138)$$

$$S_{\overline{V}_G} = [(R_{21}^T S_{\overline{U}_L})^2 + (R_{22}^T S_{\overline{V}_L})^2]^{\frac{1}{2}} \quad (D. 139)$$

$$S_{\overline{u'}_G^2} = [(R_{11} R_{11} S_{\overline{u'}_L^2})^2 + (R_{21} R_{21} S_{\overline{v'}_L^2})^2 + (R_{11} R_{21} S_{\overline{u'}_L \overline{v'}_L})^2]^{\frac{1}{2}} \quad (D. 140)$$

$$S_{\overline{v'}_G^2} = [(R_{12} R_{12} S_{\overline{u'}_L^2})^2 + (R_{22} R_{22} S_{\overline{v'}_L^2})^2 + (R_{12} R_{22} S_{\overline{u'}_L \overline{v'}_L})^2]^{\frac{1}{2}} \quad (D. 141)$$

$$S_{\overline{u'}_G \overline{v'}_G} = [(R_{11} R_{12} S_{\overline{u'}_L \overline{v'}_L})^2 + (R_{21} R_{22} S_{\overline{v'}_L \overline{u'}_L})^2 + (R_{11} R_{22} S_{\overline{u'}_L \overline{v'}_L})^2]^{\frac{1}{2}} \quad (D. 142)$$

where the subscripts ‘L’ and ‘G’ refer to the local and global coordinate value respectively and are added purely for clarity. Note that the local random uncertainties of equations (D. 85-D. 89) did not have ‘L’ subscripts even though they do here.

The systematic standard uncertainties have the same form as the random uncertainties and are given as:

$$b_{\overline{U}_G} = [(R_{11}^T b_{\overline{U}_L})^2 + (R_{12}^T b_{\overline{V}_L})^2]^{\frac{1}{2}} \quad (D. 143)$$

$$b_{\overline{V}_G} = [(R_{21}^T b_{\overline{U}_L})^2 + (R_{22}^T b_{\overline{V}_L})^2]^{\frac{1}{2}} \quad (D. 144)$$

$$b_{\overline{u'}_G^2} = [(R_{11} R_{11} b_{\overline{u'}_L^2})^2 + (R_{21} R_{21} b_{\overline{v'}_L^2})^2 + (R_{11} R_{21} b_{\overline{u'}_L \overline{v'}_L})^2]^{\frac{1}{2}} \quad (D. 145)$$

$$b_{\bar{v}_G'^2} = \left[ (R_{12}R_{12}b_{\bar{u}_L'^2})^2 + (R_{22}R_{22}b_{\bar{v}_L'^2})^2 + (R_{12}R_{22}b_{\bar{u}'\bar{v}_L'})^2 \right]^{\frac{1}{2}} \quad (D.146)$$

$$b_{\bar{u}'\bar{v}_G'} = \left[ (R_{11}R_{12}b_{\bar{u}_L'^2})^2 + (R_{21}R_{22}b_{\bar{v}_L'^2})^2 + (R_{11}R_{22}b_{\bar{u}'\bar{v}_L'})^2 \right]^{\frac{1}{2}} \quad (D.147)$$

Note again that the subscripts ‘L’ and ‘G’ refer to the local and global coordinate values respectively and are added purely for clarity.

#### D.5.2.2.1 Combined and Expanded Uncertainties

The combined and expanded uncertainties take on the same form as for the local values with the new global random and systematic standard uncertainty values replacing the local ones. The only change that occurs is that the offset quantities of each of the measurements are changed from their respective local values to the following global ones:

$$q_{G_{\bar{U}}} = f(\bar{U}_L + q_{\bar{U}_f}, \bar{V}_L + q_{\bar{V}_f}) - f(\bar{U}_L, \bar{V}_L) \quad (D.148)$$

$$q_{G_{\bar{V}}} = f(\bar{U}_L + q_{\bar{U}_f}, \bar{V}_L + q_{\bar{V}_f}) - f(\bar{U}_L, \bar{V}_L) \quad (D.149)$$

$$q_{G_{\bar{u}'^2}} = f(\bar{u}_L'^2 + q_{\bar{u}'^2_f}, \bar{v}_L'^2 + q_{\bar{v}_f}, \bar{u}'\bar{v}_L' + q_{\bar{u}'\bar{v}_f}) - f(\bar{u}_L'^2, \bar{v}_L'^2, \bar{u}'\bar{v}_L') \quad (D.150)$$

$$q_{G_{\bar{v}'^2}} = f(\bar{u}_L'^2 + q_{\bar{u}'^2_f}, \bar{v}_L'^2 + q_{\bar{v}_f}, \bar{u}'\bar{v}_L' + q_{\bar{u}'\bar{v}_f}) - f(\bar{u}_L'^2, \bar{v}_L'^2, \bar{u}'\bar{v}_L') \quad (D.151)$$

$$q_{G_{\bar{u}'\bar{v}'}} = f(\bar{u}_L'^2 + q_{\bar{u}'^2_f}, \bar{v}_L'^2 + q_{\bar{v}_f}, \bar{u}'\bar{v}_L' + q_{\bar{u}'\bar{v}_f}) - f(\bar{u}_L'^2, \bar{v}_L'^2, \bar{u}'\bar{v}_L') \quad (D.152)$$

where the functions  $f$  are from equations (D.131-D.135).

APPENDIX E:  
FLOW SEPARATION CHARACTERISTICS

E.1 Surface Flow Visualization of Downward Angled VGs Installed on the Sidewalls

The images below were acquired when downward angled VGs were installed on the wind tunnel sidewalls. For the setup and reference conditions, see Chapter 6.

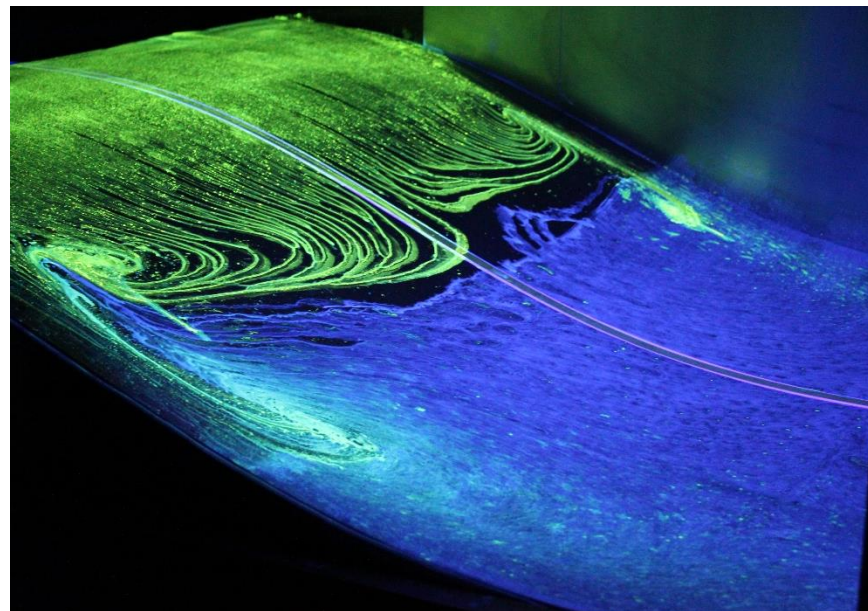


Figure E.1 Surface flow visualization with green dye placed upstream near the ramp leading edge and blue dye placed downstream in the separation and reattachment regions

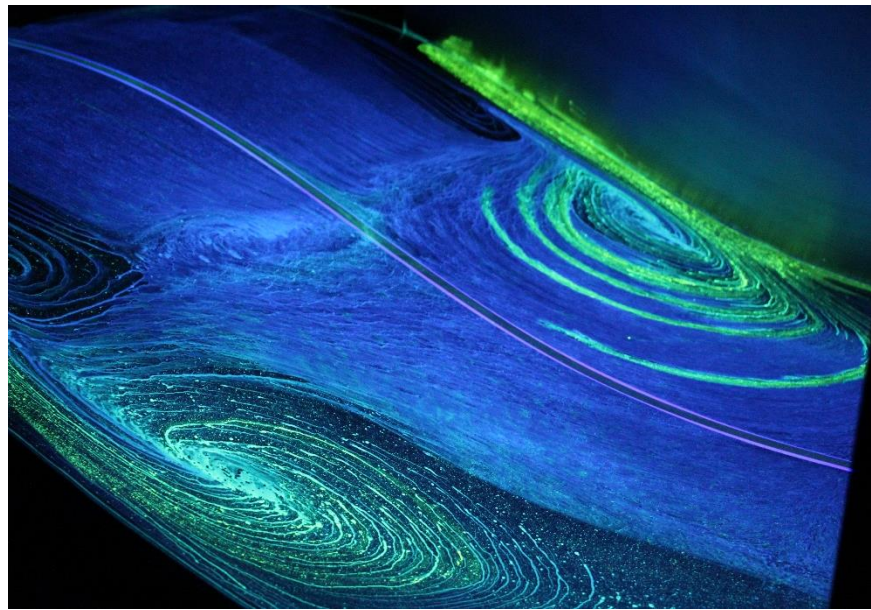


Figure E.2 Surface flow visualization with green dye placed near the sidewall/ramp juncture flow separation and blue dye placed in the central region of the flow

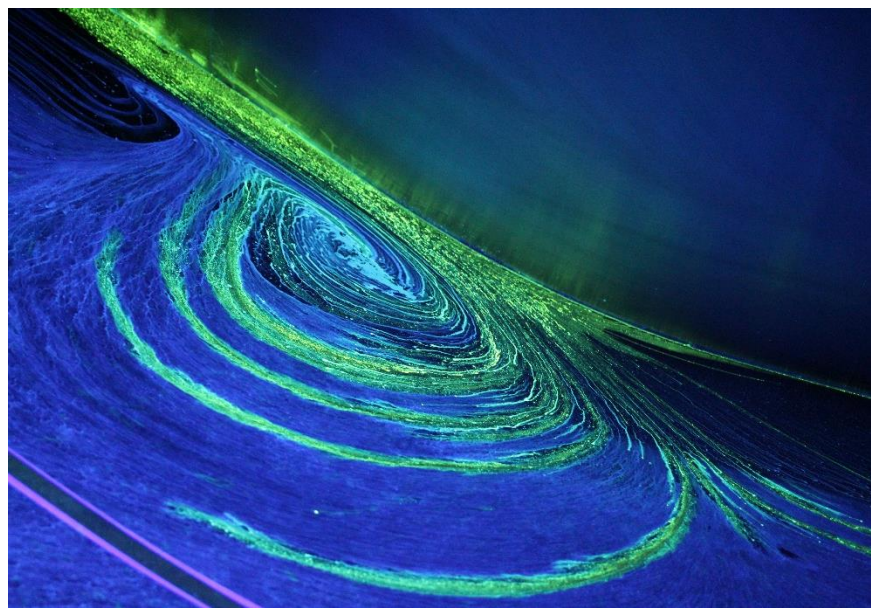


Figure E.3 Surface flow visualization with green dye placed near the sidewall/ramp juncture flow separation and blue dye placed in the central region of the flow

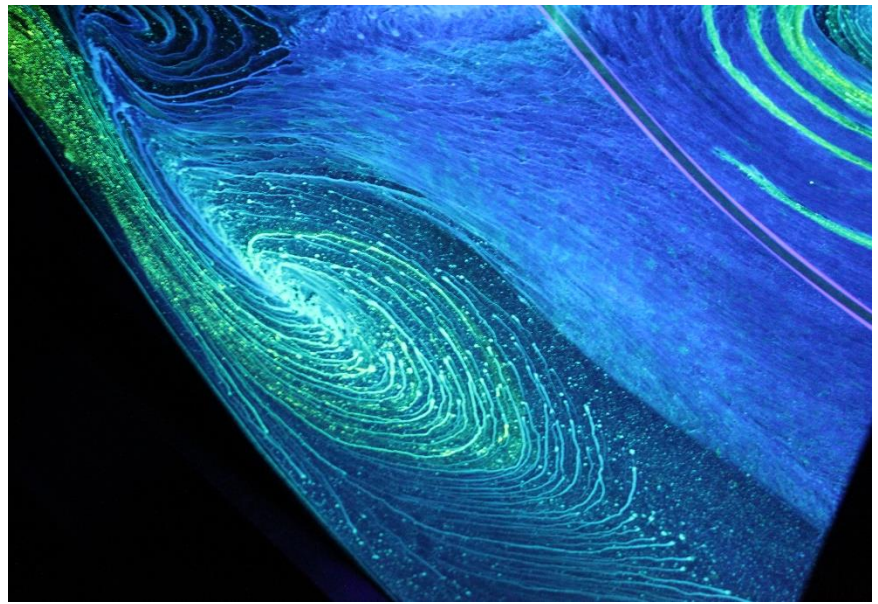


Figure E.4 Surface flow visualization with green dye placed near the sidewall/ramp juncture flow separation and blue dye placed in the central region of the flow

APPENDIX F:  
FLOW CHARACTERISTICS AND ANALYSIS

F.1 Ratio of Vorticity Thickness to Boundary Layer Thickness

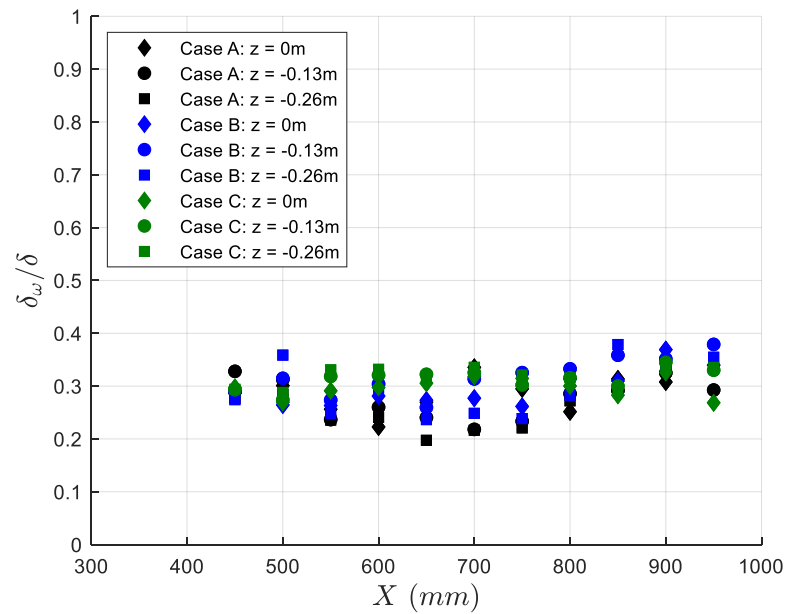


Figure F.1 Ratio of vorticity thickness to local boundary layer thickness for Cases A, B, and C all showing a roughly constant ratio of 0.3

## F.2 Embedded Shear Layer Scaling of the Mean Flow

The data in Figure F.2 include all inflection mean velocity profiles at all three spanwise locations.

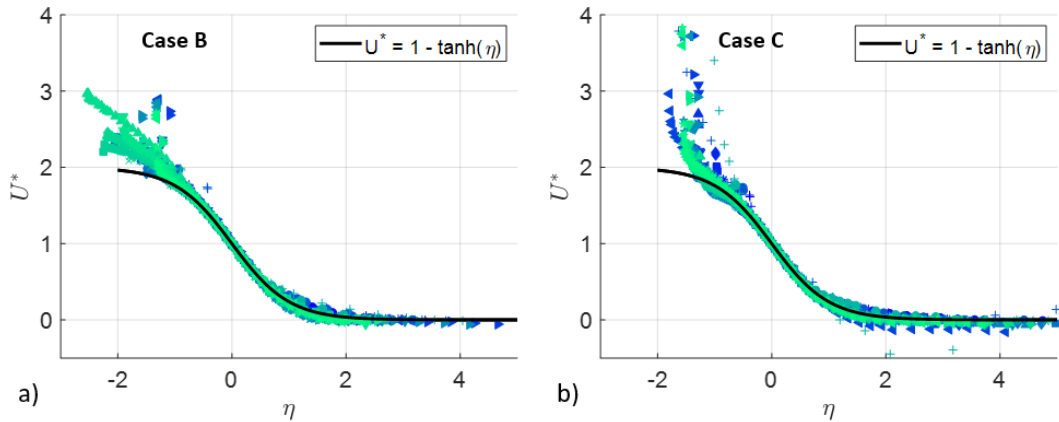


Figure F.2 Embedded shear layer scaling of all the inflectional mean flow profiles for all three spanwise locations for (a) Case B and (b) Case C

## F.3 Time Scales of the Flow

The turbulent flow time scale is defined as:

$$T_{turbulent} = \frac{\delta_\omega}{(\sqrt{u'^2})_p} \quad (F.153)$$

and the mean flow time scale of the flow is defined as:

$$T_{mean} = \frac{\delta_\omega}{U_d} \quad (F.154)$$

where  $\delta_\omega$  is the vorticity thickness,  $U_d$  is the defect velocity, and  $(\sqrt{u'^2})_p$  is the peak turbulent normal stress, all of which are defined in Chapter 8.

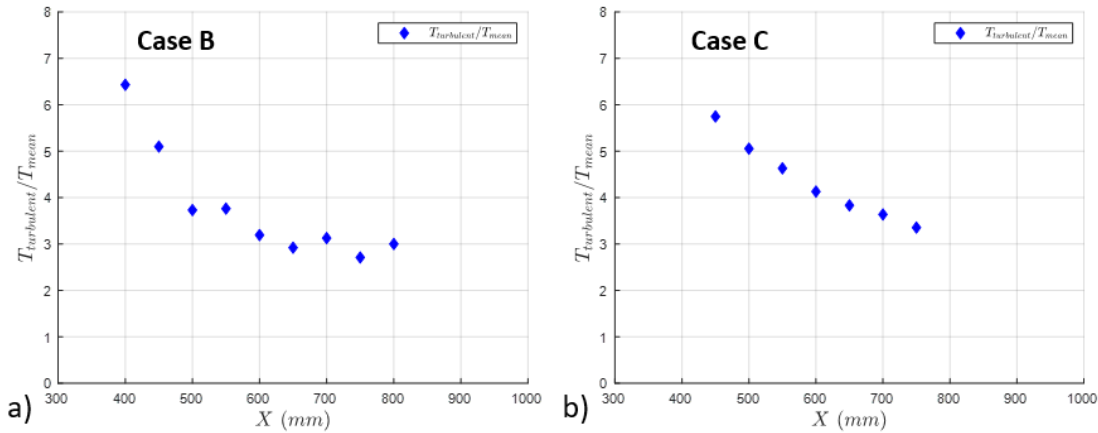


Figure F.3 Ratio of Turbulent to Mean Flow Time Scales for (a) Case B and (b) Case C

## BIBLIOGRAPHY

- [1] Rumsey, C. L. Exp: Two-Dimensional Backward-Facing Convex Ramp with Flow Separation. *NASA Langley Research Center Turbulence Modeling Resource*. [https://turbmodels.larc.nasa.gov/Other\\_exp\\_Data/notredame\\_sep\\_exp.html](https://turbmodels.larc.nasa.gov/Other_exp_Data/notredame_sep_exp.html). Accessed May 13, 2020.
- [2] Malik, M. R. B. *Role of Computational Fluid Dynamics and Wind Tunnels in Aeronautics R and D*. Publication NASA/TP-2012-217602. 2012.
- [3] Slotnick, J., Khodadoust, A., Alonso, J., Darmofal, D., Gropp, W., Lurie, E., and Mavriplis, D. *CFD Vision 2030 Study: A Path to Revolutionary Computational Aerosciences*. Publication NASA/CR-2014-218178. 2014, p. 58.
- [4] Witherden, F. D., and Jameson, A. Future Directions in Computational Fluid Dynamics. 2017.
- [5] Cuvier, C., Srinath, S., Stanislas, M., Foucaut, J.-M., Laval, J.-P., Kähler, C. J., Hain, R., Scharnowski, S., Schröder, A., Geisler, R., Agocs, J., Röse, A., Willert, C., Klinner, J., Amili, O., Atkinson, C., and Soria, J. “Extensive Characterization of a High Reynolds Number Decelerating Boundary Layer Using Advanced Optical Metrology.” *Journal of Turbulence*, Vol. 18, No. 10, 2017, pp. 929–972. <https://doi.org/10.1080/14685248.2017.1342827>.
- [6] Tinoco, E. N., Bogue, D. R., Kao, T.-J., Yu, N. J., Li, P., and Ball, D. N. “Progress toward CFD for Full Flight Envelope.” *The Aeronautical Journal*, Vol. 109, No. 1100, 2005, pp. 451–460. <https://doi.org/10.1017/S0001924000000865>.
- [7] High Lift Prediction Workshop. <https://hiliftpw.larc.nasa.gov/>. Accessed Apr. 22, 2020.
- [8] Rumsey, C., Gatski, T., Sellers, W., Vatsa, V., and Viken, S. Summary of the 2004 CFD Validation Workshop on Synthetic Jets and Turbulent Separation Control. 2004.
- [9] Uzun, A., and Malik, M. R. Wall-Resolved Large-Eddy Simulation of Flow Separation Over NASA Wall-Mounted Hump. Presented at the 55th AIAA Aerospace Sciences Meeting, Grapevine, Texas, 2017.

- [10] Spalart, P. R. “Strategies for Turbulence Modelling and Simulations.” *International Journal of Heat and Fluid Flow*, Vol. 21, No. 3, 2000, pp. 252–263. [https://doi.org/10.1016/S0142-727X\(00\)00007-2](https://doi.org/10.1016/S0142-727X(00)00007-2).
- [11] Oberkampf, W. L., and Smith, B. L. “Assessment Criteria for Computational Fluid Dynamics Model Validation Experiments.” *Journal of Verification, Validation and Uncertainty Quantification*, Vol. 2, No. 3, 2017. <https://doi.org/10.1115/1.4037887>.
- [12] Greenblatt, D., Paschal, K., Yao, C., Harris, J., Schaeffler, N., and Washburn, A. A Separation Control CFD Validation Test Case. Part 1: Baseline & Steady Suction. In *2nd AIAA Flow Control Conference*, American Institute of Aeronautics and Astronautics.
- [13] Tinoco, E. N. “An Evaluation and Recommendations for Further CFD Research Based on the NASA Common Research Model (CRM) Analysis from the AIAA Drag Prediction Workshop (DPW) Series.” 2019.
- [14] Turbulence Modeling Resource. <https://turbmodels.larc.nasa.gov/index.html>. Accessed Apr. 22, 2020.
- [15] Disotell, K. J., and Rumsey, C. L. *Development of an Axisymmetric Afterbody Test Case for Turbulent Flow Separation Validation*. Publication NASA/TM-2017-219680. NASA Langley Research Center, Hampton, Virginia, 2017, p. 34.
- [16] Deck, S. “Recent Improvements in the Zonal Detached Eddy Simulation (ZDES) Formulation.” *Theoretical and Computational Fluid Dynamics*, Vol. 26, No. 6, 2012, pp. 523–550. <https://doi.org/10.1007/s00162-011-0240-z>.
- [17] Rajasekaran, J. *On the Flow Characteristics behind a Backward-Facing Step and the Design of a New Axisymmetric Model for Their Study*. Thesis. 2011.
- [18] Bradshaw, P., and Wong, F. Y. F. “The Reattachment and Relaxation of a Turbulent Shear Layer.” *Journal of Fluid Mechanics*, Vol. 52, No. 1, 1972, pp. 113–135. <https://doi.org/10.1017/S002211207200299X>.
- [19] Eaton, J. K., and Johnston, J. P. “A Review of Research on Subsonic Turbulent Flow Reattachment.” *AIAA Journal*, Vol. 19, No. 9, 1981, pp. 1093–1100. <https://doi.org/10.2514/3.60048>.
- [20] Troutt, T. R., Scheelke, B., and Norman, T. R. “Organized Structures in a Reattaching Separated Flow Field.” *Journal of Fluid Mechanics*, Vol. 143, 1984, pp. 413–427. <https://doi.org/10.1017/S0022112084001415>.
- [21] Armaly, B. F., Durst, F., Pereira, J. C. F., and Schönung, B. “Experimental and Theoretical Investigation of Backward-Facing Step Flow.” *Journal of Fluid Mechanics*, Vol. 127, 1983, pp. 473–496. <https://doi.org/10.1017/S0022112083002839>.

- [22] Le, H., Moin, P., and Kim, J. “Direct Numerical Simulation of Turbulent Flow over a Backward-Facing Step.” *Journal of Fluid Mechanics*, Vol. 330, 1997, pp. 349–374. <https://doi.org/10.1017/S0022112096003941>.
- [23] Jovic, S. *An Experimental Study of a Separated/Reattached Flow Behind a Backward-Facing Step. Re(Sub h) = 37,000*. NASA Ames Research Center, 1996.
- [24] Driver, D. M., and Seegmiller, H. L. “Features of a Reattaching Turbulent Shear Layer in Divergent Channelflow.” *AIAA Journal*, Vol. 23, No. 2, 1985, pp. 163–171. <https://doi.org/10.2514/3.8890>.
- [25] Williams, O., Samuell, M., Sarwas, E. S., Robbins, M., and Ferrante, A. Experimental Study of a CFD Validation Test Case for Turbulent Separated Flows | AIAA SciTech Forum. Presented at the SciTech, Orlando, Florida, 2020.
- [26] Song, S., DeGraa, D. B., and Eaton, J. K. “Experimental Study of a Separating, Reattaching, and Redeveloping flow over a Smoothly Contoured Ramp.” 2000, p. 8.
- [27] Song, S., and Eaton, J. K. “Flow Structures of a Separating, Reattaching, and Recovering Boundary Layer for a Large Range of Reynolds Number.” *Experiments in Fluids*, Vol. 36, No. 4, 2004, pp. 642–653. <https://doi.org/10.1007/s00348-003-0762-2>.
- [28] Song, S., and Eaton, J. K. “Reynolds Number Effects on a Turbulent Boundary Layer with Separation, Reattachment, and Recovery.” *Experiments in Fluids*, Vol. 36, No. 2, 2004, pp. 246–258. <https://doi.org/10.1007/s00348-003-0696-8>.
- [29] Wasistho, B., and Squires, K. D. “Prediction of Turbulent Separation over a Backward-Facing Smooth Ramp.” *Journal of Turbulence*, Vol. 6, 2005, p. N1. <https://doi.org/10.1080/14685240500055012>.
- [30] Radhakrishnan, S., Piomelli, U., Keating, A., and Lopes, A. S. “Reynolds-Averaged and Large-Eddy Simulations of Turbulent Non-Equilibrium Flows.” *Journal of Turbulence*, Vol. 7, 2006, p. N63. <https://doi.org/10.1080/14685240601047736>.
- [31] El-Askary, W. A. “Turbulent Boundary Layer Structure of Flow over a Smooth-Curved Ramp.” *Computers & Fluids*, Vol. 38, No. 9, 2009, pp. 1718–1730. <https://doi.org/10.1016/j.compfluid.2009.03.004>.
- [32] Seifert, A., and Pack, L. G. “Active Flow Separation Control on Wall-Mounted Hump at High Reynolds Numbers.” *AIAA Journal*, Vol. 40, No. 7, 2002, pp. 1363–1372. <https://doi.org/10.2514/2.1796>.
- [33] Koklu, M. Application of Sweeping Jet Actuators on the NASA Hump Model and Comparison with CFDVAL2004 Experiments. Presented at the AIAA AVIATION Forum, Denver, Colorado, 2017.

- [34] Otto, C., Tewes, P., Little, J. C., and Woszidlo, R. Comparison of Various Fluidic Oscillators for Separation Control on a Wall-Mounted Hump. Presented at the AIAA Scitech 2019 Forum, San Diego, California, 2019.
- [35] Postl, D., and Fasel, H. F. “Direct Numerical Simulation of Turbulent Flow Separation from a Wall-Mounted Hump.” *AIAA Journal*, Vol. 44, No. 2, 2006, pp. 263–272. <https://doi.org/10.2514/1.14258>.
- [36] Bachalo, W. D., and Johnson, D. A. “Transonic, Turbulent Boundary-Layer Separation Generated on an Axisymmetric Flow Model.” *AIAA Journal*, Vol. 24, No. 3, 1986, pp. 437–443. <https://doi.org/10.2514/3.9286>.
- [37] Abdol-Hamid, K. S., Carlson, J.-R., and Rumsey, C. L. Verification and Validation of the K-KL Turbulence Model in FUN3D and CFL3D Codes. Presented at the 46th AIAA Fluid Dynamics Conference, Washington, D.C., 2016.
- [38] Spalart, P. R., Belyaev, K. V., Garbaruk, A. V., Shur, M. L., Strelets, M. Kh., and Travin, A. K. “Large-Eddy and Direct Numerical Simulations of the Bachalo-Johnson Flow with Shock-Induced Separation.” *Flow, Turbulence and Combustion*, Vol. 99, Nos. 3–4, 2017, pp. 865–885. <https://doi.org/10.1007/s10494-017-9832-z>.
- [39] Gildersleeve, S., and Rumsey, C. Validation Experiments for Turbulent Separated Flows over Axisymmetric Afterbodies. Seattle, Washington, Nov 25, 2019.
- [40] Bell, J., Heineck, J., Zilliac, G., Mehta, R., and Long, K. Surface and Flow Field Measurements on the FAITH Hill Model. Presented at the 50th AIAA Aerospace Sciences Meeting including the New Horizons Forum and Aerospace Exposition, Nashville, Tennessee, 2012.
- [41] Rumsey, C. L., Neuhart, D., and Kegerise, M. A. The NASA Juncture Flow Experiment: Goals, Progress, and Preliminary Testing (Invited). San Diego, California, 2016.
- [42] Kegerise, M. A., and Neuhart, D. H. *An Experimental Investigation of a Wing-Fuselage Junction Model in the NASA Langley 14- by 22-Foot Subsonic Tunnel*. Publication NASA/TM-20190229286. NASA Langley Research Center, Hampton, VA, 2019, p. 200.
- [43] Lowe, T., Borgoltz, A., Devenport, W. J., Fritsch, D. J., Gargiulo, A., Duetsch-Patel, J. E., Roy, C. J., Szoke, M., and Vishwanathan, V. Status of the NASA/Virginia Tech Benchmark Experiments for CFD Validation. 2020.
- [44] Aubertine, C. D. *Reynolds Number Effects on an Adverse Pressure Gradient Turbulent Boundary Layer*. Ph.D. Thesis. Stanford University, 2005.

- [45] Vaquero, J., Renard, N., and Deck, S. “Advanced Simulations of Turbulent Boundary Layers under Pressure-Gradient Conditions.” *Physics of Fluids*, Vol. 31, No. 11, 2019, p. 115111. <https://doi.org/10.1063/1.5126932>.
- [46] Debien, A., Aubrun, S., Mazellier, N., and Kourta, A. “Salient and Smooth Edge Ramps Inducing Turbulent Boundary Layer Separation: Flow Characterization for Control Perspective.” *Comptes Rendus Mécanique*, Vol. 342, No. 6, 2014, pp. 356–362. <https://doi.org/10.1016/j.crme.2014.05.003>.
- [47] Kourta, A., Joussot, R., and Thacker, A. “Analysis and Characterization of Ramp Flow Separation.” *Experiments in Fluids*, Vol. 56, No. 5, 2015.
- [48] Jenkins, L., Gorton, S., and Anders, S. Flow Control Device Evaluation for an Internal Flow with an Adverse Pressure Gradient. Reno, Nevada, 2002.
- [49] Stratford, B. S. “An Experimental Flow with Zero Skin Friction throughout Its Region of Pressure Rise.” *Journal of Fluid Mechanics*, Vol. 5, No. 1, 1959, pp. 17–35. <https://doi.org/10.1017/S0022112059000027>.
- [50] Elsberry, K., Loeffler, J., Zhou, M. D., and Wygnanski, I. “An Experimental Study of a Boundary Layer That Is Maintained on the Verge of Separation.” *Journal of Fluid Mechanics*, Vol. 423, 2000, pp. 227–261. <https://doi.org/10.1017/S0022112000001828>.
- [51] Kumar, V. *Separation Control in Adverse Pressure Gradients Using High-Speed Microjets*. Ph.D. Thesis. Florida State University, 2008.
- [52] Koklu, M., and Owens, L. R. “Comparison of Sweeping Jet Actuators with Different Flow-Control Techniques for Flow-Separation Control.” *AIAA Journal*, Vol. 55, No. 3, 2017, pp. 848–860. <https://doi.org/10.2514/1.J055286>.
- [53] Gardarin, B., and Jacquin, L. On the Physics of Vortex Generators for Flow Separation Control. Seoul, Korea, 2009.
- [54] Zhang, H., and Fasel, H. Direct Numerical Simulations of the Turbulent Flow over a Stratford Ramp. Presented at the 14th Computational Fluid Dynamics Conference, Norfolk, VA, U.S.A., 1999.
- [55] Fasel, H. F., Gross, A., and Postl, D. *Longitudinal Vortices in Turbulent Boundary Layers Subjected to Wall Curvature and Strong Adverse Pressure Gradients: Numerical Investigations Using LES and DNS*. University of Arizona Department of Aerospace and Mechanical Engineering, 2001.
- [56] Schatzman, D. M., and Thomas, F. O. “An Experimental Investigation of an Unsteady Adverse Pressure Gradient Turbulent Boundary Layer: Embedded Shear Layer Scaling.” *Journal of Fluid Mechanics*, Vol. 815, 2017, pp. 592–642. <https://doi.org/10.1017/jfm.2017.65>.

- [57] Jones, F. E. *The Air Density Equation and the Transfer of the Mass Unit*. 1977.
- [58] Merzkirch, W. *Techniques of Flow Visualization*. AGARD, Neuilly-sur-Seine, France, 1987.
- [59] Lu, F. K. “Surface Oil Flow Visualization.” *The European Physical Journal Special Topics*, Vol. 182, No. 1, 2010, pp. 51–63.  
<https://doi.org/10.1140/epjst/e2010-01225-0>.
- [60] Maltby, R. L. *FLOW VISUALIZATION IN WIND TUNNELS USING INDICATORS*. 1962, p. 193.
- [61] Perry, A. E., and Chong, M. S. Interpretation of Flow Visualization. In *Flow Visualization : Techniques and Examples* (Lim, T.T. and A. J. Smits, eds.), Imperial College Press, Singapore, UNITED STATES, 2014.
- [62] *Flow-Visualization Techniques Used at High Speed by Configuration Aerodynamics Wind-Tunnel-Test Team*. Publication NASA/TM-2001-210848. Langley Research Center, Hampton, Virginia, 2001.
- [63] 7.3.2 Viscosity as a Function of Temperature. *Fluent Incorporated*.  
<http://jullio.pe.kr/fluent6.1/help/html/ug/node294.htm>. Accessed Nov. 22, 2019.
- [64] Gregory Zilliac. *Further Developments of the Fringe-Imaging Skin Friction Technique*. Publication NASA-TM-110425. NASA Ames Research Center, Moffett Field, California, 1996.
- [65] P. S. Klebanoff. *Characteristics of Turbulence in Boundary Layer with Zero Pressure Gradient*. Publication NACA-TR-1247. National Advisory Committee for Aeronautics, 1955.
- [66] Nagib, H. M., and Chauhan, K. A. “Variations of von Kármán Coefficient in Canonical Flows.” *Physics of Fluids*, Vol. 20, No. 10, 2008.  
<https://doi.org/10.1063/1.3006423>.
- [67] Hutchins, N., Nickels, T. B., Marusic, I., and Chong, M. S. “Hot-Wire Spatial Resolution Issues in Wall-Bounded Turbulence | Journal of Fluid Mechanics | Cambridge Core.” *Journal of Fluid Mechanics*, Vol. 635, 2009, pp. 103–136.
- [68] Ligrani, P. M., and Bradshaw, P. “Spatial Resolution and Measurement of Turbulence in the Viscous Sublayer Using Subminiature Hot-Wire Probes.” *Experiments in Fluids*, Vol. 5, No. 6, 1987, pp. 407–417.  
<https://doi.org/10.1007/BF00264405>.
- [69] Mathis, R., Hutchins, N., and Marusic, I. Scaling of Inner and Outer Regions for FLat Plate Boundary Layers. Presented at the 17th Australasian Fluid Mechanics Conference, Auckland, New Zealand, 2010.

- [70] Tobak, M., and Peake, and D. J. “Topology of Three-Dimensional Separated Flows.” *Annual Review of Fluid Mechanics*, Vol. 14, No. 1, 1982, pp. 61–85. <https://doi.org/10.1146/annurev.fl.14.010182.000425>.
- [71] Stratford, B. S. “The Prediction of Separation of the Turbulent Boundary Layer.” *Journal of Fluid Mechanics*, Vol. 5, No. 1, 1959, pp. 1–16. <https://doi.org/10.1017/S0022112059000015>.
- [72] Kumar, V. *Flow Control in Adverse Pressure Gradient Using Supersonic Microjets*. Master’s Thesis. Florida State University, 2003.
- [73] Kumar, V., and Alvi, F. S. “Use of High-Speed Microjets for Active Separation Control in Diffusers.” *AIAA Journal*, Vol. 44, No. 2, 2006, pp. 273–281. <https://doi.org/10.2514/1.8552>.
- [74] Kumar, V., and Alvi, F. S. “Toward Understanding and Optimizing Separation Control Using Microjets.” *AIAA Journal*, Vol. 47, No. 11, 2009, pp. 2544–2557. <https://doi.org/10.2514/1.38868>.
- [75] Fairlie, B. D. Flow Separation on Bodies of Revolution at Incidence. Presented at the 7th Australasian Hydraulics and Fluid Mechanics Conference, Brisbane, 1980.
- [76] Koklu, M. “Effects of Sweeping Jet Actuator Parameters on Flow Separation Control.” *AIAA Journal*, Vol. 56, No. 1, 2017, pp. 100–110. <https://doi.org/10.2514/1.J055796>.
- [77] Délery, J. *Three-Dimensional Separated Flow Topology: Critical Points, Separation Lines and Vortical Structures*. Wiley-ISTE, 2013.
- [78] Anderson, B. H., Reddy, D. R., and Kapoor, K. “Study on Computing Separating Flows within a Diffusion Inlet S-Duct.” *Journal of Propulsion and Power*, Vol. 10, No. 5, 1994, pp. 661–667. <https://doi.org/10.2514/3.23777>.
- [79] Lin, J. C. *Control of Low-Speed Turbulent Separated Flow over a Backward-Facing Ramp*. Ph.D. Thesis. Old Dominion University, 1992.
- [80] Wang, M., and Zhou, D. Private Communication. , 2018.
- [81] Andronov, A. A., Leontovich, E. A., Gordon, I. I., and Maier, A. G. *Qualitative Theory of Second-Order Dynamic Systems*. John Wiley & Sons, New York and Toronto, 1973.
- [82] Strogatz, S. *Nonlinear Dynamics and Chaos: With Applications to Physics, Biology, Chemistry, and Engineering*. Westview Press, 2015.
- [83] Délery, J. M. “Robert Legendre and Henri Werlé: Toward the Elucidation of Three-Dimensional Separation.” *Annual Review of Fluid Mechanics*, Vol. 33, No. 1, 2001, pp. 129–154. <https://doi.org/10.1146/annurev.fluid.33.1.129>.

- [84] Hunt, J. C. R., Abell, C. J., Peterka, J. A., and Woo, H. “Kinematical Studies of the Flows around Free or Surface-Mounted Obstacles; Applying Topology to Flow Visualization.” *Journal of Fluid Mechanics*, Vol. 86, No. 1, 1978, pp. 179–200. <https://doi.org/10.1017/S0022112078001068>.
- [85] Dallmann, U. Structural Stability of Three-Dimensional Vortex Flows. In *Nonlinear Dynamics of Transcritical Flows: Proceedings of a DFVLR International Colloquium, Bonn, Germany, March 1984* (H. L. Jordan, H. O. jr, and K. Robert, eds.), Springer-Verlag, Berlin Heidelberg, 1985.
- [86] Chapman, G. T., and Yates, L. A. “Topology of Flow Separation on Three-Dimensional Bodies.” *Applied Mechanics Reviews*, Vol. 44, No. 7, 1991, pp. 329–345. <https://doi.org/10.1115/1.3119507>.
- [87] Ünal, A. “Three-Dimensional Singular Points in Aerodynamics.” *NASA Technical Memorandum*, p. 18.
- [88] Abraham, R., and Shaw, C. *Dynamics: The Geometry of Behavior: Part 1: Periodic Behavior*. Aerial Press, 2016.
- [89] Uranga, A., Drela, M., Greitzer, E., Titchener, N., Lieu, M., Siu, N., Huang, A., Gatlin, G. M., and Hannon, J. Preliminary Experimental Assessment of the Boundary Layer Ingestion Benefit for the D8 Aircraft. Presented at the 52nd Aerospace Sciences Meeting, National Harbor, Maryland, 2014.
- [90] Wicks, M., Thomas, F. O., Corke, T. C., Patel, M., and Cain, A. B. “Mechanism of Vorticity Generation in Plasma Streamwise Vortex Generators.” *AIAA Journal*, Vol. 53, No. 11, 2015, pp. 3404–3413. <https://doi.org/10.2514/1.J053997>.
- [91] Perry, A. E., and Hornung, H. “Some Aspects of Three-Dimensional Separation. II - Vortex Skeletons.” *Zeitschrift fur Flugwissenschaften und Weltraumforschung*, Vol. 8, 1984, pp. 155–160.
- [92] Chong, M. S., and Perry, A. E. “Synthesis of Two- and Three-Dimensional Separation Bubbles.” *9th Australasian Fluid Mechanics Conference, Auckland*, 1986.
- [93] Akilli, H., and Rockwell, D. “Vortex Formation from a Cylinder in Shallow Water.” *Physics of Fluids*, Vol. 14, No. 9, 2002, pp. 2957–2967. <https://doi.org/10.1063/1.1483307>.
- [94] Hansen, K. L., Rostamzadeh, N., Kelso, R. M., and Dally, B. B. “Evolution of the Streamwise Vortices Generated between Leading Edge Tubercles.” *Journal of Fluid Mechanics*, Vol. 788, 2016, pp. 730–766. <https://doi.org/10.1017/jfm.2015.611>.

- [95] Wickens, R. H. *The Vortex Wake and Aerodynamic Load Distribution of Slender Rectangular Plates (The Effects of a 20-Degree Bend at Mid-Chord)*. Publication LR-458. National Research Council, Canada, 1966.
- [96] Tobak, M., and Peake, D. Topology of Two-Dimensional and Three-Dimensional Separated Flows. In *12th Fluid and Plasma Dynamics Conference*, American Institute of Aeronautics and Astronautics, 1979.
- [97] Surana, A., Grunberg, O., and Haller, G. “Exact Theory of Three-Dimensional Flow Separation. Part 1. Steady Separation.” *Journal of Fluid Mechanics*, Vol. 564, 2006, p. 57. <https://doi.org/10.1017/S0022112006001200>.
- [98] Wang, K. C. “Boundary Layer Over a Blunt Body at High Incidence with an Open-Type of Separation.” *Proceedings of the Royal Society A: Mathematical, Physical and Engineering Sciences*, Vol. 340, No. 1620, 1974, pp. 33–55. <https://doi.org/10.1098/rspa.1974.0139>.
- [99] Tobak, M. Topological Aspects of the FAITH Experiment. Jan 07, 2010.
- [100] Detra, R. *The Secondary Flow in Curved Pipes*. The Swiss Federal Institute of Technology, Zurich, Switzerland, 1953.
- [101] Kirk, A. *ACTIVE FLOW CONTROL IN AN ADVANCED SERPENTINE JET ENGINE INLET DUCT*. Master’s Thesis. Texas A&M University, College Station, TX, 2006.
- [102] Anderson, H. A Study of Three Dimensional Turbulent Boundary Layer Separation and Vortex Flow Control Using the Reduced Navier Stokes Equations. Presented at the Turbulent Shear Flow Symposium, Munich, Germany.
- [103] Wellborn, S., Reichert, B., and Okiishi, T. An Experimental Investigation of the Flow in a Diffusing S-Duct. 1992.
- [104] Meyer, R., W. Bechert, D., and Hage, W. Secondary Flow Control on Compressor Blades to Improve the Performance of Axial Turbomachines. 2003.
- [105] Pearcey, H. H. INTRODUCTION TO SHOCK-INDUCED SEPARATION AND ITS PREVENTION BY DESIGN AND BOUNDARY LAYER CONTROL. In *Boundary Layer and Flow Control* (G. V. Lachmann, ed.), Pergamon, 1961, pp. 1166–1344.
- [106] Pauley, W. R., and Eaton, J. K. “Experimental Study of the Development of Longitudinal Vortex Pairs Embedded in a Turbulent Boundary Layer.” *AIAA Journal*, Vol. 26, No. 7, 1988, pp. 816–823. <https://doi.org/10.2514/3.9974>.
- [107] Simpson, R. L. “Review—A Review of Some Phenomena in Turbulent Flow Separation.” *Journal of Fluids Engineering*, Vol. 103, No. 4, 1981, pp. 520–533. <https://doi.org/10.1115/1.3241761>.

- [108] Simpson, R. L. *Summary Report on the Colloquium on Flow Separation*. Publication SMU-3-PU. 1979.
- [109] Simpson, R. L., Strickland, J. H., and Barr, P. W. “Features of a Separating Turbulent Boundary Layer in the Vicinity of Separation.” *Journal of Fluid Mechanics*, Vol. 79, No. 3, 1977, pp. 553–594. <https://doi.org/10.1017/S0022112077000329>.
- [110] Ashjaee, J., and Johnston, J. P. “Straight-Walled, Two-Dimensional Diffusers—Transitory Stall and Peak Pressure Recovery.” *Journal of Fluids Engineering*, Vol. 102, No. 3, 1980, pp. 275–282. <https://doi.org/10.1115/1.3240680>.
- [111] Alving, A. E., and Fernholz, H. H. “Turbulence Measurements around a Mild Separation Bubble and Downstream of Reattachment.” *Journal of Fluid Mechanics*, Vol. 322, 1996, pp. 297–328. <https://doi.org/10.1017/S0022112096002807>.
- [112] Peterson, C. J., Vukasinovic, B., and Glezer, A. Control of a Closed Separation Domain in Adverse Pressure Gradient Over a Curved Surface. 2019.
- [113] Stella, F., Mazellier, N., and Kourta, A. “Scaling of Separated Shear Layers: An Investigation of Mass Entrainment.” *Journal of Fluid Mechanics*, Vol. 826, 2017, pp. 851–887. <https://doi.org/10.1017/jfm.2017.455>.
- [114] Dandois, J., Garnier, E., and Sagaut, P. “Numerical Simulation of Active Separation Control by a Synthetic Jet.” *Journal of Fluid Mechanics*, Vol. 574, 2007, pp. 25–58. <https://doi.org/10.1017/S0022112006003995>.
- [115] Marušić, I., and Perry, A. E. “A Wall-Wake Model for the Turbulence Structure of Boundary Layers. Part 2. Further Experimental Support.” *Journal of Fluid Mechanics*, Vol. 298, 1995, pp. 389–407. <https://doi.org/10.1017/S0022112095003363>.
- [116] Coles, D. E., and Hirst, E. A. *Computation of Turbulent Boundary Layers; 1968 AFOSR-IFP-Stanford Conference*; [Stanford] Calif., Thermosciences Division, Stanford University, 1969.
- [117] Peterson, C. J., Vukasinovic, B., and Glezer, A. Characterization of Controlled Flow Separation. Presented at the SciTech Forum, 2018.
- [118] Bell, J. H., and Mehta, R. D. “Development of a Two-Stream Mixing Layer from Tripped and Untripped Boundary Layers.” *AIAA Journal*, Vol. 28, No. 12, 1990, pp. 2034–2042. <https://doi.org/10.2514/3.10519>.
- [119] Browand, F. K., and Troutt, T. R. “The Turbulent Mixing Layer: Geometry of Large Vortices.” *Journal of Fluid Mechanics*, Vol. 158, 1985, pp. 489–509. <https://doi.org/10.1017/S0022112085002737>.

- [120] Cherry, N. J., Hillier, R., and Latour, M. E. M. P. “Unsteady Measurements in a Separated and Reattaching Flow.” *Journal of Fluid Mechanics*, Vol. 144, 1984, pp. 13–46. <https://doi.org/10.1017/S002211208400149X>.
- [121] Hoffmann, P. H., Muck, K. C., and Bradshaw, P. “The Effect of Concave Surface Curvature on Turbulent Boundary Layers.” *Journal of Fluid Mechanics*, Vol. 161, 1985, pp. 371–403. <https://doi.org/10.1017/S0022112085002981>.
- [122] M C So, R., and Mellor, G. L. “Experiment on Turbulent Boundary Layers on a Concave Wall.” *Aeronautical Quarterly*, Vol. 26, No. 01, 1975, pp. 25–40. <https://doi.org/10.1017/S0001925900007174>.
- [123] Gibson, M. M., Verriopoulos, C. A., and Vlachos, N. S. “Turbulent Boundary Layer on a Mildly Curved Convex Surface.” *Experiments in Fluids*, Vol. 2, No. 1, 1984, pp. 17–24. <https://doi.org/10.1007/BF00266314>.
- [124] Muck, K. C., Hoffmann, P. H., and Bradshaw, P. “The Effect of Convex Surface Curvature on Turbulent Boundary Layers.” *Journal of Fluid Mechanics*, Vol. 161, 1985, pp. 347–369. <https://doi.org/10.1017/S002211208500297X>.
- [125] So, R. M. C., and Mellor, G. L. “Experiment on Convex Curvature Effects in Turbulent Boundary Layers.” *Journal of Fluid Mechanics*, Vol. 60, No. 1, 1973, pp. 43–62. <https://doi.org/10.1017/S0022112073000030>.
- [126] MERONEY, R. N., and BRADSHAW, P. “Turbulent Boundary-Layer Growth over a Longitudinally Curved Surface.” *AIAA Journal*, Vol. 13, No. 11, 1975, pp. 1448–1453. <https://doi.org/10.2514/3.7014>.
- [127] Ramaprian, B. R., and Shivaprasad, B. G. “The Structure of Turbulent Boundary Layers along Mildly Curved Surfaces.” *Journal of Fluid Mechanics*, Vol. 85, No. 2, 1978, pp. 273–303. <https://doi.org/10.1017/S0022112078000646>.
- [128] Patel, V. C., and Sotiropoulos, F. “Longitudinal Curvature Effects in Turbulent Boundary Layers.” *Progress in Aerospace Sciences*, Vol. 33, No. 1, 1997, pp. 1–70. [https://doi.org/10.1016/S0376-0421\(96\)00001-2](https://doi.org/10.1016/S0376-0421(96)00001-2).
- [129] Cullen, L., Nishri, B., Greenblatt, D., and Wygnanski, I. The Effect of Curvature on Boundary Layers Subjected to Strong Adverse Pressure Gradients. Presented at the 40th AIAA Aerospace Sciences Meeting & Exhibit, Reno,NV,U.S.A., 2002.
- [130] Plesniak, M. W., Mehta, R. D., and Johnston, J. P. “Curved Two-Stream Turbulent Mixing Layers Revisited.” *Experimental Thermal and Fluid Science*, Vol. 13, No. 3, 1996, pp. 190–205. [https://doi.org/10.1016/S0894-1777\(96\)00080-5](https://doi.org/10.1016/S0894-1777(96)00080-5).

- [131] Margolis, D. p., and Lumley, J. L. “Curved Turbulent Mixing Layer.” *The Physics of Fluids*, Vol. 8, No. 10, 1965, pp. 1775–1784.  
<https://doi.org/10.1063/1.1761109>.
- [132] Gibson, M. M., and Younis, B.A. “Turbulence Measurements in a Developing Mixing Layer with Mild Destabilising Curvature | SpringerLink.” *Experiments in Fluids*, Vol. 1, 1983, pp. 23–30.
- [133] Jenkins, L. N., Yao, C.-S., and Bartram, S. M. Flow-Field Measurements in a Wing-Fuselage Junction Using an Embedded Particle Image Velocimetry System. Presented at the AIAA Scitech 2019 Forum, San Diego, California, 2019.
- [134] ASME PTC 19.1 - 2005 *Test Uncertainty*. ASME, 2005.
- [135] Finn E. Jorgensen. How to Measure Turbulence with Hot-Wire Anemometers - a Practical Guide.
- [136] DeGraaff, D. B., and Eaton, J. K. “A High-Resolution Laser Doppler Anemometer: Design, Qualification, and Uncertainty.” *Experiments in Fluids*, Vol. 30, No. 5, 2001, pp. 522–530. <https://doi.org/10.1007/s003480000231>.
- [137] Benedict, L. H., and Gould, R. D. “Towards Better Uncertainty Estimates for Turbulence Statistics.” *Experiments in Fluids*, Vol. 22, No. 2, 1996, pp. 129–136.  
<https://doi.org/10.1007/s003480050030>.
- [138] Yeh, T. T., and Hall, J. M. “NIST Special Publication 250-79 Airspeed Calibration Service.” *Special Publication (NIST SP) - 250-79*, 2007.  
<http://dx.doi.org/10.1002/https://dx.doi.org/10.6028/NIST.SP.250-79>.
- [139] Edwards, R. V. “Report of the Special Panel on Statistical Particle Bias Problems in Laser Anemometry.” *Journal of Fluids Engineering*, Vol. 109, No. 2, 1987, pp. 89–93. <https://doi.org/10.1115/1.3242646>.
- [140] LDA and PDA Reference Manual.